

**UNIVERSIDADE DE LISBOA
INSTITUTO SUPERIOR TÉCNICO**

**GRAVITATIONAL WAVES AND THE
GALACTIC POTENTIAL**

FRANCISCO MIGUEL BATISTA DUQUE

Supervisor : Doctor Vítor Manuel dos Santos Cardoso

**Thesis approved in public session to obtain the PhD degree in
PHYSICS**

Jury final classification: PASS WITH DISTINCTION AND HONOUR

2023

UNIVERSIDADE DE LISBOA
INSTITUTO SUPERIOR TÉCNICO

**GRAVITATIONAL WAVES AND THE GALACTIC
POTENTIAL**

FRANCISCO MIGUEL BATISTA DUQUE

Supervisor : Doctor Vitor Manuel dos Santos Cardoso

**Thesis approved in public session to obtain the PhD degree in
PHYSICS**

Jury final classification: PASS WITH DISTINCTION AND HONOUR

JURY

CHAIRPERSON :

Doctor Ilídio Pereira Lopes, Instituto Superior Técnico da Universidade de Lisboa

MEMBERS OF THE COMMITTEE :

Doctor Scott Alexander Hughes, Massachusetts Institute of Technology, EUA

Doctor Gaurav Khanna, The University of Rhode Island, EUA

Doctor Ilídio Pereira Lopes, Instituto Superior Técnico da Universidade de Lisboa

Doctor Vítor Manuel dos Santos Cardoso, Instituto Superior Técnico da Universidade de
Lisboa

Doctor Andrea Maselli, Gran Sasso Science Institute, Itália

Doctor David Matthew Hilditch, Instituto Superior Técnico da Universidade de Lisboa

FUNDING INSTITUTION:

Fundação para a Ciência e Tecnologia

2023

GRAVITATIONAL WAVES AND THE GALACTIC POTENTIAL

FRANCISCO MIGUEL BATISTA DUQUE



JUNE 2023

ESTILO

Se eu quisesse, enlouquecia. Sei uma quantidade de histórias terríveis. Vi muita coisa, contaram-me casos extraordinários, eu próprio... Enfim, às vezes já não consigo arrumar tudo isso. Porque, sabe?, acorda-se às quatro da manhã num quarto vazio, acende-se um cigarro... Está a ver? A pequena luz do fósforo levanta de repente a massa das sombras, a camisa caída sobre a cadeira ganha um volume impossível, a nossa vida... (...) Há felizmente o estilo. Não calcula o que seja? Vejamos: o estilo é o modo subtil de transferir a confusão e a violência da vida para um plano mental de uma unidade de significação. (...) É forçoso encontrar um estilo. Seria bom colocar grandes cartazes nas ruas, fazer avisos na televisão e cinemas. Procure o seu estilo, se não quer dar em pantanas. Arranji o meu estilo estudando matemática e ouvindo um pouco de música. - João Sebastião Bach. Conhece o Concerto Brandeburguês n.º 5? Conhece com certeza essa coisa tão simples, tão harmoniosa e definitiva que é um sistema de três equações a três incógnitas. Primário, rudimentar. Resolvi milhares de equações. Depois ouvia Bach. Consegui um estilo. Aplico-o à noite, quando acordo às quatro da madrugada (...)

— Herberto Helder em "Os Passos em Volta"

Dedicado à minha avó Maria e à minha avó Peta.

RESUMO

O progresso rápido e recente da astronomia de ondas gravitacionais tornou necessário modelar fontes cada vez mais complexas. Durante a próxima década, interferómetros de terceira geração e a missão espacial LISA observarão binárias em centros galácticos envolvendo buracos negros supermassivos com milhões de massas solares. O seu sinal diferirá substancialmente das mais “comuns” binárias de buracos negros de igual massa que têm dominado as detecções de ondas gravitacionais. Medições mais precisas de eventos mais extremos que excitam campos gravitacionais mais fortes podem ter um impacto tremendo em física fundamental, astrofísica e cosmologia. Porém, à escala galáctica, discos de acreção, halos de matéria escura e densas populações de objectos compactos podem interagir gravitacionalmente com corpos em coalescência. O papel que estas estruturas astrofísicas desempenham na evolução e respectiva assinatura de ondas gravitacionais de sistemas binários continua por explorar e estudos prévios dependeram com frequência de aproximações Newtonianas ad-hoc. Nesta tese, pretendemos melhorar este panorama e responder a questões como: podem ambientes de não-vácuo comprometer testes de Relatividade Geral e da natureza de buracos negros? Podemos colocar constrangimentos nas propriedades de ambientes astrofísicos com futuras observações de ondas gravitacionais? Em particular, estudamos como deformações de maré de matéria presente à volta de buracos negros podem mascarar desvios a Relatividade Geral, ou destruir estruturas “cabeludas” que poderiam sinalizar a existência de candidatos de matéria escura como campos bosónicos ultraleves. Também exploramos a conexão profunda entre anéis de luz - órbitas fechadas de partículas sem massa - e os modos próprios de oscilação de objectos compactos. Mostramos que, independentemente da presença de um ambiente, o anel de luz controla como observadores distantes vêem matéria a cair num buraco negro, ou como o buraco negro final formado numa colisão relaxa para estacionariedade. Finalmente, desenvolvemos o primeiro *framework* completamente relativista capaz de estudar emissão de ondas gravitacionais em ambientes de não-vácuo. Aplicamo-lo a binárias de buracos negros galácticas rodeadas por um halo de matéria escura e observamos a conversão entre ondas de matéria e ondas gravitacionais. Este acoplamento resulta em diferenças significativas no fluxo de energia emitido, que poderão ajudar a constrangir as propriedades de distribuições galácticas de matéria. Os nossos métodos podem tornar-se a ferramenta de referência para estudos de efeitos de ambiente em astronomia de ondas gravitacionais

e ser implementado em *pipelines* de análise de dados de colaborações futuras.

PALAVRAS-CHAVE: relatividade geral; buracos negros; ondas gravitacionais, efeitos de ambiente, matéria escura.

ABSTRACT

The rapid progress of gravitational-wave astronomy in recent years has raised the need to model increasingly more complex sources. Over the next decade, third-generation interferometers and the space-based LISA mission will observe binaries in galactic centers involving supermassive black holes with millions of solar masses. Their signal will differ substantially from the more “standard” equal-mass black-hole binaries that have dominated gravitational-wave detections. More precise measurements of more extreme events that probe stronger gravitational fields can have a tremendous impact on fundamental physics, astrophysics, and cosmology. However, at the galactic scale, accretion disks, dark matter halos, and dense populations of compact objects can interact gravitationally with coalescing bodies. The role these astrophysical structures play in the evolution and gravitational-wave signature of binary systems remains largely unexplored and previous studies have often relied on ad-hoc Newtonian approximations. In this thesis, we aim to improve this picture and answer questions like: Can non-vacuum environments jeopardize tests of General Relativity and of the nature of black holes? Can we constrain the properties of astrophysical environments from future gravitational-wave observations? In particular, we study how tidal deformations of matter surrounding black holes can mask off deviations from General Relativity, or destroy “hairy” structures that could signal the existence of dark matter candidates like ultralight bosonic fields. We also explore the deep connection between light rings - closed orbits of massless particles - and the proper oscillation modes of compact objects. We show that independently of the presence of an environment, the light ring controls the late-time appearance of infalling matter to distant observers and how the final black hole formed in a collision relaxes to stationarity. Finally, we develop the first fully-relativistic framework capable of studying gravitational wave emission in non-vacuum environments. We apply it to galactic black-hole binaries surrounded by a dark matter halo and observe the conversion between matter and gravitational waves. This coupling results in significant changes in the energy flux emitted, which could help constraining the properties of galactic matter distributions. Our methods can become the benchmarking tool for studies of environmental effects in gravitational-wave astronomy and be implemented in the data analysis pipelines of future collaborations.

KEY-WORDS: general relativity; black holes; gravitational waves; environmental effects, dark matter;

PUBLICATIONS

Most of this doctoral thesis is based on the following publications:

V. Cardoso, K. Destounis, F. Duque, R. A. Macedo, A. Maselli, *Gravitational waves from extreme-mass-ratio systems in astrophysical environments*, Phys. Rev. Lett. 129 (2022) 24, 241103; [arXiv:2210.01133 \[gr-qc\]](#)

E. Berti, V. Cardoso, M. Ho-Yeuk Cheung, F. Di Filippo, F. Duque, P. Martens, S. Mukohyama, *Stability of the fundamental quasinormal mode in time-domain observations against small perturbations*, Phys. Rev. D106 (2022) 8, 084011; [arXiv:2205.08547 \[gr-qc\]](#).

V. Cardoso, F. Duque, *Resonances, black hole mimickers, and the greenhouse effect: Consequences for gravitational-wave physics*, Phys. Rev. D105 (2022) 10, 104023; [arXiv:2204.05315 \[gr-qc\]](#).

V. Cardoso, K. Destounis, F. Duque, R. A. Macedo, A. Maselli, *Black holes in galaxies: Environmental impact on gravitational-wave generation and propagation*, Phys. Rev. D105 (2022) 6, L061501; [arXiv:2109.00005 \[gr-qc\]](#).

V. Cardoso, F. Duque, A. Foschi, *Light ring and the appearance of matter accreted by black holes*, Phys. Rev. D103 (2021) 10, 104044; [arXiv:2102.07784 \[gr-qc\]](#).

V. Cardoso, F. Duque, G. Khanna, *Gravitational tuning forks and hierarchical triple systems*, Phys. Rev. D103 (2021) 8, L081501; [arXiv:2101.01186 \[gr-qc\]](#).

V. Cardoso, F. Duque, Taishi Ikeda, *Tidal effects and disruption in superradiant clouds: a numerical investigation*, Phys. Rev. D101 (2020) 6, 064054; [arXiv:2001.01729 \[gr-qc\]](#).

V. Cardoso, F. Duque, *Environmental effects in gravitational-wave physics: Tidal deformability of black holes immersed in matter*, Phys. Rev. D101 (2020) 6, 064028; [arXiv:1912.07616 \[gr-qc\]](#).

During the years of my doctoral program, I also coauthored the following works (not discussed in this thesis):

V. Cardoso, F. Duque, A. Maselli, D. Pereniguez, *The dipolar death of massive gravity*; [arXiv:2304.01252](#) [gr-qc]

V. Baibhav, M. Ho-Yeuk Cheung, E. Berti, V. Cardoso, G. Carullo, R. Cotesta, W. Del Pozzo, F. Duque, *Agnostic black hole spectroscopy: quasinormal mode content of numerical relativity waveforms and limits of validity of linear perturbation theory*; [arXiv:2302.03050](#) [gr-qc]

V. Baibhav, M. Ho-Yeuk Cheung, E. Berti, V. Cardoso, G. Carullo, R. Cotesta, W. Del Pozzo, F. Duque, *Nonlinear Effects in Black Hole Ringdown*, *Phys. Rev. Lett.* 130 (2023) 8, 8; [arXiv:2210.01133](#) [gr-qc]

AGRADECIMENTOS

É difícil escapar aos lugares comuns e desfile sentimentalista que se reservam aos agradecimentos de uma tese. Porém, ao fim de quatro anos de labuta sinto-me na ousadia de arriscar algo que destoe da minha natureza lacônica.

Começo por agradecer à Fundação para a Ciência e Tecnologia pelo apoio financeiro através da bolsa SFRH/BD/143657/2019. Também agradeço o suporte da European Union's 2020 ERC Consolidator Grant "Matter and strong-field gravity: New frontiers in Einstein's theory" grant agreement no. MaGRaTh-646597, European Union's H2020 ERC Advanced Grant "Black holes: gravitational engines of discovery" grant agreement no. Gravitas-101052587, e ajuda financeira para networking da GWverse COST Action CA16104, "Black holes, gravitational waves and fundamental physics." e da bolsa Marie Skłodowska-Curie No. 101007855.

Tratado o parágrafo burocrata, agradeço aos colegas com quem tive a oportunidade de trabalhar e me divertir ao longo deste doutoramento. A todo o GRIT, em especial aos meus "irmãos" científicos Arianna, David, Lorenzo e Rodrigo, pelos momentos de intenso debate e ainda mais intenso deboche. Quero também agradecer aqueles que durante as minhas visitas mais longas ao estrangeiro me faziam sentir em casa com a sua hospitalidade: aos *strongers* que fazem de Copenhaga uma cidade latina; ao *bon vivant* Andrea Maselli pelos conselhos académicos e gastronómicos; ao Gaurav Khanna, ao Nur Rifat, à Asia Haque e ao restante grupo de gravidade da UMass Dartmouth; ao Scott Hughes e ao seu grupo no MIT; e ao Emanuele Berti e a sua *mafia* da Johns Hopkins University, em particular ao Andrea Antonelli e ao Nick Speeney. Um obrigado também ao João Paulo e à Rita - que também são colegas - por tornarem toda a logística não-científica tão fácil.

Canta a sabedoria popular que um bom aluno é obra de um bom professor, e eu fui apapricado com o *filet mignon* da orientação científica. Muitas vezes me perguntam como é que trabalhar com o Vitor Cardoso, esse Sansão da gravitação. Talvez a gravidade quântica esteja escondida nos seus cabelos. Costumo responder que "é uma experiência". Daqui a alguns anos, gostava de não ter saudades das chamadas de Skype às 7 da manhã ao fim-de-semana, pois será sinal de que continuaremos a trabalhar juntos e elas lá acontecerão invariavelmente. Podia florir mais algumas palavras pomposas, mas sei que a melhor forma de lhe agradecer toda a ajuda que me dá é ir trabalhar no próximo artigo. Para lá caminho.

Quero também deixar um obrigado às minhas professoras Adelaide e Clara, por me ensinarem a importância da visão crítica. Curioso que

um aluno de Física recorde como mais marcantes as suas aulas de Português e Filosofia. Penso que não há maior elogio que lhes possa fazer. Numa mão a pena e noutra o ábaco.

Tenho também que agradecer ao meu primo Ruben pelo volume impossível de conselhos que me oferece desde que tenho idade para me lembrar de algo. É forçoso encontrar um estilo, e ele ajudou-me a encontrar o meu.

Ensaiei várias vezes um parágrafo dedicado a todos os meus amigos. Iguais vezes tive de o apagar. Sei que munidos de vaidade, só abriram esta tese para verem o vosso nome esparrado nos agradecimentos e desistirem ao fim da terceira página da Introdução. *Kaputt*. Infelizmente para vós, tenho a sorte de poder dizer que se tentasse agradacer a cada um, este parágrafo rapidamente se transformaria num capítulo por si só. Não preciso de vos nomear *a la* memorial da guerra para saberem que são merecedores de aqui estar. Enfim, é a minha queda para a iconoclastia. Um poema de João Luís Barreto Guimarães diz que "Segundo Albert Einstein o tempo/ não passa de igual modo para mim/ (que estou aqui sentado) e para aquele que/ ali vai a correr./ Tanto pior para mim. A Física só traz problemas. O sol/ (dentro de instantes) passará exactamente/ por entre os/ gargalos das garrafas que estivemos/ a beber. É o solstício da amizade./ A qualquer dia/ do ano." A Física está correcta. Espero que o resto também se verifique e o resto são gafanhotos.

Falta-me o obrigado aqueles que tiveram que lidar no dia a dia com a frustração, por vezes ira, inerente a uma ocupação que consiste em estar metade do tempo perdido sem saber bem o que fazer. Primeiro, à Carolina por me ensinar que a bondade é mais bela que o binómio de Newton. Falta escrevermos um artigo juntos.

Quis o acaso que em 2014 me sentasse ao lado da Beatriz numa aula de Relatividade de uma escola de Verão de Física da Universidade do Porto. Desde então tem sido a minha binária dançante, que por fim coalesceu. O que seria de uns agradecimentos de uma tese de Física sem um jogo de palavras carrascão de cariz romântico. Equações de Eins tein? Metafísica? Prova da existência de Deus? *Pathos*? Passarola Voadora? Tudo isto existe, tudo isto é Fado.

Por fim os Pais, de que sou Filho e Espírito Santo. Um obrigado à minha Mãe pela infundável paciência e carinho com que garante a minha sobrevivência. Deus quer, o Homem sonha, a Mãe cuida, a Obra nasce. E findado este gongórico devaneio, falta-me rasgo para honrar com palavras aquilo que o meu Pai tanto merece. Como o corte de um *haiku*, amo com um amor mais forte e mais profundo, aquela praia extasiada e nua, e a cadeira ao teu lado na mesa de jantar.

CONTENTS

Gravitational Waves and the Galactic Potential

1	Introduction	3
1.1	The GWzoic	3
1.2	Galactic Centers: gravity’s potluck	5
1.2.1	How many? Many...	5
1.2.2	Surfing the waves	6
1.2.3	The unbearable darkness of...	8
1.2.4	Third wheels	9
1.3	Structure of the thesis	10
2	Theory and Numerical Framework	13
2.1	Theory	13
2.1.1	Action and Equations of Motion	13
2.1.2	The Kerr spacetime	14
2.1.3	Black-Hole Perturbations	16
2.2	Numerical Framework	22
2.2.1	The Lax-Wendroff algorithm	22
2.2.2	A practical case: the Teukolsky equation	24
2.2.3	Hyperboloidal layers	29
I	Tides	
3	Deformability of black holes immersed in matter	35
3.1	A Brief History of Tidal Love Numbers	35
3.2	Newtonian Shell	36
3.3	Tidal deformability in General Relativity	40
3.4	Black holes surrounded by matter	41
3.4.1	Black holes with short hair	41
3.4.2	Matter away from the horizon: Thin shells	45
3.5	Implications for tests of fundamental physics	52
3.5.1	Binaries in astrophysical settings	53
3.5.2	On the minimum measurable TLN	54
4	Tidal effects in superradiant clouds	55
4.1	Setup	56
4.2	Weak tides: transitions to new stationary states	60
4.3	Strong tides: tidal disruption of clouds	63
4.4	Astrophysical systems	64
4.5	Discussion	66
II	Light-ring and the ringdown	
5	One ring to rule them all	69
5.1	Light-rings: the key to compact objects	71
5.2	How do bright objects fade out?	73

5.2.1	An outward-pointing beam	73
5.2.2	An isotropically-emitting star	76
5.2.3	An isotropic body emitting scalar waves	78
5.2.4	An infalling binary	81
5.3	Testing Horizons	82
5.4	Discussion	84
6	The Elephant the Flea	87
6.1	Perturbations of the potential	88
6.2	Stability of the waveform	90
6.3	Extraction of QNM frequencies	93
6.3.1	The full time-domain signal	94
6.3.2	The prompt ringdown	96
6.4	Discussion	97
7	Resonances in black hole mimickers	99
7.1	Toy Model: A Constant-Density Star	100
7.2	The build-up time of black hole mimickers	100
7.2.1	A scattering approach	100
7.2.2	Resonances and forced oscillators	102
7.3	Numerical Results	103
7.3.1	A point particle orbiting a compact object	103
7.3.2	The build-up time	104
7.4	Consequences for gravitational-wave physics	108
7.4.1	Adiabatic evolution of orbits and energy balance	108
7.4.2	Off resonance	109
7.4.3	Crossing resonances	110
7.5	Discussion	111
8	Gravitational tuning forks	115
8.1	Setup	115
8.2	Resonant excitation of QNMs and Energy emission	117
8.3	Waveforms: Doppler, aberration & lensing	120
8.4	Discussion	122
III Binaries in astrophysical environments		
9	Galactic Black Hole	127
9.1	Black Holes in Dark Matter Halos	129
9.1.1	The Hernquist Profile	129
9.1.2	The Einstein Cluster	129
9.1.3	Redshift and Light Rings	131
9.2	Axial sector	131
9.2.1	QNMs and Love Numbers	132
9.2.2	Extreme-mass-ratio systems	133
9.3	Polar sector	135
9.3.1	Boundary conditions and sound speed	135
9.3.2	QNM spectral stability	137
9.3.3	Extreme-mass-ratio systems	138
9.4	Discussion	139

10 Concluding Remarks	141
IV Appendix	
A Perturbation theory in Quantum Mechanics	147
B An isotropically-emitting star	153
C Unstable circular geodesics	155
D Perturbation equations in non-vacuum environments	157
D.1 Energy-momentum tensor of the secondary for circular orbits	159
D.2 Master Equations	160
D.2.1 Axial Sector	160
D.2.2 Polar Sector	161
 Bibliography	 167

LIST OF FIGURES

Figure 3.1	The quadrupolar tidal Love number k_2^E for a central BH of mass M surrounded by a Shakura-Sunayev thin accretion disk in a circular binary and a companion of the same mass. We present two different binary distances d for $M/M_\odot = 5 \times 10^4$, $M/M_\odot = 5 \times 10^5$ and $M/M_\odot = 5 \times 10^6$. For each d we present estimations in the most efficient accretion scenario (labeled by E), $f_{\text{Edd}} = 0.2$ and $\alpha = 0.01$, and in the most inefficient one (labeled by I) $f_{\text{Edd}} = 0.01$ and $\alpha = 0.1$.	54
Figure 4.1	A dipolar scalar cloud around a Schwarzschild BH. This figure shows the time evolution of initial conditions (4.6) for a dipole with gravitational coupling $M\mu = 0.1$ around a non-spinning BH, and in absence of a companion ($\epsilon = 0$). The field is extracted at $r = 60M$. For the timescales of interest for our problem, the amplitude of the field varies by only a few percent and is therefore a good description of a quasi-stationary state.	56
Figure 4.2	Field (left) and energy density (right) distribution along the equatorial plane for the same initial data as Fig. 4.1. The field is dipolar, as expected, whereas the energy density at the equator is almost – but not exactly – symmetric along the rotation axis. The length scale of these images is of order $1000M$.	57
Figure 4.3	Dependence of the field Φ along the x - axis at different instants for a coupling $M\mu = 0.1$. In the absence of a companion ($\epsilon = 0$) and despite a slight change in the profile, the field has no nodes. It has a local extremum at $\sim r = 200M$ as predicted by a small $M\mu$ expansion for the fundamental mode. When a weak tidal field is turned on ($\epsilon = 10^{-8}$) the field develops a different radial profile with one node, pointing to a significant component of overtones. Our results indicate a sizeable excitation of the second excited state $n = 4$, which has extrema at $r/M \sim 170, 850$ (see Appendix A).	58

Figure 4.4	Dipolar ($\ell = m = 1$, left) and octupolar ($\ell = 3, m = 1, 3$, right) component of the scalar cloud when in the presence of a weak tidal field $\epsilon = 10^{-8}$, for the same initial conditions as in Fig. 4.1 (non-spinning BH and gravitational coupling $M\mu = 0.1$). The $\ell = 3, m = 1$ mode amplitude relative to the $\ell = m = 3$ was rescaled by the perturbation theory prediction ($\sqrt{5/3} \sim 1.29$). The agreement is very good throughout the evolution.	60
Figure 4.5	Snapshot of a tidally deformed scalar cloud with $\epsilon = 10^{-8}$ for the strength of the tidal field and $M\mu = 0.1$ for the gravitational coupling. In the absence of a companion, the energy density is almost spherical and remains so for thousands of dynamical timescales. Instead, here we observe that after $7000M$ the system settles to a new stationary configuration.	61
Figure 4.6	Cloud being tidally disrupted as it loses energy to asymptotically far-away distances from the central BH. The field cascades to smaller angular scales, and thus transitions to higher multipoles. This figure shows the time evolution of the dipolar ($\ell = m = 2$) and octupolar ($\ell = m = 3$) components of the scalar field for a gravitational coupling $M\mu = 0.1$, and a companion with $\epsilon = 10^{-7}$. The extraction radius is $r = 60M$	62
Figure 4.7	Snapshot of a tidally disrupting cloud. The snapshot depicts the energy density along the equator of a scalar cloud which was set initially around a non-spinning BH. In the absence of a companion mass, the energy density is almost spherical and remains so for thousands of dynamical timescales. Here, the simulation starts with one symmetric initial scalar energy distribution, but in the presence of a star for which $\epsilon = 10^{-7}$. The gravitational coupling is $M\mu = 0.1$. The snapshot is taken after $7000M$ and is leading to the disruption of the cloud.	63

Figure 5.1	<p>Redshift of two different sources as they plunge radially into a Schwarzschild BH, emitting null particles (e.g. photons, gravitons) of fixed proper frequency ω_e. The source, located in the equatorial plane at $\theta = \pi/2, \phi = 0$ begins from rest at infinity, but (for numerical purposes) starts emitting only when it crosses $r = 30.65M$. Beam: this source emits only radially outwards. The observer is located at $r_o = 100M, \theta = \pi/2, \phi = 0$, and receives particles whose frequency/energy decreases with time. At late times, the frequency ω_o measured by the observer decays exponentially as $\omega_o \sim \omega_e e^{-t/(4M)}$, according to our analytic prediction (5.29). Isotropic star: the second source is a pointlike “star” emitting isotropically in its local rest frame. At a fixed instant, far-away observers distributed along the sphere at $r_o = 100M$ receive a wide range of redshifts. The lower part of the curve is due to radially propagating null particles, whereas the top part of the curve is due to particles with a near critical impact parameter $b_c \approx 3\sqrt{3}M$ that linger close to the LR, which can be blueshifted [293].</p>	73
Figure 5.2	<p>Normalized luminosity ($\mathcal{L} = dE/dt$) of the two different sources discussed in Fig. 5.1. The observed luminosity of the radial beam scales as $\mathcal{L} \sim e^{-t/(2M)}$ at late times, again in agreement with our prediction. The luminosity of the isotropic star was calculated by “binning” null particles in packets of 20, to avoid large scatters. At late times, the luminosity is dominated by those particles lingering on the LR, hence $\mathcal{L} \sim e^{-t/(3\sqrt{3}M)}$.</p>	74
Figure 5.3	<p>The blueshift distribution of photons with near-critical impact parameter, emitted from an object freely-falling onto a BH. The blueshift is maximum, $\omega_o = 4\omega_e/3$, at $r_o = 12M$, and is unit at $r_e = 3\sqrt{3}M$ (see also Ref.[337]).</p>	75

Figure 5.4	<p>The redshift distribution of light emitted by an infalling (isotropic) star as measured by observers at $r = 100M$ on the infalling axis. For $\varphi = 0$ the star is between the BH and the observer, whereas observers at $\varphi = \pi$ only see the star due to gravitational lensing, as the BH sits between them and the star. Note the delay with which the $\varphi = \pi$ observer receives the first signal, with respect to $\varphi = 0$. Note also that the signal is mostly Doppler blueshifted for $\varphi = \pi$, as the observer sees light emitted from an approaching source. Some of the details of this figure, in particular the graininess and isolated points, are due to insufficient number of null particles being sent from the star.</p>	76
Figure 5.5	<p>Total luminosity in scalar waves ($s = 0$) and GWs ($s = -2$) from a source plunging into a Schwarzschild BH, and emitting at fixed proper frequency $M\omega_e = 2.5$. The source is located on the equatorial plane at $\theta_e = \pi/2$ and starts from rest at $r_e(t = 0) = 35M$. We consider both a radial plunge ($L_e = 0$) and one with finite angular momentum ($L_e = 3.0M$). For both processes, the luminosity follows the exponential decay at late times dictated by the LR, $\mathcal{L}_o \sim e^{-t/(3\sqrt{3}M)}$, in accordance with the geometric optics limit for the isotropic star in Fig. 5.2. The different features between scalar and GWs are due to the source structure in both scenarios. The low frequency oscillations in the GW spectrum come from the plunge of the CM of the binary system. The high-frequency content of the signal for both scalar and GWs is dominated by frequencies around $M\omega_o \sim 3.0$, blueshifted with respect to ω_e by a factor ~ 1.2, which is consistent with Fig. 5.3.</p>	79

Figure 5.6	Energy flux for a scalar source plunging radially into a BH (from $r_e(t = 0) = 35M$ as in Fig. 5.5), extracted at specific angular positions on the equator. All signals exhibit the same global exponential decay dictated by the LR as seen in Figs. 5.2 and Fig. 5.5. Stationary observers now see a periodic structure, whose period may differ for different observers (notice that at $\varphi = \pi/2$ the period is half that at $\varphi = 0, \pi$). Once again, the high frequency content of the spectrum corresponds to waves with $M\omega_o \sim 3.0$, in accordance with the blueshift predictions of Fig. 5.3.	80
Figure 5.7	Same as Fig. 5.6, but for a source emitting high-frequency GWs. The source is a binary, and is plunging radially onto a massive BH, while emitting GWs of proper frequency $M\omega_e = 2.5$. The frequency of the signal measured by far away observers is blueshifted to $M\omega_o \sim 3$	81
Figure 5.8	Left panel: Luminosity in scalar waves for the system studied in Section 5.2.3. Now, the source is turned off below a certain radius (which we selected to be either $r = 2.5M$ or $r = 4M$). When the source is turned off inside or close to the LR, the flux is nearly unchanged, as it is controlled by waves emitted in the past and lingering close to the photonsphere. Right panel: Luminosity for the scalar system studied in Section 5.2.3 but whose source is suddenly increased by a factor of 10 at the same radii as in the left panel. In flat spacetimes, this would correspond to a luminosity 100 times higher. However, since the process takes place close to the LR, the luminosity is very weakly affected and has the same global exponential decay. As expected, when the increase in amplitude occurs deep inside the light ring, the increase in the luminosity is less significant.	82
Figure 5.9	Luminosity in GWs from the system described in Section 5.2.4, for which the binary is shut off below a certain radius, signaling for example a sudden merger of the binary. In line with the findings for scalar waves in Fig. 5.8, near-horizon details are irrelevant for the appearance of these objects, and it is the LR that controls the late time signal.	83

Figure 6.1	The unperturbed ($\epsilon = 0$) and perturbed potentials used in this study. The Regge-Wheeler potential with $\ell = 2$ is shown in black, while two perturbative bumps ϵV_{bump} , with $\epsilon = 0.1$, are shown in blue ($a = 10$) and orange ($a = 30$). The unperturbed potential has a peak close to the LR.	88
Figure 6.2	<i>Top panels:</i> absolute value of the waveform arising from the scattering of the Gaussian pulse of Eq. (6.4) for “bumps” with different amplitudes ϵ , located at two selected distances a from the main peak. The bump width σ in Eq. (6.3) is fixed at $\sigma = 0.5$. “Echoes” are apparent when the bumps are located at large distances ($a = 30$). The dotted and dashed vertical gray lines correspond to $t - t_{\text{max}} = a$ and $2a$, and they illustrate how the delay between echoes is related to the size of the “cavity” between the two maxima in the perturbed potential. <i>Bottom panels:</i> absolute value of the difference between the waveforms shown in the top panels and the unperturbed clean waveform without a bump ($\epsilon = 0$).	91
Figure 6.3	Waveform for $a = 30$ and $\epsilon = 0.1$ over long time windows, where the late-time behavior is dominated by the new fundamental mode QNM. The dashed blue line represents its expected decay, which corresponds to the bottom blue cross with smallest $ \omega_I $ in the top panel of Fig. 6.6.	92
Figure 6.4	The portion of the waveform used for the damped-sinusoid fitting in the two different regimes of interest. For completeness, this waveform corresponds to the case $a = 30$, $\epsilon = 0.01$, but the same procedure applies to other examples. . .	93
Figure 6.5	Comparison between the QNM frequencies computed with the shooting method in the frequency domain (crosses) and those extracted by fitting the full time domain waveform (dots). The black cross is the unperturbed clean fundamental QNM of Schwarzschild, with $M\omega = 0.374 - 0.089i$. The starting times used are $t - t_{\text{max}} = 10, 15, 20, 25, 30M$	94

Figure 6.6	<p><i>Top panel:</i> same as in Fig. 6.5 but with $a = 30$. For $\epsilon = 0.001$, the full time-domain fits can only confidently detect a mode close to the fundamental mode of Schwarzschild, because the power-law tail dominates the signal before it transitions to the new set of QNMs. <i>Bottom panel:</i> The same analysis as in the <i>top panel</i> for $\epsilon = 0.001$ but subtracting the unperturbed clean waveform to the waveform before performing the fit. The frequencies extracted do not converge exactly to the QNMs, but the structure is more similar, in particular for the real part.</p>	95
Figure 6.7	<p>Same as Fig. 6.6, but we only fit the first train of the initial ringdown without echoes. The starting times are $t - t_{\max} = 10, 11, 12, \dots, 20M$. All the dots obtained using the fitting method now cluster around the clean fundamental mode of the unperturbed potential. The zoom-in in the right panel shows that a perturbation of order ϵ can induce systematic errors (approximately of order ϵ) in the measurement of the fundamental mode's frequency and damping time.</p>	96
Figure 7.1	<p>Effective potential governing massless fields on a horizonless ultracompact spacetime. The peak of the potential is close to the location of the unstable LR, and the potential in its vicinities is indistinguishable from that of a BH spacetime (compare with the black curve in Fig. 6.1). The centrifugal barrier in the object's interior produces an effective cavity in spacetime, from which waves can slowly tunnel out. As discussed below, a cavity illuminated from the exterior "heats-up", akin to a greenhouse effect.</p>	101

Figure 7.2	<p>Evolution of the scalar energy flux \mathcal{F} (Eq. (5.38)) emitted by a point-particle of mass m_p, made to orbit a constant-density star of mass M on a circular orbit of constant radius r_p (the orbit is not allowed to evolve). The flux is normalized by the mass ratio $q = m_p/M$. The results refer to the dipolar mode ($\ell = 1$), but results are similar for higher multipoles. Except for the right bottom panel, the star has radius $R = 2.26M$, and the frequency ω corresponds to the angular frequency Ω of the circular orbit, with $a = 0.9M$ in Eq. (7.13) ($r_{\text{ISCO}} \approx 2.321M$). At late times, the flux asymptotes to a constant that agrees with the value computed in the frequency domain. The relaxation time is large for stars with photonspheres, but very short for less compact stars, where the system quickly becomes stationary, as seen in the right-bottom panel.</p>	105
Figure 7.3	<p>Scalar energy flux emitted by a point particle in circular orbit at $r_p = 1.28 r_{\text{ISCO}}$, with angular frequency Ω given by Eq. (7.13) with $a = 0.9M$, around a constant density star of radius $R = 2.26M$ (the orbit is not evolving, the particle remains at fixed r_p). There are three different timescales in the signal: a high-frequency component corresponding to the “direct signal” with an orbital period $T_{\text{Orb}}/2 = \pi/\Omega \sim 19M$ (the 1/2 factor appears since we are showing fluxes); the traveling time $T_{\text{echo}} \sim 150M$ of waves inside the cavity potential; a lower frequency “envelope” corresponding to the excitation of the QNM of the constant density star with frequency $M\omega_{\text{QNM}} = 0.16333 - i2.470 \times 10^{-5}$. This leads to a beating whose frequency is given by the semi-difference between the orbital and the QNM frequency $\tau_{\text{beating}} \sim 2\pi/(\Omega - \omega_{\text{QNM}}) \sim 1800M$.</p>	106

- Figure 7.4 Resonant excitation of the dipolar QNM of a constant-density star of radius $R = 2.26M$ with frequency $M\Omega = M\omega_R = 0.1633$ (cf. Table 7.1), corresponding to a point particle at $r_p = 3.011M$. A small deviation of this radius resulting in a frequency shift of $\delta\Omega \gtrsim 2\omega_I$ can significantly hinder the excitation of the resonance. This agrees with standard results for the driven-harmonic oscillator, where the frequency bandwidth of the resonance peak is $\delta\Omega \sim \omega_I$ 107
- Figure 7.5 Largest mass ratio q_{\max} predicted by the estimate (7.25) that would allow the resonant excitation, by GWs, of a QNM of an ECO with frequency $\omega_R = 2\Omega$. We considered that $\omega_I \sim \omega_R^{2l+3}$ [382, 383] and only took into account the quadrupolar mode in the energy flux, making this estimate conservative, since \mathcal{F} will increase if higher multipoles are considered. We show orbital frequencies Ω corresponding to radius of the particle from $r_p = 10M$ up to almost the ISCO for each spin a . For mass ratios larger than these limits, the particle crosses the resonance too quickly for it to grow effectively. 111
- Figure 8.1 Equatorial slice of a spacetime with a hierarchical triple system. In the center there is a SMBH. At large distances away from the central region, physics is nearly Newtonian. The external gray area is the entire region where stable circular motion is possible. We place a small compact binary here, with characteristic frequency ω_0 . Its CM orbits the SMBH with angular frequency Ω_{CM} . At the ISCO ($r_{\text{ISCO}} = 6M$ when the SMBH is non-spinning), circular motion is marginally stable, and unstable for smaller radius. High-frequency waves can be trapped at the LR ($r_{\text{LR}} = 3M$ for non-spinning BHs). Such motion is unstable, and as seen in previous chapter, can also be associated with the “ringdown” excited during BH mergers. 116

Figure 8.2	<p>Energy output when a small binary stands at the ISCO of a SMBH with spin $a = 0.9M$, as a function of the orbital frequency of the binary components, ω_0. The modal energy output, as measured by the ratio with respect to flat space-time ${}_{-2}\mathcal{R}$, peaks at a finite ω_0 well described by the lowest QNM (cf. Table 8.1). Also shown is the flux integrated over all modes: it has a substantial component going down the SMBH horizon (\dot{E}_H), and the total flux at infinity is modulated by QNM contributions (\dot{E}_∞). Here, $\hat{\omega}_{\ell m} = M\omega_{\text{QNM}}/2$.</p>	118
Figure 8.3	<p>Teukolsky function Ψ measured by a stationary observer at large distances (either edge- or face-on, $\theta = \pi/2, 0$ respectively), for a stellar binary around the ISCO of a non-rotating BH (we removed the CM contribution, which just causes a low-frequency modulation). The orbital CM period is $T_{\text{CM}} \approx 93M$ and at $t = 0M$ the observer is aligned with the small binary. Doppler effect induces frequency shifts, relativistic beaming and gravitational lensing modulations in the amplitude. The maximum blue-shift is well described by $\omega_{\text{max}} = \omega'_0 Y (Y + v_{\text{CM}}) / (Y - v_{\text{CM}})^{1/2}$, with $Y = \sqrt{1 - 2M/r_{\text{CM}}}$, $M\omega'_0 = 1$ the proper frequency and v_{CM} the CM velocity [156, 290]. In this case, $\omega_{\text{max}}/\omega'_0 \approx 1.4$.</p>	121
Figure 8.4	<p>Snapshots of the time-evolution of the hierarchical triple system with the CM of the small binary orbiting the SMBH at the ISCO anti-clockwise. The shaded blues illustrate the wave emission by the system projected on the equatorial plane. There is a focus of radiation along the direction of motion, corresponding to relativistic beaming. We also observe the distortion of the path taken by waves due to gravitational pull exerted by the central BH.</p>	122

Figure 9.1	<p><i>Top panel:</i> Real and imaginary part deviations of galactic axial QNMs $\omega_{\ell n}(M, a_0)$, with $M = 20M_{\text{BH}}$, from the vacuum Schwarzschild QNMs $\omega_{\ell n}(0,0)$ for $\ell = 2$ as a function of the compactness M/a_0. Different plot markers denote different overtones. The dashed black line represents a fit to the relative difference for powers of M/a_0. <i>Bottom panel:</i> Same as the top panel with $M = 10^3 M_{\text{BH}}$. The fit agrees with the LR corrections obtained in Eq. (9.18).</p>	132
Figure 9.2	<p><i>Top panel:</i> Relative difference between the energy flux emitted by a circular EMRI in the dominant axial mode $\ell = 2, m = 1$ as a function of the orbital frequency Ω_p, for different halo configurations (\dot{E}_m) and in vacuum (\dot{E}_v) (solid lines). Dashed lines represent the same comparison but with the vacuum fluxes redshifted according to Eq. (9.25). The frequencies correspond to a secondary at radius ranging from $r_p = 50M_{\text{BH}}$ down to $r_p = 6M_{\text{BH}}$; <i>Bottom panel:</i> Same as the top panel but for the dominant polar mode $\ell = 2, m = 2$. In this case, the redshift correction correctly captures the variation of the flux with the orbital frequency.</p>	134
Figure 9.3	<p>Evolution of $\delta\rho$ in a Schwarzschild background with $c_{s_r} = 0.9, c_{s_t} = 0.0$ when different boundary conditions are imposed. t_{arrival} is the time of arrival of the first direct signal coming from the initial data prescribed. When no boundary conditions are imposed (<i>No BCs</i>), and $\delta\rho$ is left free at the BH horizon, an oscillatory tail of the form $\delta\rho \propto t^{-5/6} \sin(\mu_{\text{eff}} c_{s_r})$ sets in at late times, with $\mu_{\text{eff}} = (1 - c_{s_r}^2) / 8c_{s_r}^2 M_{\text{BH}}$. This is analogous to having a scalar field of mass $\mu_{\text{eff}} c_{s_r}$. On the other hand, when Dirichlet boundary conditions (<i>BCs</i>), $\delta\rho = 0$, are imposed at a cut-off radius r_{cut} (here $r_{\text{cut}} = 3M_{\text{BH}}$), we find a universal power-law decay independent of r_{cut} and c_{s_r}, consistent with $\delta\rho \propto t^{-3}$.</p>	136

Figure 9.4	Evolution of the metric and density perturbation K , $\delta\rho$, with $M = 10M_{\text{BH}}$, $a_0 = 10M$. We impose Dirichlet conditions at $r_{\text{cut}} = 3M_{\text{BH}}$ and $c_{s,r} = [(2M_{\text{BH}} + a_0) / (r + a_0)]^4$, so that the radial speed of sound asymptotes to zero at large distances. At early times, a standard BH ringdown is excited, as can be seen in the inset for K ; at late times, the signal is dominated by a slowly-decaying, fluid-driven mode with period $\sim a_0$. There is a mutual conversion between gravitational and matter density waves, which is a manifestation of the spectral instability of BH QNMs. The qualitative conclusions are independent of the initial data given and the profile chosen for $c_{s,r}$	138
Figure C.1	Same analysis as in Fig. 7.2 but considering circular geodesics around Schwarzschild, i.e. $a = 0M$ in Eq. (7.13)-(7.16). We do not show an analogous plot for the $M\omega = 0.192$ since the particle would have to be put at the light-ring ($r_p = 3.0M$) and we are only considering timelike motion.	156

LIST OF TABLES

Table 4.1	<p>Timescales t_{trans} and relative amplitudes predicted by time-independent perturbation theory (see Appendix A) and those obtained from numerical simulations data at $t = 1000M$, for the most relevant 1st order transitions from the initial dipolar state ($\ell = m = 1$) for a gravitational coupling of $M\mu = 0.1$. The second column shows the timescale to transition from the initial to the $(n\ell m)$ state, as obtained from time-dependent perturbation theory. The third column shows the relative amplitude of the overtones with respect to the fundamental mode, predicated by time-independent perturbation theory (in parenthesis is the corresponding ratio of the field components at $r = 60M$). The last column shows this same quantity but for our numerical results. They agree with perturbation theory within a factor of two, except for the $\ell = m = 1, n = 3$ mode. In this case, the timescale needed for excitation is larger than the instant at which the coefficients were extracted.</p>	59
Table 7.1	<p>The lowest $\ell = 1$ scalar quasinormal frequencies of a uniform-density relativistic star with $R = 2.26M$. We also show the corresponding orbital radius at which the mode would be excited, calculated by equating the orbital frequency Ω in Eq. (7.13) to the real part of the QNM frequency and solving for r_p. The value of a corresponds to the used in the expression for the orbital frequency Ω (7.13). For less compact stars, resonant frequencies are impossible to excite with matter on circular orbits outside the object. For example, for $R = 6M$ the lowest dipolar QNM frequency is $M\omega = 0.262189 - i0.204880$.</p>	103
Table 8.1	<p>Frequency $M\omega_{0X}$ which maximizes the energy output of a small binary standing at location X close to a SMBH, in a given (ℓ, ℓ) mode, as measured by the ratio ${}_s\mathcal{R}$ ($s = 0, -2$ for scalar or gravitational perturbations, respectively). The binary's CM is static, and sitting at the LR or at the ISCO. Notice the excellent agreement with the lowest QNM frequency. The results for orbiting binaries are similar.</p>	119

Table 9.1	<p>Energy flux (in units of m_p^2/M_{BH}^2) emitted in GWs to infinity in different modes by a particle in a circular orbit at radius $r_p = 7.9456M_{\text{BH}}$ around a BH surrounded by a Hernquist-type DM halo. We show results for vacuum (first line of each mode) and for a halo with $(c_{s,r}, c_{s,t}) = (0.9, 0)$, $M = 10M_{\text{BH}}$ and $a_0 = 10M$ (second line of each mode). \dot{E}_∞^t is computed with the time-domain framework, whereas \dot{E}_∞^f are computed in the frequency domain and $\dot{E}_\infty^{\text{BHPT}}$ corresponds to results available online from the BH perturbation toolkit, available only in vacuum. $\ell = m$ modes correspond to polar excitations whereas $\ell = m + 1$ correspond to axial ones.</p>	133
Table A.1	<p>First order corrected frequencies $\omega_{n\ell m}$ predicted by time-independent theory, for a non-rotating BH and a companion with the configuration $M\mu = 0.1$, $\epsilon = 10^{-8}$. A spinning BH would break the degeneracy between states with the same ℓ but different m quantum number. However, these corrections enter the frequency spectrum (A.6) only at order α^5. For the above configuration, these would yield $\omega_{n33} - \omega_{n31} \sim 10^{-6}a/Mn^3$.</p>	151

CONVENTIONS, NOTATION AND UNITS

In this thesis I follow the conventions of Refs. [1, 2]. Unless stated otherwise, I use geometrized units ($c = G = 1$) and work with the *mostly positive* metric signature $(- + + +)$.

$\alpha, \beta, \gamma, \dots$	spacetime indices (from 0 to 3)
i, j, k, \dots	3-spatial indices (from 1 to 3)
$V_\alpha W^\alpha \equiv \sum_{\alpha=0}^3 V_\alpha W^\alpha$	Einstein's notation
$T_{(\alpha_1 \dots \alpha_l)} \equiv \frac{1}{l!} \sum_{\sigma} T_{\alpha_{\sigma(1)} \dots \alpha_{\sigma(l)}}$	symmet. over all permutat. σ
$g_{\alpha\beta}, \eta_{\alpha\beta}$	curved, flat spacetime metric
$(\cdot)_{,\alpha} = \partial_\alpha(\cdot) = \frac{\partial}{\partial x^\alpha}(\cdot)$	coord. derivative
$(\cdot)_{;\alpha} = \nabla_\alpha(\cdot)$	Levi-Civita derivative
$\square(\cdot) \equiv \nabla_\alpha \nabla^\alpha(\cdot)$	Levi-Civita d'Alembertian

ACRONYMS

AGN	active galactic nucleus/nuclei
BH	black hole
BHB	black hole binary
CDM	cold dark matter
CM	center of mass
DM	dark matter
ECO	exotic compact object
EMRI	extreme-mass-ratio inspiral
EOM	equation(s) of motion
GR	General Relativity
GW	gravitational wave
IMRI	intermediate-mass-ratio inspiral
ISCO	innermost stable circular orbit
LIGO	Laser Interferometer Gravitational-Wave Observatory
LISA	Laser Interferometer Space Antenna
LR	light ring
LVK	LIGO-Virgo-Kagra (collaboration)
QNM	quasinormal mode
SMBH	supermassive black hole
SNR	signal-to-noise ratio
TLN	tidal Love number

GRAVITATIONAL WAVES AND THE GALACTIC
POTENTIAL

INTRODUCTION

1.1 THE GWZOIC

The theory of General Relativity (GR) is often regarded as one of humanity's most outstanding intellectual achievements. Its mathematical elegance and ability to pass experimental tests remain unmatched in the history of science. For over a century, tests were limited to the weak gravity regime. Yet, the excitement about the theory stemmed from its puzzling predictions when a large amount of mass concentrates in a small region of space. According to GR, if stars become too massive, they can collapse under their gravity, forming black holes (BHs) - regions of space where the gravitational attraction is so strong that not even light can escape. They are deceptively simple. The "no-hair" theorem states that any isolated BH in the Universe belongs to the Kerr family and is fully characterized by just two numbers: its mass and spin (how fast it rotates) [3].

GR also predicts that when accelerated, BHs, or any other compact objects, create tidal deformations of the gravitational field that propagate at the speed of light: gravitational waves (GWs). In 2015, the Laser Interferometer Gravitational-Wave Observatory (LIGO), in the U.S.A., detected a GW signal from the coalescence of two BHs with masses of 36 and 24 M_{\odot} ¹. This event became known as GW150914² [4]. It originated billions of years ago, around ~ 410 Mpc away from the Earth³, and lasted for 0.2s causing a disturbance of 10^{-21} m on its passage, smaller than the size of a proton. Until this point, we based our observations of the outer Universe almost solely on detecting light, but since then, we can also "hear" it through GWs.

Unlike their electromagnetic relatives, GWs interact weakly with matter and remain mostly unaffected during their journey. They offer an almost perfect fingerprint of some of the most violent events in the Universe, where objects with masses exceeding that of the Sun are compressed to a few kilometers and collide at speeds surpassing half the speed of light. GW150914 reached a peak power emission rate of $\sim 10^{49}$ W in GWs, more than the power radiated by all the

¹ $M_{\odot} = 1.9891 \times 10^{31}$ kg is the mass of the Sun

² GW events are named as GW-YEAR-MONTH-DAY

³ 1 pc $\approx 3.1 \times 10^{16}$ m

known stars in the Universe. In this regime, GR is pushed to its limits, and GW150914 sparked what many have called the dawn of the *gravitational-wave astronomy era*. Welcome to the *GWzoic*.

Since then, two new detectors, Virgo (Italy) and KAGRA (Japan), were added to the network, and more than 90 GW-events were confirmed by the LIGO-Virgo-KAGRA (LVK) collaboration [5–7]. These have included stellar mass BH binaries (BHs) as well as neutron star binaries with an electromagnetic counterpart [8–10], neutron star-BH binaries [11], asymmetric binaries [12], a curious object which is either the lightest BH or the heaviest neutron star ever observed (or perhaps, even “something else”) [13], and BHs that are too massive to be formed via standard stellar collapse [14]. In the latter event, GW190521, the first intermediate-mass BH with $\sim 142 M_{\odot}$, whose existence in the Universe was often questioned, was also discovered [14]. This vast catalog has provided opportunities to test GR with unprecedented levels of precision, impose constraints and exclude possible modifications of it, and gain insights about dense matter [15], the formation of heavy elements in nature, and the astrophysical populations of BHs, i.e. their masses, spins, or distance to the Earth [16, 17].

And the future *sounds* even brighter. The LVK is starting a new run with increased sensitivity [18], and it is planned that LIGO-India will join the network by the end of the decade. There are also ambitious plans to build third-generation detectors, such as the Einstein Telescope in Europe [19] and Cosmic Explorer in the U.S.A. [20]. These advanced detectors will feature longer arms and better technology, boosting their sensitivity by one order of magnitude beyond that of LVK [21]. We expect to detect $\sim 10^6$ GW events per year with signal-to-noise ratios (SNR) on the order of $\sim 10^3$, far surpassing GW150914’s SNR of 24. These *louder* sources will decrease the relative error in parameter estimation by several orders of magnitude, improve the sky localization of the sources ($\sim 1 \text{ deg}^2$ vs the current $\sim 10^2 \text{ deg}^2$), and observe events originated in the early Universe.

In the late 2030s, the European Space Agency will also launch the Laser Interferometer Space Antenna (LISA) [22]. This space-based GW detector will consist of three spacecrafts separated by approximately 2.5×10^6 km, working together like an interferometer. While ground-based detectors are sensitive to GWs between $[1, 10^3]$ Hz, LISA will operate in the much lower frequency range of $[10^{-4}, 10^{-1}]$ Hz. It will *hear* a very different class of sources compared to ground-based detectors, from millions of white dwarf binaries lurking in our galactic center to binaries involving supermassive black holes (SMBH) with masses of $10^5 - 10^{10} M_{\odot}$, possibly at very high redshift ($z \sim 20$) [23]. The latter may appear as monstrous SMBH-SMBH binaries [24, 25], or in extreme-mass-ratio inspirals (EMRIs), where a stellar-mass object such as a BH or a neutron star orbits around the central SMBH [26, 27]. EMRIs perform around $10^4 - 10^5$ orbital cycles while in the LISA

band [28], allowing the measurement of parameters like the masses, the SMBH spin, and orbital eccentricity with statistical errors of order $10^{-4} - 10^{-6}$ [26]. The scientific potential of EMRIs in both astrophysics [23] cosmology [29], and fundamental physics [30] is almost immeasurable. However, we need extremely accurate models to follow the waveform for months, possibly years, with errors below 1 radian in the GW phase [31–33].

Finally, the International Pulsar Timing Array has very recently reported evidence for a stochastic GW background in the nanoHertz range, due to a cosmic population of SMBHs with billions of solar masses [34–37]. These observations are based on correlated shifts on the period of millisecond pulsars, caused by the passing of GWs. Together with the ground and space-based interferometers, they allow for the detection of GWs across a frequency band spanning almost 10 orders of magnitude.

1.2 GALACTIC CENTERS: GRAVITY'S POTLUCK

It is common belief that most SMBHs grow in the center of galaxies [38–44]. These are far from being simple *ecosystems*, as perfectly illustrated by the BH images captured by the Event-Horizon Telescope [45, 46] and the pictures taken by the James Webb Telescope. The SMBH residing there can efficiently accrete matter, forming active galactic nuclei (AGNs), which are the brightest sources of electromagnetic radiation in the Universe. AGNs consist of gas orbiting in a thin accretion disk, with surface densities between $10^3 - 10^6 \text{ g} \cdot \text{cm}^{-2}$ and temperatures as high as 10^6 K [47–49]. Galaxies are also thought to be surrounded by dark-matter (DM) distributions, which play a key role in their formation and evolution [50–53]. Finally, the various stars and other compact objects orbiting close to the central SMBH attract each other gravitationally, making the motion of binary systems more complex. We need very accurate models for their orbital evolution to do proper precision physics with EMRIs. The question to make is whether non-vacuum environments in galactic centers lead to non-negligible effects in an EMRI that are detectable with future GW experiments. Or can we ignore the environment and safely model these systems as isolated binaries in vacuum GR?

1.2.1 How many? Many...

Before trying to answer this question, we should first assess how many EMRIs in AGNs is LISA expected to observe. In the standard “dry” formation channel, stellar-mass compact objects evolve through gravitational scattering between each other until they are close enough to the central SMBH to become gravitationally bound to it. EMRI population rates will therefore depend on the typical number of stars

and stellar mass BHs in galactic centers, whose density distribution can reach $10^6 M_{\odot} \cdot \text{pc}^{-3}$ [54], their initial positions and velocities, the distribution of SMBHs in the Universe, and the fraction of these which is present in dense stellar clusters. It should come as no surprise that forecasts on the number of detectable EMRIs formed via this multibody scattering mechanism ranges between $1 - 10^3$ [26, 55].

Despite the uncertainties, there is astrophysical evidence for binaries evolving in galactic centers. For instance, OJ287 [56, 57] is a binary system made up of two SMBHs, with masses of $10^{10} M_{\odot}$ and $10^8 M_{\odot}$, orbiting in an accretion disk with $10^2 M_{\odot}$. Their orbit is slightly inclined with respect to the plane of the disk. Hence, as the lighter BH (often referred to as the *secondary*) crosses the disk, periodic electromagnetic flares are emitted [58]. Additionally, the large masses of the BHs coalescing in GW195021 [14], $85 - 66 M_{\odot}$, suggest they are second generation BHs that formed in previous mergers, which typically requires these objects to be in dense environments [49, 59–62]. Moreover, the Zwicky Transient Facility observed an electromagnetic flare 34 days after GW195021, which has been proposed to be due to the movement of the remnant BH in an AGN at $200 \text{ km} \cdot \text{s}^{-1}$ [63, 64].

However, the estimates mentioned above for detectable EMRI population rates ignore the interaction of the small compact object with the environment around it. Just as a ball moving through a fluid experiences drag and pressure differentials that lead to interesting phenomena like the Magnus effect [65], a compact object moving through gas-rich environments will experience several dynamical effects related to accretion flows. The same applies to DM distributions. Typically, these effects accelerate the inspiral towards the central BH. Recent estimates point out that these “wet” EMRIs may actually dominate the fraction of detectable EMRIs by LISA and be several orders of magnitude more common than the ones born through the “dry” formation channel [66, 67] (see Fig. 1 in Ref. [67]).

1.2.2 *Surfing the waves*

An EMRI evolving in an accretion disk experiences various dynamical effects not present in vacuum. Both the SMBH and the stellar-mass compact object accrete matter, which increases their masses through the inspiral [68, 69]. The disk’s self-gravity modifies the gravitational potential, altering the acceleration of the secondary object and potentially inducing orbital precession. Additionally, as the compact object pierces through the gas, it generates density wakes that trail behind and interact with itself, exerting additional torques and drag. These effects are broadly referred to as dynamical friction [70–76]⁴. GWs tend to circularize orbital motion, but the dynamical effects created

⁴ The astrophysics community dubs them differently depending on the origin of the interaction, e.g. hydrodynamical drag, migration torques...

by the environment compete with this and may increase the orbit's eccentricity [77].

A systematic study of the effects mentioned above, focusing on geometrically thin, radiatively efficient, stationary accretion disks described by the Shakura-Sunayev model [47], found that dynamical friction from *planetary-migration*-like torques results in the largest deviation from vacuum waveform templates for circular, non-inclined EMRIs targeted by LISA [78, 79] (see Fig. 1 of Ref. [78]). This study predicts a dephasing in the GW signal as large as $\sim 10^2$ rad, which could severely constrain the binary environmental density.

Further order-of-magnitude estimates confirm this picture [80, 81]. A Bayesian analysis using the state-of-the-art waveform models for circular-equatorial EMRIs suggests that GW observations will be able to distinguish between different accretion models [31, 82, 83]. If environmental effects are not included in waveform templates, the estimation of the mass and spin of the objects could be biased and compromise tests of fundamental physics [84]. In addition, environmental effects are expected to dominate over still unmodelled vacuum corrections in the waveform [85].

Unfortunately, most literature on environmental effects in EMRIs has only modeled the environment at the Newtonian level or utilized the lowest-order quadrupole formula to estimate GW emission and dynamics. Neither of these approximations is expected to hold for EMRIs, whose large number of orbital cycles in the LISA band naturally probe the strong-field regime of gravity. This has been corroborated by 2D general-relativistic-hydrodynamic simulations of intermediate-mass-ratio inspirals (IMRIs)⁵ [86]. The gas torques exerted on the inspiralling body depend on the disc parameters and the mass ratio of the binary. For the early inspiral, the analytical estimates from planetary migration [73] capture the correct evolution of the torque with the inspiral rate. However, their order of magnitude may differ (check Fig. 3 and 5 of Ref. [86]). In some configurations, the torques can even become positive, acting as a thrust instead of a drag, which slows down the inspiral. In the later stages, the torque evolution is highly oscillatory because the inspiral timescale becomes comparable to the relaxation timescale of the disk, which depends on its viscosity and temperature. However, this work still uses simplified disc models, focuses only on circular orbits, and considers Newtonian gravity and the quadrupole formula for the binary's evolution, so further investigations are necessary. Gas torques also exhibit stochastic fluctuations that may result in non-zero secular phase shifts when accumulated over many orbits and introduce high-frequency glitches in the waveform. These can also appear as a stochastic background in the mHz band [87].

⁵ EMRIs have mass ratios between the secondary and the SMBH $\lesssim 10^{-5}$ while IMRIS have $10^4 - 10^{-3}$.

Detecting an [EMRI](#) evolving in an [AGN](#) is also interesting from the perspective of electromagnetic observations. The angular resolution to which these systems can be localized should highly reduce the number of possible [AGNs](#) hosting the [EMRI](#). The combination of [GW](#) and electromagnetic observations could provide a direct measurement of the disk viscosity [84] and allow for independent tests of cosmology through distance measurements of the system using electromagnetic redshift and [GW](#) luminosity [88, 89].

1.2.3 *The unbearable darkness of...*

We already mentioned that another important *player* at the galactic scale is [DM](#). Extensive experimental evidence supports its existence, including the flatness of rotation curves of stars in spiral galaxies [50–53, 90] and gravitational lensing [91]. According to the standard model of cosmology, [DM](#) behaves as a collisionless, non-relativistic fluid, hence the name cold dark matter ([CDM](#)). Its local density and dispersion velocity are approximately $\rho_{\text{DM}} \sim 10^{-2} M_{\odot} \cdot \text{pc}^{-3}$ and $v_{\text{DM}} \sim 150 \text{ km} \cdot \text{s}^{-1}$, respectively. [CDM](#) tends to clump in halos, where baryonic matter can become gravitationally bound and form large-scale structures like galaxies. Our own Milky Way is expected to be immersed in a [DM](#) halo with $\sim 10^{12} M_{\odot}$, in comparison with the $\sim 10^{11} M_{\odot}$ of luminous matter, and a radius of $\sim 10^2 \text{ kpc}$ [92, 93].

However, [CDM](#) suffers from several pathologies at subgalactic scales [94, 95]. Two illustrative examples are the *cuspy-halo* problem [96, 97], where N -body simulations favor “cuspy” halos with a steep increase in the density of [DM](#) at their center, while galaxy rotation curves indicate more flat profiles; and the *dwarf-galaxy* problem, which arises from the conflict between the small number of dwarf galaxies observed and the larger number of subhalos predicted by simulations.

Many of these problems are due to our limited understanding of some astrophysical processes and the actual fundamental nature of [DM](#). There is an entire *zoo* of possible answers [98] ranging from macroscopic objects with a few solar masses, such as primordial [BHs](#) formed in the early universe due to curvature fluctuations [99, 100], to new ultralight bosonic fields with masses as light as $\mu \sim 10^{-22} \text{ eV}$ [101–104]. The latter provides a natural solution to the cuspy-halo problem, as they admit stable, self-gravitating compact configurations, known as *boson stars*, which are a good description of flat [DM](#) halo cores [105–108]. If different [DM](#) models have a particular signature in the waveform, we could then use [GW](#) observations to constrain the properties of [DM](#).

The small local densities of [DM](#) might initially suggest that it has minimal impact on the evolution of compact binaries. However, the presence of a [BH](#) that grows adiabatically in the center of a [DM](#) configuration can result in the formation of a density cusp with a peak very close to the [BH](#) horizon [109–111]. The [DM](#) density is expected to be

significantly enhanced, possibly up to 10 orders of magnitude at the center, and be scaling as $\rho_{\text{DM}} \sim r^{-\gamma}$, where r is the radial distance to the BH and $\gamma = 1.5 - 2.5$, depending on the DM model considered. DM annihilation, accretion, and other dynamical processes, like mergers, can deplete the overdensity and flat out the core of the DM distribution [112, 113]. The orbits of S-stars have already been used to place constraints on the properties of the DM spike at the center of our own Milky Way [114–117].

Despite its uncertainty, the large overdensity at galactic centers could make DM accretion and dynamical friction relevant for binary inspirals. This mechanism has been suggested to explain the abnormally fast orbital decay of the two closest stellar-mass X-ray binary systems, which are inspiralling two orders of magnitude faster than expected from GW emission [118]. As in accretion disks, most literature has applied results from Newtonian treatments [70] and applied it to EMRIs to estimate its effect in the dephasing of compact binaries [81, 119]. Only recently have the first relativistic studies of dynamical friction in homogeneous mediums composed of an ultralight scalar field been conducted [107, 120–123].

When included in state-of-the-art waveform models [31, 82, 83], these relativistic corrections can significantly impact the forecasts for the detectability and parameter estimation of an EMRI evolving in a DM environment during the LISA mission lifetime [124]. Another nuance to bear is that for binaries involving intermediate-mass BHs, the energy dissipated via dynamical friction can become comparable to the gravitational binding energy of the DM distribution. In this case, one needs to consider backreaction on the environment, which hinders the dephasing in the waveform [125, 126].

Ultralight bosons can also extract rotational energy from rotating BHs through a process known as superradiance and condensate into macroscopic clouds with a structure reminiscent of the hydrogen atom [103]. These superradiant clouds are expected to create gaps in the mass-spin distribution of astrophysical BHs [127]. They also emit monochromatic GWs which can appear as individual signals or stochastic backgrounds [128–131]. LVK has already placed constraints for masses around $\sim 10^{-13}$ eV based on null observations [132, 133]. Nonetheless, when present in a binary, the superradiant clouds will interact with the companion of their BH hosts, causing their deformation [134–137]. A proper understanding of the evolution of these structures in binary coalescences is necessary so that the constraints already imposed can be trusted.

1.2.4 *Third wheels*

Finally, we have already mentioned that some GW-events observed by LVK should involve BHs which are remnants of previous coales-

cences [12, 138–140]. These “hierarchical mergers” typically require the presence of a third body to induce coalescence [141–144]. In fact, triple systems are expected in AGNs [145–148] and other dense stellar environments [149–151], with around 90% of low mass binaries with periods shorter than three days belonging to some hierarchical structure [152–154]. Even at the Newtonian level, the presence of a third body is known to lead to interesting dynamical effects [155]. It can accelerate the binary’s center-of-mass (CM), which causes a time-dependent Doppler shift [156–160] and relativistic beaming [161, 162] in the waveform. It can also lead to secular changes in the orbital eccentricity and inclination through the Kozai-Lidov mechanism [155, 163, 164], triggering periods of high eccentricity where GW emission increases significantly [165–168], causing periodic bursts of GWs [169, 170]. However, as with the previous environmental effects, most of these studies were restricted to the Newtonian regime and did not capture strong-field physics.

1.3 STRUCTURE OF THE THESIS

The punchline of our discussion is that we lack the proper relativistic modeling of environmental effects in the evolution of binary systems necessary to fulfill the ambitious goals that GW astronomy has set for the next decades. The Fundamental Physics Working Group of LISA has recently emphasized this problem in their white paper [30] by dedicating an entire chapter to environmental effects (Chapter VII). The following *burning questions and needed developments* were identified:

- *Can accretion, plasma effects or other stellar compact objects in the vicinity of an EMRI induce observable changes in the GW frequency evolution during the inspiral or ringdown that can spoil fundamental physics tests?*
- *Self-force calculations for generic BHs in vacuum or embedded in a background (e.g. DM boson cloud) at second-order are necessary for proper modeling of EMRIs, so that reliable waveforms are available to test for fundamental physics.*
- *A combination of the effects of bosonic DM and modified gravity must be considered in order to be able to understand how more complex deviations from standard GR can take place.*

In this Ph.D. thesis we will address some of these questions and point towards the necessary steps to further advance this research program. We end this introduction with an outline of how the thesis

is organized. All my publications referenced below resulted from collaborations with my supervisor Vitor Cardoso.

In Chapter 2 we present the theoretical framework on which most of our work is based, including the necessary equations of motion (EOM) and numerical methods often employed.

In Part i we focus on studying static tidal deformations to distributions of matter surrounding BHs induced by external companions. In Chapter 3 we start by showing that the correction to waveforms due to tidal deformations of non-vacuum environments can be comparable to those signaling deviations from GR. This can compromise tests on the nature of BHs based on the measurement of tidal deformations, as an ultracompact object without a horizon would be indistinguishable from the presence of an accretion disk around a BH [171]. Chapter 4 follows from a collaboration with Taishi Ikeda [134], where we investigated the evolution of superradiant clouds when subject to static tidal fields from binary companions. We find they can deform the structure of the cloud or even disrupt it when too strong. This mechanism could be relevant for known BH systems, such as Sagittarius A* at the center of our galaxy, or Cygnus X-1.

Part ii delves into the exquisite role that the LR has on the physics of ultracompact objects, specifically its connection with the proper oscillation modes of a compact object. In Chapter 5, based on Ref. [172] co-authored with Arianna Foschi, we conclude that the appearance to distant observers of emitting sources of electromagnetic or gravitational waves being accreted by a BH is controlled by the LR properties and not particularly sensitive to near horizon details. Chapter 6 is a collaboration with Emanuele Berti, Mark Ho-Yeuk Cheung, Francesco Di Filippo, Paul Martens and Shinji Mukohyama [173], where we revisited the problem of the stability of the quasinormal (QNM) spectrum of BHs, but from the point of view of time-domain observations. Our analysis reveals that changes in the amplitude of the fundamental mode in the prompt ringdown, which is the relevant portion of the signal for GW observations, are parametrically small, even though formally the QNM spectrum is unstable. In Chapter 7, building upon Ref. [174], we continue to explore the subtle differences between frequency and time-domain analysis and show the excitation of very sharp resonances in compact binaries may be hindered due to radiation-reaction effects which quickly move the system away from the resonant state. We end this part with Chapter 8, based on work with Gaurav Khanna [175]. In this chapter, we study GW emission, in the strong-field regime, by a hierarchical triple system composed of a binary placed in the vicinity of a SMBH. We observe interesting phenomena such as the resonant excitation of the QNMs of the SMBH, as in the resonant excitation of two tuning forks with matching frequencies. We also observe Doppler shifts, aberration, lensing, and strong amplitude modulations in the waveform.

Finally, in the last part of the thesis, Part [iii](#), we develop the first fully-relativistic framework to handle [GW](#) emission in spherically-symmetric but otherwise generic spacetimes, including non-vacuum ones. This formalism was first laid out in Refs. [[176](#), [177](#)], in collaboration with Andrea Maselli, Kyriakos Destounis and Rodrigo Panosso Macedo. It is based on applying [BH](#) perturbation theory to spacetimes describing extended distributions of matter around [BHs](#), treating both matter and gravitational perturbations on an equal footing. This approach allows us to naturally account for accretion, gravitational drag, and halo feedback. We apply this newly developed framework to a relativistic solution of a non-rotating [BH](#) immersed in a galactic [DM](#) halo, as found in Ref. [[176](#)] using the *Einstein Cluster* construction. We observe the manifestation of the spectral instability mentioned above for an astrophysical system. Moreover, our methods open up the possibility to infer galactic properties with [EMRIs](#). We conclude the thesis with remarks on our findings and discussions on future work.

2

THEORY AND NUMERICAL FRAMEWORK

In this chapter we give a brief presentation of the theoretical and numerical framework necessary for the rest of the thesis.

2.1 THEORY

2.1.1 Action and Equations of Motion

We consider the Einstein-Hilbert action in a 4-dimensional space-time [2]

$$S_{\text{EH}} = \int d^4x \sqrt{-g} \left[\frac{R - 2\Lambda}{8\pi} + \mathcal{L}_M \right], \quad (2.1)$$

where R is the Ricci scalar, g is the determinant of the metric $g_{\mu\nu}$, Λ is the cosmological constant, and \mathcal{L}_M is the Lagrangian density of matter fields.

The variation of the Einstein-Hilbert action with respect to $g_{\mu\nu}$ leads to the Einstein's equations

$$G_{\mu\nu} + \Lambda g_{\mu\nu} = 8\pi T_{\mu\nu}, \quad (2.2)$$

where $G_{\mu\nu} = R_{\mu\nu} - \frac{1}{2}R g_{\mu\nu}$ is the Einstein tensor and $T_{\mu\nu}$ is the energy-momentum tensor of matter

$$T^{\mu\nu} = -\frac{g^{\mu\alpha} g^{\nu\beta} \delta(\sqrt{-g} \mathcal{L}_M)}{\delta g^{\alpha\beta}}. \quad (2.3)$$

The contracted Bianchi identities ($\nabla_\mu G^{\mu\nu} = 0$) imply that $T_{\mu\nu}$ is divergenceless

$$\nabla_\mu T^{\mu\nu} = 0, \quad (2.4)$$

which dictates the equations of motion (EOM) for matter.

A pedagogical example relevant for ultralight bosonic DM is a complex scalar field Φ minimally coupled to gravity

$$\mathcal{L}_M = \mathcal{L}_\Phi = -\nabla_\mu \Phi^* \nabla^\mu \Phi - \mathcal{U}_\Phi(|\Phi|^2) - J_\Phi(\Phi^* + \Phi), \quad (2.5)$$

where \mathcal{U}_Φ is the interaction potential of Φ (e.g. $\mathcal{U}_\Phi = \mu^2 |\Phi|^2$, with $m_\Phi = \hbar\mu$ being the mass of the scalar field and μ the inverse Compton

wavelength) and J_Φ is a putative current sourcing the scalar field. The corresponding energy-momentum tensor given by Eq. (2.3) is

$$T_\Phi^{\mu\nu} = \nabla^{(\mu} \Phi^* \nabla^{\nu)} \Phi - \frac{1}{2} g^{\mu\nu} \left(\nabla_\alpha \Phi^* \nabla^\alpha \Phi + \mathcal{U}_\Phi (|\Phi|^2) \right), \quad (2.6)$$

and its EOM is the Klein-Gordon equation with some effective potential

$$\square \Phi = \frac{\delta \mathcal{U}_\Phi}{\delta \Phi^*} + J_\Phi. \quad (2.7)$$

Another important case in the study of EMRIs is when the matter Lagrangian represents a point particle of mass m_p minimally coupled to gravity

$$\mathcal{L}_M = \mathcal{L}_p = -2m_p \int d\tau \frac{\delta^{(4)}(x^\alpha - x_p^\alpha(\tau))}{\sqrt{-g}}, \quad (2.8)$$

where $x_p(\tau)$ is the worldline of the particle parametrized by the proper time τ . This Lagrangian implies the point particle follows geodesics of the background spacetime

$$\frac{dx^\alpha}{d\tau} \nabla_\alpha \left(\frac{dx^\mu}{d\tau} \right) = 0, \quad (2.9)$$

and has the energy-momentum tensor

$$T_p^{\mu\nu} = m_p \int d\tau \frac{\delta^{(4)}(x^\alpha - x_p^\alpha(\tau))}{\sqrt{-g}} \frac{dx_p^\mu}{d\tau} \frac{dx_p^\nu}{d\tau}. \quad (2.10)$$

2.1.2 The Kerr spacetime

We are interested in studying systems on timescales where the expansion of the Universe is negligible (e.g. the LISA mission lifetime). Hence, we can set $\Lambda = 0$. Additionally, in many scenarios we can treat the environment as a small perturbation to a particular vacuum BH spacetime. In GR, any stationary, axisymmetric, and asymptotically flat spacetime corresponding to a vacuum solution with an event horizon (i.e. a black hole solution) is a member of the 2-parameter Kerr solution [3]. In Boyer-Lindquist coordinates (t, r, θ, φ) this solution is expressed as

$$ds_{\text{Kerr}}^2 = - \left(1 - \frac{2Mr}{\Sigma} \right) dt^2 - \frac{4aMr}{\Sigma} \sin^2 \theta dt d\varphi + \frac{\Sigma}{\Delta} dr^2 + \Sigma d\theta^2 + \left(r^2 + a^2 + \frac{2Ma^2 r \sin^2 \theta}{\Sigma} \right) \sin^2 \theta d\varphi^2, \quad (2.11)$$

where $\Sigma = r^2 + a^2 \cos^2 \theta$ and $\Delta = r^2 + a^2 - 2Mr$. Far away from the BH, $r \gg M, a$, one recovers spherical coordinates in Minkowski. The Kerr solution has a two-parameter group of isometries generated

by the commuting Killing vector fields $k = \partial/\partial t$ and $m = \partial/\partial\varphi$. k is asymptotically timelike near infinity and is associated with the conserved mass M of the BH. m is asymptotically spacelike near infinity and generates rotations under the axis of symmetry of the BH, leading to the conserved charge $J = aM$, where J is the angular momentum of the BH. Note that $0 \leq a/M < 1$, otherwise the BH possesses a naked singularity.

The Kerr solution has two horizons at the roots of $\Delta = 0$, which are $r_{\pm} = M \pm \sqrt{M^2 - a^2}$. r_+ is the BH event horizon while r_- is a Cauchy horizon. Note also that the event horizon is a null hypersurface with normal $\xi = k + \Omega_H m$, where

$$\Omega_H = \frac{a}{a^2 + r_+^2}, \quad (2.12)$$

and one interprets Ω_H as the angular velocity of the BH.

There is a region outside the BH horizon, known as the *ergoregion*, where k is spacelike and therefore no stationary observers exist. The ergoregion is limited by $r_+ < r < M + \sqrt{M^2 - a^2 \cos^2 \theta}$. In the ergoregion, the strong gravitational field causes a frame-dragging effect, which forces any observer to rotate along with the BH.

It will also be useful to introduce the radial tortoise coordinate r_*

$$\begin{aligned} \frac{dr_*}{dr} &= \frac{r^2 + a^2}{\Delta} \Rightarrow \\ \Rightarrow r_* &= r + \frac{r_+^2 + a^2}{r_+ - r_-} \log \left| \frac{r - r_+}{2M} \right| - \frac{r_-^2 + a^2}{r_+ - r_-} \log \left| \frac{r - r_-}{2M} \right|, \end{aligned} \quad (2.13)$$

which pushes the BH horizon to $r_* \rightarrow -\infty$.

In the non-rotating limit ($a = 0$), the Kerr metric reduces to Schwarzschild

$$ds_{\text{Schw}}^2 = - \left(1 - \frac{2M}{r} \right) dt^2 + \frac{1}{1 - \frac{2M}{r}} dr^2 + r^2 d\Omega^2, \quad (2.14)$$

with $d\Omega^2 = d\theta^2 + \sin^2 \theta d\varphi^2$ the metric on the 2-sphere. The event horizon goes to $r_+ = 2M$, there is no Cauchy horizon, and the tortoise coordinate becomes

$$r_* = r + 2M \log \left| \frac{r}{2M} - 1 \right|. \quad (2.15)$$

The Schwarzschild solution is a particular case of spherically-symmetric spacetimes, which in general can be described by the line element

$$ds_{\text{Spherical}}^2 = -A(r) dt^2 + \frac{1}{B(r)} dr^2 + r^2 d\Omega^2. \quad (2.16)$$

The generalization of the radial tortoise coordinate for these spacetimes is

$$\frac{dr_*}{dr} = \frac{1}{\sqrt{A(r)B(r)}}. \quad (2.17)$$

2.1.3 Black-Hole Perturbations

EMRIs can also be modeled as a point particle of mass m_p , representing the stellar-mass compact object, perturbing the SMBH of mass M , where $m_p/M \ll 1$. To handle this, the natural framework is BH perturbation theory [178, 179], which describes the spacetime using a background metric $g_{\mu\nu}^{(0)}$, and adds a perturbation $h_{\mu\nu}$ such that the full metric is given by

$$g_{\mu\nu}(x^\alpha) = g_{\mu\nu}^{(0)}(x^\alpha) + \epsilon h_{\mu\nu}(x^\alpha) + \mathcal{O}(\epsilon^2), \quad (2.18)$$

where $\epsilon \ll 1$ is an expansion parameter. In the case of EMRIs, this would be the mass ratio $q = m_p/M$. For accurate parameter estimation with LISA, this expansion will have to be carried until second order in the mass ratio q [28, 180, 181].

REGGE-WHEELER AND ZERILLI EQUATION

We will often focus on spherically-symmetric backgrounds (e.g. Schwarzschild), where any perturbation can be decomposed into irreducible representations of $SO(2)$. Then, gravitational perturbations can be expanded in ten spherical harmonics, which are the tensorial version of the standard spherical harmonics $Y^{\ell m}(\theta, \varphi)$ for scalars [182]. The perturbations can be grouped into polar/electric/even type or axial/magnetic/odd type, depending on their behavior under parity transformations $(\theta, \varphi) \rightarrow (\pi - \theta, \pi - \varphi)$ [183, 184]

$$\begin{aligned} \mathbf{h}^{\text{axial}} &= \sum_{\ell, m} \frac{\sqrt{2\ell(\ell+1)}}{r} \left[i h_1^{\ell m} \mathbf{c}_{\ell m} - h_0^{\ell m} \mathbf{c}_{\ell m}^0 + \frac{\sqrt{(\ell+2)(\ell-1)}}{2} h_2^{\ell m} \mathbf{d}_{\ell m} \right], \\ \mathbf{h}^{\text{polar}} &= \sum_{\ell, m} \left[A H_0^{\ell m} \mathbf{a}_{\ell m}^0 - i\sqrt{2} H_1^{\ell m} \mathbf{a}_{\ell m}^1 + \frac{1}{B} H_2^{\ell m} \mathbf{a}_{\ell m} + \sqrt{2} K^{\ell m} \mathbf{g}_{\ell m} \right. \\ &\quad + \frac{\sqrt{2\ell(\ell+1)}}{r} \left(h_1^{(e)\ell m} \mathbf{b}_{\ell m}^1 - i h_0^{(e)\ell m} \mathbf{b}_{\ell m}^0 \right) \\ &\quad \left. + \left(\sqrt{\frac{(\ell+2)(\ell+1)\ell(\ell-1)}{2}} \mathbf{f}_{\ell m} - \frac{\ell(\ell+1)}{\sqrt{2}} \mathbf{g}_{\ell m} \right) \mathbf{G}^{\ell m} \right], \end{aligned} \quad (2.19)$$

where $\sum_{\ell, m} = \sum_{\ell=0}^{\infty} \sum_{m=-\ell}^{\ell}$. We are omitting the dependences on (t, r, θ, φ) to avoid cluttering, but the mode perturbations $h_1^{\ell m}, h_0^{\ell m}, \dots$

are only functions of (t, r) , while $\mathbf{a}_{\ell m}^0, \mathbf{a}_{\ell m}, \dots$, are the ten tensor spherical harmonics independent of t

$$\mathbf{a}_{\ell m}^0 = \begin{pmatrix} Y_{\ell m} & 0 & 0 & 0 \\ 0 & 0 & 0 & 0 \\ 0 & 0 & 0 & 0 \\ 0 & 0 & 0 & 0 \end{pmatrix}, \quad (2.20)$$

$$\mathbf{a}_{\ell m}^1 = \frac{i}{\sqrt{2}} \begin{pmatrix} 0 & Y_{\ell m} & 0 & 0 \\ \text{Sym} & 0 & 0 & 0 \\ 0 & 0 & 0 & 0 \\ 0 & 0 & 0 & 0 \end{pmatrix}, \quad (2.21)$$

$$\mathbf{a}_{\ell m} = \begin{pmatrix} 0 & 0 & 0 & 0 \\ 0 & Y_{\ell m} & 0 & 0 \\ 0 & 0 & 0 & 0 \\ 0 & 0 & 0 & 0 \end{pmatrix}, \quad (2.22)$$

$$\mathbf{b}_{\ell m}^0 = \frac{ir}{\sqrt{2\ell(\ell+1)}} \begin{pmatrix} 0 & 0 & \partial_\theta Y_{\ell m} & \partial_\varphi Y_{\ell m} \\ 0 & 0 & 0 & 0 \\ \text{Sym} & 0 & 0 & 0 \\ \text{Sym} & 0 & 0 & 0 \end{pmatrix}, \quad (2.23)$$

$$\mathbf{b}_{\ell m} = \frac{r}{\sqrt{2\ell(\ell+1)}} \begin{pmatrix} 0 & 0 & 0 & 0 \\ 0 & 0 & \partial_\theta Y_{\ell m} & \partial_\varphi Y_{\ell m} \\ 0 & \text{Sym} & 0 & 0 \\ 0 & \text{Sym} & 0 & 0 \end{pmatrix}, \quad (2.24)$$

$$\mathbf{c}_{\ell m}^0 = \frac{r}{\sqrt{2\ell(\ell+1)}} \begin{pmatrix} 0 & 0 & \frac{1}{\sin\theta} \partial_\varphi Y_{\ell m} & -\sin\theta \partial_\theta Y_{\ell m} \\ 0 & 0 & 0 & 0 \\ \text{Sym} & 0 & 0 & 0 \\ \text{Sym} & 0 & 0 & 0 \end{pmatrix}, \quad (2.25)$$

$$\mathbf{c}_{\ell m} = \frac{ir}{\sqrt{2\ell(\ell+1)}} \begin{pmatrix} 0 & 0 & 0 & 0 \\ 0 & 0 & \frac{1}{\sin\theta} \partial_\varphi Y_{\ell m} & -\sin\theta \partial_\theta Y_{\ell m} \\ 0 & \text{Sym} & 0 & 0 \\ 0 & \text{Sym} & 0 & 0 \end{pmatrix}, \quad (2.26)$$

$$\mathbf{d}_{\ell m} = \frac{ir^2}{\sqrt{2(\ell+2)(\ell+1)\ell(\ell-1)}} \begin{pmatrix} 0 & 0 & 0 & 0 \\ 0 & 0 & 0 & 0 \\ 0 & 0 & -\frac{1}{\sin\theta} X_{\ell m} & \sin\theta W_{\ell m} \\ 0 & 0 & \text{Sym} & \sin\theta X_{\ell m} \end{pmatrix}, \quad (2.27)$$

$$\mathbf{f}_{\ell m} = \frac{r^2}{\sqrt{2(\ell+2)(\ell+1)\ell(\ell-1)}} \begin{pmatrix} 0 & 0 & 0 & 0 \\ 0 & 0 & 0 & 0 \\ 0 & 0 & W_{\ell m} & X_{\ell m} \\ 0 & 0 & \text{Sym} & -\sin^2\theta W_{\ell m} \end{pmatrix}, \quad (2.28)$$

$$\mathbf{g}_{\ell m} = \frac{r^2}{\sqrt{2}} \begin{pmatrix} 0 & 0 & 0 & 0 \\ 0 & 0 & 0 & 0 \\ 0 & 0 & Y_{\ell m} & 0 \\ 0 & 0 & 0 & \sin^2\theta Y_{\ell m} \end{pmatrix}. \quad (2.29)$$

where ‘‘Sym’’ is the symmetric of that respective matrix entry and

$$X_{\ell m} = 2\partial_\varphi(\partial_\theta - \cot\theta)Y_{\ell m}, \quad (2.30)$$

$$W_{\ell m} = \left(\partial_\theta^2 - \cot\theta\partial_\theta - \frac{1}{\sin^2\theta}\partial_\varphi^2 \right) Y_{\ell m}. \quad (2.31)$$

Introducing the inner product (\cdot, \cdot) on the two-sphere

$$\left(\mathbf{R}^{\ell' m'}, \mathbf{S}^{\ell m} \right) = \int_{S_2} d\Omega \left(R_{\mu\nu}^{\ell' m'} \right)^* S_{\lambda\rho}^{\ell m} \eta^{\mu\lambda} \eta^{\nu\rho}, \quad (2.32)$$

where

$$\eta_{\mu\nu} = \text{diag}(-1, 1, r^2, r^2 \sin^2\theta), \quad (2.33)$$

one can check that the harmonics defined above are orthonormal, i.e. $\left(\mathbf{R}^{\ell' m'}, \mathbf{S}^{\ell m} \right) = \delta_{RS} \delta_{l'l} \delta_{m'm}$.

In a similar fashion, the energy-momentum tensor can be expanded as

$$\begin{aligned} \mathbf{T} = \sum_{\ell, m} & \left[\mathcal{A}_{\ell m}^0 \mathbf{a}_{\ell m}^0 + \mathcal{A}_{\ell m}^1 \mathbf{a}_{\ell m}^1 + \mathcal{A}_{\ell m} \mathbf{a}_{\ell m} + \mathcal{B}_{\ell m}^0 \mathbf{b}_{\ell m}^0 + \mathcal{B}_{\ell m} \mathbf{b}_{\ell m} \right. \\ & \left. + \mathcal{Q}_{\ell m}^0 \mathbf{c}_{\ell m}^0 + \mathcal{Q}_{\ell m} \mathbf{c}_{\ell m} + \mathcal{D}_{\ell m} \mathbf{d}_{\ell m} + \mathcal{G}_{\ell m} \mathbf{g}_{\ell m} + \mathcal{F}_{\ell m} \mathbf{f}_{\ell m} \right]. \end{aligned} \quad (2.34)$$

where, for a given source, the expansion coefficients can be obtained by projecting the energy-momentum tensor on the respective spherical harmonic, e.g. $\mathcal{A}_{\ell m}^0 = (\mathbf{a}_{\ell m}^0, \mathbf{T})$.

It is important to recall that GR is invariant under diffeomorphisms. Infinitesimally

$$x_\mu \rightarrow x'_\mu = x_\mu + \xi_\mu \Rightarrow h_{\mu\nu} \rightarrow h'_{\mu\nu} = h_{\mu\nu} - 2\nabla_{(\mu} \xi_{\nu)}, \quad (2.35)$$

where ξ is the vector field generating the diffeomorphism. ξ can also be expanded in a set of polar and axial harmonics

$$\begin{aligned}\xi &= \sum_{\ell,m} \left(-\frac{\xi_t^{\ell m}}{A}, B\zeta_r^{\ell m}, 0, 0 \right) Y_{\ell m} \\ &+ \frac{\xi_\Omega^{\ell m}}{r^2 \sin \theta} (0, 0, \sin \theta \partial_\theta Y_{\ell m}, \partial_\varphi Y_{\ell m}) \\ &+ \frac{\xi_{\text{ax}}^{\ell m}}{\sqrt{2\ell(\ell+1)}} \left(0, 0, \frac{1}{r \sin \theta} \partial_\varphi Y_{\ell m}, -\frac{1}{r} \partial_\theta Y_{\ell m} \right), \quad (2.36)\end{aligned}$$

where $\xi_t^{\ell m}$, $\xi_r^{\ell m}$, $\xi_\Omega^{\ell m}$, $\xi_{\text{ax}}^{\ell m}$ are only functions of t and r . The first two terms on the right-hand side are the polar ones and the second is the single axial degree of freedom. Then

$$\begin{aligned}2\nabla_{(\mu}\xi_{\nu)} &= (2\partial_t \xi_t - A'B\zeta_r) \mathbf{a}^0 \\ &- i\sqrt{2} \left(\partial_r \xi_t + \partial_t \xi_r - \frac{A'}{A} \xi_t \right) \mathbf{a}^1 \\ &+ \left(2\partial_r \xi_r + \frac{B'}{B} \xi_r \right) \mathbf{a} - i \frac{\sqrt{2\ell(\ell+1)}}{r} (\xi_t + \partial_t \xi_\Omega) \mathbf{b}^0 \\ &+ \frac{\sqrt{2\ell(\ell+1)}}{r} \left(\partial_r \xi_\Omega + \xi_r - \frac{2}{r} \xi_\Omega \right) \mathbf{b} + \partial_t \xi_{\text{ax}} \mathbf{c}^0 \\ &- i \left(\partial_r \xi_{\text{ax}} - \frac{\xi_{\text{ax}}}{r} \right) \mathbf{c} + i \frac{\sqrt{(\ell+2)(\ell-1)}}{r} \xi_{\text{ax}} \mathbf{d} \\ &+ \frac{\sqrt{2(\ell+2)(\ell+1)\ell(\ell-1)}}{r^2} \xi_\Omega \mathbf{f} \\ &+ \frac{\sqrt{2}}{r^2} (2rB\zeta_r - \ell(\ell+1)\xi_\Omega) \mathbf{g}, \quad (2.37)\end{aligned}$$

where the prime denotes a derivative with respect to r , and from now on we omit (ℓ, m) indices unless necessary to avoid cluttering. Therefore, we can pick ξ^μ judiciously to eliminate four components of the metric perturbations, one in the axial sector and three in the polar one. A common choice is the *Regge-Wheeler* gauge, where we set to zero terms involving angular derivatives of the highest order

$$h_2 = h_0^{(e)} = h_1^{(e)} = G = 0. \quad (2.38)$$

In the founding work of BH perturbation theory, Regge and Wheeler employed this gauge to derive a decoupled wave equation for a master function Ψ_{RW} , which encodes all the dynamics of the axial sector around a Schwarzschild BH [185]. Years later, Zerilli obtained the same for the polar sector [186, 187]¹. However, their derivation involves a lengthy manipulation of Einstein's equations, which we will revisit in Chapter 9, when we study EMRIs in non-vacuum environments. For

¹ Zerilli's original papers contain numerous typos, namely in the definitions of the spherical harmonics. Ref. [183] corrects them, and we follow it in our definitions.

now, it is sufficient to state the final master wave equations for the axial (“RW”) and polar sectors (“Z”) [188, 189]

$$(-\partial_t^2 + \partial_{r_*}^2 - V_{Z/RW}) \Psi_{Z/RW} = S_{Z/RW}. \quad (2.39)$$

$\Psi_{Z/RW}$ are the master functions, which are related to the metric perturbations above through

$$\Psi_{RW} = \frac{1}{r} \left(1 - \frac{2M}{r}\right) h_1, \quad (2.40)$$

$$\Psi_Z = \frac{r}{\lambda + 1} \left[K + \frac{1 - 2M/r}{\lambda + 3M/r} (H_2 - r \partial_r K) \right], \quad (2.41)$$

where $\lambda = (\ell - 1)(\ell + 2)/2$, while the effective potentials are [188]

$$V_{RW} = \left(1 - \frac{2M}{r}\right) \left[\frac{\ell(\ell + 1)}{r^2} - \frac{6M}{r^3} \right], \quad (2.42)$$

$$V_Z = \frac{2}{r^3} \left(1 - \frac{2M}{r}\right) \frac{9M^3 + 3\lambda^2 M r^2 + \lambda^2 (1 + \lambda) r^3 + 9M^2 \lambda r}{(3M + \lambda r)^2}. \quad (2.43)$$

Finally, $S_{Z/RW}$ are source terms which depend on the energy-momentum tensor. Assuming the source is localized, close to the BH horizon and at large distances the master equations become

$$r \rightarrow 2M, \infty \Rightarrow (-\partial_t^2 + \partial_{r_*}^2) \Psi_{Z/RW} = 0. \quad (2.44)$$

Therefore, they admit two physical linearly independent solutions traveling at the speed of light. Physical boundary conditions are represented by ingoing waves at the horizon, $A_{in} e^{-i\omega(t+r_*)}$, and the other outgoing waves at infinity, $A_{out} e^{-i\omega(t-r_*)}$.

$\Psi_{Z/RW}$ are gauge invariant quantities and control the two radiative degrees of freedom of GR at large distances [184, 189]

$$h_+ - ih_\times = \lim_{r \rightarrow \infty} \frac{1}{2r} \sum_{\ell=2}^{\infty} \sum_{m=-\ell}^{\ell} \sqrt{\frac{(\ell+2)!}{(\ell-2)!}} \left(\Psi_Z^{\ell m} - 2i \int_{-\infty}^t \Psi_{RW}^{\ell m} \right) {}_{-2}Y^{\ell m},$$

with

$${}_{-2}Y^{\ell m}(\theta, \varphi) = \sqrt{\frac{(\ell-2)!}{(\ell+2)!}} \left(W^{\ell m}(\theta, \varphi) - \frac{i}{\sin \theta} X^{\ell m}(\theta, \varphi) \right),$$

the spin-2 weighted spherical harmonic.

The total energy flux carried to infinity by GWs can also be computed through these master functions [184, 189]

$$\begin{aligned} \dot{E}_\infty^{\ell m} &= \frac{1}{64\pi} \frac{(\ell+2)!}{(\ell-2)!} \left[\left| \dot{\Psi}_Z^{\ell m} \right|^2 + 4 \left| \Psi_{RW}^{\ell m} \right|^2 \right], \\ \dot{E}_\infty &= \sum_{\ell=2}^{\infty} \sum_{m=-\ell}^{\ell} \dot{E}_\infty^{\ell m}, \end{aligned} \quad (2.45)$$

where the overdot denotes differentiation with respect to time.

The last two sums over the multipoles only started at $\ell = 2$. The monopole ($\ell = 0$) and dipole ($\ell = 1$) perturbations are pure gauge in GR and do not contribute to the radiative degrees of freedom, though the perturbations may be non-zero in some spacetime regions. Additionally, we have that $\mathbf{b}_{\ell m}^0 = \mathbf{b}_{\ell m} = \mathbf{c}_{\ell m}^0 = \mathbf{c}_{\ell m} = 0$ for $\ell = 0$, and $\mathbf{d}_{\ell m} = \mathbf{f}_{\ell m} = 0$ for $\ell \leq 1$. So the Regge-Wheeler gauge (2.38) is not completely fixed for $\ell \leq 1$.

This property is related to the fundamental nature of gravity, which according to GR should be mediated by a massless spin-2 boson, the “graviton”. As a result, GR exhibits conservation of the energy-momentum tensor, analogous to vector current conservation in electromagnetism that is mediated by a massless spin-1 boson, the photon. Therefore, there is no dipolar radiation in GR, similarly to the absence of monopole radiation in electromagnetism.

TEUKOLSKY EQUATION

Obtaining a master equation for linear perturbations in Kerr is more complicated since the loss of spherical symmetry means that separation in spherical harmonics is no longer possible. Instead, Teukolsky was able to decouple the equations governing any type of linear perturbations to Kerr using the Newman-Penrose formalism, in which tensors are projected onto a null tetrad $\{n, l, m, \bar{m}\}$ [190] (the overbar in \bar{m} denotes complex conjugation). The details of this formalism are not necessary to follow the thesis, and we refer the interested readers to Refs. [178, 179, 190–193] for more detailed descriptions. Here it will suffice to work with the final master equation describing any type of linear perturbations to Kerr, which in Boyer-Lindquist coordinates and using the Kinnersley tetrad

$$l = \left(\frac{r^2 + a^2}{\Delta}, 1, 0, \frac{a}{\Delta} \right), \quad (2.46)$$

$$n = \frac{1}{2\Sigma} (r^2 + a^2, -\Delta, 0, a), \quad (2.47)$$

$$m = \frac{1}{\sqrt{2}(r + ia \cos \theta)} \left(ia \sin \theta, 0, 1, \frac{i}{\sin \theta} \right), \quad (2.48)$$

reads

$$\begin{aligned} & \left[\frac{(r^2 + a^2)^2}{\Delta} - a^2 \sin^2 \theta \right] \partial_t^2 \Psi - \Delta^{-s} \partial_r \left(\Delta^{s+1} \partial_r \Psi \right) \\ & + \frac{4aMr}{\Delta} \partial_\varphi \partial_t \Psi + 2s \left[r + \frac{M(a^2 - r^2)}{\Delta} + ia \cos \theta \right] \partial_t \Psi \\ & - \frac{1}{\sin \theta} \partial_\theta (\sin \theta \partial_\theta \Psi) - 2s \left[\frac{a(r - M)}{\Delta} + \frac{i \cos \theta}{\sin^2 \theta} \right] \partial_\varphi \Psi \\ & - \left[\frac{1}{\sin^2 \theta} - \frac{a^2}{\Delta} \right] \partial_\varphi^2 \Psi + (s^2 \cot^2 \theta - s) \Psi = 4\pi \Sigma T. \end{aligned} \quad (2.49)$$

Here, s determines the spin-weight of the master variable Ψ , which corresponds to $s = 0$ for scalars, $s = \pm 1$ for electromagnetic perturbations (i.e. vectors), and $s = \pm 2$ for gravitational ones. T encodes the source term and depends on the energy-momentum tensor. We particularize it below for a point-particle orbiting a Kerr BH.

For $s = 0$ the Teukolsky equation reduces to the Klein-Gordon equation for a massless scalar field. For $s = \pm 2$, it describes perturbations to the Weyl tensor that govern the radiative degrees of freedom at the BH horizon ($s = 2$), and at infinity ($s = -2$). Since we are interested in studying GW emission, we will mostly focus on the $s = -2$ case, for which the master variable is $\Psi = \rho^{-4}\psi_4$, with $\rho = -1/(r - ia \cos \theta)$. ψ_4 is then related to the GW polarizations at large distances through

$$\frac{1}{2} \left(\frac{\partial^2 h_+}{\partial t^2} - i \frac{\partial^2 h_\times}{\partial t^2} \right) = \lim_{r \rightarrow \infty} \psi_4. \quad (2.50)$$

The flux of energy carried by GWs to infinity can also be computed through ψ_4

$$\dot{E}^\infty = \lim_{r \rightarrow \infty} \frac{r^2}{4\pi} \int_{S_2} d\Omega \int_{-\infty}^t dt' \Psi(t', r, \theta, \varphi). \quad (2.51)$$

2.2 NUMERICAL FRAMEWORK

In general, analytic solutions to the master equations we discussed are not possible, and numerical methods must be used instead. In this thesis, we will often use a two-step Lax-Wendroff algorithm with second-order finite differences appropriate to solve “wave-like” partial differential equations in the time-domain [194–197]. In this section we provide an overview of the algorithm.

2.2.1 The Lax-Wendroff algorithm

Let us assume that we have manipulated our wave equation (e.g. the Teukolsky equation) so that in the homogeneous version it reads

$$\partial_\tau^2 \Psi = \left[\tilde{A}^{\tau\rho} \partial_\tau \partial_\rho + \tilde{A}^{\rho\rho} \partial_\rho^2 + \tilde{A}^{\theta\theta} \partial_\theta^2 + \tilde{B}^\tau \partial_\tau + \tilde{B}^\rho \partial_\rho + \tilde{B}^\theta \partial_\theta + \tilde{C} \right] \Psi. \quad (2.52)$$

Here, τ and ρ are redefined time and radial variables, respectively. This coordinate ρ should not be confused with the ρ variable appearing in the definition of the master variable Ψ in terms of ψ_4 , and we adopt it for consistency with Ref. [197]. The coefficients depend only on ρ and θ , which can be achieved even for rotating BHs due to the axisymmetry of Kerr. In spherical symmetry, we could further eliminate the θ dependence by expanding in spherical harmonics, which would be absorbed in the \tilde{C} coefficient. This procedure is easily

generalizable for a system of two or more coupled wave equations, in which case the coefficients above would be promoted to matrices.

Eq. (2.52) can be reduced to a system of first-order partial differential equations by defining the auxiliary variable Π

$$\Pi = (\partial_\tau + b \partial_\rho) \Psi, \quad (2.53)$$

$$b = - \left(\tilde{A}^{\tau\rho} + \sqrt{(\tilde{A}^{\tau\rho})^2 + 4\tilde{A}^{\rho\rho}} \right) / 2. \quad (2.54)$$

We can then rewrite it as

$$\partial_\tau \mathbf{u} + \mathbf{M} \cdot \partial_\rho \mathbf{u} + \mathbf{L} \cdot \mathbf{u} + \mathbf{A} \cdot \mathbf{u} = \mathbf{T}, \quad (2.55)$$

where we reintroduced the source term \mathbf{T} and

$$\mathbf{u} = \{ \Psi_R, \Psi_I, \Pi_R, \Pi_I \}, \quad (2.56)$$

and the subscripts R and I refer to the real and imaginary part. The matrices \mathbf{M} , \mathbf{A} , \mathbf{L} have the general structure

$$\mathbf{M} = \begin{pmatrix} b & 0 & 0 & 0 \\ 0 & b & 0 & 0 \\ m_{31} & m_{32} & -b & 0 \\ -m_{32} & m_{31} & 0 & -b \end{pmatrix}, \quad (2.57)$$

$$\mathbf{A} = \begin{pmatrix} 0 & 0 & -1 & 0 \\ 0 & 0 & 0 & -1 \\ a_{31} & a_{32} & a_{33} & a_{34} \\ -a_{32} & a_{31} & -a_{34} & a_{33} \end{pmatrix}, \quad (2.58)$$

$$\mathbf{L} = \begin{pmatrix} 0 & 0 & 0 & 0 \\ 0 & 0 & 0 & 0 \\ l_{31} & 0 & 0 & 0 \\ 0 & l_{31} & 0 & 0 \end{pmatrix}. \quad (2.59)$$

Further below, we will make this coefficients explicit for the Teukolsky equation. The matrix \mathbf{L} contains the angular derivatives in θ (in spherical symmetry $\mathbf{L} = 0$). This decomposition is particularly useful for inferring the hyperbolicity of the system by computing the eigenvalues/eigenvectors of \mathbf{M} . Since \mathbf{L} contains second-order derivatives, hyperbolicity is not guaranteed even if \mathbf{M} has a complete set of linearly independent eigenvectors with real eigenvalues. However, this method was numerically well-behaved and convergent in all the cases we studied.

We can finally construct a time-explicit evolution scheme based on the two-step, second-order Lax-Wendroff finite-difference method. First, we rewrite Eq. (2.55) in the form of an advection equation

$$(\partial_\tau + \mathbf{D} \partial_\rho) \mathbf{u} = \mathbf{S}, \quad (2.60)$$

with

$$\mathbf{D} = \text{diag}(b, b, -b, -b), \quad (2.61)$$

$$\mathbf{S} = -(\mathbf{M} - \mathbf{D}) \cdot \partial_\rho \mathbf{u} - \mathbf{L} \cdot \mathbf{u} - \mathbf{A} \cdot \mathbf{u} + \mathbf{T}. \quad (2.62)$$

We discretize this equation on a uniform two-dimensional grid, with grid steps $\delta\rho$ and $\delta\theta$. Each iteration of the numerical integration has two steps. In the first step, we compute an intermediate solution between the main grid points

$$\mathbf{u}_{i+1/2}^{n+1/2} = \frac{1}{2} (\mathbf{u}_{i+1}^n + \mathbf{u}_i^n) - \frac{\delta\tau}{2} \left[\frac{1}{\delta\rho} \mathbf{D}_{i+1/2}^n (\mathbf{u}_{i+1}^n - \mathbf{u}_i^n) - \mathbf{S}_{i+1/2}^n \right]. \quad (2.63)$$

We omit angular indexes to avoid cluttering and $\delta\tau$ is the time step. The fields are centered in the angular direction and angular derivatives are approximated by a centered second-order difference stencil

$$\partial_\theta \mathbf{u}_j = \frac{\mathbf{u}_{j+1} - \mathbf{u}_{j-1}}{2\delta\theta} + \mathcal{O}(\delta\theta^2), \quad (2.64)$$

$$\partial_\theta^2 \mathbf{u}_j = \frac{\mathbf{u}_{j+1} - 2\mathbf{u}_j + \mathbf{u}_{j-1}}{\delta\theta^2} + \mathcal{O}(\delta\theta^2), \quad (2.65)$$

while the radial derivatives are approximated using centered second-order differences on the values i and $i+1$. The algebraic terms in $\mathbf{D}_{i+1/2}^n$ and $\mathbf{S}_{i+1/2}^n$ are given by an average between the values at i and $i+1$. This intermediate solution is then used to update the solution at the next time step

$$\mathbf{u}_i^{n+1} = \mathbf{u}_i^n - \delta\tau \left[\frac{1}{\delta\rho} \mathbf{D}_i^{n+1/2} (\mathbf{u}_{i+1/2}^{n+1/2} - \mathbf{u}_{i-1/2}^{n+1/2}) - \mathbf{S}_i^{n+1/2} \right], \quad (2.66)$$

while now the centered radial differences and averages are taken on the values $\mathbf{u}_{i+1/2}^{n+1/2}$ and $\mathbf{u}_{i-1/2}^{n+1/2}$. The only missing step is to impose appropriate boundary conditions for ρ and θ . We will illustrate this with a concrete example below.

2.2.2 A practical case: the Teukolsky equation

Let us now apply this method to the Teukolsky equation (2.49).

COORDINATE TRANSFORMATIONS.

Boyer-Lindquist coordinates suffer from several pathologies that need to be cured for numerical schemes. The radial coordinate becomes singular at the BH horizon and there is a frame-dragging effect along φ due to the BH rotation. Furthermore, the asymptotic behavior of Ψ at both the BH horizon and infinity needs to be considered to

prevent a numerical blow-up of the solution. The general behavior for spin-weight s is different for ingoing and outgoing waves

$$\lim_{r \rightarrow +\infty} |\Psi| \sim \begin{cases} 1/r^{2s+1} & \text{outgoing} \\ 1/r & \text{ingoing} \end{cases}, \quad (2.67)$$

$$\lim_{r \rightarrow r_+} |\Psi| \sim \begin{cases} 1 & \text{outgoing} \\ \Delta^{-s} & \text{ingoing} \end{cases}. \quad (2.68)$$

To deal with the radial singularity at the BH horizon we use the radial tortoise coordinate r_* introduced in Eq. (2.13). As mentioned above, r_* pushes the BH horizon to $-\infty$, which in the numerical domain is put at some finite distance where artificial ingoing boundary conditions are imposed.

To handle the angular twisting in the ergoregion, we introduce a modified azimuthal coordinate

$$\begin{aligned} d\tilde{\varphi} &= d\varphi + \frac{a}{\Delta} dr \Rightarrow \\ \Rightarrow \tilde{\varphi} &= \varphi + \frac{a}{r_+ - r_-} \log \left| \frac{r - r_+}{r - r_-} \right|. \end{aligned} \quad (2.69)$$

Finally, we rescale the master variable according to the respective asymptotic behavior at large distances (2.67). The axisymmetry of the Kerr background also allows us to separate the azimuthal dependence in $\tilde{\varphi}$ with the mode number m

$$\Psi(t, r, \theta, \varphi) = e^{im\tilde{\varphi}} r^{(-2s+1)} \psi(t, r, \theta). \quad (2.70)$$

Applying these transformations to the Teukolsky equation (2.49) we arrive at

$$\begin{aligned} & \left[\frac{(r^2 + a^2)^2}{\Delta} - a^2 \sin^2 \theta \right] \partial_t^2 \psi - \frac{(r^2 + a^2)^2}{\Delta} \partial_{r_*}^2 \psi \\ & - \partial_\theta^2 \psi - \cot \theta \partial_\theta \psi - \frac{2}{\Delta} \left[Ms(r^2 - a^2) - rs\Delta \right. \\ & - \left. ia(s\Delta \cos \theta + 2Mmr) \right] \partial_t \psi - \frac{1}{r\Delta} \left[2iamr(r^2 + a^2) \right. \\ & - \left. 2rs(r^2 + a^2)(M - r) - (4(r^2 + a^2)s + 2a^2)\Delta \right] \partial_{r_*} \psi \\ & - \frac{1}{r^2\Delta} \left[2(1+s)(1+2s)\Delta^2 - r\Delta[r(s \cot \theta + m \csc \theta)^2 \right. \\ & - \left. r(s - 2(1+s)(1+2s)) - 2M(1+s)(1+2s) \right] \\ & - \left. 2iamr[2rs(M - r) + (1+2s)\Delta] \right] \psi = 4\pi \Sigma r^{2s+1} e^{-im\tilde{\varphi}} T. \end{aligned} \quad (2.71)$$

Multiplying it by Δ/σ^2 , where

$$\sigma^2 = (r^2 + a^2)^2 - \Delta a^2 \sin^2 \theta, \quad (2.72)$$

we finally bring it to the form in Eq. (2.52) with the following coefficients

$$\begin{aligned} b &= \frac{r^2 + a^2}{\sigma}, \\ m_{31} &= -2 \frac{rs(M-r)(r^2+a^2) + (2(r^2+a^2)s+a^2)\Delta}{r\sigma^2} \\ &\quad - b2s \frac{M(a^2-r^2) + r\Delta}{\sigma^2} + b\partial_{r^*} b, \\ m_{32} &= 2am \frac{r^2+a^2}{\sigma^2} + b2a \frac{s\Delta \cos \theta + 2Mmr}{\sigma^2}, \\ a_{31} &= \frac{\Delta}{r^2\sigma^2} [r^2(s \cot \theta + m \csc \theta)^2 - 2Mr(1+s)(1+2s) \\ &\quad + r^2(4s^2 + 5s + 2) - 2(1+s)(1+2s)\Delta], \\ a_{32} &= -2am \frac{2rs(M-r) + (1+2s)\Delta}{r\sigma^2}, \\ a_{33} &= 2s \frac{M(a^2-r^2) + r\Delta}{\sigma^2}, \quad a_{34} = -2a \frac{2mMr + s\Delta \cos \theta}{\sigma^2}, \\ l_{31} &= -\frac{\Delta}{\sigma^2} \partial_\theta^2 - \frac{\Delta}{\sigma^2} \cot \theta \partial_\theta. \end{aligned} \quad (2.73)$$

BOUNDARY CONDITIONS

To evolve the system described above, we need to impose appropriate boundary conditions for ψ . The physical solution corresponds to having ingoing waves at the BH horizon and outgoing waves at infinity. At the inner boundary, we exploit the asymptotic behavior of ingoing waves $\psi \sim \Delta^{-s}$ as in Eq. (2.68). For $s = -2$, which describes the gravitational perturbations of interest, we can then set $\psi = \Pi = 0$. Imposing outgoing boundary conditions at the outer boundary is more complicated and often one obtains spurious reflections there. One solution is to set the outer boundary far enough away so that it does not affect the interior domain in the maximal Cauchy development of our initial data. For example, if we evolve the system for $t = 10^3 M$ and extract the fields at $r_*^{\text{ext}} = 500M$, then the outer boundary should be placed further than $r_*^{\text{out}} = 10^3 M$ to prevent any signal from being reflected back and affect the field values at the extraction radius. The same strategy can be used at the inner boundary when the asymptotic behavior of ψ is less trivial, as in the scalar case where it asymptotes to a constant.

Finally, we use the symmetries of spheroidal harmonics, which are the generalization of spherical harmonics to axisymmetric backgrounds, to impose boundary conditions on the rotation axis [182]

$$\psi \Big|_{\theta=0,\pi} = 0 \quad , \quad m \text{ odd} \quad (2.74)$$

$$\partial_\theta \psi \Big|_{\theta=0,\pi} = 0 \quad , \quad m \text{ even} . \quad (2.75)$$

This numerical method has been used extensively in the literature for over two decades. Initially, it was used to study the late-time polynomial tail decay of perturbations in Kerr [194, 195, 198, 199], which require high precision and stable codes over long computational times. The method exhibited second-order convergence and a Courant condition $\delta t \leq (\delta r_*, 5\delta\theta)$. More recently, it has been applied to the study of EMRIs [197, 200–202], as we will do. Typical choices for the grid discretization are $\delta r_*/M = 0.05$, $\delta\theta = \pi/64$, and $\delta t = \delta r_*/2$.

POINT-PARTICLE SOURCE TERM

We will now explain how to incorporate point-particle source terms in the Teukolsky equation, which can model the secondary object in an EMRI. The source term T appearing in Eq. (2.71) is [190, 200]

$$T = 2\rho^{-4}T_4, \quad (2.76)$$

$$\begin{aligned} T_4 &= (\tilde{\Delta} + 3\gamma - \bar{\gamma} + 4\mu + \bar{\mu}) (\tilde{\Delta} + 2\gamma - 2\bar{\gamma} + \bar{\mu}) T_{\bar{m}\bar{m}} \\ &\quad - (\tilde{\Delta} + 3\gamma - \bar{\gamma} + 4\mu + \bar{\mu}) (\bar{\delta} - 2\bar{\tau} + 2\alpha) T_{n\bar{m}} \\ &\quad + (\bar{\delta} - \bar{\tau} + \bar{\beta} + 3\alpha + 4\pi) (\bar{\delta} - \bar{\tau} + 2\bar{\beta} + 2\alpha) T_{nn} \\ &\quad - (\bar{\delta} - \bar{\tau} + \bar{\beta} + 4\pi) (\tilde{\Delta} + 2\gamma + 2\bar{\mu}) T_{n\bar{m}}, \end{aligned} \quad (2.77)$$

where we alert again that now this $\rho = -1(r - ia \cos \theta)$ and not the general ρ radial coordinate we used in the description of the Lax-Wendroff method. Also $T_{n\bar{m}} = n^\mu \bar{m}^\nu T_{\mu\nu}$, $T_{nn} = n^\mu n^\nu T_{\mu\nu}$, $T_{\bar{m}\bar{m}} = \bar{m}^\mu \bar{m}^\nu T_{\mu\nu}$. $\tilde{\Delta}$ and $\bar{\delta}$ are the differential operators

$$\begin{aligned} \tilde{\Delta} &= n^\mu \partial_\mu \\ &= \frac{\rho^2 (r^2 + a^2)}{2} \frac{d}{dt} - \frac{\rho^2 \Delta}{2} \frac{d}{dr} + \frac{aim\rho^2}{2}, \end{aligned} \quad (2.78)$$

$$\begin{aligned} \bar{\delta} &= \bar{m}^\mu \partial_\mu \\ &= -\frac{ia \sin \theta \rho^2 (r + ia \cos \theta)}{\sqrt{2}} \frac{d}{dt} \\ &\quad + \frac{(r + ia \cos \theta) \rho^2}{\sqrt{2}} \frac{d}{d\theta} + \frac{m\rho^2 (r + ia \cos \theta)}{\sqrt{2} \sin \theta}, \end{aligned} \quad (2.79)$$

and the other coefficients are [190]

$$\beta = \frac{1}{r + ia \sin \theta} \frac{\cot \theta}{2\sqrt{2}}, \quad (2.80)$$

$$\pi = ia \frac{1}{(r - ia \sin \theta)^2} \frac{\sin \theta}{\sqrt{2}}, \quad (2.81)$$

$$\mu = -\rho^2 \frac{1}{r - ia \sin \theta} \frac{\Delta}{2}, \quad (2.82)$$

$$\gamma = \mu + \rho^2 \frac{r - M}{2}, \quad (2.83)$$

$$\tau = -ia\rho^2 \frac{\sin \theta}{\sqrt{2}}, \quad (2.84)$$

$$\alpha = \pi - \bar{\beta}. \quad (2.85)$$

The energy-momentum tensor of the point-particle can be integrated in t and rewritten as

$$T_p^{\mu\nu} = \frac{m_p}{\Sigma \sin \theta} \frac{dt_p}{d\tau} \frac{dx^\mu}{dt} \frac{dx^\nu}{dt} \delta(r - r_p(t)) \delta(\theta - \theta_p(t)) \delta(\varphi - \varphi_p(t)). \quad (2.86)$$

Axial symmetry also allows for the mode separation of the energy momentum tensor

$$T_{\mu\nu} = \sum_{m=0}^{\infty} T_{\mu\nu}^m e^{im\varphi}. \quad (2.87)$$

Finally, the Dirac delta distributions need to be represented in the numerical grid. For the azimuthal decomposition, we use the representation in modes

$$\delta[\varphi - \varphi_p(t)] = \frac{1}{2\pi} \sum_{m=0}^{\infty} e^{im(\varphi - \varphi_p(t))}. \quad (2.88)$$

For the radial and θ directions, we approximate the Dirac delta by a narrow Gaussian distribution

$$\begin{aligned} \delta(r - r_p(t)) &= \frac{\delta[r^* - r_p^*(t)]}{|dr/dr_*|} \\ &= \frac{|dr^*/dr|}{\sqrt{2\pi}\lambda_{r_*}} \exp\left[-(r^* - r_p^*(t))^2 / 2\lambda_{r_*}^2\right], \end{aligned} \quad (2.89)$$

$$\delta(\theta - \theta_p(t)) = \frac{1}{\sqrt{2\pi}\lambda_\theta} \exp\left[-(\theta - \theta_p(t))^2 / 2\lambda_\theta^2\right], \quad (2.90)$$

where λ_{r_*} and λ_θ are varied to ensure convergence of the numerical results as they approach 0. Numerical experience shows $\lambda_{r_*} \approx 4dr_*$ and $\lambda_\theta \approx 4d\theta$ yield the best results [203]. Although there are more refined numerical representations of the Dirac delta in the literature [196], the one we follow is more practical and versatile for modeling different orbital motion.

When doing simulations with point-particles, we generate them at $t = 0$ and prescribe as initial data for the field $\psi(t = 0) = \partial_t \psi(t = 0) = 0$. This leads to a burst of initial junk radiation which needs to dissipate before the “physical” solution is observed. The junk radiation can, however, be reduced by multiplying the source by a starting “window” function that varies between 0 and 1 on some timescale T , such as $(1 - \exp(-t/T))^4$.

2.2.3 Hyperboloidal layers

One drawback of the method described above is that the outer boundary needs to be pushed to very large radius to avoid spurious reflections in the numerical solution. Additionally, GWs are only defined in a gauge-invariant manner at null infinity. Therefore, to study radiation numerically, one often needs to go to very large values of the radial coordinate r_* to ensure that extraction is performed in a region where the fields already behave like outgoing waves.

These obstacles have motivated the study of how to include null infinity in the computational domain. A successful strategy is hyperboloidal foliations. These are surfaces everywhere spacelike, that still approach null infinity [197, 204, 205]. We will follow the method of scri-fixing gauges [204], in which null infinity is fixed at some spatial coordinate independent of the time coordinate. This can even coincide with the numerical outer boundary, eliminating the need for imposing boundary conditions.

The first step in this construction is to compactify the radial coordinate

$$r_* = \frac{\rho}{\Omega(\rho)}, \quad (2.91)$$

where Ω is a conformal factor whose zero set S corresponds to infinity in r_* and ρ is the new radial coordinate. It obeys to $\Omega(S) = 0$ and $d\Omega(S)/d\rho \neq 0$.

The second step is to introduce a new time coordinate τ that preserves the timelike Killing vector field, i.e. $\partial_\tau = \partial_t$. This is achieved by a transformation $\tau = t - h(r, \theta, \varphi)$, where h is called the *height* function. Since we are interested in studying the emission of GWs, it is useful to pick h so that it depends only on r_*

$$\tau = t - h(r_*). \quad (2.92)$$

In this way, surfaces of constant τ are hyperboloidal.

One advantage of this method is that the strong-field region where the motion of the source takes place can be kept unaltered. At some radius, a truncated hyperboloidal layer is introduced, which must be

matched in a sufficiently smooth way. The matching procedure we adopt follows that of Ref. [197]

$$\Omega = 1 - \left(\frac{\rho - R_{\text{layer}}}{S - R_{\text{layer}}} \right)^4 \Theta(\rho - R_{\text{layer}}), \quad (2.93)$$

where Θ is the Heaviside function and S is the location of the outer boundary in the numerical domain. $\Omega = 1$ for $\rho < R_{\text{layer}}$, so $\rho = r_*$ in this region.

To choose the height function we require that outgoing null waves have the same representation in the strong field region and the exterior layer, which means $t - r = \tau - \rho$. Eq. (2.92) then implies

$$h = t - \tau = r_* - \rho(r_*) = \frac{\rho}{\Omega(\rho)} - \rho. \quad (2.94)$$

For $\rho < R_{\text{layer}}$, $\Omega = 1$ and therefore $h = 0$, so that in interior region $\tau = t$.

How does this affect the Teukolsky equation? Suppose we have it written in the form

$$\left[A^{tt} \partial_t^2 + A^{tr_*} \partial_t \partial_{r_*} + A^{r_* r_*} \partial_{r_*}^2 + A^{\theta\theta} \partial_\theta^2 + B^t \partial_t + B^{r_*} \partial_{r_*} + B^\theta \partial_\theta + C \right] \Psi = 0. \quad (2.95)$$

The coordinate transformations in Eq. (2.91) and (2.92) change the derivative operators

$$\partial_t = \partial\tau, \quad \partial_{r_*} = -H \partial_\tau + (1 - H) \partial_\rho, \quad (2.96)$$

where H is the boost function

$$H = \frac{dh}{dr_*}, \quad (2.97)$$

which for our choice of the height function in Eq. (2.94) is

$$H = 1 - \frac{d\rho}{dr_*} = 1 - \frac{\Omega^2}{\Omega - \rho \frac{d\Omega}{d\rho}}. \quad (2.98)$$

The transformed Teukolsky equation now has the form

$$\left[A^{\tau\tau} \partial_\tau^2 + A^{\tau\rho} \partial_\tau \partial_\rho + A^{\rho\rho} \partial_\rho^2 + A^{\theta\theta} \partial_\theta^2 + B^\tau \partial_\tau + B^\rho \partial_\rho + B^\theta \partial_\theta + C \right] \Psi = 0, \quad (2.99)$$

with the new coefficients

$$A^{\tau\tau} = A^{tt} - HA^{tr_*} + H^2 A^{r_* r_*}, \quad (2.100)$$

$$A^{\tau\rho} = (1 - H) (A^{tr_*} - 2HA^{r_* r_*}), \quad (2.101)$$

$$A^{\rho\rho} = (1 - H)^2 A^{r_* r_*}, \quad (2.102)$$

$$B^\tau = B^t - HB^{r_*} - \frac{dH}{d\rho} (1 - H) A^{r_* r_*}, \quad (2.103)$$

$$B^\rho = (1 - H) \left(B^{r_*} - \frac{dH}{d\rho} A^{r_* r_*} \right). \quad (2.104)$$

Note that Eq. (2.99) can be put in the form of the original wave equation (2.52) by dividing everything by $-A^{\tau\tau}$.

This set of hyperboloidal coordinates preserves the regularity of the Teukolsky equation, and all the coefficients appearing in it are finite at the outer boundary $\Omega(S) = 0$ [197]. Moreover, it ensures that the equation does not admit ingoing solutions at the outer boundary [197].

Part I

TIDES

3

DEFORMABILITY OF BLACK HOLES IMMERSSED IN MATTER

Tidal interactions are responsible for many astrophysical phenomena that have caught our attention since the dawn of Newton’s theory of gravitation [155]. An obvious example is ocean tides, caused by differences in the gravitational field produced by the Moon at different Earth locations. Their tidal interaction also explains why the Earth is losing angular momentum to the Moon, resulting in longer days. Tidal effects play a crucial role in close binary systems, as demonstrated by the spectacular tidal disruption events of stars that orbit *too* close to SMBHs [206, 207].

In the first part of this thesis, we study two problems where the matter surrounding a BH gets tidally deformed by a companion in a binary system and examine their implications for GW astronomy.

3.1 A BRIEF HISTORY OF TIDAL LOVE NUMBERS

The tidal distortion of a compact object by an external gravitational field is quantified, at a linear level, through its tidal Love numbers (TLNs) [155]. They are the gravitational analogue of the electric susceptibility. The TLNs depend only on the dynamics of the gravitational field, i.e. the underlying theory of gravity and the internal structure of the deformed body. They appear in the orbital equation of motions of a binary system at leading Newtonian order [208, 209], and introduce corrections in the gravitational waveform at fifth post-Newtonian order [210, 211]. The prospects of using GWs measurements to understand the structure of more compact objects have motivated the development of a relativistic theory of TLNs[212–214].

Initially, works on TLNs focused on neutron stars and provided access to the equation of state above the currently understood nuclear densities [215, 216]. More recently, tidal deformations have been proposed as a good candidate to test strong-field gravity, the BH paradigm and to search for new exotic, compact objects (ECOs) [217–221]. A crucial aspect of this is the fact that TLNs of BHs vanish in GR [212, 213, 222, 223], even when the BH is rotating [224–227]. This property has been geometrically linked to hidden near-horizon enhanced symmetries [228–230]. Therefore, a measurement of a nonvanishing TLN is

evidence for new physics: either the object is not a BH, or GR is not the most accurate description of gravity.

Consider the first possibility. Quantum corrections at the horizon scale or exotic matter could form horizonless ECOs [231]. As the BH limit is approached,

$$C = M/R \rightarrow 1/2, \quad (3.1)$$

where M and R are, respectively, the mass and radius of the ECO, its TLNs generically converge to the BH limit (zero), but, for many models, logarithmically [231]. LVK and the Einstein Telescope can only set constraints on low compact ECOs, but LISA would probe tidal deformability almost up to the BH limit [218–220, 231]. Nonzero TLNs may also signal corrections to GR. Extra degrees of freedom create extra tidal fields for which a theory of TLNs is still poorly formulated [232], but in some of the extensions studied in the literature, BHs in modified gravity theories can have nonzero TLNs [231, 233] (e.g. Chern-Simons gravity [234]).

There is, however, a third unexplored option that could be responsible for the (apparent) nonvanishing of TLNs of a BH: the presence of external matter. Any astrophysically plausible self-gravitating object will be surrounded by some matter, which could contribute with small but nonzero effective TLNs. In the rest of this chapter, we will quantify this contribution and conclude whether the matter surrounding a binary coalescence limits our ability to test GR with TLNs.

3.2 NEWTONIAN SHELL

As a proxy for the relativistic case, let us start by studying the tidal deformability of a spherical shell of matter in Newtonian gravity. Consider an object formed by a perfect fluid (isotropic with no shear stresses and viscosity) with matter density ρ , pressure p and velocity u^j , that obeys the Poisson-Euler equations [155]

$$\partial_i \partial^i \Phi = -4\pi G \rho, \quad (3.2)$$

$$\rho \frac{du_j}{dt} = \rho \partial_j \Phi - \partial_j p, \quad (3.3)$$

where Φ is the Newtonian gravitational potential and we temporarily recover Newton's gravitational constant $G = 6.67 \times 10^{-11} \text{ N} \cdot \text{m}^2/\text{kg}^2$. This system is complemented with a mass continuity equation

$$\frac{\partial \rho}{\partial t} + \partial^i (\rho u_i) = 0. \quad (3.4)$$

The isotropy inherent to a perfect fluid implies that, in equilibrium, it is spherically symmetric and we can use spherical coordinates centered at the body's center of mass.

Next, we introduce an external tidal field, V , which perturbs the equilibrium configuration of the body. We assume the regime of static tides, meaning that the time variations of the tidal perturber are small compared to the dynamical timescale of the system, and thus tides are independent of time. In this regime, the condition of hydrostatic equilibrium becomes

$$\partial_j p = \rho \partial_j \Phi. \quad (3.5)$$

In order to exploit the spherical symmetry of the system, it is useful to define the mass function $m(r)$

$$\frac{dm(r)}{dr} = 4\pi r^2 \rho, \quad (3.6)$$

and rearrange Eq. (3.5) as

$$\frac{dp}{dr} = -\rho \frac{Gm}{r^2}. \quad (3.7)$$

For the condition of hydrostatic equilibrium to hold, the tidal field must be sufficiently far away from the central body. In fact, we will assume that it is located in vacuum and satisfies Laplace's equation

$$\partial_i \partial^i V = 0. \quad (3.8)$$

which admits as solution

$$V = \sum_{\ell, m} \frac{4\pi}{2\ell + 1} d_{\ell m} r^\ell Y^{\ell m}, \quad (3.9)$$

where $d_{\ell m}$ are called the *tidal moments*.

At this point, we introduce fluid perturbations. We follow a surface of constant density, ρ_0 , which in the unperturbed configuration is at radius r_0 . Then, we need to consider perturbations in the mass density, $\delta\rho$, and in the radius of the surface, δr . There are two possible ways to approach this. The Eulerian/macroscopic framework compares quantities at the same position in space, while the Lagrangian/microscopic framework describes changes in the same fluid element as it is perturbed. We will not delve into how to handle the differences between them and refer the reader to Ref. [155] for a more detailed treatment.

If we follow a spherical surface of density matter ρ in the microscopic description, the following macroscopic statements are true

$$\delta\rho = -\rho' \delta r, \quad (3.10)$$

$$\delta p = -p' \delta r, \quad (3.11)$$

where primes denote derivatives with respect to r .

The fluid perturbations change the body's gravitational potential so that a perturbed Poisson equation holds

$$\partial_i \partial^i \delta\Phi = -4\pi G \delta\rho. \quad (3.12)$$

Outside the body, where $\delta\rho$ is zero, the solution to this equation is

$$\Phi_{lm}^{\text{out}} = \frac{4\pi G}{2\ell + 1} \frac{I_{lm}}{r^{\ell+1}}, \quad (3.13)$$

where I_{lm} are the body's multipole moments. The TLNs are defined as the ratio

$$k_\ell = \frac{1}{2} \left(\frac{c^2}{GM} \right)^{2\ell+1} \frac{G I_{lm}}{d_{lm}}, \quad (3.14)$$

where we also recovered the speed of light c and M is the total mass of the object

$$M = \lim_{r \rightarrow \infty} m(r). \quad (3.15)$$

To actually compute the TLNs explicitly, we need to solve Eq. (3.12) inside the body and then match the internal and external potential perturbations at the body's surface.

To solve the internal problem, we start by decomposing every perturbation in spherical harmonics [182]

$$\delta r = \sum_{\ell, m} r f_{\ell m}(r) Y_{\ell m}(\theta, \varphi), \quad (3.16)$$

$$\delta X = \sum_{\ell, m} \delta X_{\ell m}(r) Y_{\ell m}(\theta, \varphi), \quad (3.17)$$

with $X = \rho, p, \Phi$ or V . Inserting in Eq. (3.12)

$$r^2 \delta \Phi_{\ell m}'' + 2r \delta \Phi_{\ell m}' - \ell(\ell + 1) \delta \Phi_{\ell m} = -4\pi G r^2 \delta \rho_{\ell m}. \quad (3.18)$$

Euler's equation (3.3) expanded to first order gives

$$\delta p_{\ell m}' = -\frac{Gm}{r^2} \delta \rho_{\ell m} + \rho (\delta \Phi_{\ell m}' + V_{\ell m}'), \quad (3.19)$$

$$\delta p_{\ell m} = \rho (\delta \Phi_{\ell m} + V_{\ell m}). \quad (3.20)$$

Differentiating the second equation and inserting it in the first one, and using Eq. (3.10) and (3.11), we arrive at

$$\frac{Gm}{r} f_{\ell m} = \delta \Phi_{\ell m} + V_{\ell m}. \quad (3.21)$$

Finally, we match this expression with the external one (3.13) at the body's surface by demanding that the gravitational potential has to be smooth. In practice, we impose continuity of $\delta\Phi$ and its first derivative, arriving at

$$k_\ell = \left(\frac{c^2 R}{GM} \right)^{2\ell+1} \frac{\ell + 1 - \eta_\ell(R)}{2(\ell + \eta_\ell(R))}, \quad (3.22)$$

where η_ℓ is called the Radau's function

$$\eta_\ell(r) = r \frac{f_{\ell m}'(r)}{f_{\ell m}(r)}. \quad (3.23)$$

We find that the fractional deformation modes $f_{\ell m}$ completely determine the structure of the tidally deformed body. To compute them, we transform the differential equation for $\Phi_{\ell m}$ (3.18) into one for $f_{\ell m}$ by making use of Eq. (3.21)

$$r^2 f_{\ell m}'' + 6\mathcal{D}(r) (r f_{\ell m}' + f_{\ell m}) - \ell(\ell + 1) f_{\ell m} = 0, \quad (3.24)$$

where

$$\mathcal{D}(r) = \frac{4\pi\rho(r)r^3}{3m(r)}. \quad (3.25)$$

$\mathcal{D}(r)$ contains the information about the internal structure of the deformed body, namely it depends on its equation of state.

We will now solve this problem for a spherical shell model given by Vogt and Letelier [235]. This model is represented by the gravitational potential and matter density

$$\Phi(r) = -\frac{GM}{(r^n + r_0^n)^{1/n}}, \quad (3.26)$$

$$\rho(r) = \frac{M(n+1)b^n r^{n-2}}{4\pi(r^n + r_0^n)^{2+1/n}}, \quad (3.27)$$

where r_0 is a parameter with units of length, M is the total mass of the shell (3.15) and $n > 0$. For $n > 2$, ρ vanishes at $r = 0$ and the mass distribution indeed represents a shell. As n increases, the shell becomes thinner and localized around $r = r_0$. In the limit $n \rightarrow \infty$ this model describes an infinitesimal thin shell located at $r = r_0$.

The formalism developed to compute the TLNs relies on making a match at the surface of the compact object. However, this shell does not possess a hard surface. A possible solution to this problem occurs if the matter density is sufficiently localized so that the matching is well defined in the limit $R \rightarrow \infty$. This occurs in boson stars, whose tidal deformations in Newtonian gravity and GR were studied in Refs. [217, 236].

The solution of Eq. (3.24) for this model which is regular at $r = 0$ is

$$f_{\ell m}(y) = c_1 y^{-d} {}_2\tilde{F}^1\left(a, b, 1 + \frac{c}{n}; -y^n\right), \quad (3.28)$$

$$y = \frac{r}{r_0}, \quad (3.29)$$

$$a = -1 - \frac{\ell}{n} + \frac{c-3}{2n}, \quad (3.30)$$

$$b = -1 + \frac{\ell}{n} + \frac{c-1}{2n}, \quad (3.31)$$

$$c = \sqrt{-7 + 4n(n-1) + 4\ell(\ell+1)}, \quad (3.32)$$

$$d = n + \frac{1-c}{2}, \quad (3.33)$$

where ${}_2\tilde{F}^1(a, b, c; x)$ are the regularized hypergeometric functions [182]. The TLNs of the shell can then be computed by plugging this solution

in Eq. (3.22) and taking the limit $R \rightarrow \infty$. We conclude that the solution only converges for $n > 2\ell + 1$. For smaller values of n , the equality (3.21) is not respected in the $R \rightarrow \infty$ limit. When the problem is well-posed, we find

$$k_\ell = -\frac{(1+n)(1-2n+c)\Gamma(a-b)}{2n^2(b+1)\Gamma(b-a)} \times \frac{\Gamma(b)}{\Gamma(a+1)} \frac{\Gamma\left(2+\frac{1-2\ell}{n}+b\right)}{\Gamma\left(2+\frac{3+2\ell}{n}+a\right)} \left(\frac{c^2 r_0}{GM}\right)^{2\ell+1}.$$

We conclude that the TLNs of this Newtonian shell are of order $\mathcal{O}\left(\frac{c^2 r_0}{GM}\right)^{2\ell+1}$ and bounded below in the thin shell limit by

$$\lim_{n \rightarrow \infty} k_\ell = \frac{\ell+2}{2(\ell-1)} \left(\frac{c^2 r_0}{GM}\right)^{2\ell+1}. \quad (3.34)$$

For the quadrupole mode $\ell = 2$, which typically dominates GW emission, we obtain the scaling $k_2 \propto r_0^5$.

3.3 TIDAL DEFORMABILITY IN GENERAL RELATIVITY

We now move to the theory of tidally deformed objects in GR. The starting setup is the same, an isolated, self-gravitating compact object perturbed by an external tidal field. As before, we wish to describe the gravitational field of the two bodies in terms of their multipole moments, but now using the geometric point of view of GR. We follow Thorne's approach, which holds for stationary, asymptotically flat spacetimes and requires adopting asymptotically Cartesian and mass-centered coordinates at the isolated object [212, 213, 237].

First, we decompose the external tidal field as

$$\mathcal{E}_{a_1 \dots a_\ell} = [(\ell-2)!]^{-1} \langle C_{0a_1; a_3 \dots a_\ell} \rangle, \quad (3.35)$$

$$\mathcal{B}_{a_1 \dots a_\ell} = \left[\frac{2}{3}(\ell+1)(\ell-2)!\right]^{-1} \langle \epsilon_{a_1 bc} C_{a_2 0; a_3 \dots a_\ell}^{bc} \rangle, \quad (3.36)$$

where C_{abcd} is the Weyl tensor, ϵ_{abc} is the permutation tensor and the angular brackets denote symmetrization and trace removal. $\mathcal{E}_{a_1 \dots a_\ell}$ ($\mathcal{B}_{a_1 \dots a_\ell}$) are the polar (axial) moments, and since we will only study spherical symmetric configurations, they can be expanded in spherical harmonics.

To describe the deformation induced by the tidal field on the equilibrium configuration of the compact object, we use the framework of linear BH perturbation theory as introduced in Sec. 2.1.3. Since we have a spherically symmetric background, we can separate perturbations in the polar and axial sectors and adopt the Regge-Wheeler gauge (2.38).

The tidal fields and induced multipole moments are then extracted from the asymptotic behavior of the full metric

$$g_{tt} = -1 + \frac{2M}{r} + \sum_{\ell \geq 2} \left(\frac{2}{r^{\ell+1}} \left[\sqrt{\frac{4\pi}{2\ell+1}} M_\ell Y^{\ell 0} + (\ell' < \ell \text{ pole}) \right] - \frac{2}{\ell(\ell-1)} r^\ell \left[\mathcal{E}_\ell Y^{\ell 0} + (\ell' < \ell \text{ pole}) \right] \right), \quad (3.37)$$

$$g_{t\varphi} = \frac{2J}{r} \sin^2 \theta + \sum_{\ell \geq 2} \left(\frac{2}{r^\ell} \left[\sqrt{\frac{4\pi}{2\ell+1}} \frac{S_\ell}{\ell} \sin \theta \partial_\theta Y^{\ell 0} + (\ell' < \ell \text{ pole}) \right] + \frac{2r^{\ell+1}}{3\ell(\ell-1)} \left[\mathcal{B}_\ell \sin \theta \partial_\theta Y^{\ell 0} + (\ell' < \ell \text{ pole}) \right] \right), \quad (3.38)$$

where M_ℓ are the mass multipole moments, S_ℓ are the current multipole moments, and \mathcal{E}_ℓ and \mathcal{B}_ℓ are, respectively, the amplitudes of the polar and axial components of the external field with harmonic number ℓ , where spherical symmetry was used to fix $m = 0$.

Finally, we define the polar and axial TLNs, respectively, as the dimensionless ratios [217]

$$k_\ell^E = -\frac{1}{2} \frac{\ell(\ell-1)}{M^{2\ell+1}} \sqrt{\frac{4\pi}{2\ell+1}} \frac{M_\ell}{\mathcal{E}_{\ell 0}}, \quad (3.39)$$

$$k_\ell^B = -\frac{3}{2} \frac{\ell(\ell-1)}{(\ell+1)M^{2\ell+1}} \sqrt{\frac{4\pi}{2\ell+1}} \frac{S_\ell}{\mathcal{B}_{\ell 0}}, \quad (3.40)$$

where M is the mass of the deformed object. Note that the axial TLNs have no Newtonian analogous. Also, most references [212–214] normalize the TLNs in powers of the object radius R instead of M , because they study bodies with a hard surface (e.g. neutron stars). Here, we instead adopt the convention of Ref. [217] since the radius of distributions of matter surrounding BHs is in general ill-defined, as occurs for some ECOs. The two definitions are related by

$$k_{\text{ours}}^\ell = \left(\frac{R}{M} \right)^{2\ell+1} k_{\text{standard}}^\ell. \quad (3.41)$$

3.4 BLACK HOLES SURROUNDED BY MATTER

3.4.1 Black holes with short hair

We consider two models for BHs surrounded by matter. The first one is a static, spherically symmetric spacetime containing an anisotropic fluid surrounding a BH, which satisfies both the weak and strong energy condition [238]. Its line element is of the form in Eq. (2.16) with

$$A(r) = B(r) = 1 - \frac{2M}{r} - \frac{Q^{2k}}{r^{2k}}, \quad (3.42)$$

$$\rho = \frac{Q^{2k}(2k-1)}{8\pi r^{2k+2}}, \quad P = k\rho, \quad (3.43)$$

where ρ and P are, respectively, the matter density and the pressure on the isotropic θ - φ surfaces, while Q is a constant. The energy-momentum tensor of the fluid is

$$T_{\mu\nu} = \rho (u_\mu u_\nu - n_\mu n_\nu) + P \sigma_{\mu\nu}, \quad (3.44)$$

where u^μ is the fluid's 4-velocity, while n_ν and $\sigma_{\mu\nu}$ are, respectively, the unit normal and metric of the isotropic 2-spheres

$$u^\mu = \left(-\frac{1}{\sqrt{A(r)}}, 0, 0, 0 \right), \quad (3.45)$$

$$n_\nu = \left(0, \frac{1}{\sqrt{B(r)}}, 0, 0 \right), \quad (3.46)$$

$$\sigma_{\mu\nu} = \text{diag} (0, 0, r^2, r^2 \sin^2 \theta). \quad (3.47)$$

For $k = 1$, this class of BHs yields the Reissner-Nordström solution [238]. For $k > 1$, the parameter Q corresponds to a *matter-hair* [80, 238], which can be arbitrarily short by taking k to be arbitrarily large.

As in the Newtonian analysis, to determine the TLNs of this configuration, we need to complement the gravitational perturbations with the ones from matter, where any equilibrium background quantity $X = X_0$ gets perturbed by the external tide, $X \rightarrow X_0 + \delta X(t, r, \theta, \varphi)$. Again, we consider static tides, so all the perturbations introduced are independent of the coordinate time t . This immediately fixes u^μ and n^μ by imposing the normalizations $u^2 = -1$ and $n^2 = 1$, and that u^μ remains proportional to the timelike killing vector field $\partial/\partial t$

$$\delta u^\mu = \sum_{\ell, m} \left(\frac{1}{2\sqrt{A}} H_0^{\ell m} Y^{\ell m}, 0, 0, 0 \right), \quad (3.48)$$

$$\delta n_\mu = \sum_{\ell, m} \left(0, \frac{1}{2\sqrt{B}} H_2^{\ell m} Y^{\ell m}, 0, 0 \right). \quad (3.49)$$

For $\sigma_{\mu\nu}$, we allow one more degree of freedom that respects the background spherical symmetry

$$\delta \sigma_{\mu\nu} = \sum_{\ell, m} \text{diag} \left(0, 0, r^2 K_2^{\ell m}(r) Y^{\ell m}, r^2 \sin^2 \theta K_2^{\ell m}(r) Y^{\ell m} \right). \quad (3.50)$$

Finally, we perturb

$$\rho = \rho_0 + \sum_{\ell, m} \delta \rho^{\ell m}(r) Y^{\ell m}, \quad (3.51)$$

$$P = P_0 + \sum_{\ell, m} \delta P^{\ell m}(r) Y^{\ell m}. \quad (3.52)$$

3.4.1.1 Axial perturbations

The axial sector of stationary gravitational perturbations is entirely decoupled from matter perturbations [212, 213, 239]. Consequently,

the $t\varphi$ -component of Einstein's equations gives a decoupled ordinary differential equation for h_0

$$\begin{aligned} & r^2 \left(1 - \frac{2M}{r} + \frac{Q^{2k}}{r^{2k}} \right) h_0'' = \\ & = \left(\ell(\ell+1) - \frac{4M}{r} + 2k(1+2k) \frac{Q^{2k}}{r^{2k}} \right) h_0. \end{aligned} \quad (3.53)$$

We now follow a similar approach to that in Ref. [217] and treat the matter-hair perturbatively. We expand the metric perturbations in powers of the adimensionalized coupling Q^{2k}/M^{2k} ,

$$h_{\mu\nu} = h_{\mu\nu}^{(0)} + \frac{Q^{2k}}{M^{2k}} h_{\mu\nu}^{(2)}, \quad (3.54)$$

where $h_{\mu\nu}^{(0)}$ is the vacuum GR solution. For $\ell = 2$, the 0th-order axial perturbation regular at the horizon is

$$h_0^{(0)} = \frac{\mathcal{B}_2}{3} r^3 \left(1 - \frac{2M}{r} \right). \quad (3.55)$$

Expanding Eq. (3.53) to order $\mathcal{O}(\epsilon)$ we find

$$\begin{aligned} & \left(\frac{d^2}{dr^2} + 2 \frac{2M-3r}{r^2(r-2M)} \right) h_0^{(2)} = \frac{2\mathcal{B}_2}{3} \left(\frac{M}{r} \right)^{2k} \times \\ & \times \frac{r((2k^2+k-3)r - (2k^2+k-1)2M)}{r-2M}. \end{aligned} \quad (3.56)$$

This equation admits a solution in closed form in terms of the homogeneous solution and a hypergeometric function. From it, we read the TLNs

$$k_2^B = \frac{1}{5} \frac{2^{5-2k} (2k-1) Q^{2k}}{2k^2 - 9k + 10} \frac{Q^{2k}}{M^{2k}}, \quad k > 2. \quad (3.57)$$

For $k = 1$ we find $k_2^B = 0$ which agrees with the literature for the charged BH solution [217]. For $k = 2$, we find a new dominant logarithmic term $\log(r)/r^2$, for which we lack a physical interpretation. We can express the above in terms of the mass $\delta M \sim (Q^{2k}/M^{2k}) M$ contained in the fluid: $k_2^B \sim \delta M/M$.

3.4.1.2 Polar perturbations

In the polar sector, matter perturbations are no longer decoupled from gravitational ones. The tr - and $\theta\theta$ -component of Einstein's equations, respectively give

$$H_1 = 0, \quad H_2 = H_0. \quad (3.58)$$

The θ -component of the energy-momentum tensor conservation fixes the pressure perturbation to be

$$\delta P = 2k(2k-1) \frac{Q^{2k} K - K_2}{r^{2k} 16\pi r^2}. \quad (3.59)$$

The tt , rr , and the $\theta\theta$ component of Einstein's equations provide expressions for K_0'' , K_0' and K_0 in terms of H_0'' , H_0' , H_0 . Substituting these in the tr -component of Einstein's equations gives the following decoupled ordinary differential equation for H_0

$$\begin{aligned} & r^2 \left(1 - \frac{2M}{r} + \frac{Q^{2k}}{r^{2k}}\right)^2 H_0'' \\ & + 2r \left(1 - \frac{2M}{r} + \frac{Q^{2k}}{r^{2k}}\right) \left(1 - \frac{M}{r} + (1-k) \frac{Q^{2k}}{r^{2k}}\right) H_0' \\ & = \left[\ell(\ell+1) + \frac{4M^2}{r^2} - 2\ell(\ell+1) \frac{M}{r} \right. \\ & \left. + \left(\ell(\ell+1) + 2k \left(1 - \frac{6M}{r}\right) - 4k^2 \left(1 - \frac{2M}{r}\right) \right) \frac{Q^{2k}}{r^{2k}} + 2k \frac{Q^{4k}}{r^{4k}} \right] H_0. \end{aligned} \quad (3.60)$$

Following the same approach as in the axial case, we treat the matter-hair as a perturbation to GR using the expansion in Eq. (3.54). For $\ell = 2$, the polar perturbation regular at the horizon is

$$H_0^{(0)} = -\mathcal{E}_2 r^2 \left(1 - \frac{2M}{r}\right), \quad (3.61)$$

and Eq. (3.60) can be written as

$$\left(\frac{d^2}{dr^2} + \frac{(r-M)}{r(r-2M)} \frac{d}{dr} - \frac{2(2M^2 - 6Mr + 3r^2)}{r^2(r-2M)} \right) H_0^{(2)} = \mathcal{S}_p^{(2)},$$

with

$$\mathcal{S}_p^{(2)} = 2 \frac{M^{2k}}{r^{2k}} \mathcal{E}_2 \frac{c_1 - c_2 r + (3+k(2k-3))r^2}{(r-2M)^2}, \quad (3.62)$$

$$c_1 = 2(3+4k(k-2))M^2, \quad (3.63)$$

$$c_2 = 2(4+k(4k-7))M. \quad (3.64)$$

Even though this differential equation admits a solution in closed form, it is simpler to work in terms of Green's functions. The two linearly independent solutions to the homogeneous equation are

$$\Psi_- = \frac{3A_1}{M^2} r^2 \left(1 - \frac{2M}{r}\right), \quad (3.65)$$

$$\begin{aligned} \Psi_+ &= \frac{A_2}{M^2 r (r-2M)} \left((r-M)(3r^2 - 6Mr - 2M^2) M \right. \\ & \left. + 3r^2 (r-2M)^2 \operatorname{arctanh} \left(1 - \frac{M}{r}\right) \right), \end{aligned} \quad (3.66)$$

with A_1 and A_2 constants. The Wronskian is

$$W(r) = \Psi'_+(r) \Psi_-(r) - \Psi_+(r) \Psi'_-(r) = \frac{24MA_1A_2}{r(2M-r)}. \quad (3.67)$$

$\Psi_-(r)$ is regular at the horizon and $\Psi_+(r)$ at infinity. Imposing the correct physical boundary conditions, we find the solution to the inhomogeneous problem directly

$$\begin{aligned} H_0^{(2)}(r) &= \Psi_+(r) \int_{2M}^r dr' \frac{\mathcal{S}_P^{(2)}(r') \Psi_-(r')}{W(r')} \\ &+ \Psi_-(r) \int_r^\infty dr' \frac{\mathcal{S}_P^{(2)}(r') \Psi_+(r')}{W(r')}. \end{aligned} \quad (3.68)$$

For $k > 2$ the first integral converges as $r \rightarrow \infty$, and we find that the second one does not contribute to the induced mass quadrupole moment. Again, the TLNs vanish for $k = 1$ as expected, but in general

$$k_2^E = \frac{1}{5} \frac{2^{5-2k} (2k-1) Q^{2k}}{2k^2 - 9k + 10 M^{2k}} = k_2^B, \quad k > 2. \quad (3.69)$$

Remarkably, the polar TLNs are the same as the axial ones. This feature was already present in the TLNs of ECOs in the BH limit [217]¹. A similar procedure can be used to obtain the octupolar $\ell = 3$ or higher TLNs.

3.4.2 Matter away from the horizon: Thin shells

While the previous results are interesting, astrophysical BHs should have surrounding matter distributions localized away from the horizon. It is challenging to construct stationary solutions describing astrophysically realistic BH spacetimes. As a surrogate for those setups, we will pack all the interstellar material in a (infinitesimally) thin shell surrounding a Schwarzschild BH. The dynamics of thin shells are a vastly explored subject, both in GR [240–245] and in modified theories of gravity; we refer the interested reader to Ref. [246] for a pedagogical introduction to the subject. As physical systems, thin shells are nothing more than very crude approximations. However, their mathematical description is much simpler than more realistic distributions of matter and they often present the key features of these. While there are many studies regarding the stability of thin shells, little has been made in studying the explicit form of gravitational perturbations in spacetimes containing them [80, 247–251].

Let us then consider the tidal deformation of a distribution of matter whose metric is again given by the general spherically symmetric line element in Eq. (2.16) with

$$\begin{cases} A(r) = \bar{\alpha} \left(1 - \frac{2M}{r}\right), & B(r) = \frac{1}{\bar{\alpha}} A(r), & r < r_0 \\ A(r) = \left(1 - \frac{2M_0}{r}\right), & B(r) = A(r), & r > r_0 \end{cases}, \quad (3.70)$$

¹ We are grateful to Lam Hui for highlighting this property.

where r_0 is the radius at which the shell is located, $\bar{\alpha} = \frac{1-2M_0/r_0}{1-2M/r_0}$, M is the BH horizon mass, M_0 the ADM mass and for future reference we define the shell energy

$$\delta M = M_0 - M. \quad (3.71)$$

3.4.2.1 Unperturbed solution

We start by analyzing the unperturbed configuration. The worldline of matter elements of the shell is parametrized by

$$x_{\pm}^{\mu} = x_{\pm}^{\mu}(y^a), \quad (3.72)$$

where y^a are the intrinsic coordinate functions of the shell, the subscript $+$ or $-$ refers to, respectively, the coordinate chart used outside and inside the shell, and momentarily latin indices denote objects defined on the 3D hypersurface of the shell. We choose the intrinsic coordinates of the shell to be

$$y^a = (T, \Theta, \Phi), \quad (3.73)$$

and the unperturbed shell is located at

$$x_{+}^{\mu} = (T, r_0, \Theta, \Phi), \quad (3.74)$$

$$x_{-}^{\mu} = (A_T T, r_0, \Theta, \Phi). \quad (3.75)$$

The constant A_T reflects a possible time-rescaling so that the proper time of the shell is the same for both the exterior and interior coordinate chart. These two regions have to be matched according to the Darmois-Israel junction conditions, which relate the discontinuities on the metric functions with the matter properties of the thin shell [240]. The first of these imposes that the induced metric, γ_{ab} , on the 3D hypersurface defined by the shell is continuous

$$[[\gamma_{ab}]] = 0, \quad (3.76)$$

where $[[\dots]]$ denotes a jump on a quantity across the shell

$$[[E]] = E(r_{0+}) - E(r_{0-}). \quad (3.77)$$

The induced metric can be computed through

$$\gamma_{ab} = g_{\mu\nu} e_a^{\mu} e_b^{\nu}, \quad (3.78)$$

where e_a^{μ} are a set of three linearly independent tangent vectors to the shell

$$e_a^{\mu} = \frac{\partial x^{\mu}}{\partial y^a}. \quad (3.79)$$

The second junction condition determines the stress-energy tensor of the shell, S_{ab} , in terms of the jump of the extrinsic curvature K_{ab}

$$S_{ab} = -\frac{1}{8\pi} ([[K_{ab}]] - \gamma_{ab} [[K]]), \quad (3.80)$$

$$K_{ab} = e_a^\mu e_b^\nu \nabla_\mu n_\nu, \quad (3.81)$$

$$K = \gamma_{ab} K^{ab}, \quad (3.82)$$

where n^μ is the unit normal to the thin shell

$$n_\mu e_a^\mu = 0, \quad n^\mu n_\mu = 1. \quad (3.83)$$

The first junction equation (3.76) yields

$$A_T^2 = \frac{A_+(r_0)}{A_-(r_0)}, \quad (3.84)$$

which for our model gives $A_T = 1$. Since the configuration is stationary, we can always rescale time such that this is verified and we assume it hereafter. From the second junction condition (3.80) we obtain

$$S_{TT} = -\frac{1}{4\pi r_0} [[A\sqrt{B}]], \quad (3.85)$$

$$S_{\Theta\Theta} = \frac{1}{8\pi} [[\sqrt{B}]] + \frac{r_0}{16\pi} \left[\left[\frac{A'}{A} \sqrt{B} \right] \right]. \quad (3.86)$$

If we consider the thin shell to be composed of a perfect fluid, its stress-energy tensor is simply

$$S_{ab} = (\sigma + p) u_a u_b + p \gamma_{ab}, \quad (3.87)$$

where σ is the surface energy density, p the surface tension and u^a is the fluid's velocity (normalized as $u^a u_a = -1$). For the unperturbed configuration, the latter is given by

$$u^a = \left(\frac{1}{\sqrt{A(r_0)}}, 0, 0 \right). \quad (3.88)$$

Using Eqs. (3.85)-(3.86) the surface energy density and pressure are determined by

$$\sigma = -\frac{1}{4\pi r_0} [[\sqrt{B}]], \quad (3.89)$$

$$\sigma + 2p = \frac{1}{8\pi} \left[\left[\frac{A'}{A} \sqrt{B} \right] \right], \quad (3.90)$$

which agrees with previous results on thin shell dynamics [241, 247, 250, 252].

3.4.2.2 Perturbed configuration

To compute the TLNs of this object, we need to derive the junction conditions for the stationary, axisymmetric perturbed configuration when the external tidal field is introduced. First, we perturb the shell radius by

$$\delta r_{\pm} = \sum_{\ell, m} \delta r_{\pm}^{\ell m} Y^{\ell m}(\Theta, \Phi). \quad (3.91)$$

The junction condition (3.76) evaluated at first order yields

$$[[h_0]] = 0, \quad (3.92)$$

$$[[H_0]] = \left[\left[\frac{\delta r A'}{A} \right] \right], \quad (3.93)$$

$$\frac{2}{r_0} [[\delta r]] = -[[K]], \quad (3.94)$$

where from now on, we omit the harmonic indexes ℓ, m in the junction conditions to avoid cluttering.

To apply the second junction condition, we need to consider perturbations to the surface energy density, $\delta\sigma$, and the surface tension, δp . These are scalars and therefore can be expanded as

$$(\delta\sigma, \delta p) = \sum_{\ell, m} (\delta\sigma^{\ell m}, \delta p^{\ell m}) Y^{\ell m}(\Theta, \Phi). \quad (3.95)$$

Finally, we need to perturb the fluid velocity and the unit normal to the shell. The former is determined by imposing the correct normalization and the stationarity condition as in the previous sections

$$\delta u^a = \sum_{\ell, m} \frac{1}{2\sqrt{A}} \left(H_0^{\ell m} - \frac{A'}{A} \delta r^{\ell m}, 0, 0 \right) Y^{\ell m}, \quad (3.96)$$

while the latter is computed using (3.83)

$$\delta n_{\mu\pm} = \sum_{\ell, m} \frac{1}{\sqrt{B}} \left(0, \frac{1}{2} H_2^{\ell m} Y^{\ell m}, -\delta r_{\pm}^{\ell m} \partial_{\theta} Y^{\ell m}, 0 \right). \quad (3.97)$$

The second junction condition (3.80) gives

$$\left[\left[h_1 \sqrt{B} \right] \right] = 0, \quad (3.98)$$

$$\frac{1}{2} \left[\left[h'_0 \sqrt{B} \right] \right] - \frac{2}{r_0} \left[\left[\sqrt{B} \right] \right] h_0 - \frac{1}{2} \left[\left[\frac{A'}{A} \sqrt{B} \right] \right] h_0 = 8\pi\sigma h_0. \quad (3.99)$$

While the first of these agrees with previous results [247, 250], as far as we are aware, the second equation above has not been presented in this form anywhere.

The polar sector couples to matter perturbations and we find more complicated junction conditions

$$\left[\left[H_1 \sqrt{B} \right] \right] = \left[\left[\frac{\delta r}{\sqrt{B}} \right] \right] = 0, \quad (3.100)$$

$$\begin{aligned} & \frac{2}{r_0^2} \left[\left[\delta r \sqrt{B} \right] \right] + \frac{2}{r_0} \left[\left[H_0 \sqrt{B} \right] \right] + \frac{1}{r_0} \left[\left[H_2 \sqrt{B} \right] \right] \\ & - \left[\left[K' \sqrt{B} \right] \right] - \frac{1}{r_0} \left[\left[\frac{\delta r B'}{\sqrt{B}} \right] \right] - \frac{2}{r_0} \left[\left[\delta r \frac{A'}{A} \sqrt{B} \right] \right] \\ & = 8\pi \delta\sigma + 8\pi\sigma \left(\frac{A'}{A} \delta r - H_0 \right), \end{aligned} \quad (3.101)$$

$$\begin{aligned} & \frac{1}{2r_0^2} \left[\left[\delta r \sqrt{B} \right] \right] - \frac{1}{2r_0} \left[\left[H_2 \sqrt{B} \right] \right] + \frac{2}{r_0} \left[\left[K \sqrt{B} \right] \right] \\ & - \frac{1}{4} \left[\left[H_2 \frac{A'}{A} \sqrt{B} \right] \right] + \frac{1}{2} \left[\left[K \frac{A'}{A} \sqrt{B} \right] \right] + \frac{1}{2} \left[\left[A' \sqrt{B} \right] \right] \\ & - \frac{1}{2} \left[\left[H_0' \sqrt{B} \right] \right] + \frac{1}{2r_0} \left[\left[\frac{\delta r B'}{\sqrt{B}} \right] \right] + \frac{1}{r_0} \left[\left[\delta r \frac{A'}{A} \sqrt{B} \right] \right] \\ & + \frac{1}{2} \left[\left[\delta r \frac{A'}{A} \sqrt{B} \right] \right]' = 8\pi \delta p + 8\pi p \left(K + 2 \frac{\delta r}{r_0} \right). \end{aligned} \quad (3.102)$$

We have to complement this with an equation of state

$$\delta p = v_s^2 \delta\sigma, \quad v_s^2 = \left(\frac{dp}{d\sigma} \right) \Big|_{\sigma_0}. \quad (3.103)$$

For ordinary matter, v_s is the sound of speed of the fluid and ranges between $0 < v_s^2 < 1$. Again, the first two of the above conditions agree with previous results [250] while we could not find the last two written in this manner anywhere.

3.4.2.3 Axial TLNs

The exterior spacetime has the form of a Schwarzschild metric, so using known results [212, 217, 247]

$$h_1^{\text{ext}} = 0, \quad (3.104)$$

$$\begin{aligned} h_0^{\text{ext}} &= A_1 r_2^2 F^1 \left(1 - \ell, \ell + 2; 4; \frac{r}{2M_0} \right) \\ &+ A_2 G_{2,0}^{2,2} \left(\frac{r}{2M_0} \middle| \begin{array}{cc} 1 - \ell & \ell + 2 \\ -1 & 2 \end{array} \right), \end{aligned} \quad (3.105)$$

where $G_{2,0}^{2,2}$ is the Meijer function [182]. The first term of h_0^{ext} corresponds to the external tidal field and the second to the object's response.

For the interior region, the final equation for h_0^{int} is similar to that in the exterior, with M_0 replaced by M

$$\left(h_0^{\text{int}} \right)'' = \frac{4M - \ell(\ell + 1)r}{r^2(2M - r)} h_0^{\text{int}}. \quad (3.106)$$

Consequently, the solution is of the form above substituting M by M_0 . Imposing regularity of h_0 at the BH horizon means the term with Meijer function has to vanish

$$h_0^{\text{int}} = A_3 r_2^2 F^1 \left(1 - \ell, \ell + 2; 4; \frac{r}{2M} \right), \quad (3.107)$$

and $h_1^{\text{int}} = 0$.

Now, we can impose the junction conditions derived previously. For $\ell = 2$, the general large-distance behavior of h_0 is given by a complicated expression. In the limit where the shell is far away

$$k_2^B = \frac{\delta M}{5M_0} \frac{r_0^4}{M_0^4}, \quad r_0 \rightarrow \infty. \quad (3.108)$$

Notice that when the shell disappears, $\delta M \rightarrow 0$, $k_2^B \rightarrow 0$. This agrees with the vanishing of the TLNs of a BH [212, 217]. The TLN is proportional to the mass in the shell, as we had found for the “short-hair” solution. However, the presence of a length scale r_0 now implies that the TLNs are very sensitive to the location of the matter. In fact, the r_0^4/M^4 dependence is expected on general dimensional grounds and from comparison with the TLNs of extended configurations, such as boson stars.

In the BH limit, when $M_0 \rightarrow M$ and $r \rightarrow 2M$

$$k_2^B \rightarrow \frac{8}{5} \frac{\delta M}{M} \left(\frac{r_0}{M} - 2 \right), \quad (3.109)$$

which is also compatible with the result for an isolated BH.

It is also interesting to see the system’s behavior when we start without a BH, i.e. $M = 0$. In this case, one finds the exact result

$$k_2^B = \frac{8\zeta}{10\mathcal{C} \left(3 - 3\mathcal{C} - 2\mathcal{C}^2 + 2\mathcal{C}^3 \sqrt{\frac{1}{\zeta}} \right) + 15\zeta \log \zeta},$$

$$\zeta = 1 - \frac{2M_0}{r_0}, \quad \mathcal{C} = \frac{M_0}{r_0}.$$

This result seems to be at odds with the claims of Ref. [231] that the general scaling of the TLNs of an ECO in the BH limit is $k \sim 1/\log \zeta$ (see their discussion around Eq. (95)). The proof presented there relies on imposing Robin-type boundary conditions, $a\Psi + b\Psi' = c$, on the Zerilli function Ψ , at the surface of the compact object, where a , b and c depend on the background spacetime. However, the true scaling goes as $k \propto 1/(b + \log \zeta)$, so if in the BH limit b is diverging faster than the logarithm, the claim does not hold. Notice that the factor b is related with the term containing information about the derivatives of the perturbations at the boundary. For a thin shell, the perturbations will not be differentiable at such boundary. Therefore, it is not clear how we can rephrase the boundary conditions imposed in Eqs. (3.92) and (3.99), which relate quantities on both sides of the boundary but which are not well defined at it, in terms of Robin-type boundary conditions for which the result of Ref. [231] applies.

3.4.2.4 Polar perturbations

For the polar sector, the behavior of the perturbations inside and outside the shell is similar to the axial case. They are [212, 217, 247]

$$H_0^{\text{ext}} = A_1 P_\ell^2 (r/M_0 - 1) + A_2 Q_\ell^2 (r/M - 1), \quad (3.110)$$

$$H_0^{\text{int}} = A_3 P_\ell^2 (r/M - 1), \quad (3.111)$$

$$H_1^{\text{int}} = H_1^{\text{ext}} = 0, \quad (3.112)$$

where regularity of H_0^{int} at the BH horizon fixes one of the constants. K is determined by the field equations

$$\begin{aligned} K = & \frac{(4M_i^2 + 2(\ell^2 + \ell - 4)M_i r - (\ell^2 + \ell - 2)r^2)H_i}{(\ell^2 + \ell - 2)(2M_i - r)r} \\ & + \frac{2M_i(2M_i - r)H_i'}{(\ell^2 + \ell - 2)(2M_i - r)r'} \end{aligned} \quad (3.113)$$

where i labels the interior or exterior solution which correspond, respectively, to M or M_0 .

We can impose the junction conditions and obtain the polar TLNs. For $\ell = 2$, the large distance behavior of H_0 is again given by a complicated expression. However, in the large shell radius pressureless limit ($v_s = 0$), the polar TLN is simply

$$k_2^E = \left(1 + \frac{M_0}{M}\right) \frac{\delta M}{2M} \frac{r_0^5}{M_0^5}, \quad r_0 \rightarrow \infty, \quad (3.114)$$

in such a way that k_2^E vanishes when $\delta M \rightarrow 0$, as it should. We note an important dependence on the speed of sound v_s . As consequence, k_2^E is positive for small v_s (in the Newtonian limit), but can become negative at large values of v_s . Negative TLNs have been found in other models involving infinitesimal thin shells [250, 253] and extended configurations of ECOs [217]. They are usually interpreted as leading to a prolation of the deformed compact object instead of a more intuitive oblate shape. We find the same scaling $k_2^E \sim r_0^5$ as in the Newtonian analysis (3.69).

In the BH limit, $M_0 \rightarrow M$ and $r_0 \rightarrow 2M$, we find

$$k_2^E \rightarrow \frac{8(3 - 8v_s^2)}{5} \frac{\delta M}{M} \left(\frac{r_0}{M} - 2\right), \quad (3.115)$$

which has a similar dependence as the axial case (3.109). Although the numerical coefficients do not exactly match, as occurred for the short hair and ECOs [217], we can attribute this difference to the lack of specification of the equation of state. There is perfect agreement between the $\ell = 2$ axial TLN (3.109) and the corresponding polar one (3.115) when $v_s^2 = 0.25$, which is in the allowed range for v_s . Also when $v_s^2 > 3/8$, the $\ell = 2$ polar TLN becomes negative.

If we start without a BH, i.e. $M = 0$, and analyze now the BH limit $r_0 \rightarrow 2M_0$ we obtain

$$k_2^E \rightarrow \frac{8}{5 \left(9 + \sqrt{\frac{2}{\xi}} + 4v_s^2 + 3 \log \xi \right)}. \quad (3.116)$$

3.5 IMPLICATIONS FOR TESTS OF FUNDAMENTAL PHYSICS

We showed that the leading tidal deformability of a thin shell of matter surrounding a BH scales with the shell radius as $k_2^E \propto r_0^5$. Let us then extrapolate it for more generic matter distributions. We would be led to conclude that TLNs diverge when matter is located sufficiently far away, as $r_0 \rightarrow \infty$, which would have a massive impact on GW signals. This sounds physically unreasonable and has not been observed.

Consider a binary system composed of two objects of masses M_1 and M_2 (total mass $M_{\text{tot}} = M_1 + M_2$) at a Newtonian level. To simplify, consider that both bodies only develop a non-negligible mass quadrupole moment through tidal interactions. The EOM for the relative position between the objects, $r^j = r_1^j - r_2^j$, to linear order in the quadrupole moments is [155, 209]

$$\frac{d^2 r^j}{dt^2} = -\frac{M_{\text{tot}}}{r^2} \left(1 + \frac{9}{r^5} \left(\lambda_1 \frac{M_2}{M_1} + \lambda_2 \frac{M_1}{M_2} \right) \right) n^j, \quad (3.117)$$

where

$$\lambda_i = \frac{2}{3} k_{2_i} M_i^5, \quad r = |r^j|, \quad n^j = \frac{r^j}{r}, \quad (3.118)$$

being k_{2_i} the $\ell = 2$ polar TLN of each object.

Simplifying even further, take only object “1” to be immersed in matter, the other being “isolated.” This fixes $k_{2_2} = 0$ [212, 217]. Then, inserting our results for the $r_0 \rightarrow \infty$ limit of the $\ell = 2$ polar TLNs of a BH surrounded by a thin shell (3.114) in the EOM (3.117), we expect a dependence as

$$\frac{d^2 r^j}{dt^2} \sim \frac{\delta M}{M_1} \frac{r_0^5}{r^5} \frac{M_2}{M_1} n^j, \quad (3.119)$$

where we have used that in realistic astrophysical scenarios $\delta M \ll M_0$.

We assumed that tidal interactions are weak and can be treated perturbatively. The external tidal field is caused by a body in a region far away from the deformed one, which fixes $r_0/r \ll 1$. However, this condition might not be sufficient. From Eq. (3.117) and the results for the asymptotic behavior of k_2^E in the limit $r_0 \rightarrow \infty$ (3.114), to treat the tidal terms as perturbations we can only consider matter in a region around the compact objects such that

$$\frac{r_0}{r} \ll \min \left(1, \left(\frac{M_1}{\delta M} \frac{M_1}{M_2} \right)^{1/5} \right). \quad (3.120)$$

Although this does not fix r_0 to an unambiguous value, it justifies why the divergence of the TLNs with r_0 is not problematic.

3.5.1 Binaries in astrophysical settings

Let us now consider a realistic astrophysical system in which the environment may have a measurable impact. As discussed in the previous section, the leading order effect of tidal interactions in the dynamics of a binary comes from the polar $\ell = 2$ TLN. We also concluded that to use our results for the TLNs of a thin shell, we had to consider a lengthscale r_0 for the environment smaller than the typical separation r between the binary objects.

LISA will observe in the frequency band $[10^{-4}, 1]$ Hz. For a circular binary, the relation between the orbital separation r and the GW frequency f_{GW} is

$$r \sim \left(\frac{GM_{\text{tot}}}{(\pi f_{\text{GW}})^2} \right)^{1/3}. \quad (3.121)$$

Consequently, the lower bound of the LISA frequency band corresponds to binaries separated by $r \sim 10^6 (M_{\text{tot}}/M_{\odot})^{1/3}$ km.

To obtain the properties of the environmental matter, we can use the steady-state model of a Shakura-Sunyaev thin accretion disk [47, 48, 80]. This is an axisymmetric, vertically thin disk, i.e. $H < r$ being H the height of the disk. Following Ref. [80], we parametrize the mass accretion rate with the mass Eddington ratio f_{Edd} , which for thin disks varies between $10^{-2} \lesssim f_{\text{Edd}} \lesssim 0.2$. The surface density of the thin disk Σ_{disk} and the disk height H can be written as

$$\frac{\Sigma_{\text{disk}}}{10^9} \approx \frac{f_{\text{Edd}}^{7/10}}{\tilde{r}^{3/4}} \left(1 - \sqrt{\frac{\tilde{r}_{\text{in}}}{\tilde{r}}} \right)^{7/10} \left(\frac{0.1}{\alpha} \right)^{4/5} \left(\frac{M}{10^6 M_{\odot}} \right)^{1/5} \text{ kg} \cdot \text{m}^{-2}, \quad (3.122)$$

$$\frac{10^3 H}{GM/c^2} \approx f_{\text{Edd}}^{3/20} \left(1 - \sqrt{\frac{\tilde{r}_{\text{in}}}{\tilde{r}}} \right)^{3/20} \left(\frac{0.1}{\alpha} \right)^{1/10} \left(\frac{10^6 M_{\odot}}{M} \right)^{1/10} \tilde{r}^{9/8}, \quad (3.123)$$

where M is the mass of the accreting object, $\tilde{r} = r / (GM/c^2)$, $\alpha \sim 0.01 - 0.1$ is the viscosity parameter and $\tilde{r}_{\text{in}} \sim 6$ is the radius of the inner edge of the disk. The total mass of the disk is then

$$\delta M \approx 2\pi \int_{r_{\text{in}}}^{r_{\text{out}}} \Sigma_{\text{disk}} r \, dr, \quad (3.124)$$

where r_{out} is the radius of the disk's outer edge.

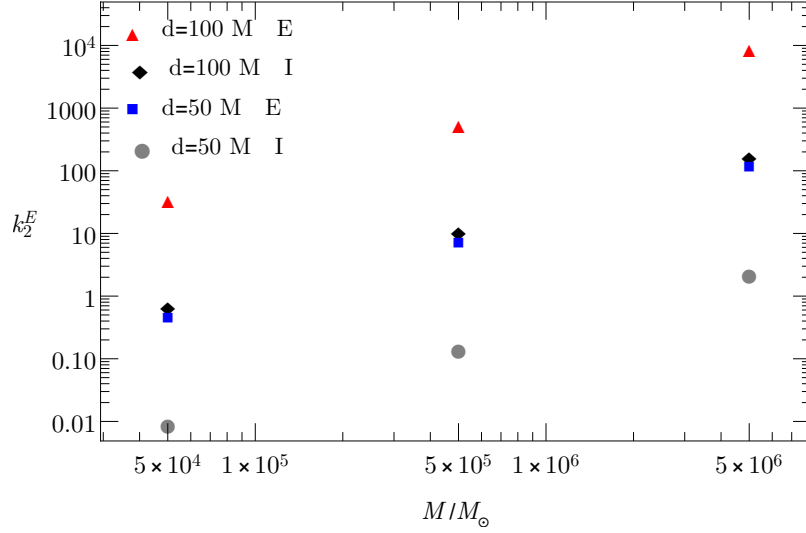


Figure 3.1: The quadrupolar tidal Love number k_2^E for a central BH of mass M surrounded by a Shakura-Sunayev thin accretion disk in a circular binary and a companion of the same mass. We present two different binary distances d for $M/M_\odot = 5 \times 10^4$, $M/M_\odot = 5 \times 10^5$ and $M/M_\odot = 5 \times 10^6$. For each d we present estimations in the most efficient accretion scenario (labeled by E), $f_{\text{Edd}} = 0.2$ and $\alpha = 0.01$, and in the most inefficient one (labeled by I) $f_{\text{Edd}} = 0.01$ and $\alpha = 0.1$.

3.5.2 On the minimum measurable TLN

We can finally compute the dominant TLN, k_2^E , of a “dirty” BH. Fig. 3.1 shows k_2^E for representative values of the distance $d = (50, 100)M$ and for two different accretion scenarios, an efficient (“E”) with $f_{\text{Edd}} = 0.2$, $\alpha = 0.01$, and an inefficient (“I”) with $f_{\text{Edd}} = 0.01$, $\alpha = 0.1$.

The lesson to be learned from Fig. 3.1 is that massive objects are typically surrounded by enough matter that they are perceived as having TLNs of order $\gtrsim 1$. Thus, extreme care and account of environmental effects must be considered when inferring the properties and nature of ultracompact objects from a measurement of TLNs [217–219]. This is especially important for EMRIs, where the long time in band would ideally allow for extremely precise constraints on TLNs [220]. More recent studies for other types of matter distribution have confirmed our conclusions [254–257].

4

TIDAL EFFECTS IN SUPERRADIANT CLOUDS

As discussed in the Introduction, ultralight bosonic fields are predicted in various extensions of the Standard Model [101–104] and have been proposed as a component of DM [104]. Through superradiance [103], they can extract rotational energy from spinning BHs and grow into macroscopic clouds. This mechanism only requires the bosonic field to be minimally coupled to gravity. However, for it to be efficient in astrophysical timescales, the BH radius needs to be of the order of the Compton wavelength $G/(c^2\mu)$ of the field, where $\mu = Gm_B/(c\hbar)$ and m_B is the mass of boson. Restoring geometric units, we therefore require $M\mu \sim 1$. Considering BHs in the Universe appear across ten orders of magnitude, superradiance allows to constrain the existence of new bosonic fields by the same range [103, 127, 258].

As also mentioned before, the existence of superradiant clouds would lead to observable signatures, such as peculiar holes in the mass-spin plane of BHs [127, 258], monochromatic emission of GWs [127, 259], and a significant stochastic background of GWs [128, 129]. They can also leave dynamical imprints through Lindblad and co-rotation resonances [260, 261], or through floating or sinking orbits [136, 262–264]. However, there are a few factors that could alter, in a significant way, the formation of boson clouds around BHs. For example, in the presence of couplings with standard model fields the cloud growth can be suppressed, while stimulating bursts of light [265, 266].

In this chapter, we will focus on the effects that a companion object, like a BH, has on the structure of the boson cloud. Previous works have looked into this problem from the analytical standpoint, restricting the analysis to Newtonian dynamics and non-relativistic fields [135, 136, 263, 264, 267, 268]. At specific orbital frequencies, the motion of the binary can induce resonant transitions between growing and decaying modes, that enhance the cloud’s depletion or transfer energy and angular momentum to the companion [269]. This would leave distinctive imprints in the GW signal emitted by the binary, both in the monochromatic signal from the cloud or as modifications in the GW waveform of the binary, due to finite-size effects like variations on the spin-induced quadrupole or the TLNs [135].

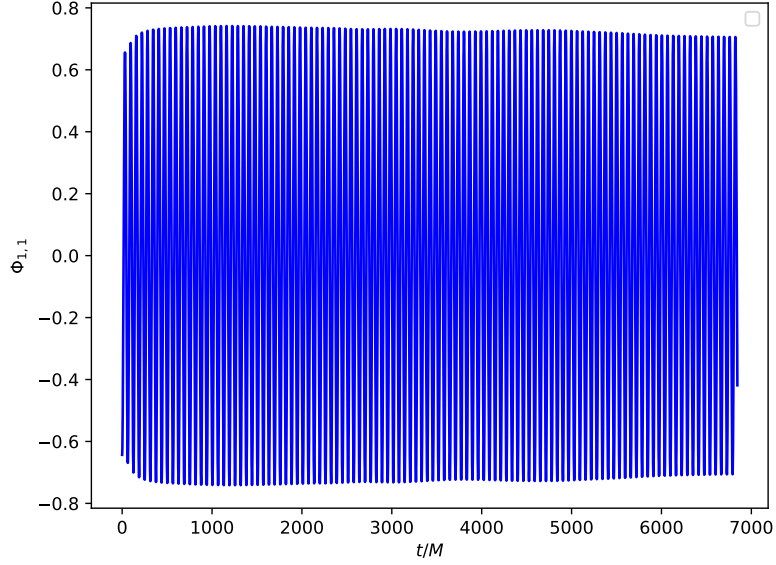


Figure 4.1: A dipolar scalar cloud around a Schwarzschild BH. This figure shows the time evolution of initial conditions (4.6) for a dipole with gravitational coupling $M\mu = 0.1$ around a non-spinning BH, and in absence of a companion ($\epsilon = 0$). The field is extracted at $r = 60M$. For the timescales of interest for our problem, the amplitude of the field varies by only a few percent and is therefore a good description of a quasi-stationary state.

4.1 SETUP

Our starting point is that of a Kerr BH surrounded by a superradiant cloud being perturbed by a distant companion at a fixed location. We also assume the test-field approximation in which the backreaction of the cloud in the spacetime geometry is negligible. This is a good approximation because the timescales we will probe are much shorter than any superradiant-growth timescales [127] ($\tau_{\text{growth}}^s \sim (M\mu)^{-9}M$ for scalar fields [270]). The unperturbed background is therefore assumed to be described by a Kerr BH (line element in Eq. (2.11)).

The tidal field is created by a companion of mass M_c , at a distance R , and located at $\theta = \theta_c$, $\varphi = \varphi_c$ in the BH sky. The companion induces a change $\delta ds_{\text{tidal}}^2$ in the geometry, so our full spacetime is

$$ds^2 = ds_{\text{Kerr}}^2 + \delta ds_{\text{tidal}}^2. \quad (4.1)$$

For the tidal perturbation, we consider the non-spinning approximation and import the results from the previous chapter. Taking into account only the dominant quadrupole term [171, 217, 271]

$$\begin{aligned} \delta ds_{\text{tidal}}^2 &= \sum_{m=-2}^2 r^2 \mathcal{E}_{2m} Y_{2m}(\theta, \phi) (A^2 dt^2 + dr^2 + (r^2 - 2M^2) d\Omega^2) \\ \mathcal{E}_{2m} &= \frac{8\pi\epsilon}{5M^2} Y_{2m}^*(\theta_c, \phi_c), \end{aligned} \quad (4.2)$$

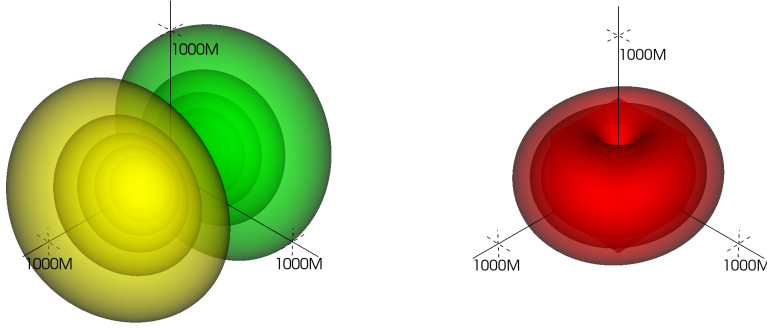


Figure 4.2: Field (left) and energy density (right) distribution along the equatorial plane for the same initial data as Fig. 4.1. The field is dipolar, as expected, whereas the energy density at the equator is almost – but not exactly – symmetric along the rotation axis. The length scale of these images is of order $1000M$.

where $A(r) = 1 - 2M/r$ and we neglect subdominant magnetic-type contributions and higher multipoles. We introduce a dimensionless tidal parameter

$$\epsilon = \frac{M_c M^2}{R^3}, \quad (4.3)$$

which measures the strength of the tidal moment.

The tidal field we are considering is not accurate close to the central BH, where spin effects will change the tidal potential. Yet, in the parameter space we will explore, most of the cloud is localized far away from the horizon, where these effects are minimal and should not affect our qualitative conclusions. As in the previous chapter, we will focus exclusively on static tides, which are independent of coordinate time t . We stress that we are using coordinates adapted to the BH: the companion position should in general be time-dependent, but we focus exclusively on slowly moving companions (or equivalently, large separations R).

The superradiant cloud is described by a massive, minimally coupled scalar field Φ evolving on the above fixed geometry

$$\square\Phi = \mu^2\Phi. \quad (4.4)$$

We evolve this equation numerically using a $3 + 1$ decomposition in Cartesian Kerr-Schild coordinates (t, x, y, z) . We refer the reader to Ref. [272] for more details on the numerical implementation.¹

We will be interested in extracting from our numerical simulation the multipolar components of the scalar Φ

$$\Phi_{\ell,m}(t, r) = \int_{S_2} d\Omega \Phi(t, r, \theta, \varphi) Y_{\ell,m}(\theta, \varphi). \quad (4.5)$$

¹ The numerical implementation of this work was performed by Taishi Ikeda.

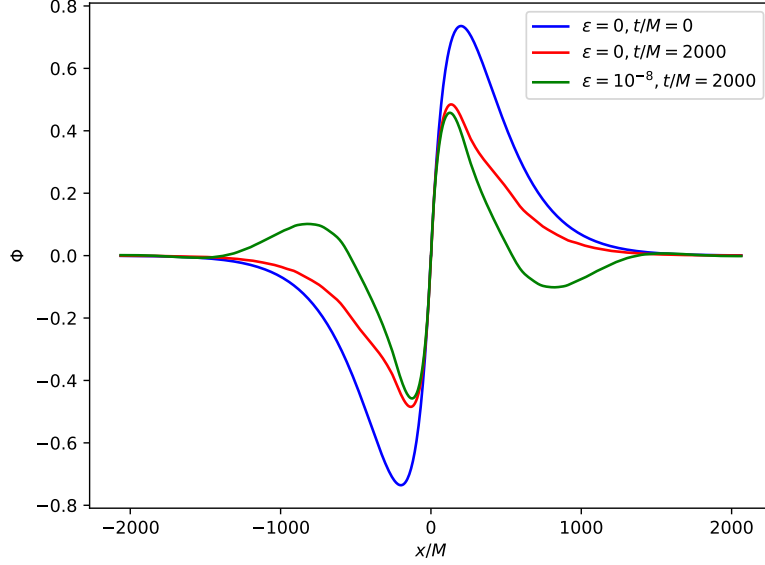


Figure 4.3: Dependence of the field Φ along the x -axis at different instants for a coupling $M\mu = 0.1$. In the absence of a companion ($\epsilon = 0$) and despite a slight change in the profile, the field has no nodes. It has a local extremum at $\sim r = 200M$ as predicted by a small $M\mu$ expansion for the fundamental mode. When a weak tidal field is turned on ($\epsilon = 10^{-8}$) the field develops a different radial profile with one node, pointing to a significant component of overtones. Our results indicate a sizeable excitation of the second excited state $n = 4$, which has extrema at $r/M \sim 170, 850$ (see Appendix A).

As initial data for our numerical evolutions we will use a fundamental superradiant dipolar mode adequate to describing quasi-stationary states around a BH [127, 273]

$$\Phi(t, r, \theta, \varphi) = A_0 r M \mu^2 e^{-r M \mu^2 / 2} \cos(\varphi - \omega_R t) \sin \theta. \quad (4.6)$$

A_0 is an amplitude related to the mass in the axion cloud, and $\omega_R \sim \mu$ is the bound-state frequency.

The spacetime of a real astrophysical binary is asymptotically flat. However, because we are using only an approximation to the full problem, where the companion is supposed to be far away, the geometry (4.2) is no longer asymptotically flat. To avoid unphysical behavior at large distances, we force the geometry to be asymptotically flat by replacing the far region with

$$ds^2 = ds_{\text{Kerr}}^2 + (1 - \mathcal{W}) \delta ds_{\text{tidal}}^2, \quad (4.7)$$

where $\mathcal{W} = \mathcal{W}(\tilde{r})$ is a following piecewise function

$$\mathcal{W}(\tilde{r}) = \begin{cases} 1 & (\tilde{r} > 1) \\ \mathcal{W}_5 & (0 < \tilde{r} < 1) \\ 0 & (\tilde{r} < 0). \end{cases} \quad (4.8)$$

$(n \ell m)$	t_{trans}/M	$\frac{c_{n\ell m}}{c_{211}} \left(\frac{\phi_{n\ell m}}{\phi_{211}} \right)$	$\frac{c_n^{\text{Num}}}{c_2^{\text{Num}}}$
311	1888	1.03(0.85)	0.221
411	458	0.236(0.13)	0.094
511	173	0.113(0.046)	0.058

Table 4.1: Timescales t_{trans} and relative amplitudes predicted by time-independent perturbation theory (see Appendix A) and those obtained from numerical simulations data at $t = 1000M$, for the most relevant 1st order transitions from the initial dipolar state ($\ell = m = 1$) for a gravitational coupling of $M\mu = 0.1$. The second column shows the timescale to transition from the initial to the $(n\ell m)$ state, as obtained from time-dependent perturbation theory. The third column shows the relative amplitude of the overtones with respect to the fundamental mode, predicated by time-independent perturbation theory (in parenthesis is the corresponding ratio of the field components at $r = 60M$). The last column shows this same quantity but for our numerical results. They agree with perturbation theory within a factor of two, except for the $\ell = m = 1, n = 3$ mode. In this case, the timescale needed for excitation is larger than the instant at which the coefficients were extracted.

Here, $\tilde{r} = (r - r_{\text{th}})/w$ and $\mathcal{W}_5(\tilde{r})$ is chosen to match smoothly with the required asymptotic behavior, so we choose a 5th-order polynomial satisfying $\mathcal{W}_5(1) = 1, \mathcal{W}_5(0) = \mathcal{W}'_5(0) = \mathcal{W}''_5(0) = \mathcal{W}'_5(1) = \mathcal{W}''_5(1) = 0$. The transition region has a width $w = 500M$ and is located at $r_{\text{th}}/M \simeq \sqrt{0.9 \times 5/(8\pi\epsilon)}$. These parameters were chosen to ensure that the bosonic cloud sits entirely in a region described by Eq. (4.2). Accuracy requirements, finite size of the numerical grid and computational power all contribute to limit the timescales that one is able to access numerically. Here, we evolve these systems for timescales $\sim 7000M$.

Although we have results for general BH spin, we focus mostly on states around a *non-spinning* BH. These states are not superradiant in origin and arise due to the fine-tuned initial data. However, they are extremely long-lived (the decay timescale is of the order of the superradiant growth timescale if the BH was spinning), as we show below, with a lifetime that far exceeds that of all the tidally-induced transitions studied here. Thus, BH spin is important to generate the scalar clouds but has little impact on *some* of the physics of tides. In addition, the tidal field in Eq. (4.2) is adapted to a non-spinning BH. Our numerical results show only a very mild dependence on BH spin. With the exception of Ref. [268], all previous results on tidal effects in superradiant clouds focus on the small $M\mu$ coupling parameter, consider a flat background on which the superradiant states evolve, and have only used linearized analysis for small tidal fields. Our framework can go beyond all these limitations.

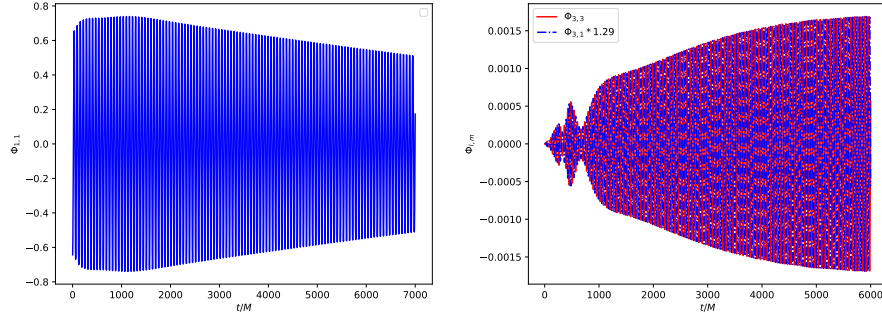


Figure 4.4: Dipolar ($\ell = m = 1$, left) and octupolar ($\ell = 3, m = 1, 3$, right) component of the scalar cloud when in the presence of a weak tidal field $\epsilon = 10^{-8}$, for the same initial conditions as in Fig. 4.1 (non-spinning BH and gravitational coupling $M\mu = 0.1$). The $\ell = 3, m = 1$ mode amplitude relative to the $\ell = m = 3$ was rescaled by the perturbation theory prediction ($\sqrt{5/3} \sim 1.29$). The agreement is very good throughout the evolution.

4.2 WEAK TIDES: TRANSITIONS TO NEW STATIONARY STATES

To show that our initial dipolar state is a (quasi-)stationary state in the timescales of interest of our problem, we start by evolving the initial data described above (4.6) around an isolated, non-spinning BH ($\epsilon = 0$). Its non-vanishing multipolar component, the dipole $\ell = m = 1$, is shown in Fig. 4.1. The amplitude of the field varies by a few percent over a time interval of $\sim 7000M$, which corresponds to ~ 100 scalar field periods of oscillation ($\sim 2\pi/\mu$). The scalar field and energy density along an equatorial slice are shown in Fig. 4.2 at $t = 7000M$. The density is almost (but not exactly) symmetric along this slice.

We now turn on a tidal field with $\epsilon = 10^{-8}$ produced by a companion star on the x -axis. We consider this to be a weak tide since no nonperturbative feature is seen on timescales of $\sim 6000M$. The first feature we observe is the transition from the fundamental dipolar state to higher excited overtones, in the same spirit as previous analytical studies [135, 268]. The n -th overtone is localized at a radius $r_{\text{Bohr}} \sim n^2/(M\mu^2)$, which means their excitation leads to an expansion of the cloud. Fig. 4.3 shows the x -dependence of the field initially and at $t = 2000M$. If the cloud stayed on the fundamental dipolar mode it should not have any node along the radial direction, as it happens for $t = 0M$. Instead, we observe one node at $t = 2000M$, meaning the cloud is transitioning to excited states. This profile also includes the octupolar $\ell = 3$ component, though this is two orders of magnitude smaller than the dipolar term.

In Appendix A we outline how to study the transition between bound states of the cloud using standard perturbation theory in Quantum Mechanics. In the small coupling limit, $M\mu \ll 1$, the description of the cloud state is analogous to that of the hydrogen atom, with

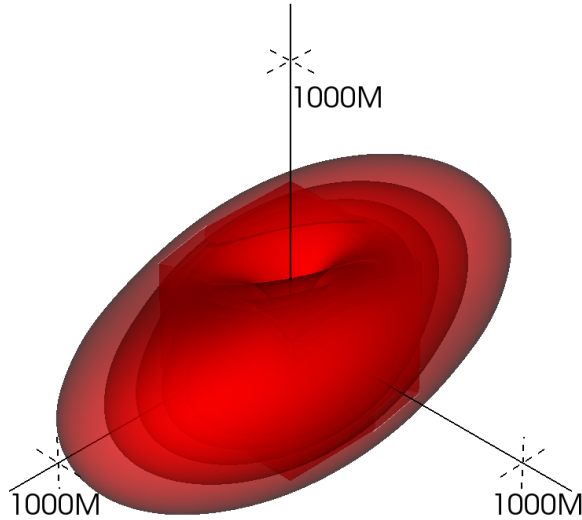


Figure 4.5: Snapshot of a tidally deformed scalar cloud with $\epsilon = 10^{-8}$ for the strength of the tidal field and $M\mu = 0.1$ for the gravitational coupling. In the absence of a companion, the energy density is almost spherical and remains so for thousands of dynamical timescales. Instead, here we observe that after $7000M$ the system settles to a new stationary configuration.

$\alpha = M\mu$ playing the role of a gravitational fine-structure constant. The properties of the radial distribution of the cloud can then be studied using the typical radial “hydrogenic” functions $R_{n\ell}(r)$. From them, we know the $n = 3$ state has extrema at $r/M = 175,1024$, which are not apparent in Fig. 4.3 (in our convention, states are labeled by an integer $n = \ell + 1, \ell + 2, \dots$). Instead, the second excited state $n = 4$ is known to have extrema at $r/M = 170,875,2155$, which agrees with those of the numerical results (the last point is challenging to confirm, as the grid size and spurious reflections affect a proper evaluation of eigenfunctions at large distances).

Moreover, since in this limit the eigenstates of the cloud are orthonormal, we can extract the amplitude c_n of a specific overtone from the numerical data by a simple projection

$$c_n = \int_0^\infty dr r^2 R_{n1}^*(r) \Phi(r), \quad (4.9)$$

where $\Phi(r)$ corresponds to the numerical data at a given radial direction (e.g. $\theta = \pi/2$ and $\varphi = 0$). We are implicitly assuming that our data is only composed of $\ell = 1$ modes, which again, as we will see below, is a reasonable approximation. Since our grid size is limited,

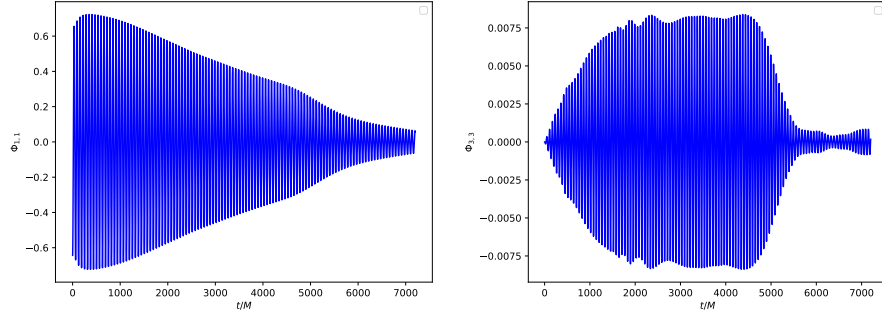


Figure 4.6: Cloud being tidally disrupted as it loses energy to asymptotically far-away distances from the central BH. The field cascades to smaller angular scales, and thus transitions to higher multipoles. This figure shows the time evolution of the dipolar ($\ell = m = 2$) and octupolar ($\ell = m = 3$) components of the scalar field for a gravitational coupling $M\mu = 0.1$, and a companion with $\epsilon = 10^{-7}$. The extraction radius is $r = 60M$.

we can only capture a few nodes along the radial direction and for later times our data at large radius will be contaminated by spurious reflections from the outer boundary. For this reason we restrict this analysis to times $t \lesssim 1000M$.

Our results are shown in Table 4.1. They are within a factor two from the estimates of perturbation theory, which is an excellent agreement considering: 1. perturbation theory uses a small $M\mu$ expansion which is already inaccurate at $M\mu \gtrsim 0.1$ (e.g. Fig. 1 in Ref. [268] shows how factors of two can easily arise from such an approximation); 2. there can be intermediate transitions between states which complicate the analysis. Nevertheless, perturbation theory justifies why the first excited state, the $n = 3$ mode, is not yet dominant, since the timescale for its excitation is larger than higher overtones. Our numerical results are consistent with transition occurring on the timescales predicted from the table for the $n = 3, 4, 5$ overtones.

Another important feature of our simulations are transitions to octupolar and higher multipoles, as illustrated in Fig. 4.4. There we show the time evolution of the dipolar $\ell = m = 1$ and octupolar $\ell = m = 3$ mode. It is apparent that the magnitude of the dipolar mode is now decreasing, and that a fraction of this energy is going into higher multipoles, specifically the octupolar $\ell = 3, m = 1, 3$. Such migration changes the spatial distribution of energy density, as depicted in Fig. 4.5.

Again, our results are consistent with the prediction from perturbation theory, in particular that the amplitude of the $\ell = 3$ mode scales with the external tide ϵ [135, 268]. One of the cleanest indications of the validity of the perturbative framework is the excitation of the $\ell = 3, m = 1$ mode. Perturbation theory predicts that the relative amplitude of the $\ell = m = 3$ mode is $\sqrt{5/3} \sim 1.29$ larger than that of the

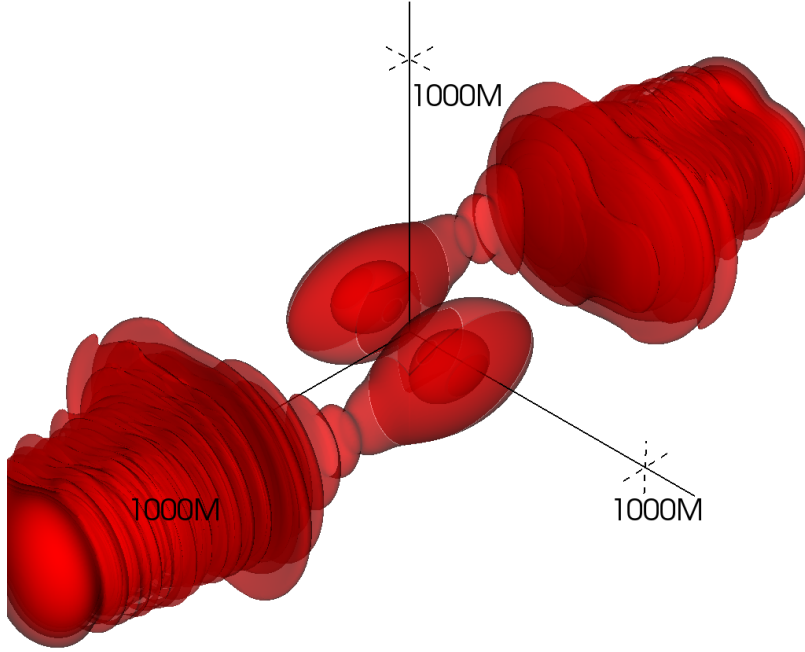


Figure 4.7: Snapshot of a tidally disrupting cloud. The snapshot depicts the energy density along the equator of a scalar cloud which was set initially around a non-spinning BH. In the absence of a companion mass, the energy density is almost spherical and remains so for thousands of dynamical timescales. Here, the simulation starts with one symmetric initial scalar energy distribution, but in the presence of a star for which $\epsilon = 10^{-7}$. The gravitational coupling is $M\mu = 0.1$. The snapshot is taken after $7000M$ and is leading to the disruption of the cloud.

$\ell = 3, m = 1$ mode, and this depends exclusively on an angular matrix with no radial dependence. Our results show a relative amplitude across all times and extraction radii consistent with such prediction, as shown in the figure.

4.3 STRONG TIDES: TIDAL DISRUPTION OF CLOUDS

We now move to study stronger tidal fields. If too strong, we expect the scalar configuration to be tidally disrupted. A star of mass M_* , radius R_* , in the presence of a companion of mass M_c at distance R is on the verge of disruption when the tidal force surpasses its own self-gravity, known as the *Roche* limit. Up to numerical factors of order one this is

$$M_*/R_*^2 = 2M_c R_*/R^3 . \quad (4.10)$$

When the mass in the scalar cloud is a fraction of that of the BH, $M_* \approx M$ and its radius is of the order of $R_* \gtrsim 5/(M\mu^2)$ (see Appendix A). This corresponds to a critical tide

$$\epsilon_{\text{crit}} \approx \frac{(M\mu)^6}{250}. \quad (4.11)$$

The simulations presented in Figs 4.6–4.7 corroborate this behavior. For large masses of the companion, the initial dipolar mode quickly transfers energy to the octupole, which then drains into higher and higher multipoles. This signals a transfer of energy to smaller and smaller angular scales, as the cloud is disrupted and loses mass to far-away distances, as illustrated in Fig. 4.7.

Extracting precise values for the critical tide from our simulations is complicated because: 1. these are extended scalar configurations, and to understand whether there is mass being lost to large distances requires large numerical grids; 2. a seemingly stable cloud on the simulation timescale can eventually be disrupted when evolved for longer times. Typically, our numerical simulations last for $\sim 6000M$. With this in mind, we estimate $\epsilon_{\text{crit}} \sim 2 \times 10^{-7}$ for $M\mu = 0.2$, for which disruption is clear after $4000M$. This critical tide agrees remarkably well with our crude estimate of Eq. (4.11). On the other hand, for $M\mu = 0.1$ we see disruption on the simulated timescales only for $\epsilon \gtrsim 2 \times 10^{-8}$, a factor of four bigger than Eq. (4.11). Disruption may occur for smaller tides, but on timescales that we are currently unable to probe. Disruption can also be stimulated by transitions to overtones which would “puff up” the cloud and increase its size to a few times the estimate $\sim 1/(M\mu^2)$. Consequently, the critical tide would be reduced.

To summarize, our results are consistent with the behavior of Eq. (4.11), though longer evolutions are needed to understand better the correct prefactor in the critical tide ϵ_{crit} .

4.4 ASTROPHYSICAL SYSTEMS

We will now apply our results to some known astrophysical systems. Examples of BHs with companions are the Cygnus X-1 system and Sagittarius A* at the center of our galaxy. Cygnus X-1 is a binary system composed of a BH of mass $M_{\text{BH}} \sim 15M_\odot$ and a companion with $M_c \sim 20M_\odot$ at a distance $R \sim 0.2 \text{ AU} \sim 3 \times 10^{10} \text{ m}$ [274]. Plugging these in Eq. (4.3) we find $\epsilon \sim 5 \times 10^{-19}$. Then, for it to sit at the critical tide, $M\mu \sim 2 \times 10^{-3}$. The growth timescale τ of scalar clouds via superradiance is of order $\tau_{\text{growth}}^s \sim (M\mu)^{-9} M \sim (M\mu/(2 \times 10^{-3}))^{-9} (M/10^5 M_\odot) 10^{16} \text{ years}$ [103], which for Cygnus X-1 is too large to be meaningful compared to the age of the universe ($\sim 10^{10}$ years). However, for vector fields the growth timescale is smaller, $\tau_{\text{growth}}^v \sim (M\mu)^{-7} M$ [272, 275, 276]. If our results extrapolate

to vector fields, this mechanism becomes astrophysically relevant for this system. Note also that the tide is small enough that it should not affect any of the constraints derived from the non-observation of GWs emitted by the cloud [277, 278].

Moving to Sagittarius A*, there is a supermassive BH at the center of our galaxy with mass $\sim 4 \times 10^6 M_\odot$. The closest known companion is the S2 star [279, 280], with mass $M_{S2} \sim 20 M_\odot$ and a pericenter distance of $\sim 1400 M_{\text{BH}} \sim 120 \text{ AU}$ [281]. Then $\epsilon \sim 2 \times 10^{-15}$, which corresponds to a critical coupling for disruption of $M\mu \sim 9 \times 10^{-3} \sim (M\mu/10^{-2})^{-9} (M/10^5 M_\odot) 10^{10} \text{ years}$. This means tidal disruption may occur in astrophysically relevant timescales, which would affect the estimates of GW emission using just the dipolar mode. However, note that our approximations always require that the companion sits outside the cloud ($R > R_*$, or the approximation in Eq. (4.2) would break down). Using Eq. (4.10), disruption together with such a condition always requires $M_c > M/2$, which is not the case here.

At the verge of tidal disruption, the binary system composed of the central BH and the companion is emitting GWs which carry energy at a rate approximately given by the quadrupole formula

$$\dot{E}_{\text{binary}} = \frac{32}{5} \frac{M_c^2 M^3}{R^5}, \quad (4.12)$$

where we assume the companion to be much lighter than the BH. On the other hand, the GW flux emitted by the cloud-BH system scales as [127, 129, 273]

$$\dot{E}_{\text{cloud}} \sim \frac{1}{50} \left(\frac{M_S}{M} \right)^2 (M\mu)^{14}, \quad (4.13)$$

with M_S being the mass of the scalar cloud. Thus, GW emission by the binary dominates the signal when

$$\frac{M_c}{M_S} \gtrsim \left(\frac{M_S}{M} \right)^5 \left(\frac{5}{2} M\mu \right)^{12}, \quad (4.14)$$

Therefore, in the context of GW emission and detection, disruption will not affect our ability to probe the system: if it was visible via monochromatic emission by the cloud before disruption, it would be seen after disruption as a binary.

Note that tidal disruption of the cloud is a relevant possibility for these systems, since the cloud is generically not depleted due to mode mixing by the time the system reaches the Roche radius. In fact, for cloud depletion due to mode mixing to be effective, the system needs to be in a resonant epoch for a long time [135]. This requires a particular combination of the mass ratio and gravitational coupling $M\mu$, which can only be realized in a small region in the possible parameter space (see Figs. 7 and 8 in Ref. [135]).

4.5 DISCUSSION

In this chapter, we performed the first numerical study of the impact of a possible companion star or BH on the development of such superradiant cloud. We observe transitions to higher overtones and to higher multipoles, which *stretch* and *deform* the cloud. Weak tidal fields slightly deform the cloud, affecting GW emission by the system. These changes have not been computed. For tidal fields larger than the threshold of Eq. (4.11), the companion simply breaks the cloud apart. This could potentially occur for BH systems such as the one at the center of our galaxy or the Cygnus X-1 binary system.

Our results generalize to a number of situations. Although we have discussed only tides acting along the equator, we have performed evolutions for polar tides along the z -axis, and found the same phenomenology. This includes overtone excitation and transitions between multipoles and tidal disruption, even if quantitatively different. Our setup is that of a real scalar field, but the results generalize to complex scalars.

The phenomena we studied are in similar spirit to the *cloud ionization* discussed recently in Refs. [137, 282, 283]. In this case, the cloud is depleted by the transition from bounded to unbounded states induced by the orbital motion of the binary. The necessary energy for this transition comes from gravitational binding energy of the binary, so ionization accelerates the inspiral and acts as an effective dynamical friction.

Part II

LIGHT-RING AND THE RINGDOWN

5

ONE RING TO RULE THEM ALL

In the previous chapters, we discussed various physical processes involving BHs, where we assumed a stationary “background”, where “matter probes” and evolves. These setups are, therefore, particularly apt at providing detailed information on the geometry and underlying theory of gravity. For instance, Earth’s gravitational multipole moments can be determined in this way by studying the motion of orbiting satellites [284–286]. In astrophysics, accretion flows around SMBHs can also be well described as flows on a fixed Kerr geometry. The matter density outside the BH is so low that its backreaction can be safely neglected for practical purposes [287].

Thus, a fixed Kerr geometry suffices to understand and study the physics associated with observations by the Event Horizon Telescope [288] or GRAVITY [289]. The appearance of BHs is determined by photons reaching far-away observers [290–295]. It is therefore no surprise that the separatrix between photons escaping to infinity and those eventually plunging into the BH horizon plays an important role in BH imaging. Photons sent in from large distances with a decreasing impact parameter will be deflected with a larger angle, probing stronger-gravity regions before being scattered to far-away observers. Below a critical impact parameter, they fall onto the BH. At the critical impact parameter, the photon circles the BH an infinite number of times. These trajectories asymptote to a closed, unstable, circular orbit, known as the light-ring (LR). For non-rotating BHs, it is located at radius $r_{\text{LR}} = 3M$.

The LR is therefore associated with the amount of information that one can gather related to the BH geometry, and this does not restrict just to electromagnetic waves. If we give a little “kick” to a BH, it will relax to stationarity as it vibrates according to some proper frequencies - its *quasinormal modes* (QNMs). They are quasinormal because there is a loss of energy to both infinity and the BH horizon, leading to an imaginary part in their frequencies. Formally, the QNM modes are the eigenfunctions of the Teukolsy equation (2.49) (or the Zerilli/Regge-Wheeler for non-rotating BHs) with ingoing behavior at the BH horizon and outgoing at far-away distances. The Zerilli and Regge-Wheeler equation are actually *isospectral*, i.e. they have the same QNM frequencies [296].

In a binary coalescence, the final BH remnant approaches stationarity as it *ringdowns* and emits GWs that can be described by a superposition of exponentially damped sinusoids [188, 297–301]. Each multipole (ℓ, m) is described by a sum over possible overtones (labeled by n)

$$\psi_{\ell m}(t) = \sum_n A_{\ell mn} e^{-i[\omega_{\ell mn}(t-t_{\text{start}})+\phi_{\ell mn}]}, \quad (5.1)$$

where $\omega_{\ell mn}$ are the QNM frequencies, which depend only on the mass M and spin a of the remnant. On the other hand, t_{start} is an arbitrary starting time and $A_{\ell mn}$ and $\phi_{\ell mn}$ are, respectively, an amplitude and phase that depend on the source of the perturbation, i.e. the full history of the merger. By extracting the frequencies $\omega_{\ell mn}$ from the waveform we can then estimate the mass and spin of the remnant, and if multiple overtones are detected, perform tests of the no-hair theorem. This program is dubbed *BH spectroscopy* [302–305]. Its importance was accurately foretold by Detweiler in 1980 [306, 307]

After the advent of GW astronomy, the observation of [the BH's] resonant frequencies might finally provide direct evidence of BHs with the same certainty as, say, the 21 cm line identifies interstellar hydrogen.

So far, the LVK has only confirmed the presence of the fundamental $\ell = m = 2$ mode in its ringdown catalog [17, 308]. These observations have provided constraints on BH charge [309], the Bekenstein-Hound bound on the BH information emission rate [310], and modifications to GR [311, 312]. Independent analyses have suggested the inclusion of overtones in the ringdown model improves agreement with numerical relativity simulations up to (or even before) the peak amplitude of radiation [313–316]. Subsequent works claimed the presence of one overtone in GW150914 [317–321]. However, including these overtones in the early ringdown appears to be an overfit of the signal which lacks physical significance [307, 322–324]. More recently, two independent studies found nonlinearities in the early ringdown of numerical relativity waveforms [325, 326]¹.

Returning to our discussion, what is the connection between the QNMs and the LR after all? It turns out the *ringdown* can be interpreted in terms of high-frequency waves trapped in unstable orbits at the LR that slowly leak out to infinity. The real part of the QNMs, $\omega_{\text{QNM}} = \omega_{\text{R}} + i\omega_{\text{I}}$, is determined by the angular velocity at the LR, while the imaginary part is related to the instability timescale of the orbit, i.e. how fast particles can escape from the LR [298, 327, 328]. Then, the presence of a non-trivial environment can change the structure of geodesics, including the LR, but also interact and excite the waves that are trapped there. In this second part of the thesis, we will explore the latter possibility and draw consequences for the observation of compact objects.

¹ We recommend the interested reader the introduction of Ref. [307] for a more detailed discussion on this topic

5.1 LIGHT-RINGS: THE KEY TO COMPACT OBJECTS

Let us again consider generic spherically symmetric spacetimes described by the line element in Eq. (2.16). Null geodesics are described by Eq. (2.9) together with the condition they are null, i.e. $g_{\mu\nu} \frac{dx^\mu}{d\lambda} \frac{dx^\nu}{d\lambda} = 0$, where λ parametrizes the geodesic. Spherical symmetry allows to restrict movement to the $\theta = \pi/2$ plane, while the other EOM are [2, 178, 328]

$$\frac{dt}{d\lambda} = \frac{E}{A(r)}, \quad (5.2)$$

$$\frac{d\varphi}{d\lambda} = \frac{L}{r^2}, \quad (5.3)$$

$$\frac{dr}{d\lambda} = E \sqrt{1 - A(r) \frac{b^2}{r^2}} = \sqrt{V_r(r)}, \quad (5.4)$$

$$b = \frac{L}{E}. \quad (5.5)$$

where E , L are, respectively, the “energy” and “angular momentum” constants of motion, and b is the *impact parameter*. Circular orbits are defined by the condition

$$\frac{dr}{d\lambda} = \frac{d^2r}{d\lambda^2} = 0 \Rightarrow V_r = \frac{dV_r}{dr} = 0, \quad (5.6)$$

which have as implicit solution

$$r_{\text{LR}} = 2 \frac{A(r_{\text{LR}})}{A'(r_{\text{LR}})}, \quad (5.7)$$

$$b_c^2 = \frac{r_{\text{LR}}^2}{A(r_{\text{LR}})}, \quad (5.8)$$

$$\Omega_{\text{LR}} = \frac{d\varphi}{dt} = \sqrt{\frac{A'(r_{\text{LR}})}{2r} \frac{\sqrt{A(r_{\text{LR}})}}{r_{\text{LR}}}}. \quad (5.9)$$

For Schwarzschild they are

$$r_{\text{LR}} = 3M, \quad (5.10)$$

$$b_c = 3\sqrt{3}M, \quad (5.11)$$

$$\Omega_{\text{LR}} = \frac{1}{3\sqrt{3}M}. \quad (5.12)$$

Since we are considering spherically symmetric spacetimes, the LR defines more broadly a photonsphere, where high-frequency waves can be trapped, whether they are photons or GWs. It is an unstable trapping since any small perturbation $r = r_{\text{LR}} + \delta$ grows exponentially. Expanding the potential close to the LR one finds

$$\left(\frac{d\delta}{d\lambda}\right)^2 = V_r(r_{\text{LR}}) + V_r'(r_{\text{LR}})(r - r_{\text{LR}}) + \frac{V_r''(r_{\text{LR}})}{2}(r - r_{\text{LR}}) + \dots \quad (5.13)$$

By the definition of circular orbit (5.6) the first two terms vanish and one is left with

$$\left(\frac{d\delta}{d\lambda}\right)^2 = \frac{\delta^2}{2} V_r''(r_{\text{LR}}). \quad (5.14)$$

Rewriting it as

$$\frac{d\delta/dt}{\delta} = \sqrt{\frac{V_r''(r_{\text{LR}})}{2(dt/d\lambda)^2}}, \quad (5.15)$$

we arrive at the solution

$$\delta \sim \delta_0 e^{\lambda_L t}, \quad (5.16)$$

$$\lambda_L = \sqrt{\frac{V_r''(r_{\text{LR}})}{2(dt/d\lambda)^2}} = \frac{A(r_{\text{LR}})}{E} \sqrt{\frac{V_r''(r_{\text{LR}})}{2}}. \quad (5.17)$$

λ_L is known as the Lyapunov exponent, and for Schwarzschild $\lambda_L = \Omega_{\text{LR}}$. In other words, a null ray slightly displaced off the LR will orbit on a timescale $t \sim \log \delta / \lambda_L$, during which the null particle does a number of orbits

$$N \sim \frac{\Omega_{\text{LR}} t}{2\pi} = -\frac{\log \delta}{2\pi}, \quad (5.18)$$

close to the LR.

Because of the above trapping properties, LRs play a crucial role in our understanding of BHs. They are, for many purposes, the inner surface probed by high-frequency observations. Ref. [328] formalized this relation by showing that in this high-frequency limit the QNM frequencies of spherically symmetric, asymptotically flat spacetimes are

$$\omega_{\text{QNM}} = \Omega_{\text{LR}} \ell - i \left(n + \frac{1}{2} \right) \lambda_L, \quad (5.19)$$

where $n = 0, 1, \dots$, labels the overtone. This correspondence is only valid in the eikonal limit ($\ell \gg 1$) but gives excellent predictions even for low values of ℓ [329] (relative differences below 5 % already for $\ell = 4$).

In this chapter, we will show that the LR also dictates the late-time behavior of the luminosity of sources plunging into BHs. Such events appear to occur periodically in the vicinities of Sagittarius A* [330, 331]. Similar events were reported in the past for Cygnus X-1. In particular, dying pulses from BH accretion were discussed in the context of Cygnus X-1 years ago [332, 333]. Emitters falling onto BHs may also radiate in the GW window. These could be, for example, a hierarchical triple system where the CM of a small binary is inspiralling onto a SMBH [175].

Previous studies on the dynamical appearance of bright sources follow a number of approximations and are restricted to spherically symmetric gravitational collapse [334–336]. Here, we extend those and investigate how a pointlike source that emits GWs or electromagnetic waves fades out as it is accreted by a BH.

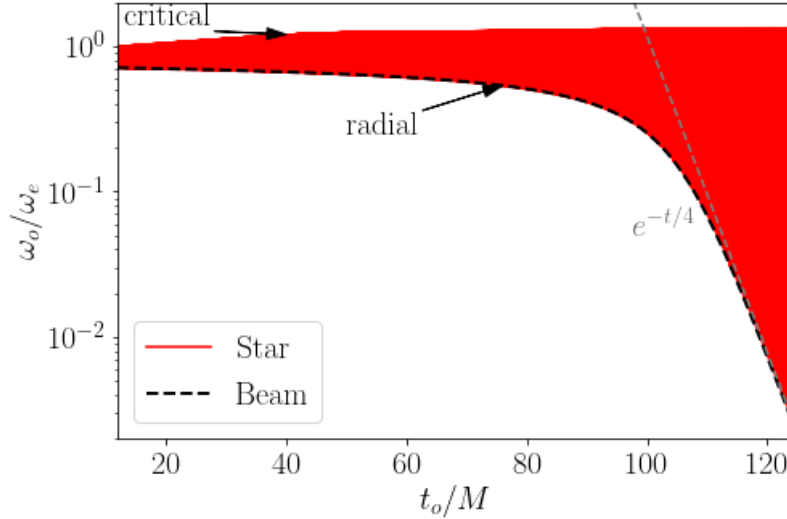


Figure 5.1: Redshift of two different sources as they plunge radially into a Schwarzschild BH, emitting null particles (e.g. photons, gravitons) of fixed proper frequency ω_e . The source, located in the equatorial plane at $\theta = \pi/2$, $\phi = 0$ begins from rest at infinity, but (for numerical purposes) starts emitting only when it crosses $r = 30.65M$. **Beam:** this source emits only radially outwards. The observer is located at $r_o = 100M$, $\theta = \pi/2$, $\phi = 0$, and receives particles whose frequency/energy decreases with time. At late times, the frequency ω_o measured by the observer decays exponentially as $\omega_o \sim \omega_e e^{-t/(4M)}$, according to our analytic prediction (5.29). **Isotropic star:** the second source is a pointlike “star” emitting isotropically in its local rest frame. At a fixed instant, far-away observers distributed along the sphere at $r_o = 100M$ receive a wide range of redshifts. The lower part of the curve is due to radially propagating null particles, whereas the top part of the curve is due to particles with a near critical impact parameter $b_c \approx 3\sqrt{3}M$ that linger close to the LR, which can be blueshifted [293].

5.2 HOW DO BRIGHT OBJECTS FADE OUT?

5.2.1 An outward-pointing beam

We start by focusing on the geometric optics regime, where one considers that high-frequency waves follow null geodesics on a fixed background geometry, independently of their nature.

Let us imagine a laser pointer shooting a “beam” of light outwards as it falls radially onto a Schwarzschild BH from rest at infinity. The

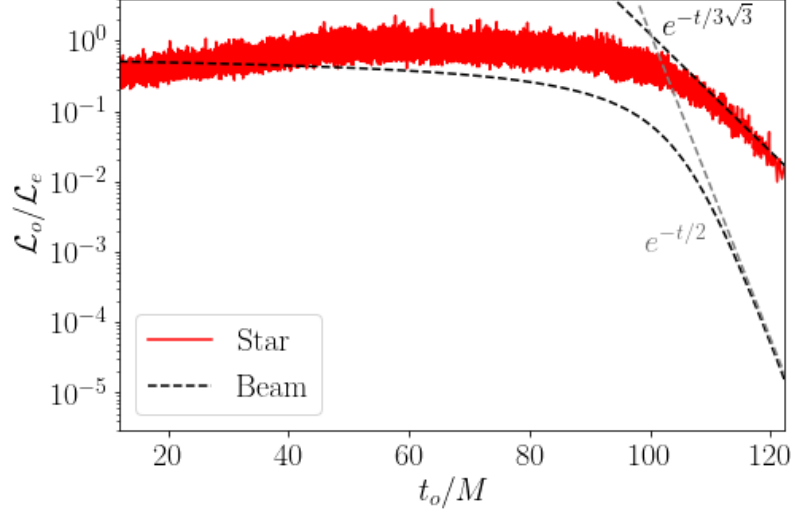


Figure 5.2: Normalized luminosity ($\mathcal{L} = dE/dt$) of the two different sources discussed in Fig. 5.1. The observed luminosity of the radial beam scales as $\mathcal{L} \sim e^{-t/(2M)}$ at late times, again in agreement with our prediction. The luminosity of the isotropic star was calculated by “binning” null particles in packets of 20, to avoid large scatters. At late times, the luminosity is dominated by those particles lingering on the LR, hence $\mathcal{L} \sim e^{-t/(3\sqrt{3}M)}$.

4-velocity of this source and its radial position in terms of the proper time is

$$v_e^\mu = \frac{dx_e^\mu}{d\tau_e} = \left(\frac{1}{1 - 2M/r_e}, -\sqrt{\frac{2M}{r_e}}, 0, 0 \right), \quad (5.20)$$

$$r_e = 2M \left(-\frac{3\tau_e}{4M} \right)^{2/3}, \quad (5.21)$$

and the coordinate time at the source position is given implicitly by

$$\frac{dt_e}{d\tau_e} = \frac{1}{1 - 2M/r_e}. \quad (5.22)$$

Now, consider a photon with 4-momentum k^μ such that its proper frequency is $\omega_e = -v_e^\mu k_\mu$. This photon will intersect the world-line of an observer with 4-velocity v_o which measures a frequency $\omega_o = -v_o^\mu k_\mu$. For a static observer at large distances and for radial null geodesics followed by the photon

$$v_o^\mu = (1, 0, 0, 0), \quad (5.23)$$

$$k^\mu = E \left(\frac{1}{1 - 2M/r}, 1, 0, 0 \right), \quad (5.24)$$

which implies

$$\omega_o = \omega_e \left(1 - \sqrt{\frac{2M}{r_e}} \right). \quad (5.25)$$

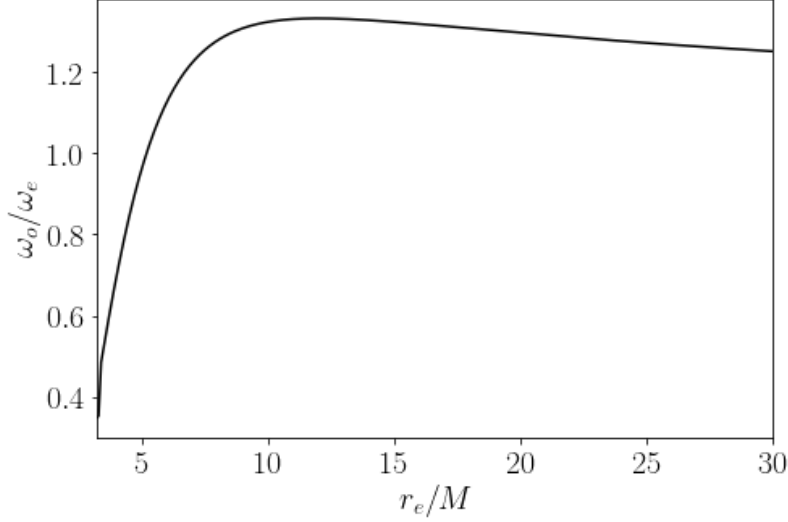


Figure 5.3: The blueshift distribution of photons with near-critical impact parameter, emitted from an object freely-falling onto a BH. The blueshift is maximum, $\omega_0 = 4\omega_e/3$, at $r_0 = 12M$, and is unit at $r_e = 3\sqrt{3}M$ (see also Ref.[337]).

We now want to compute the redshift as seen by a distant observer as a function of the coordinate time t . We need to take into account that the null particle is being emitted by a source that is getting closer to the horizon and which also needs time to reach the observer. An outward-directed photon obeys

$$\frac{dt_{\text{travel}}}{dr} = \frac{1}{1 - 2M/r}. \quad (5.26)$$

We can integrate this to find the arrival time of the null particle as measured by a far-away observer

$$t_o = t_e + (r_o - r_e) + 2M \log \left(\frac{r_o - 2M}{r_e - 2M} \right). \quad (5.27)$$

We can obtain the behavior when the source is close to the BH horizon by solving

$$\frac{dr_e}{dt_e} = -\sqrt{\frac{2M}{r_e}} \left(1 - \frac{2M}{r_e} \right), \quad (5.28)$$

when $r_e \sim 2M$. We find $t_e \sim -2M \log(r_e - 2M)$, and plugging these in Eq. (5.27) we find $r_e - 2M \propto e^{-t_o/(4M)}$. Therefore, at late times

$$\frac{\omega_0}{\omega_e} \sim e^{-t_o/(4M)}. \quad (5.29)$$

The total luminosity dE_o/dt_o can be calculated similarly. At late times $dE_o/dt_o \sim e^{-t_o/(2M)}$.

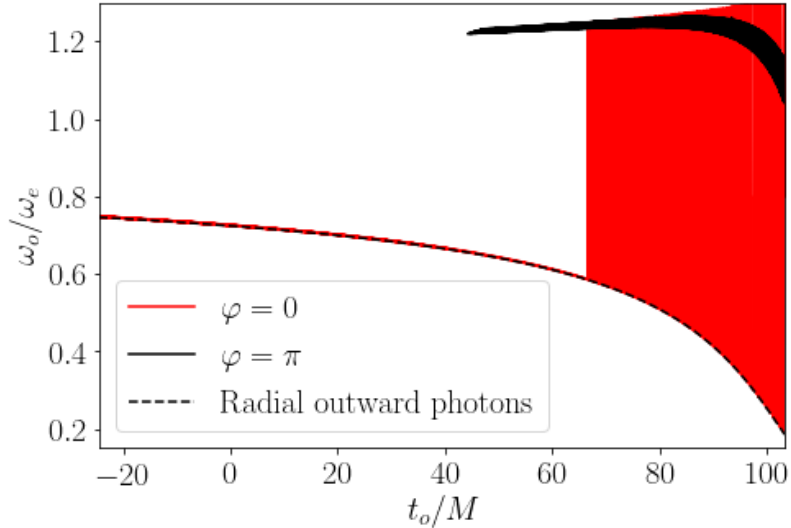


Figure 5.4: The redshift distribution of light emitted by an infalling (isotropic) star as measured by observers at $r = 100M$ on the infalling axis. For $\varphi = 0$ the star is between the BH and the observer, whereas observers at $\varphi = \pi$ only see the star due to gravitational lensing, as the BH sits between them and the star. Note the delay with which the $\varphi = \pi$ observer receives the first signal, with respect to $\varphi = 0$. Note also that the signal is mostly Doppler blueshifted for $\varphi = \pi$, as the observer sees light emitted from an approaching source. Some of the details of this figure, in particular the graininess and isolated points, are due to insufficient number of null particles being sent from the star.

Figure 5.1-5.2 shows the numerical solution of this problem (black dashed line). An emitter starts falling at $r_i = 30.65M$ and sources 20000 null particles, one every (proper) time interval $\delta\tau_e = 4 \times 10^{-3}M$. These particles are collected by an observer at $r_o = 100M$. Our numerical results show that at late times the frequency as measured by far-away observers decreases exponentially as described by Eq. (5.29). Note that ω_o is always *redshifted*. The same applies to the luminosity, shown in Fig. 5.2.

5.2.2 An isotropically-emitting star

Most astrophysical sources of radiation are not “beams”. Even if they can be studied within the geometric optics limit, they should be emitting in different directions. The easiest generalization one can then make is to consider an isotropic pointlike source. Now, there are two new physical structures: the BH horizon, which captures null particles, and the LR, which traps them in unstable geodesics.

We consider a similar situation as before, where a body is falling radially from rest at infinity onto a BH. However, now it constitutes a luminous “hot spot” which emits radiation isotropically *in its rest*

frame, where it has total luminosity \mathcal{L}_e . To compute the total luminosity \mathcal{L}_o measured by a stationary far-away observer as a function of time, we need to follow each particle emitted.

Spherical symmetry allows us to focus on the emission on the equatorial plane without loss of generality. The conserved quantities E and L characterizing each emitted particle should be related to observables in the local freely falling frame, where they have energy ω_e and are emitted at an angle α with respect to the radial direction. In Appendix B, we outline how to obtain the following relations

$$\omega_o = \omega_e \left(1 + \sqrt{\frac{2M}{r}} \cos \alpha \right), \quad (5.30)$$

$$b = r_e \frac{\sin \alpha}{1 + \sqrt{\frac{2M}{r}} \cos \alpha}. \quad (5.31)$$

We can now study the infall of an isotropic star by shooting null particles uniformly distributed in α and collecting them at some fixed radius r_o . Particles with impact parameter smaller than the critical impact parameter b_c (5.11) will fall into the BH and are not considered in our calculation.

Equations (5.30)-(5.31) can be solved for the redshift of particles with critical impact parameter

$$\frac{\omega_o}{\omega_e} = \frac{r_e^3 + \sqrt{2M} \sqrt{r_e^5 - b_c^2 r_e^2 (r_e - 2M)}}{2M b_c^2 + r_e^3}. \quad (5.32)$$

This relation is shown in Fig. 5.3 as the star falls. For most of the fall, radiation with near-critical impact parameter is blueshifted for values of around 1.2 – 1.3 (in particular, it is larger than 1.2 for $6.7M < r_e < 49M$). The blueshift peaks at $r_e = 12M$ and crosses unit at $r_e = b$

$$\left. \frac{\omega_o}{\omega_e} \right|_{\max} = \frac{4}{3}, \quad r = 12M, \quad (5.33)$$

$$\frac{\omega_o}{\omega_e} = 1, \quad r = 3\sqrt{3}M, \quad (5.34)$$

in agreement with previous results [337].

We repeated the same numerical analysis as in the collimated beam but now distributing 1600 particles uniformly in the emission angle α . The results are illustrated in red in Figs. 5.1-5.2.

The first difference with respect to the “beam” is that now radiation reaches far-away observers (distributed along the whole sky) with different redshifts, depending on their propagation history. As can be seen in Fig. 5.1, the most redshift occurs for photons emitted radially outwards (the lower part of the red region that is limited by the dashed-black line corresponding to the collimated “beam”). On the other hand, some null rays can also be *blueshifted* ($\omega_o/\omega_e > 1$). These occur due to the extreme bending of rays close to or at the LR, where

rays with near-critical impact parameter can make a U-turn. This example is similar to having a moving source and a mirror, as studied in Ref. [293], where a similar blueshift was observed. Note that as the critical impact parameter is approached, the rays linger longer and closer to the LR, and consequently take more time to reach the observer.

Now, we focus on a fixed angular position to understand what a particular observer measures. We selected among all the outgoing photons those that reach the observer with $\cos \varphi > 0.99$ (which we label “ $\varphi = 0$ ”) and those with $\cos \varphi < -0.99$ (which we label “ $\varphi = \pi$ ”). The former sees the BH behind the source, while the latter sees the opposite. The corresponding redshift distributions are shown in Fig. 5.4 for observers at $r_o = 100M$. At early times, “ $\varphi = 0$ ” observers see only radially-outward particles, with maximum redshift. At late times, particles with near-critical impact parameter circle the BH and return to reach this observer, with maximum blueshift. Recall that the source starts infalling at $r_i \sim 30M$. The first blueshifted particles should then arrive at a time $\Delta t_1 \sim T_{\text{LR}}/2 + 60M \sim 76M$ after the first outwards particles reach the observer, with $T_{\text{LR}}/2$ being the time it takes to circle the LR and come back in the opposite direction. On the other hand, an observer on the opposite side of the BH would see the first null particles to be always blueshifted, since the observer sees an approaching source, a time $\Delta t_2 \sim 60M$ after the first signal arrives at the $\varphi = 0$ observer. These estimates do not take into account Shapiro time delay, but the estimate $\Delta t_1 - \Delta t_2 \sim T_{\text{LR}}/2 \sim 16M$ should be more reliable. All these features are apparent in Fig. 5.4.

The total luminosity is shown in Fig. 5.2 and follows the same trend. Note that due to the finite number of “photons” that we used in our numerical study, the total luminosity is not smooth. The jagged features carry no physical information and are purely a result of the numerical method used to estimate the luminosity. We opted to “bin” 20 particles at a time, and we have explicitly checked that larger binnings produce smoother luminosity functions, as it should. For realistic sources the true curve is single-valued and smooth. At late times our results are consistent with a decay controlled by LR $\mathcal{L} \sim e^{-t_o/(3\sqrt{3}M)}$ (recall the LR frequency in Eq. (5.12), which as we see below is generic for similar sources.

5.2.3 An isotropic body emitting scalar waves

With the geometric-optics limit in control, we generalize the problem by solving for the full dynamics of wave propagation. We first consider a toy-model where a source with *scalar* charge is emitting *scalar* waves. This problem can be modeled by the Klein-Gordon equation for a massless scalar field, which is the $s = 0$ case of the Teukolsky equation (2.49). For the source term, we take the trace T of the

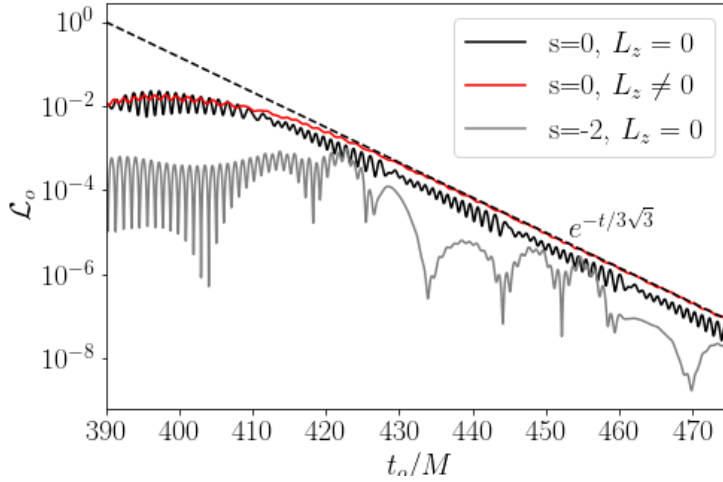


Figure 5.5: Total luminosity in scalar waves ($s = 0$) and GWs ($s = -2$) from a source plunging into a Schwarzschild BH, and emitting at fixed proper frequency $M\omega_e = 2.5$. The source is located on the equatorial plane at $\theta_e = \pi/2$ and starts from rest at $r_e(t = 0) = 35M$. We consider both a radial plunge ($L_e = 0$) and one with finite angular momentum ($L_e = 3.0M$). For both processes, the luminosity follows the exponential decay at late times dictated by the LR, $\mathcal{L}_o \sim e^{-t/(3\sqrt{3}M)}$, in accordance with the geometric optics limit for the isotropic star in Fig. 5.2. The different features between scalar and GWs are due to the source structure in both scenarios. The low frequency oscillations in the GW spectrum come from the plunge of the CM of the binary system. The high-frequency content of the signal for both scalar and GWs is dominated by frequencies around $M\omega_o \sim 3.0$, blueshifted with respect to ω_e by a factor ~ 1.2 , which is consistent with Fig. 5.3.

stress-energy tensor of a pointlike body of mass m_p (2.10) vibrating at constant proper frequency ω_e (and therefore emitting spherical waves in its rest frame) [338, 339]. This body couples to the scalar field through a scalar charge q

$$\square\Psi = qT \sin(\omega_e\tau_e(t)) , \quad (5.35)$$

which we can set to 1 in our analysis without loss of generality. Again, spherical symmetry allows us to restrict the motion of the point-particle to the equator. The emitter can have non-zero angular momentum L_e , so its EOM are

$$\frac{dr_e}{dt} = -\sqrt{E_e^2 - \left(1 - \frac{2M}{r_e}\right) \left(1 + \frac{L_e^2}{r_e^2}\right)} , \quad (5.36)$$

$$\frac{d\varphi_e}{dt} = \frac{L_e}{E_e} \frac{1 - 2M/r_e}{r_e^2} . \quad (5.37)$$

We solved this problem using the time-domain code described in Sec. 2.2.

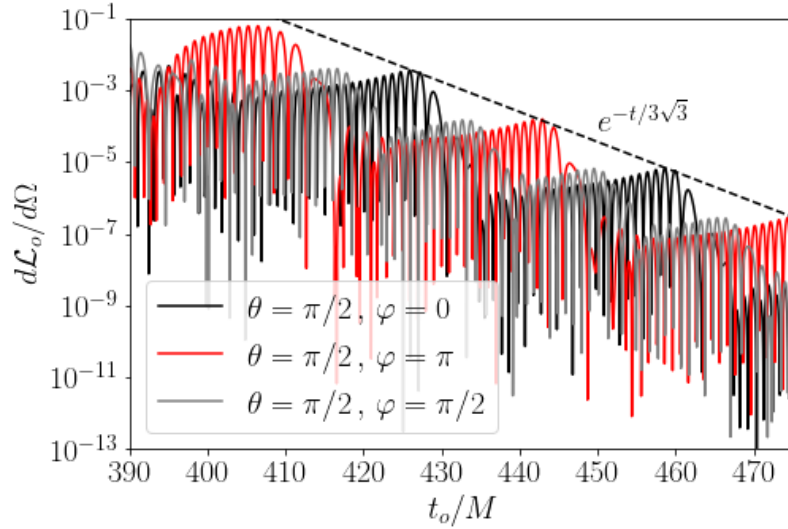


Figure 5.6: Energy flux for a scalar source plunging radially into a BH (from $r_e(t=0) = 35M$ as in Fig. 5.5), extracted at specific angular positions on the equator. All signals exhibit the same global exponential decay dictated by the LR as seen in Figs. 5.2 and Fig. 5.5. Stationary observers now see a periodic structure, whose period may differ for different observers (notice that at $\varphi = \pi/2$ the period is half that at $\varphi = 0, \pi$). Once again, the high frequency content of the spectrum corresponds to waves with $M\omega_o \sim 3.0$, in accordance with the blueshift predictions of Fig. 5.3.

In Fig. 5.5 we show the total luminosity for this system for a monochromatic source with $M\omega_e = 2.5$, with and without angular momentum. This flux of energy is computed through

$$\begin{aligned} \dot{E}^\infty = \mathcal{L}_o &= \lim_{r \rightarrow \infty} \int_{S_2} d\Omega \sqrt{-g} T_\Phi^{tr} = \\ &= \lim_{r \rightarrow \infty} \int_{S_2} d\Omega r^2 \sin \theta \partial_t \Phi \partial_r \Phi. \end{aligned} \quad (5.38)$$

Even though the source is now emitting radiation whose wavelength is comparable to the BH size, the late time behavior is still described by the exponential decay, $\mathcal{L}_o \propto e^{-t_o/(3\sqrt{3}M)}$, independently of whether the body falls with non-zero angular momentum or not.

The luminosity per solid angle at different angular positions is presented in Fig. 5.6. The global LR decay is the same but we notice the presence of additional structure. In particular, there are periodic oscillations whose period may differ for different observers. Their frequency is a multiple of half of the frequency of the LR $M\omega_{LR} \approx 0.192$ (corresponding to a period $T_{LR} \approx 32.6M$). Each of these LR pulsations is succeeded by a sharp, fast transition, lasting for $\sim 5M$, a behavior and timescale that we do not fully understand.

As we might have anticipated, the spectral content is dominated by blueshifted radiation emitted in the past with a near-critical angle, which is absorbed by the LR and re-emitted later. Referring to

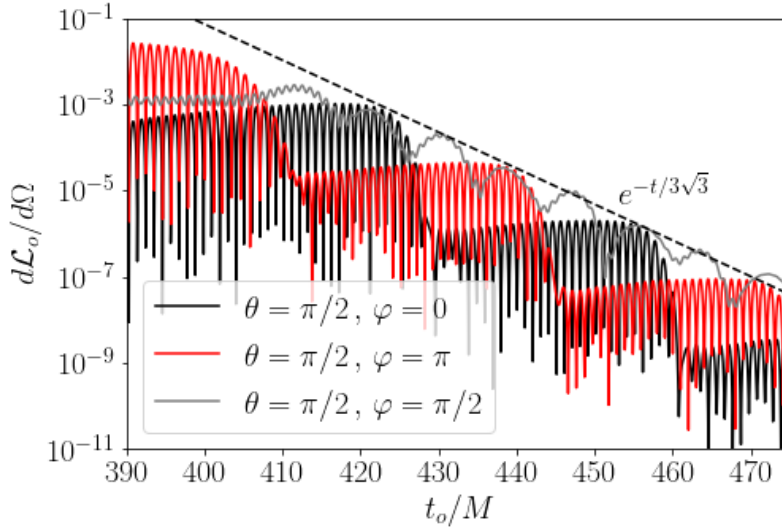


Figure 5.7: Same as Fig. 5.6, but for a source emitting high-frequency GWs. The source is a binary, and is plunging radially onto a massive BH, while emitting GWs of proper frequency $M\omega_e = 2.5$. The frequency of the signal measured by far away observers is blueshifted to $M\omega_o \sim 3$.

Fig. 5.3, such radiation is blueshifted to $\omega_o \sim 1.2 - 1.3\omega_e$, in this case corresponding to $M\omega_o \sim 3.0 - 3.1$ during most of the infall.

5.2.4 An infalling binary

The final system we will study is a possible astrophysical realization of the previous toy model. We consider a BHB whose CM is falling onto a massive BH. We consider that the binary is composed of two pointlike masses, which can be treated within linear perturbation theory on the background spacetime of the massive BH. This system constitutes a hierarchical triple system and it emits GWs which can be studied using the Teukolsky equation, where the source term is characterized by two pointlike particles.

To simplify the analysis, we assume the binary has a very eccentric orbit while its CM is radially plunging into the central BH

$$r^\pm = r_{\text{CM}}(t), \quad \theta^\pm = \theta_{\text{CM}}(t), \quad (5.39)$$

$$\varphi^\pm = \varphi_{\text{CM}} + \epsilon \sin(\omega_e \tau_e), \quad (5.40)$$

where \pm refers to the two bodies composing the binary and $\epsilon = \epsilon(r_{\text{CM}})$ defines the axis of the very eccentric ellipse followed by the binary

$$\epsilon = \left(1 - \frac{2M}{r_{\text{CM}}}\right) \frac{\delta r}{r_{\text{CM}}}, \quad (5.41)$$

where δr is the proper length of the binary axis around its CM. For the examples we will discuss, we fix $\delta r = 0.1M$, but our qualitative

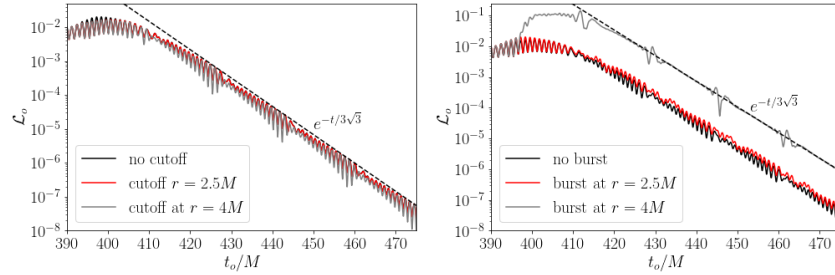


Figure 5.8: **Left panel:** Luminosity in scalar waves for the system studied in Section 5.2.3. Now, the source is turned off below a certain radius (which we selected to be either $r = 2.5M$ or $r = 4M$). When the source is turned off inside or close to the LR, the flux is nearly unchanged, as it is controlled by waves emitted in the past and lingering close to the photonsphere. **Right panel:** Luminosity for the scalar system studied in Section 5.2.3 but whose source is suddenly increased by a factor of 10 at the same radii as in the left panel. In flat spacetimes, this would correspond to a luminosity 100 times higher. However, since the process takes place close to the LR, the luminosity is very weakly affected and has the same global exponential decay. As expected, when the increase in amplitude occurs deep inside the light ring, the increase in the luminosity is less significant.

conclusions are independent of this value. The two point-particles enter as sources of the Teukolsky equation for $s = -2$ as described in Sec. 2.2.2.

The flux of energy carried by GWs to infinity (cf. Eq. (2.51)) is shown in Fig. 5.7 for different angular locations. Even though it is impossible to decouple the contribution of the motion of the CM from that of the binary itself, we see again the late time exponential decay $d\mathcal{L}_o/d\Omega \sim e^{-t/(3\sqrt{3}M)}$.

The peculiar nature of gravity is manifest in the low-frequency components in Fig. 5.7. They are contributions to the flux due to the motion of the CM, which modulates the high-frequency components of the signal emitted by the small binary. As a consequence, for certain directions, such as $\theta = \pi/2$, $\varphi = 0, \pi$, the high-frequency content dominates the spectrum, whereas for others the signal is controlled by the lower frequencies from the plunge of the CM.

5.3 TESTING HORIZONS

Our results strengthen the point of view that LRs control how dynamical processes look to outside observers, while horizons play a secondary role on this. We can test this further by studying how our results change when the near-horizon physics of the compact object is altered, or when we change the properties of the source close to or within the LR. We have tested this with two different processes:

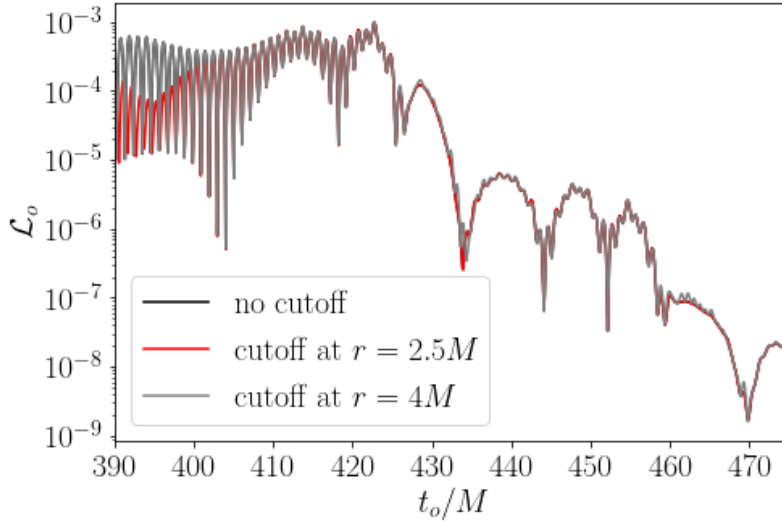


Figure 5.9: Luminosity in GWs from the system described in Section 5.2.4, for which the binary is shut off below a certain radius, signaling for example a sudden merger of the binary. In line with the findings for scalar waves in Fig. 5.8, near-horizon details are irrelevant for the appearance of these objects, and it is the LR that controls the late time signal.

- First, we turn off the source after it reaches a selected radius (e.g. $r = 4M, 2.5M$). This could represent a merging binary before its CM plunges on the BH. Our results are summarized in Figs. 5.8-5.9. For both types of waves, the spectrum is mostly independent of the cutoff radius if this is located close or inside the LR. The late-time decay is still given by the exponential law we observed previously, which reinforces the interpretation that it really describes waves trapped close to the LR (which accumulated during the infall), and are slowly leaking out to infinity (and the horizon). This result also indicates that two different compact objects with similar LR structures may be hard to distinguish based on observations of matter surrounding it, whether they possess a horizon or not.
- In the second case the source becomes suddenly brighter, increasing its proper luminosity after it falls within some radius. In Fig. 5.8 we show results when the proper luminosity is increased by a factor of 100. As before, the late-time behavior decay is unaltered and the change in the luminosity measured by far-away observers is small when the burst occurs inside the LR.

The punchline is *What happens inside the light ring stays inside the light ring*, or more seriously, near horizon details are mostly irrelevant for how matter accreted onto a BH appears to distant observers.

5.4 DISCUSSION

In this chapter, we showcased how the properties of LRs control the appearance and late-time dynamics of BHs and other compact objects [231, 290–295, 328, 335, 336, 340–343]. The LR can be seen as a region where high frequency waves are trapped on timescales $\sim 3\sqrt{3}M$ or more [231]. A GW or bright electromagnetic source falling onto a BH will “heat up” this cavity as it falls. As the source enters the photonsphere, the transfer of energy from the source to the LR is maximum. From then onwards, the source gets progressively redshifted away, and the energy leaking from the LR dominates emission. Thus, observers see a late-time appearance of infalling stars dominated by the LR cooling down process: the signal has a spectral content dominated by frequencies slightly blueshifted with respect to the proper frequency of the source, and a luminosity dying off as $\mathcal{L} \sim e^{-t/(3\sqrt{3}M)}$.

This behavior is best understood within a null-particle approach. Literature on waves around BHs usually discusses, instead, a mode analysis where the late-time behavior is dominated by QNM ringdown and power-law tails from the backscattering of radiation from curvature [188, 300]. GWs are emitted by coherent motion of sources, and usually excite only a few modes. For high-frequency sources, however, a large number of multipoles are excited. The quasinormal frequencies at large mode number ℓ , are described by Eq. (5.19) [188], and the ringdown amplitude is given by Eq. (5.1). If we plug the asymptotic expression above in this sum over all the multipoles, we obtain a ringdown stage with a global modulation given by $\Phi \propto e^{-\Omega_{\text{LR}} t/2}$, which in the Schwarzschild case corresponds exactly to the decay in luminosity we observed ($\mathcal{L} \propto |\Phi|^2$). In other words, both results (geometric optics and wave propagation) are compatible. Finally, late-time polynomial tails are extremely challenging to observe in the presence of these sources, as their amplitude is expected to be many orders of magnitude below the ringdown signal [344]. Consequently, they should only appear at later timescales than the ones we probed and for this reason are not expected to be astrophysically relevant.

The decay timescale is controlled by the LR, whose properties depend on the BH spin. We studied only non-spinning BHs, but geometric-optics approximation can be used to predict that rapidly spinning BHs will show a much larger relaxation timescale, and a breaking of degeneracy with respect to different angular directions [328, 340]. This raises the interesting possibility of determining the BH spin from the ratio of amplitudes of different redshifts.

Dying pulses from BH accretion were discussed in the context of Cygnus X-1, years ago [332, 333]. These works assume that light from such pulses mimics the motion of the source, which as we discussed is not correct. It is challenging to explain such observations through LR properties, since timescales seem to be off by almost an order of

magnitude. Nevertheless, these observations show how LR relaxation could show up in observations with enough precision. This is relevant for BH imaging [45, 46, 294, 345], in particular for the next generation Event Horizon Telescope [346, 347]. This collaboration plans to add 10 new observation points to the current Event Horizon Telescope, which will increase the precision of current images and open the possibility of producing movies monitoring the evolution of matter being accreted by BHs, which could be compared with our general results for the luminosity decay.

 THE ELEPHANT THE FLEA

In the previous chapter, we discussed [BH](#) spectroscopy, the research program that aims to measure the characteristic frequencies of the late-time ringdown of a binary coalescence, where the waveform is described by a superposition of exponentially damped sinusoids, and compare them with the theoretically predicted [QNM](#) frequencies of [BHs](#) in [GR](#). However, for this comparison to make sense, the [QNM](#) spectrum should be stable, meaning that the [QNM](#) frequencies should not be very sensitive to possible perturbations in the spacetime. Otherwise, small environmental perturbations could produce large deviations in the [QNM](#) spectrum and hide hypothetical signatures of new physics.

It turns out this is exactly the case! Recent computations of the pseudospectrum ¹ in [GR](#) confirm that the [QNM](#) spectrum is unstable under small perturbations [[349–351](#)] (see also [[352](#)] for a preliminary suggestion of this result). For example, the fundamental [QNM](#) of Schwarzschild, which dominates the ringdown, can have order $\mathcal{O}(1)$ corrections if a “tiny” perturbation is added to the gravitational potential (see Fig. 1 and 2 in Ref. [[353](#)]).

However, the instability has been demonstrated in the frequency domain. This only describes the late-time behavior of a binary coalescence. Although results in the frequency domain should translate to the time domain by a Fourier transformation, in practice, this could be challenging to achieve in an experiment, as one would need to observe the [GW](#) signal for very long times and with precision above what is achievable.

This is what happens for horizonless exotic (ultra)compact objects ([ECO](#)) [[231](#)]. To recall, these are [BH](#) mimickers where the [BH](#) horizon is substituted by reflecting surfaces, and the exterior geometry and dynamics are usually left unchanged. This leads to a [QNM](#) spectrum very distinct from that of a [BH](#). In particular, [ECOs](#) develop cavity modes that are trapped between the [LR](#) and their surface/interior, which decay much slower than the fundamental [QNM](#) of Schwarzschild. However, by causality, the time-domain response of a [BH](#) and an [ECO](#)

¹ The pseudospectrum of an operator are the level sets of numbers that are “close” to the eigenvalues of the operator, where the meaning of close can be put more formally. This notion is particularly useful to study non-self-adjoint operators, as those arising in [BH](#) spacetimes, where the eigenvectors are not complete and orthogonal [[348](#)].

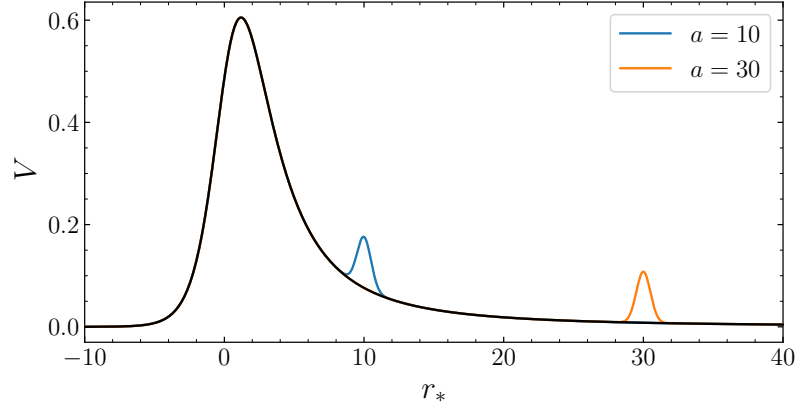


Figure 6.1: The unperturbed ($\epsilon = 0$) and perturbed potentials used in this study. The Regge-Wheeler potential with $\ell = 2$ is shown in black, while two perturbative bumps ϵV_{bump} , with $\epsilon = 0.1$, are shown in blue ($a = 10$) and orange ($a = 30$). The unperturbed potential has a peak close to the LR.

is the same for the time necessary for a perturbation to travel to the surface of the ECO, which should be close to the BH horizon limit, and then be reflected back [341, 354, 355]. The prompt ringdown is instead controlled by the LR (5.19), in line with our results from the previous chapter.

In this chapter, we are thus interested in understanding how the QNM spectrum instability manifests itself in GW observations, and if it jeopardizes the BH spectroscopy program.

6.1 PERTURBATIONS OF THE POTENTIAL

In order to do that, we will study a modified version of the equations that govern (linear) gravitational perturbations around nonrotating BHs in GR, which were introduced in Sec. 2.1.3 [185, 187]. There, we saw they have the general homogeneous form

$$-\frac{\partial^2 \Psi}{\partial t^2} + \frac{\partial^2 \Psi}{\partial r_*^2} - V \Psi = 0, \quad (6.1)$$

where Ψ is the complex “master” function. $V = V(r)$ is the perturbed effective gravitational potential

$$V = V_0 + \epsilon V_{\text{bump}}. \quad (6.2)$$

V_0 denotes the unperturbed potential of a Schwarzschild BH, and ϵV_{bump} , with $\epsilon \ll 1$, represents a small perturbation or “bump” to it. These perturbations can arise in different physical scenarios, such as modifications to GR [356, 357], environmental matter [80, 248, 358, 359], and non-linearities [325, 360–367]. For concreteness, we will mostly focus on the Regge-Wheeler case with $\ell = 2$. Also, in this chapter, we

will exceptionally work in units where $M = 1/2$, to be consistent with the work of Ref. [353] on this problem.

Following Ref. [353], we assume that the bump is localized around some radius $r_* = a$ and that it goes to zero faster than V_0 as $r_* \rightarrow \infty$. We will study a Gaussian bump of the form

$$V_{\text{bump}} = \exp \left[-\frac{(r_* - a)^2}{2\sigma^2} \right]. \quad (6.3)$$

The specific form of the bump in Eq. (6.3) is chosen as an illustrative example. However, we have considered other perturbations, such as: 1. a bump which is concave rather than convex, corresponding to negative ϵ ; 2. a bump which decays as r^{-3} at large distances and which is exactly zero for small r , mimicking a perturbation due to a thin shell of matter. The qualitative behavior of the time-domain signal is the same in all these different cases, so we will not report all the results here. In fact, the only relevant aspect of the perturbation is that it introduces a second small peak. When this is not the case, e.g., when a is very small, the instability is not present [353]. Note also that the isospectrality of the Zerilli and Regge-Wheeler potentials is broken even if we use the *same* perturbative bump in both equations [356, 357], though in realistic astrophysical scenarios the odd- and even-parity perturbative ‘‘bumps’’ are not expected to be the same.

To solve the perturbed Regge-Wheeler equation, we again use the numerical framework introduced in Sec. (2.2). We prescribe as initial data for the perturbation, a Gaussian pulse of the form

$$\Psi \Big|_{t=0} = 0 \quad , \quad \frac{\partial \Psi}{\partial t} \Big|_{t=0} = e^{-(r_*-5)^2/2}, \quad (6.4)$$

but our qualitative conclusions are independent of this choice.

We also want to extract the spectrum at late times, when the time-domain signal is decaying as a linear combination of exponentially damped sinusoids. Their frequencies and damping times can be extracted by fitting the waveform with the N -mode template ²

$$\Psi(t) = \text{Re} \sum_{n=0}^{N-1} A_n e^{-i(\omega_n t - \phi_n)} \quad (6.5)$$

$$= \sum_{n=0}^{N-1} A_n e^{\omega_{nI} t} \cos(\omega_{nR} t - \phi_n), \quad (6.6)$$

where the index n labels the different modes we find by fitting, and it does not necessarily coincide with the overtone number. Each mode is characterized by four parameters: an amplitude A_n , a phase ϕ_n , and the real and imaginary parts of the QNM frequency $\omega_n = \omega_{nR} + i\omega_{nI}$. We will find that several QNMs could have similar decay times, and

² The fitting procedure and frequency-domain analysis was conducted by Mark Ho-Yeuk Cheung.

hence comparable amplitudes. In this situation, a good fit of the waveform requires a relatively large number of modes N . The largest number of modes we will look for is $N = 8$, corresponding to $8 \times 4 = 32$ fitting parameters.

The eigenfrequencies ω_n of Eq. (6.5) can also be computed directly from Eq. (6.1) with a Laplace transform

$$\frac{\partial^2 \Psi}{\partial r_*^2} + (\omega^2 - V) \Psi = 0. \quad (6.7)$$

The QNM frequencies ω_n correspond to the poles of the Green's function of Eq. (6.7) with boundary conditions of ingoing waves at $r_* = -\infty$ (the BH horizon), and outgoing waves at $r_* = +\infty$ (far-away distances). The frequencies can be found by a shooting method [296]: starting from each of the two boundaries and numerically integrate inwards or outwards iteratively searching for the values of ω for which the two solutions match smoothly in an intermediate region.

We have performed this direct-integration analysis using a modification of the *Mathematica* notebook used in Ref. [368] and available online [369].

6.2 STABILITY OF THE WAVEFORM

We will say that “destabilization” occurs when a quantity that characterizes the BH's response (e.g. the QNM frequency or the waveform amplitude) changes by an amount much larger than the magnitude of the perturbation. We will now show that while the fundamental QNM mode of Schwarzschild is spectrally unstable, in accordance to Ref. [353], the change in the time-domain waveform amplitude is of the same order as the size of the perturbation. In this sense, the time-domain waveform itself is stable under perturbations. Furthermore, the *observed* QNM frequency is also stable because the *early part* of the waveform is not significantly affected by the perturbation.

In Fig. 6.2, we show the waveform resulting from the scattering of Gaussian pulses for different locations a and magnitudes ϵ of the bump. t_{\max} is the time at which $|\Psi|$ reaches its maximum value, and we only show the signal afterward. In the “clean” Schwarzschild case ($\epsilon = 0$ in black), we observe the typical exponentially decaying ringdown followed by an expected power-law tail coming from the backscattering of radiation at large distances [300, 370]. As expected, the larger the ϵ , the larger the difference in the waveform with respect to Schwarzschild, even at early times. For times $t - t_{\max} \lesssim a$, the absolute difference of the waveform with respect to the unperturbed potential scales linearly with ϵ . The *prompt* ringdown signal close to the waveform peak is affected by environmental disturbances but not destabilized in the sense defined above. This is the portion of the ringdown with the most interest to GW astronomy, meaning such

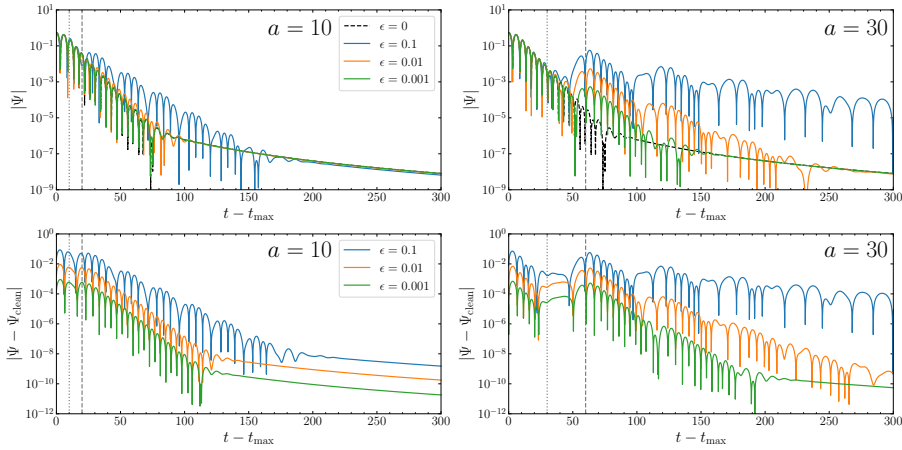


Figure 6.2: *Top panels*: absolute value of the waveform arising from the scattering of the Gaussian pulse of Eq. (6.4) for “bumps” with different amplitudes ϵ , located at two selected distances a from the main peak. The bump width σ in Eq. (6.3) is fixed at $\sigma = 0.5$. “Echoes” are apparent when the bumps are located at large distances ($a = 30$). The dotted and dashed vertical gray lines correspond to $t - t_{\max} = a$ and $2a$, and they illustrate how the delay between echoes is related to the size of the “cavity” between the two maxima in the perturbed potential. *Bottom panels*: absolute value of the difference between the waveforms shown in the top panels and the unperturbed clean waveform without a bump ($\epsilon = 0$).

differences are not expected to be observable with the SNRs achievable by today’s interferometers [80, 231].

After this initial regime, for $t_{\max} \gtrsim 2a$, we start to observe *echoes* of the original ringdown due to the leakage of waves being reflected between the peak of the potential and the bump. At late times, the bump can drastically modify the signal’s frequency content. At this stage, the waveform is well-described by a superposition of the long-lived QNMs of the perturbed potential, as illustrated in Fig. 6.3. For smaller ϵ , the late time power-law tail can hide the difference in the late-time behavior with respect to the unperturbed waveform.

In general, when we add a large bump in the potential, the QNMs have a longer damping time, and hence they survive longer before “diving below the tail”. When the bump is located far from the original potential peak, we first observe lower amplitude echoes of the original pulse, which eventually give way to a different ringdown signal. For large a , there is a clear separation of timescales between the ringdown pulse produced at the LR and the light travel time characterizing the “cavity” between the LR and the bump. Thus, we have a pulse bouncing back and forth within the cavity and gradually losing its high-frequency component, which tunnels out more easily. This produces a sequence of echoes repeating at a characteristic frequency defined by the cavity size and damped on a timescale defined by the

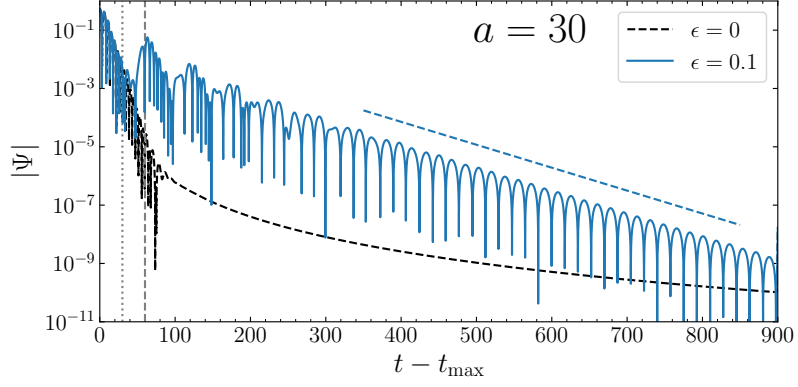


Figure 6.3: Waveform for $a = 30$ and $\epsilon = 0.1$ over long time windows, where the late-time behavior is dominated by the new fundamental mode QNM. The dashed blue line represents its expected decay, which corresponds to the bottom blue cross with smallest $|\omega_I|$ in the top panel of Fig. 6.6.

transmission coefficient of the small peak, as shown in Fig. 6.2 (see also Refs. [231, 341, 342, 371] for similar behavior when the bump is arbitrarily close to the horizon). These two scales determine the QNM spectrum of the bumpy potential, which can be nonperturbatively different from the $\epsilon = 0$ case. A simple rule of thumb for the echoes to be visible is that the prompt ringdown lifetime $\sim 9\sqrt{3}M$ (allowing for three e-folding times) should be smaller than the travel time within the cavity $\sim 2a$ [231, 371], and therefore we should require $a \gtrsim 4$ (in units where $M = 1/2$). Note that, however, the amplitude of the echoes and the induced QNM ringing is proportional to ϵ .

The prompt ringdown is excited mainly at the peak of the potential, which broadly coincides with location of the LR. If the bump is placed close to the peak, it will change its shape and consequently the frequency content of the prompt ringdown. When the bump is placed farther, the spectrum still changes because the QNMs are sensitive to the entire potential. However, the wave train excited at the LR should be similar to the one in the case of the unperturbed potential. As it meets the bump, part of it will be reflected and the other will tunnel out to far-away distances. The reflection coefficient is $\mathcal{O}(\epsilon)$ for any frequency, and consequently the change in the prompt ringdown also scales with this factor.

In the prompt ringdown, the relative difference in the waveform $|\Psi - \Psi_{\text{clean}}| / |\Psi|$ scales linearly with ϵ , while in the echo-dominated regime the difference is larger. The reason for this is the following: the original ringdown signal decays as $e^{-\omega_I t}$. Each reflection of the waves in the cavity reduces their order of magnitude by $\sim \epsilon$. On the other hand, each back-and-forth bounces inside the cavity occurs on timescales of $t_{\text{bounce}} \sim 2a$. This means the amplitude of the n -th echo will be larger than the ringdown by a factor of $(\epsilon/e^{-\omega_I t_{\text{bounce}}})^n$, or

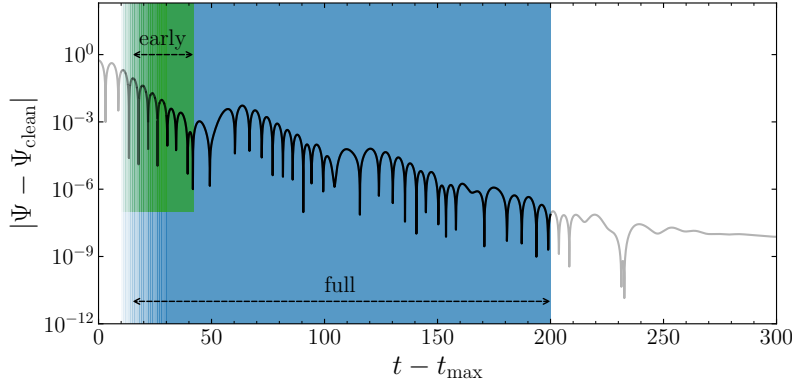


Figure 6.4: The portion of the waveform used for the damped-sinusoid fitting in the two different regimes of interest. For completeness, this waveform corresponds to the case $a = 30$, $\epsilon = 0.01$, but the same procedure applies to other examples.

$\epsilon^n e^{n2a|\omega_l|}$. When the power-law tail starts dominating, the modification returns to order ϵ because the tail can be formally seen as a “direct” zero-frequency signal.

6.3 EXTRACTION OF QNM FREQUENCIES

We now move to the core problem of BH spectroscopy, which is the comparison between the QNM frequency theoretically predicted and those extracted by fitting the waveform with damped sinusoids.

Regarding the fitting of time-domain waveforms, we wish to answer two separate questions:

1. How the spectral instability affects the prompt ringdown radiation emitted in binary coalescences, which is the louder portion of the signal and consequently more easily detectable by GW interferometers.
2. If the full waveform, in particular the late-time portion, is well described by the destabilized QNM spectrum, including the long-lived cavity trapped modes.

In Fig. 6.4 we highlight the portions of the signal used in the investigation of both problems. In all cases, we discard times $t - t_{\max} \lesssim 5$, where there is contamination from the direct signal coming from the initial data. For the full signal (shaded in blue), we also discard the portion of the waveform dominated by the power-law tail. For the prompt ringdown analysis (shaded in green), we only consider the portion of the signal before the appearance of the first echo ($t - t_{\max} \lesssim a$). In both cases the starting time of the fit is varied to ensure convergence of the frequencies obtained.

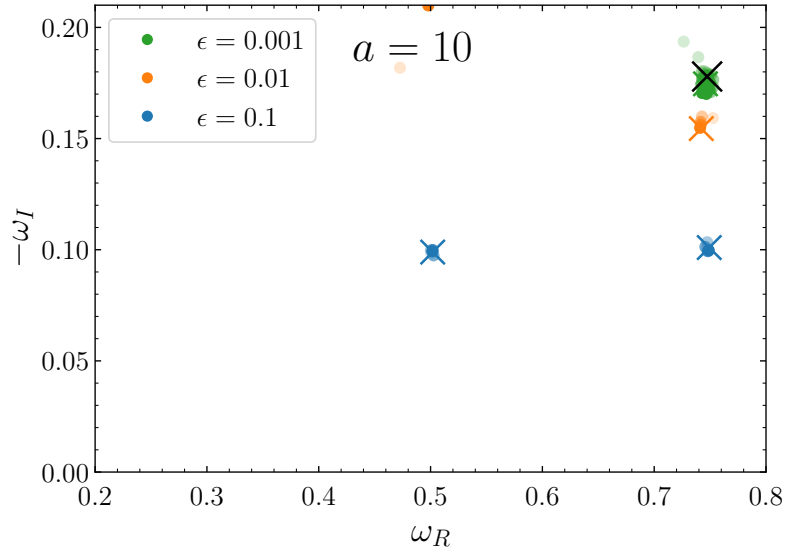


Figure 6.5: Comparison between the QNM frequencies computed with the shooting method in the frequency domain (crosses) and those extracted by fitting the full time domain waveform (dots). The black cross is the unperturbed clean fundamental QNM of Schwarzschild, with $M\omega = 0.374 - 0.089i$. The starting times used are $t - t_{\max} = 10, 15, 20, 25, 30M$.

6.3.1 The full time-domain signal

We start by addressing the second problem, where the full signal is used (shaded in blue in Fig. 6.4).

In Fig. 6.5, we present results for a bump located close to the peak of the unperturbed potential ($a = 10$) and in Fig. 6.6 another case where the bump is farther away ($a = 30$). The frequencies recovered from the fitting procedure using different starting times are shown as dots with different shades, where the darker the dot, the later the starting time. The crosses correspond to the QNM frequencies computed with the shooting method in the frequency domain, with the black cross representing the fundamental QNM of the unperturbed potential ($\epsilon = 0$). Finally, different colors refer to different values of ϵ used.

The fitted frequencies for the bump closer to the potential peak are in very good agreement with the ones predicted by the frequency-domain computations for all values of ϵ presented. The minor discrepancies can be attributed to numerical error and contamination by the initial data and the power-law tail.

For the further bump, the destabilization of the spectrum is more noticeable. Since in this case the new QNMs are longer lived, after one echo the waveform transitions to a combination of new QNMs from the cavity in the effective potential until their amplitude becomes so small that they are masked by the late-time power-law tail. For $\epsilon = 0.1$

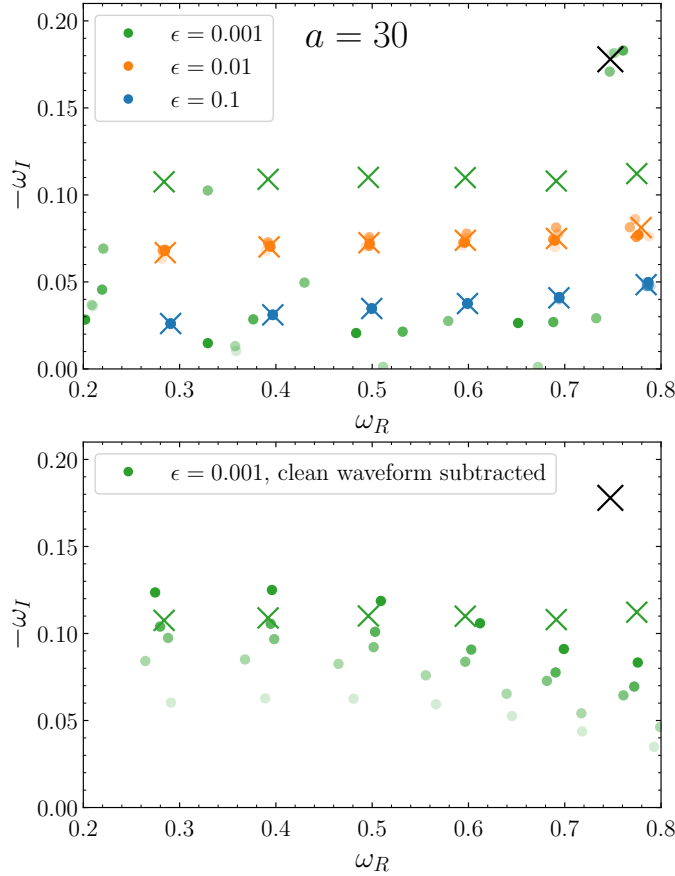


Figure 6.6: *Top panel*: same as in Fig. 6.5 but with $a = 30$. For $\epsilon = 0.001$, the full time-domain fits can only confidently detect a mode close to the fundamental mode of Schwarzschild, because the power-law tail dominates the signal before it transitions to the new set of QNMs. *Bottom panel*: The same analysis as in the *top panel* for $\epsilon = 0.001$ but subtracting the unperturbed clean waveform to the waveform before performing the fit. The frequencies extracted do not converge exactly to the QNMs, but the structure is more similar, in particular for the real part.

it can even transition to a clean exponential decay controlled by the new fundamental mode, as illustrated in Fig. 6.3. Because of this, we are able to extract multiple slowly decaying modes from the fit as long as $\epsilon \gtrsim 0.01$.

The time-domain fit is more difficult when $\epsilon \lesssim 0.001$. Our fits can only confidently detect a mode close to the clean fundamental mode of the unperturbed potential, because the QNMs have a very short decay time for such small ϵ , and the waveform does not have time to transition to the “new” trapped QNM spectrum before decaying below the power-law tail. Therefore, the fitting algorithm can only pick up the clean mode, which is excited promptly at the LR and therefore observable at early times. To remove the contribution of the tail, in the bottom panel of Fig. 6.6 we subtract the clean ($\epsilon = 0$) waveform from

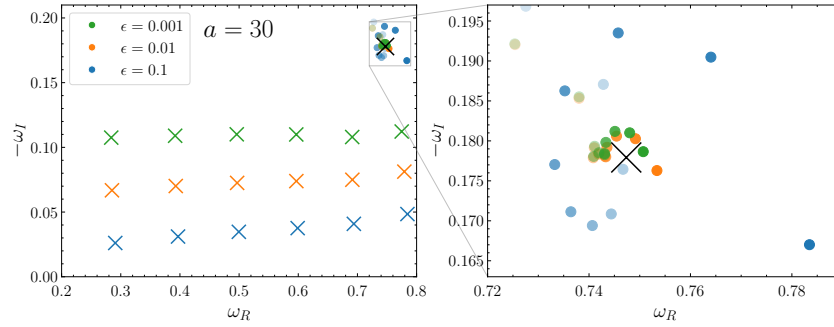


Figure 6.7: Same as Fig. 6.6, but we only fit the first train of the initial ringdown without echoes. The starting times are $t - t_{\max} = 10, 11, 12, \dots, 20M$. All the dots obtained using the fitting method now cluster around the clean fundamental mode of the unperturbed potential. The zoom-in in the right panel shows that a perturbation of order ϵ can induce systematic errors (approximately of order ϵ) in the measurement of the fundamental mode's frequency and damping time.

the signal and repeat the fit using the green curve in the bottom-right panel of Fig. 6.2, which as we can see contains more QNM oscillation periods that were previously hidden below the late-time power-law tail. The fitted modes do not converge as in the cases with $\epsilon \geq 0.01$, but their general structure is now in good agreement with the trapped QNM spectrum computed in the frequency domain.

6.3.2 The prompt ringdown

As mentioned before, in a real detector we do not have access to the full signal due to noise. Also, for astrophysical systems, the perturbation bump should be rather small. The presence of matter typically introduces corrections on the potential of amplitude $\epsilon V_{\text{bump}} \sim \rho$, where ρ is the matter density [176, 301, 353]. In units of the BH mass

$$\rho M^2 = 1.6 \times 10^{-18} \frac{\rho}{\rho_{\text{water}}} \frac{M^2}{M_{\odot}^2}, \quad (6.8)$$

so ϵ will be very small for most realistic scenarios. Consequently, with current SNRs we should only have access to the prompt ringdown.

Considering this, in Fig. 6.7 we repeated the analysis of the previous section but restricting it to *prompt* ringdown, i.e. the portion of the signal before the appearance of the first echo ($t - t_{\max} \lesssim a$, shaded in green in Fig. 6.4). We find it is well fitted by a *single* mode, whose frequency appears to converge to the frequency of the unperturbed fundamental QNM, instead of the rich QNM spectrum recovered using the full signal. We then conclude that as the waveform itself, the *observed* QNM frequency associated with the prompt ringdown is not destabilized.

6.4 DISCUSSION

In this chapter, we studied how the QNM spectral instability manifests in time-domain waveforms. Formally, our analysis should be equivalent to frequency-domain results if we could observe the full GW signal, which in practice is not achievable due to noise. We concluded that it is necessary to include the late-time portion of the signal in the fitting procedure to recover the “correct” destabilized QNM spectrum predicted in the frequency domain. Even that might not be sufficient if the power-law tail dominates over the amplitude of the perturbations at late times. Thus, all calculations of QNM frequencies using modified potentials or modified boundary conditions should be complemented by time-domain studies to verify that these modifications affect the prompt ringdown. In the problem we studied, if we only analyze this early part of the signal, which is the portion relevant for GW astronomy, we instead detect the fundamental QNM with corrections of the same order as those introduced in the potential. Therefore, even though the QNM spectrum of BHs is unstable, the BH spectroscopy program is not compromised. Nonetheless, an immediate question that arises is what is the needed SNR to observe structure beyond the prompt ringdown. In principle, this can be computed using specific astrophysical models, such as the one studied in Chapter 9 for a BH immersed in a galactic DM halo. We leave this exploration for future work.

In addition to that, it is important to note that we restricted the analysis to the spectral instability of the *fundamental* QNM. Overtone destabilization tends to be more dramatic for the type of short-wavelength perturbations used in our study [350], and these modes affect the signal at early times. Yet, the extraction of overtones from waveforms is highly nontrivial, even at the linear level, and is a subject of current research and debate [307, 324, 372]. Any future investigation of the impact of overtone spectral instability in GW signals needs to be complemented by a better understanding of how to fit them accurately.

RESONANCES IN BLACK HOLE MIMICKERS

In our previous discussions, we have been assuming that very compact dark objects are **BHs** described by **GR**. However, we have already seen how the absence a horizon can dramatically change the dynamics of compact objects. Horizonless exotic compact objects (**ECOs**) have a **QNM** spectrum very different from that of **BHs**. Even though the prompt ringdown should be the same, these **BH** mimickers exhibit late-time echoes in the ringdown similar to the ones we observed in the previous chapter [231, 308, 341, 342, 373–375]. Echoes of **ECOs** have already been searched in **GW** data with conflicting conclusions [17, 308, 376–380]. In Chapter 3 we also mentioned that **ECOs** have nonzero **TLNs**, while **BHs** in **GR** have vanishing **TLNs**. Finally, since they lack a horizon, **ECOs** absorb radiation very differently from **BHs**, which could impact the inspiral of a binary [218, 381].

Additionally, it has been observed that massive bodies on stable orbits around **ECOs** could resonantly excite the small-frequency, long-lived **QNMs** that characterize them [382–387]. This cannot occur in **BHs** because their proper modes are localized close to the **LR**, and their frequency is always greater than that of stable orbits.

However, previous analyses of detectability of resonance-crossing in **BH** mimickers were conducted in the frequency domain [382–386], assuming that the field is stationary and superposing an adiabatic evolution to evolve the binary, as driven by **GW** emission. However, as we have seen in the previous chapter, the frequency and time domain results only coincide when the physical process occurs for an “infinite” time. Here, infinite refers to a time much longer than the relevant timescales of the problem. For the resonant excitation of **ECOs** in a binary, the time it takes for the resonance to develop compete with the inspiral timescale. The resonance does not have time to grow if the latter is much shorter than the former .

In this chapter, we will complement the previous studies on inspirals around **BH** mimickers but with a time domain analysis using our numerical framework.

7.1 TOY MODEL: A CONSTANT-DENSITY STAR

For the background spacetime of our BH mimicker we use constant-density stars. They are spherically symmetric and, therefore, their interior is described by the line element in Eq. (2.16). The metric functions [388] are

$$A = \left(\frac{3}{2} \left(1 - \frac{2M}{R} \right)^{1/2} - \frac{1}{2} \left(1 - \frac{2Mr^2}{R^3} \right)^{1/2} \right)^2, \quad (7.1)$$

$$B = 1 - \frac{8\pi\rho}{3}r^2, \quad (7.2)$$

where R is the star's radius, M is its mass, and $\rho = 3M/(4\pi R^3)$ is its density. Outside the star, Birkhoff's theorem asserts that the geometry is Schwarzschild, described by the line element in Eq. (2.14).

The geometry above only describes "realistic" stars when $R > 9M/4$. Otherwise, the pressure diverges somewhere inside the star. Above some compactness, the geometry admits two LRs at the roots of $2A = rA'$ [328]¹. When $R < 3M$, they are located at

$$r_{\text{LR}}^+ = 3M, \quad (7.3)$$

$$r_{\text{LR}}^- = \frac{R\sqrt{4R^2 - 9MR}}{\sqrt{9MR - 18M^2}}, \quad (7.4)$$

where r_{LR}^+ coincides with the unstable LR in Schwarzschild, and the second solution corresponds to a stable LR located inside the star.

We can also compute the transit time between the unstable LR and the center of the star, which dictates the period of trapped oscillations, and thus of the ensuing echoes in the waveform [231, 341, 342]. It turns out that this time, T_{echo} , is also approximately $T_{\text{echo}} \approx 2\pi/\Omega_{\text{LR}}^+$, although this may be a fortuitous aspect of very compact constant density stars [389].

For definiteness, we will primarily focus on a configuration with $R = 2.26M$ and compare it with less compact geometries. This choice is close to the maximum possible compactness for this equation of state (the so-called Buchdahl limit), and the spacetime has two photonspheres, sufficiently compact to mimic some aspects of BHs.

We will perturb the constant density star with the toy model already used in Chapter 5.2.3, the massless scalar field being sourced by the trace of a point-particle coupled to the scalar field.

7.2 THE BUILD-UP TIME OF BLACK HOLE MIMICKERS

7.2.1 A scattering approach

An object sufficiently compact as to develop photonspheres is expected to behave as a cavity [231, 341, 342, 371, 390, 391], in the sense that

¹ If needed revisit the discussion on Sec. 5.1 where we discussed null circular orbits

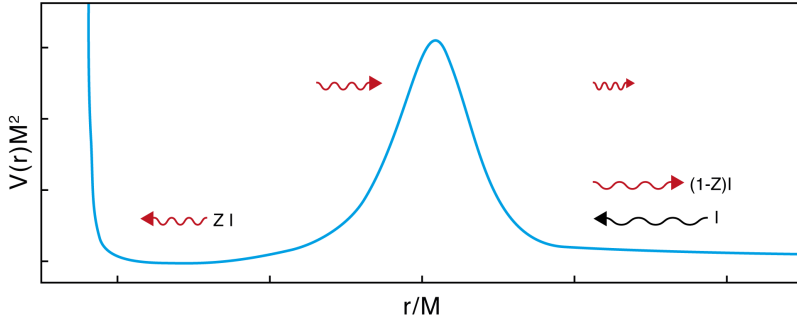


Figure 7.1: Effective potential governing massless fields on a horizonless ultracompact spacetime. The peak of the potential is close to the location of the unstable LR, and the potential in its vicinities is indistinguishable from that of a BH spacetime (compare with the black curve in Fig. 6.1). The centrifugal barrier in the object’s interior produces an effective cavity in spacetime, from which waves can slowly tunnel out. As discussed below, a cavity illuminated from the exterior “heats-up”, akin to a greenhouse effect.

radiation is trapped in its interior, bouncing back and forth between its center (or surface) and the unstable photonsphere. Massless fields are subject to an effective potential with two “barriers”, as illustrated in Fig. 7.1, in contrast with BHs where the potential still has the peak near the LR but asymptotes to zero in both boundaries.

Now let us consider the following *gedankenexperiment*: we bombard a cavity with a constant flux of radiation \mathcal{I} from a spin- s wave carrying angular mode ℓ . This flux may correspond to radiation emitted directed toward the central object by the secondary body in orbit. When the wave meets the barrier, a small fraction Z tunnels in, and another part is reflected back. Conservation of energy implies that the reflected flux is $(1 - Z)\mathcal{I}$, where the absorption coefficient Z is frequency-dependent ($Z = Z(\omega)$).

The transmitted part will then meet the interior barrier and be reflected. For simplicity, consider this interior is a reflecting mirror, so reflection is total (there is no absorption). After a roundtrip time within the cavity, T_{echo} , radiation will now be impinging the outside barrier from within. Again, a fraction Z of this incident radiation tunnels out, corresponding to $Z^2\mathcal{I}$ of the initial one. This outgoing re-transmitted fraction of radiation will add up to the flux of outgoing radiation that is directly emitted to far-away distances.

The reflection/outward transmission keeps happening inside the cavity. After N reflections (or a time interval NT_{echo}), the outgoing flux of radiation is

$$\mathcal{F}_{NT_{\text{echo}}} = (1 - Z)\mathcal{I} + Z^2\mathcal{I} \sum_{j=0}^{N-1} (1 - Z)^j = \mathcal{I} - \mathcal{I}Z(1 - Z)^{N+1}. \quad (7.5)$$

This tells us that the flux at large distances should be increasing in time steps of T_{echo} and relaxing to the final state on a timescale

$$\tau_{\text{relax}} = \frac{T_{\text{echo}}}{Z}. \quad (7.6)$$

The final state is that of an outgoing flux \mathcal{I} , as it should be since the object is not absorbing.

The absorption factors can be computed analytically in the low-frequency limit [103, 392, 393] from solving the Teukolsky equation (2.49)

$$Z_{s\ell m} = C \left[\frac{(\ell-s)!(\ell+s)!}{(\ell!)^2} \right]^2, \quad (7.7)$$

$$C = 4(2M\omega)^{2\ell+2} \left[\frac{(\ell!)^2}{(2\ell)!(2\ell+1)!!} \right]^2 \prod_{k=1}^{\ell} \left[1 + \frac{16M^2\omega^2}{k^2} \right]. \quad (7.8)$$

For example, for small frequencies where we can ignore the terms involving $16M^2\omega^2/k^2$

$$Z_{010} = \frac{16M^4\omega^4}{9}, \quad Z_{020} = \frac{64M^6\omega^6}{2025}, \quad Z_{220} = \frac{256M^6\omega^6}{225}.$$

For binary systems, $M\omega \sim 10^{-2} - 10^{-1}$, so we conclude that the build-up time can be very large. This puts in question the assumption of stationarity for the evolution of astrophysical binaries. As a side note, this calculation is very similar to how the greenhouse effect for planet Earth is estimated in a naïve approach.

The timescale in Eq. (7.6) is the time the system needs to “settle”. We will see below that this also corresponds to the resonant timescale, which is implied through the QNMs.

7.2.2 Resonances and forced oscillators

Before diving into our results, it is pedagogical to recall the results of a simple forced system with resonances, the driven harmonic oscillator [394]

$$\frac{d^2\Psi}{dt^2} + \Gamma \frac{d\Psi}{dt} + \omega_0^2\Psi = F_0 \cos \omega t, \quad (7.9)$$

with F_0 being a generic force per unit mass, ω_0 the natural frequency of the system and Γ a dissipation coefficient. The solution that starts off at $\Psi(t=0) = \partial_t\Psi(t=0) = 0$ is

$$\begin{aligned} \Psi(t) &= F_0 \frac{(\omega_0^2 - \omega^2)}{(\omega_0^2 - \omega^2)^2 + \Gamma^2\omega^2} \left(\cos \omega t - e^{-\Gamma t/2} \cos \omega_{\Gamma} t \right) \\ &+ F_0 \frac{\Gamma\omega}{(\omega_0^2 - \omega^2)^2 + \Gamma^2\omega^2} \left(\sin \omega t - e^{-\Gamma t/2} \sin \omega_{\Gamma} t \right), \end{aligned} \quad (7.10)$$

where $\omega_\Gamma = \sqrt{\omega_0^2 - \Gamma^2/4}$. When $\Gamma t \ll 1$ and for small damping $\Gamma \ll \omega_0$, Ψ grows on a timescale

$$\tau_{\text{DHO}} \approx \frac{2\pi}{\omega - \omega_0}. \quad (7.11)$$

This is valid for short timescales and off the resonance. On resonance, i.e. $\omega = \omega_0$, the field attains a maximum on a timescale of $\tau \sim 1/\Gamma$. Γ is intrinsic to the resonating system and corresponds roughly to ω_Γ , so as we suggested above, for compact horizonless objects one should identify $1/\Gamma$ with the relaxation timescale in Eq. (7.6).

7.3 NUMERICAL RESULTS

7.3.1 A point particle orbiting a compact object

$M\omega_{\text{QNM}}$	r_p/M	
	$a = 0M$	$a = 0.9M$
$0.0881 - i1.197 \times 10^{-7}$	5.051	4.780
$0.1259 - i2.687 \times 10^{-6}$	3.981	3.674
$0.1633 - i2.470 \times 10^{-5}$	3.347	3.011

Table 7.1: The lowest $\ell = 1$ scalar quasinormal frequencies of a uniform-density relativistic star with $R = 2.26M$. We also show the corresponding orbital radius at which the mode would be excited, calculated by equating the orbital frequency Ω in Eq. (7.13) to the real part of the QNM frequency and solving for r_p . The value of a corresponds to the used in the expression for the orbital frequency Ω (7.13). For less compact stars, resonant frequencies are impossible to excite with matter on circular orbits outside the object. For example, for $R = 6M$ the lowest dipolar QNM frequency is $M\omega = 0.262189 - i0.204880$.

We now place a pointlike particle of mass m_p in a circular orbit around a constant-density star,

$$r_p(t) = \text{const}, \quad \theta_p(t) = \frac{\pi}{2}, \quad \varphi_p(t) = \Omega t. \quad (7.12)$$

The Schwarzschild geometry admits stable timelike circular geodesics for radius larger than the ISCO at $r_{\text{ISCO}} = 6M$ [178] with $\Omega_{\text{ISCO}} = \sqrt{M/r_{\text{ISCO}}^3} \sim 0.068M$. While they can excite some proper modes of very compact constant-density stars (reference values are shown in Table 7.1), the timescales of these resonances are too large to be probed by our numerical setup in a reasonable time frame. The only possibility would be to consider unstable circular geodesics, which have larger frequencies and can excite modes that grow on smaller timescales.

However, since we eventually want to understand the impact of energy loss on the orbit, unstable motion is not the best option to study.

To circumvent this, we consider non-geodesic motion. To keep the analysis simple and satisfy the requirement that it excites resonant modes, we consider the orbital motion to be equivalent to that around a Kerr BH with mass M and spin a . While this is not geodesic motion, prescribing it allows us to numerically investigate resonances and resonance-crossing scenarios in feasible timescales with acceptable accuracy. The actual nature of the motion is not relevant for the excitation of the resonances. We therefore take [2]

$$\Omega = \frac{\sqrt{M}}{r_p^{3/2} + a\sqrt{M}}, \quad (7.13)$$

$$(7.14)$$

where $0 \leq a/M \leq 1$ should be seen as a free “knob” (which, were the central object a Kerr BH, would be the BH spin). The energy E and angular momentum L of these orbits is

$$\frac{E}{m_p} = \frac{r_p^{3/2} - 2Mr_p^{1/2} + a\sqrt{M}}{r_p^{3/4} \sqrt{r_p^{3/2} - 3Mr_p^{1/2} + 2a\sqrt{M}}}, \quad (7.15)$$

$$\frac{L}{m_p} = \frac{\sqrt{M} (r_p^2 - 2a\sqrt{M}r_p^{1/2} + a^2)}{r_p^{3/4} \sqrt{r_p^{3/2} - 3Mr_p^{1/2} + 2a\sqrt{M}}}. \quad (7.16)$$

We will also show in Appendix C that the timescale associated with the excitation of the resonance is independent of this choice, being completely controlled by the frequency of the circular orbit. Our imposition of this artificial motion is purely pragmatic, as this is a simple way to make circular orbits have higher frequency without changing the geometry of the central object.

To solve this problem in the time-domain, we again used the numerical framework presented in Sec. 2.2. The only difference is that we also solve the Klein-Gordon equation inside the star and impose regular boundary conditions for the scalar field at the center of the star. To compare both results, we also solved the problem in the frequency domain using standard Green function techniques [191, 395–397]. Similar techniques have been employed in the past for the problem of particle scattering by the constant density stars [398–401], where a transient excitation of QNMs can also be observed.

7.3.2 The build-up time

We consider $a = 0.9M$ in Eq. (7.13) because it is one of the smallest values for the spin that allow us to probe a fast-growing resonance while keeping the circular motion stable. Our time-domain numerical results are summarized in Figs. 7.2–7.3.

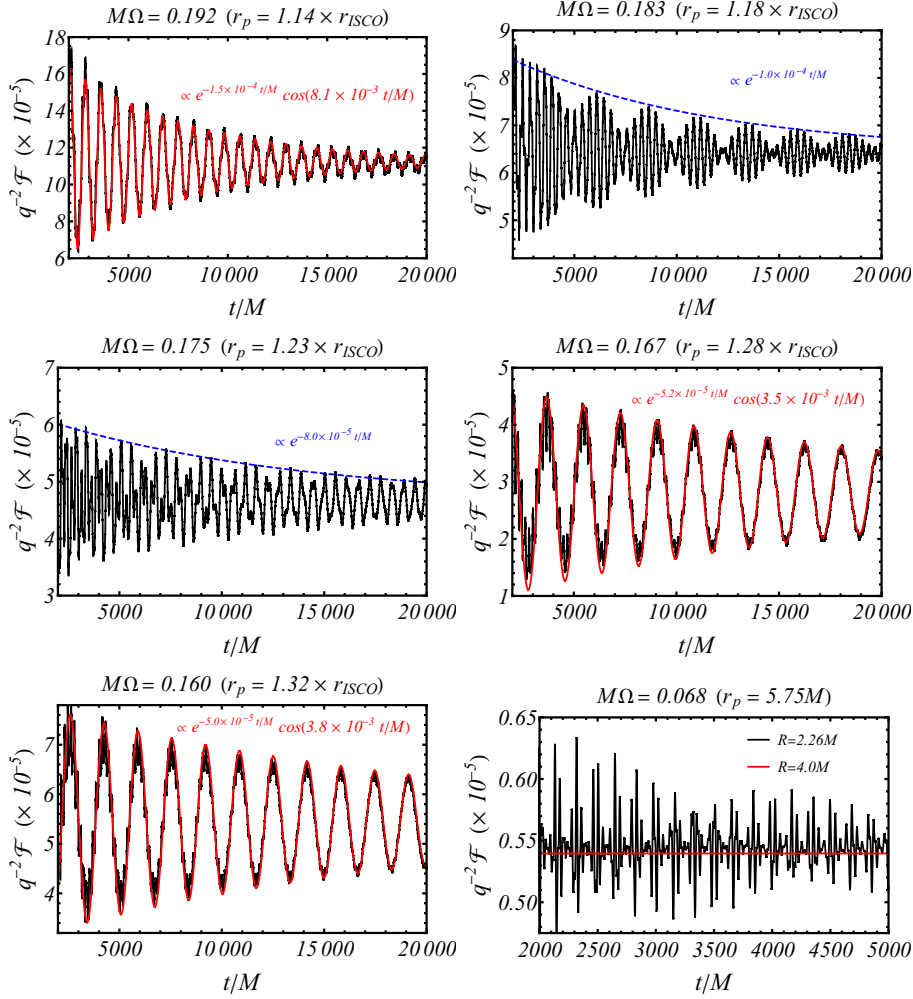


Figure 7.2: Evolution of the scalar energy flux \mathcal{F} (Eq. (5.38)) emitted by a point-particle of mass m_p , made to orbit a constant-density star of mass M on a circular orbit of constant radius r_p (the orbit is not allowed to evolve). The flux is normalized by the mass ratio $q = m_p/M$. The results refer to the dipolar mode ($\ell = 1$), but results are similar for higher multipoles. Except for the right bottom panel, the star has radius $R = 2.26M$, and the frequency ω corresponds to the angular frequency Ω of the circular orbit, with $a = 0.9M$ in Eq. (7.13) ($r_{\text{ISCO}} \approx 2.321M$). At late times, the flux asymptotes to a constant that agrees with the value computed in the frequency domain. The relaxation time is large for stars with photonspheres, but very short for less compact stars, where the system quickly becomes stationary, as seen in the right-bottom panel.

For the less compact spacetimes, which do not have trapping regions (in this context without LRs), the initial data relaxes on a few dynamical timescales to a final stationary result, which coincides with that obtained via a frequency-domain approach. This behavior is apparent

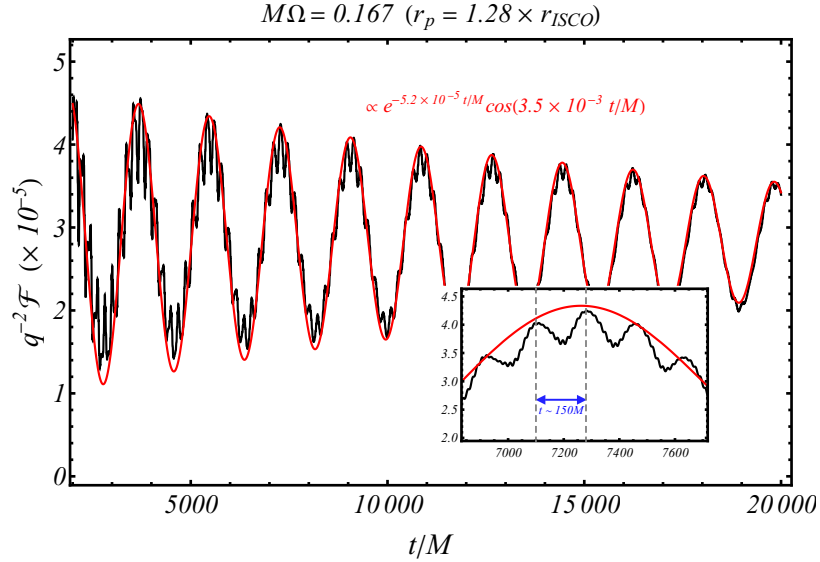


Figure 7.3: Scalar energy flux emitted by a point particle in circular orbit at $r_p = 1.28 r_{\text{ISCO}}$, with angular frequency Ω given by Eq. (7.13) with $a = 0.9M$, around a constant density star of radius $R = 2.26M$ (the orbit is not evolving, the particle remains at fixed r_p). There are three different timescales in the signal: a high-frequency component corresponding to the “direct signal” with an orbital period $T_{\text{Orb}}/2 = \pi/\Omega \sim 19M$ (the 1/2 factor appears since we are showing fluxes); the traveling time $T_{\text{echo}} \sim 150M$ of waves inside the cavity potential; a lower frequency “envelope” corresponding to the excitation of the QNM of the constant density star with frequency $M\omega_{\text{QNM}} = 0.16333 - i2.470 \times 10^{-5}$. This leads to a beating whose frequency is given by the semi-difference between the orbital and the QNM frequency $\tau_{\text{beating}} \sim 2\pi/(\Omega - \omega_{\text{QNM}}) \sim 1800M$.

for the dipolar mode of an $R = 4M$ uniform-density star in Fig. 7.2 (results are similar for other modes).

By contrast, for spacetimes sufficiently compact as to have photonspheres, the approach to stationarity is a long process. As explained above, the photonsphere is responsible for a potential barrier, through which waves need to tunnel and “build-up” until a stationary state is reached. The very first stages of this process are – in accordance with the analysis of Section 7.2.1 – a slow growth of the outgoing flux in steps of T_{echo} , the light travel time inside the photonsphere (see also the inset of Fig. 7.3, where the steps are clear). The relaxation timescale is also in good agreement with our *greenhouse* estimate made in Section 7.2.1. For $R = 2.26M$ and $r_p = 1.14 r_{\text{ISCO}}$ ($M\Omega = 0.193$ as set by Eq. (7.13)) our results indicate a relaxation timescale $\tau_{\text{relax}} \sim 6500M, 4500M$ for $\ell = 1, 2$, whereas Eq. (7.6) would indicate $\tau_{\text{relax}} \sim 4000M, 3100M$, respectively. The relaxation time increases when the circular orbit radius increases, again in line with our prediction (7.6).

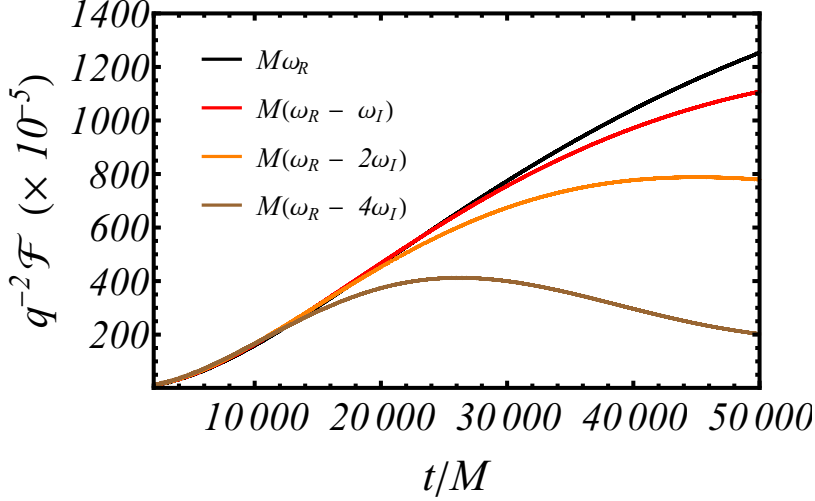


Figure 7.4: Resonant excitation of the dipolar QNM of a constant-density star of radius $R = 2.26M$ with frequency $M\Omega = M\omega_R = 0.1633$ (cf. Table 7.1), corresponding to a point particle at $r_p = 3.011M$. A small deviation of this radius resulting in a frequency shift of $\delta\Omega \gtrsim 2\omega_I$ can significantly hinder the excitation of the resonance. This agrees with standard results for the driven-harmonic oscillator, where the frequency bandwidth of the resonance peak is $\delta\Omega \sim \omega_I$.

Our results also show finer details, in particular beatings and finer structure at small timescales, apparent in Fig. 7.2. A zoom-in for $M\Omega = 0.167M$ ($r_p = 1.28r_{\text{ISCO}}$) is shown in Fig. 7.3 for the dipolar mode. These features can be understood with the three different scales of the problem: **1.** the orbital timescale, $T_{\text{Orb}}/2 = \pi/\Omega \sim 19M$ shows up as the smallest timescale in the problem and is clear in the inset of Fig. 7.3 (the $1/2$ factor appears since we are discussing fluxes); **2.** the orbital frequency $M\Omega = 0.1668$ is close to the resonant QNM frequency $M\omega_R = 0.1633$ (see Table 7.1). By our parallelism with the driven harmonic oscillator, we then anticipate a beating mode of frequency $\Omega - \omega_R$, i.e. a beating period $\tau_{\text{beating}} \sim 1800M$, in good agreement with our numerics; **3.** the travel time of waves inside the cavity. This is clear in Fig. 7.3 where we see steps of $T_{\text{echo}} \sim 150M$ for the build-up of the field in the cavity.

To excite resonances, we need to tune the orbital frequency closer to the resonant QNM. Our results are shown in Fig. 7.4, for the dipolar mode. The flux reaches amplitudes which are two orders of magnitude larger, but large timescales of order $\sim \mathcal{O}\left[\min\left(\frac{1}{\omega_I}, \frac{2\pi}{\Omega - \omega_R}\right)\right]$ are required for this build-up. The frequency needs to be very fine-tuned in order to properly excite the resonance, since as expected from the driven-harmonic oscillator, the bandwidth of the resonance peak is $\delta\omega \sim \omega_I$. Hence, when ω_I is very small, as it happens for the proper modes of horizonless ultracompact objects, the region of the param-

eter space where the resonance can be triggered is very limited and the resonance takes a long time to grow. These two conditions can jeopardize the ability to excite a resonance in a binary coalescence effectively .

One could question the generality of our results considering the artificial motion we took for the point particle. However, in Appendix C we repeat the analysis for $a = 0M$, which makes motion geodesic. By placing the particle at radii that yields the same orbital angular frequency as the ones presented in Fig. 7.2, we observe that the timescales involved are exactly the same for every single case, with only the relative magnitude between the fluxes changing. Note that in order to excite the QNM with $M\omega_{\text{QNM}} = 0.16333 - i2.470 \times 10^{-5}$ with a circular geodesic, the point particle would have to be placed at $r_p = 3.347M$.

7.4 CONSEQUENCES FOR GRAVITATIONAL-WAVE PHYSICS

We have shown that very compact objects can effectively absorb GWs for a significant time due to the spacetime geometry that traps waves within the photonsphere. This trapping process occurs on timescales of the order of Eq. (7.6), after which radiation is re-emitted. The physics of these objects must take into account such delay, which has not been considered with due care in the literature [382–386].

First, we consider the dynamics away from resonances. When they happen on short timescales, such as the final stages of a coalescence, then the cavity has no time to “fuel up” and absorbs most of the impinging radiation. In this regime, horizonless compact objects behave similarly to BHs, with equivalent absorption properties, and possibly indistinguishable from them.

The second effect concerns the crossing of resonances, a generic effect not particular to compact horizonless objects. We show that frequency-domain adiabatic evolutions do not capture the entire physics and must be complemented by additional constraints when time evolutions are prohibitive.

7.4.1 Adiabatic evolution of orbits and energy balance

To study GW-driven inspirals, we consider adiabatic evolutions, where the point particle is always on a circular orbit with some associated energy E and angular momentum L . We place the particle at some initial radius r_0 , and determine its initial energy and angular momentum as dictated by the EOM. Then, we need to evaluate the backreaction on these due to energy emission (and angular momentum). As argued, the flux needs to include the energy loss to infinity, but it should also include the energy piling up within the cavity. However, considering the effects of the cavity is a challenging problem that we will not ad-

dress here. We will only consider the energy radiated away to infinity, but we insist that the cavity may play an important role. For circular orbits, the angular momentum net balance is completely determined by the energy balance, so we only need to solve

$$\frac{dE}{dt} = -\mathcal{F}, \quad (7.17)$$

with the appropriate initial energy and use this to evolve

$$\frac{dr}{dt} = -\mathcal{F} \left(\frac{dr}{dE} \right), \quad (7.18)$$

again with the appropriate initial conditions. Having the updated value for r_p , we can compute the angular frequency Ω again.

This procedure can be applied both for the time and the frequency domain. However, the flux computed in the frequency domain implicitly assumes stationarity, i.e. that the oscillations around the average flux vary out to zero much faster than the timescale on which the particle inspirals. For the systems we are discussing, this implies the cavity has had time to fuel-up. For the time domain instead, the energy balance is done at every instant and therefore can account for the inhomogeneities in the flux as the star is relaxing or the cavity is fueling-up.

7.4.2 Off resonance

As a binary coalesces, its orbital frequency changes. For objects on quasi-circular orbit millions of years prior to the merger, a “stationary state” (to be read as where the frequency-domain calculation yields the same result as the time-domain) is reached. However, in the late stages of the inspiral, the frequency varies rapidly, hence not allowing the compact object to “fuel up”. This happens whenever the frequency changes by $\Delta\omega \gtrsim \omega_R$ and the corresponding inspiral time is small enough that it does not allow for relaxation.

Let us start the inspiral at some radius $r_p(t=0) = r_i$. Then, for quasi-circular orbits, and including only the leading terms in GW reaction [402]

$$r_p(t) = (r_i - 4\beta t)^{1/4}, \quad (7.19)$$

$$\beta = \frac{64}{5} M^2 m_p. \quad (7.20)$$

The time taken to inspiral from r_0 to $r_p(t)$ can also be written in terms of the initial and final GW frequency ω_i, ω_f as [402]

$$t_{\text{inspiral}} = \frac{2^{2/3} M^{4/3} (1 - (\omega_i/\omega_f)^{8/3})}{\beta \omega_i^{8/3}}, \quad (7.21)$$

and therefore

$$\frac{t_{\text{inspiral}}}{\tau_{\text{relax}}} \sim 10^{-2} \frac{100M}{T_{\text{echo}}} \frac{10^{-5}M}{m_p} \left(\frac{M\omega}{0.06} \right)^{10/3}. \quad (7.22)$$

Considering the typical values for EMRIs ($m_p/M \lesssim 10^{-5}$, $M\omega \sim 10^{-2} - 10^{-1}$), the result above implies that cavity effects should be taken into account in the evolution of the inspiral. Time or frequency domain analysis should include the temporary pile-up of energy in the cavity in the computation of radiation-reaction effects as the inspiral progresses.

Our results also show how the BH limit is approached naturally when $T_{\text{echo}} \rightarrow \infty$ in the previous construction. In this limit, the central object is a perfect absorber during the entire inspiral. We forecast that properly handling the cavity problem in radiation-reaction should recover the BH result continuously.

Previous works suggested that the cavity would only be important for the evolution of the binary when the traveling time inside it is comparable (or larger) than the radiation-reaction timescale [218, 383]. However, as discussed above, energy can be trapped by being reflected back and forth in the cavity until it saturates. This process corresponds to multiple travel times, as dictated by Eq. (7.6). In general, this timescale can be much bigger than the travel time inside the cavity, making the latter more relevant for larger mass-ratios than previously considered.

7.4.3 Crossing resonances

The above results strongly suggest that in order to excite a resonance, the system needs to spend at least a time $\sim 1/\omega_I$ in a frequency band $\delta\omega \sim \omega_I$ around the resonance at ω_R . Rigorous estimates for simple linear differential equations were obtained in Refs. [403, 404]. We can work out the consequences for GW science: the time δt_{cross} that the system takes to cross the resonance is [382]

$$\delta t_{\text{cross}} \sim \omega_I / (d\Omega/dt), \quad (7.23)$$

with

$$\frac{d\Omega}{dt} = \left(\frac{d\Omega}{dr} \right) \left(\frac{dr}{dE} \right) \mathcal{F}. \quad (7.24)$$

Then, for the resonance to be effectively excited

$$\begin{aligned} \omega_I \delta t_{\text{cross}} &\gtrsim 1 \\ \Leftrightarrow q &\lesssim q_{\text{max}} = \frac{(M\omega_I)^2}{q^{-2}\mathcal{F}} \left(\frac{1}{m_p} \frac{dE}{dr} \right) / \left(M \frac{d\Omega}{dr} \right). \end{aligned} \quad (7.25)$$

In this estimate, orbital quantities on the right-hand side are meant to be evaluated at the radius where the resonance is excited, and the flux is to be taken *outside* the resonance since this is the actual energy flux emitted by the binary while the resonance grows.

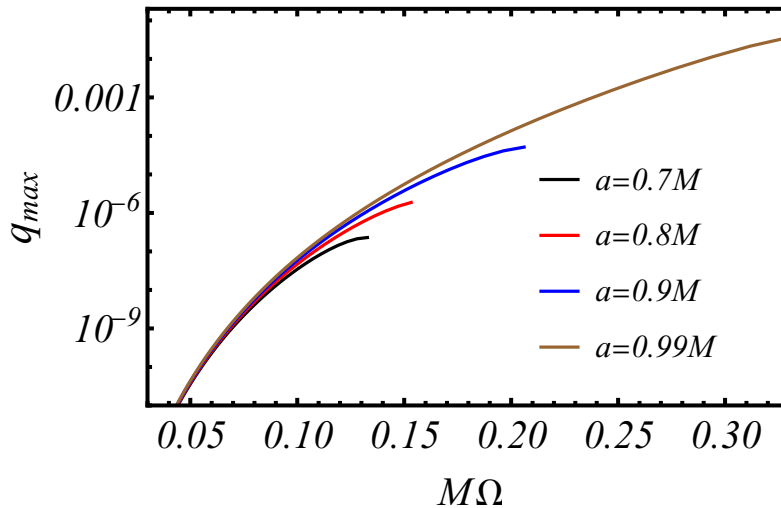


Figure 7.5: Largest mass ratio q_{\max} predicted by the estimate (7.25) that would allow the resonant excitation, by GWs, of a QNM of an ECO with frequency $\omega_R = 2\Omega$. We considered that $\omega_I \sim \omega_R^{2l+3}$ [382, 383] and only took into account the quadrupolar mode in the energy flux, making this estimate conservative, since \mathcal{F} will increase if higher multipoles are considered. We show orbital frequencies Ω corresponding to radius of the particle from $r_p = 10M$ up to almost the ISCO for each spin a . For mass ratios larger than these limits, the particle crosses the resonance too quickly for it to grow effectively.

7.5 DISCUSSION

In this chapter, we have demonstrated that spacetimes with LRs behave as cavity resonators. They have large “build-up” times, determined by the transmission amplitudes at the LR, and are prone to resonances. To properly evolve binaries composed by ECOs, it is necessary to take into account the energy piling up within the photonsphere. For systems evolving rapidly under radiation reaction, these objects act as effective absorbers and may mimic BHs. A proper modeling of this process and the full evolution of an EMRI is therefore an open problem. Additionally, the secondary object can excite resonances of these objects, but for the resonances to fully develop, the binary has to evolve slower than the time needed for the resonance to grow.

We focused on a simple toy-model of a scalar field around a constant-density star and considered an artificial motion for the point-particle that is not dictated by its equations of motion. Nonetheless, all our analytical estimates for the relaxation timescale (7.6), resonance growth time, and the upper limit on the mass ratio that excites a resonance in an inspiralling binary (7.25) are model independent, and agree with the numerical results for the particular system that we studied. Therefore, our conclusions should be applicable to any astrophysical system.

Refs. [383, 386] studied EMRIs around spinning horizonless compact objects (see also [382, 384] for the non-spinning case). As in our toy-model, the low-frequency QNMs of the spinning ECO can be resonantly excited during the inspiral, leading to non-negligible effects in the waveform that must be considered for the detection and parameter estimation of these sources. However, their work in the frequency domain ignores the growth time of the resonance, implicitly assuming stationarity at all instants. This approximation is only correct when the mass ratio of the system obeys the condition of Eq. (7.25).

In Fig. 7.5, we apply this estimate to the type of systems studied in Refs. [383, 386]. Typically, the resonance width for these exotic compact objects is $\delta\omega \sim \omega_I \sim \omega_R^{2\ell+3}$ [382, 383]. In a binary system, the frequency of the emitted GWs is determined by the orbital frequency and, for circular orbits, corresponds to $\omega_{\text{GW}} = 2\Omega$. We can then compute, for every orbital frequency Ω (or radial location of the particle), how light the point particle must be to resonantly excite an ECO with a QNM of frequency $\omega_R = 2\Omega$, $\omega_I \sim (2\Omega)^{2\ell+3}$. For the off-resonance flux \mathcal{F} , we used the same values as in Kerr since the relative difference with respect to a horizonless ultracompact object should be small (though non-negligible when accumulated over many orbits). We only took into consideration the quadrupolar mode $\ell = 2$, and higher multipoles will typically increase \mathcal{F} , therefore placing even more stringent limits on the mass ratio. We conclude that for the reference value of $q = 3 \times 10^{-5}$ used in most results presented in Ref. [383], the particle should only be able to excite resonances in ECOs with spins $a > 0.9M$, and on a limited region of the parameter space where it is very close to the central object.

Our conclusions should apply to other systems where resonances are excited, such as massive scalar theories [405–407]. In these theories, matter orbiting a Kerr BH can resonantly excite superradiant modes, which might lead to so-called *floating orbits* [103, 408], where the energy absorbed by the horizon is positive and counterbalances the loss of energy to infinity [262, 409]. As a consequence, the inspiral freezes and the radiated energy is solely provided by the rotational energy of the BH. These resonances occur for $\omega_{\text{res}}^2 = \mu_s^2 - \mu_s^2 (M\mu_s/(\ell + 1 + n))^2$, where $\mu = m_s/\hbar$ is the reduced mass of the scalar field, and have typical widths of $\delta\omega \sim \omega_I \propto \mu_s^{4\ell+5}$ [262, 270]. These are even more narrow than the QNMs of ECOs we have been discussing. Generically, the off-resonance energy flux is dominated by GWs, which means that for the same orbital frequency, the mass ratios needed to properly excite superradiant resonances of massive scalars would be even smaller than the ones in Fig. 7.5.

Additional dissipation mechanisms could undermine the fueling-up of the cavity and the excitation of resonances. However, GWs are known to interact very weakly with matter, with effects only being relevant at the Hubble timescale [410–413]. Hence, any additional

channel of dissipation should be subdominant with respect to the emission of waves to infinity and the trapping of energy by the central object on the timescales of interest for these systems. We cannot rule out, however, that extremely stiff equations of state giving rise to large viscosities and large sound speeds strongly suppress resonances in compact objects. Even in such case, our results still apply to other systems, e.g. the resonances of massive boson fields around spinning BHs discussed in the Introduction of Chapter 4 [136, 137].

Our conclusions have obvious implications to GW astronomy, and highlight the necessity of a better understanding of GW emission in less conventional systems that are not typical BHs in vacuum GR. The proper modeling of “transient” resonances which do not have time to fully develop in binary inspirals has already been tackled in Refs. [414–417], in the context of tidal resonances induced by a third companion. The steps laid there could be adapted for EMRIs involving ECOs.

GRAVITATIONAL TUNING FORKS

At the end of the Introduction, we discussed how hierarchical triple systems are common in a variety of astrophysical scenarios, such as globular clusters, AGNs, and other dense stellar environments [143, 145–151, 418]. “Hierarchical” here refers to the distinct length scales between the orbit of a binary and the one of its CM around the third body. Recalling, around 90% of low mass binaries with periods shorter than 3 days are expected to belong to some hierarchical structure [152–154].

This has motivated recent studies on the dynamics and GW emission in hierarchical triple systems. Kozai-Lidov resonances, in particular, have attracted some attention [155, 163, 164]. As we had already mentioned, these describe secular changes in the binary eccentricity and inclination with respect to the orbit described by its CM around the third object. This mechanism triggers periods of high eccentricity, where GW emission increases significantly, potentially inducing coalescence in eccentric orbits detectable by LISA [165–168], that then enter in the frequency band of ground-based detectors still at high eccentricities [418–421]. A direct integration of the EOM confirms these systems have unique GW signatures [169, 170], which may be detected indirectly via radio observations of binary pulsars [422]. There are also attempts at modeling the effects of a third body directly into the waveform. These include Doppler shifts [156–160], relativistic beaming effects [161, 162], gravitational lensing [423, 424] and other dynamical effects [414, 415, 425].

In this final chapter of the second part of this thesis, we will study hierarchical triples using BH perturbation theory and investigate GW emission from binaries around SMBHs. Using the methods we already applied in previous chapters, we will be able to probe resonant excitation of QNMs in triple systems, and capture for free all of the relativistic effects which have so far been included only at a phenomenological level in the literature.

8.1 SETUP

Our setup is similar to the one used in Chapter. 5, where we had a small binary in the vicinity of a large BH. An illustration of this system

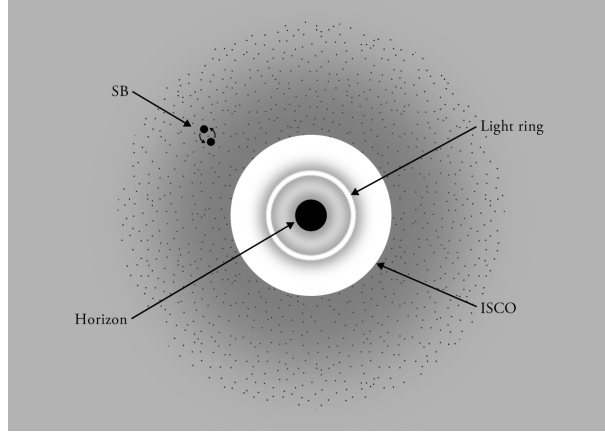


Figure 8.1: Equatorial slice of a spacetime with a hierarchical triple system. In the center there is a **SMBH**. At large distances away from the central region, physics is nearly Newtonian. The external gray area is the entire region where stable circular motion is possible. We place a small compact binary here, with characteristic frequency ω_0 . Its **CM** orbits the **SMBH** with angular frequency Ω_{CM} . At the **ISCO** ($r_{\text{ISCO}} = 6M$ when the **SMBH** is non-spinning), circular motion is marginally stable, and unstable for smaller radius. High-frequency waves can be trapped at the **LR** ($r_{\text{LR}} = 3M$ for non-spinning **BHs**). Such motion is unstable, and as seen in previous chapter, can also be associated with the “ringdown” excited during **BH** mergers.

can be found in Fig. 8.1. We consider the small binary is sourcing perturbations to a Kerr background (2.11) and model it as two point-particles. In Chapter 5 we considered the **CM** of the small binary was plunging onto the central **BH**, but here we will take it to be at some fixed radius, r_{CM} , while it describes a circular orbit around the central **BH**. For the small binary, we again take elliptic orbits around its **CM**

$$r^\pm = r_{\text{CM}}, \quad (8.1)$$

$$\varphi^\pm = \Omega_{\text{CM}}t \pm \epsilon_\varphi \sin \omega_0 t, \quad \theta^\pm = \pi/2 \pm \epsilon_\theta \cos \omega_0 t, \quad (8.2)$$

where $\epsilon_\theta, \epsilon_\varphi \ll 1$ parametrize the two axis of the ellipse $\delta r_\theta = \epsilon_\theta r_{\text{CM}}$, $\delta r_\varphi = \epsilon_\varphi r_{\text{CM}}$ of the small binary, and Ω_{CM} is the angular velocity of the **CM**. Ω_{CM} and ω_0 are coordinate frequencies, while the proper oscillation frequency of the small binary, ω'_0 , is obtained by rescaling the time component of the 4-velocity of the **CM**, i.e. $\omega'_0 = u_{\text{CM}}^t \omega_0$. For concreteness, we focus exclusively on equal-mass binaries, $m_p^\pm = m_p$ and a highly eccentric orbit with $\epsilon_\theta = 0$. We do not see any qualitatively new phenomena in the general case, and this particular choice could mimic high-eccentricity binaries driven by Kozai-Lidov resonances [155, 163, 164].

There is a physical relation between ϵ_φ and ω_0 . In the rest frame of the small binary, $\delta r'_\varphi \propto 1/(\omega'_0)^{2/3}$, where the prime refers to *proper*

quantities. For binaries on circular geodesics, for example, doing the appropriate rescaling $\omega'_0 = u_{\text{CM}}^t \omega_0$ and $\delta r_\varphi = \Delta/\rho^2 \cdot \delta r'_\varphi$, we find

$$\epsilon_\varphi \propto \frac{\Delta}{\rho^2} \frac{1}{r_{\text{CM}}(u_{\text{CM}}^t \omega_0)^{2/3}}. \quad (8.3)$$

We will be looking for possible resonances in this triple system, which may happen when the forcing frequency of the binary equals the natural frequencies of the background, i.e its QNMs. There are three important frequencies in the problem: the angular frequency of the CM, the frequency of the LR, which as we saw in Chapter 5 controls the QNMs [188]), and the angular velocity of the BH horizon Ω_{H} (2.12). Close to the central BH, all of them are of order $\mathcal{O}(1/M)$. To have $M\omega_0 \sim 1$, we need to ensure $\delta r_\varphi/m_p \sim (M/m_p)^{2/3}$. For a SMBH with $M \sim 10^4 - 10^6 M_\odot$, like Sagittarius A*, and a small binary composed by stellar-mass BHs with $m_p \sim 1 - 100 M_\odot$, this would correspond to $\delta r/m_p \sim 10^2 - 10^4$, so well within the inspiral phase.

As before, the small binary enters as a source term in the Teukolsky equation (2.49), which governs perturbations to the background space-time of the central Kerr BH. We study both the case of GWs ($s = -2$ in the Teukolsky equation) and also scalar radiation ($s = 0$) where the source term is again given by the trace of the energy-momentum tensor of the point particles composing the binary, as presented in Sec. 5.2.3.

Again, we solve this problem numerically in the time domain with the Lax-Wendroff method introduced in Sec. 2.2.

8.2 RESONANT EXCITATION OF QNMS AND ENERGY EMISSION

We start by using the small binary as a tuning fork, placing it at some fixed radius, with its CM fixed with respect to distant observers, and letting its frequency ω_0 vary. We want to compare the (time-averaged) flux of energy in each (ℓ, m) mode with the corresponding value in flat space. We define this as the ratio

$${}_s\mathcal{R}_{\ell m} = {}_s\dot{E}_{\ell m} / {}_s\dot{E}_{N\ell m}, \quad (8.4)$$

where N refers to the result in flat space, i.e setting the mass of the central BH to zero. This can be computed numerically or through analytical estimates using the method of matched asymptotic expansions [382]. When the binary is put at large distances from the central BH this ratio tends to unity.

Figure 8.2 shows the behavior of ${}_2\mathcal{R}_{33}$ as the small binary frequency ω_0 changes, for a binary sitting at the ISCO of a SMBH. The behavior is similar for other modes and fields. We observe a peak which we identify as a resonant excitation of the $\ell = m = 3$ QNM. As shown in Table 8.1, the location of the peak is well described by the lowest QNM frequency [188], for general binary locations. When the small

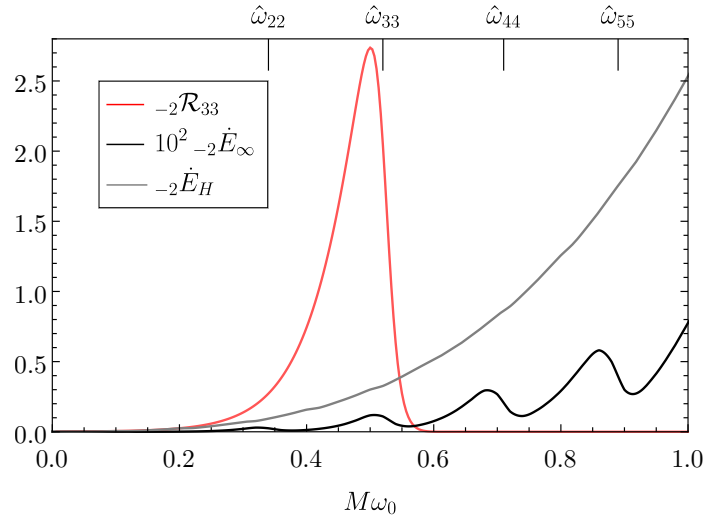


Figure 8.2: Energy output when a small binary stands at the ISCO of a SMBH with spin $a = 0.9M$, as a function of the orbital frequency of the binary components, ω_0 . The modal energy output, as measured by the ratio with respect to flat spacetime ${}_{-2}\mathcal{R}$, peaks at a finite ω_0 well described by the lowest QNM (cf. Table 8.1). Also shown is the flux integrated over all modes: it has a substantial component going down the SMBH horizon (\dot{E}_H), and the total flux at infinity is modulated by QNM contributions (\dot{E}_∞). Here, $\hat{\omega}_{\ell m} = M\omega_{\text{QNM}}/2$.

binary is placed at the LR, the agreement is excellent (better than 1% for scalars, and 4% for GWs for the lowest modes). Recall from our discussion at the beginning of Chapter 5, that QNMs can be interpreted as waves marginally trapped in unstable orbits at the LR [328]. We conclude that a hierarchical triple system behaves as a driven harmonic oscillator [394], where the small binary is the external harmonic force and the central BH behaves as a damped oscillator.

As a side note, this behavior is analogous to the Purcell effect in quantum electrodynamics [426, 427], describing the enhancement in the spontaneous decay of a quantum emitter inside a cavity, when its frequency matches those of the cavity modes. Our results are consistent with recent findings [427], namely that the contribution to the power spectrum independent of r_{CM} is described by a Lorentzian curve $\mathcal{R} \propto \omega_{\text{QNM}}^2 / (\omega_{\text{QNM}}^2 + 4Q^2(\omega_0 - \omega_{\text{QNM}})^2)$, where $Q = \text{Re}(\omega_{\text{QNM}}) / 2\text{Im}(\omega_{\text{QNM}})$ is the quality factor of the central BH. Our results extend those of Ref. [428], which also observed the resonant excitation of QNMs in very eccentric EMRIs, during passage on the periapsis. The effect is stronger the closer the particle can get to the LR [429].

As a rule of thumb, the flux peaks at lower frequencies the further the small binary is placed from the BH, in agreement with blueshift/redshift corrections. Note that \mathcal{R} smaller than unity does not imply that the system is emitting less energy than expected, since a portion of the radiation falls into the BH. Also, a possible CM orbital

ℓ	s	a/M	$M\omega_{\text{QNM}}/2$	$M\omega_{0,\text{LR}}$	$M\omega_{0,\text{ISCO}}$	${}_s\mathcal{R}_{\text{LR}}$	${}_s\mathcal{R}_{\text{ISCO}}$
2	0	0	0.242	0.242	0.189	4.5	2.0
2	-2	0	0.186	0.175	0.156	0.6	1.5
2	-2	0.9	0.335	0.332	0.319	88.0	0.8
3	0	0	0.338	0.337	0.255	10.0	2.5
3	-2	0	0.300	0.289	0.250	2.0	2.3
3	-2	0.9	0.522	0.520	0.500	515.8	2.7
4	0	0	0.434	0.433	0.317	21.6	3.0
4	-2	0	0.405	0.395	0.326	5.6	3.0
4	-2	0.9	0.705	0.704	0.675	1896.4	5.4

Table 8.1: Frequency $M\omega_X$ which maximizes the energy output of a small binary standing at location X close to a SMBH, in a given (ℓ, ℓ) mode, as measured by the ratio ${}_s\mathcal{R}$ ($s = 0, -2$ for scalar or gravitational perturbations, respectively). The binary's CM is static, and sitting at the LR or at the ISCO. Notice the excellent agreement with the lowest QNM frequency. The results for orbiting binaries are similar.

motion contributes to a shift in the resonant frequencies by $\pm m\Omega_{\text{CM}}$, fully consistent with our results. The maximum value of \mathcal{R} in the entire $(r_{\text{CM}}, \omega_0)$ parameter space does not occur precisely at the LR, but close to it. The maximum is attained at locations r_{CM} closer to the horizon for large ℓ . Finally, the magnitude of the resonance grows with ℓ . For a fixed CM location r_{CM} and multipole ℓ we searched for ω_0 for which ${}_s\mathcal{R}$ is a maximum ${}_s\mathcal{R}_{\text{peak}}$. We find an exponential dependence on ℓ , ${}_s\mathcal{R}_{\text{peak}} \sim a + b \exp(c \cdot \ell)$, at large ℓ with a, b, c constants.

Since we are using a mode decomposition centered at the SMBH, radiation has support in higher modes as the binary is placed further away from it [430, 431]. Consequently, the lowest modes will not be dominant, and we need to sum over a sufficient amount of modes for the total fluxes to converge. Already for a small binary at the ISCO of a non-rotating BH, we find that the GW flux at infinity is comparable to that at the horizon of the SMBH. To compute it we use the Starobinsky identities that relate ψ_0 , which controls the radiative degrees of freedom at the BH horizon, with ψ_4 which controls them at infinity as seen in Eq. (2.50) [432, 433]. At the BH horizon, the ingoing solution of the $s = -2$ master function in the Teukolsky equation (2.49) behaves as

$$\Psi \sim \Delta^2 Z_{\text{in}} e^{-i(\omega t + kr_*)} e^{im\varphi} {}_{-2}S_{\ell m}(\theta), \quad (8.5)$$

with $k = \omega - m\Omega_{\text{H}}$ and $S_{\ell m}(\theta)$ the spin-weighted spheroidal harmonic obeying to [182]

$$\begin{aligned} & \frac{1}{\sin\theta} \frac{d}{d\theta} \left(\sin\theta \frac{dS}{d\theta} \right) \\ & + \left(a^2\omega^2 \cos^2\theta - \frac{m^2}{\sin^2\theta} - \frac{2a\omega s \cos\theta}{\sin^2\theta} - \frac{2ms \cos\theta}{\sin^2\theta} \right) S \\ & = -(\lambda - s^2) S, \end{aligned} \quad (8.6)$$

where the eigenvalues λ are available online from the Black Hole Perturbation Theory Toolkit [434]. We can then compute the energy flux carried by GWs through the BH event horizon with

$$\dot{E}^H = \frac{128\omega k (k^2 + 4\epsilon_{\text{BH}}^2) (k^2 + 16\epsilon_{\text{BH}}^2) (2Mr_+)^5}{|C|^2} |Z_{\text{in}}|^2, \quad (8.7)$$

$$\epsilon_{\text{BH}} = \frac{\sqrt{M^2 - a^2}}{4Mr_+}, \quad (8.8)$$

$$\begin{aligned} |C|^2 &= (Q^2 + 4a\omega m - 4a^2\omega^2) \left[(Q - 2)^2 + 36a\omega m - 36a^2\omega^2 \right] \\ &+ (2Q - 1) (96a^2\omega^2 - 48a\omega m) + 144\omega^2 (M^2 - a^2), \end{aligned} \quad (8.9)$$

$$Q = \lambda + a^2\omega^2 - 2a\omega m. \quad (8.10)$$

Formally, this equivalence is valid only in the frequency-domain but has been shown to yield correct results for circular orbits in the time-domain also.

As seen in Fig. 8.2, the effect is more dramatic when spin is included. This peculiar aspect is due to the similar length scales of the central BH horizon and the radiation wavelength. GWs are then efficiently absorbed by the BH, in clear contrast with the inspiral phase of an EMRI, whose wavelength is much larger than the BH radius. This is our second result: hierarchical triple systems where the SMBH occupies a large fraction of the small binary's sky will naturally probe strong-field physics, since the fraction of radiation that falls into the SMBH is non-negligible. This property is essential for the dynamical evolutions of these systems.

For a fixed radius r_{CM} , the field has support on higher ℓ modes as the binary is vibrating at higher frequencies ω_0 . If we place it close enough to the SMBH, it can resonantly excite its QNMs, leading to characteristic peaks in the flux at infinity/horizon, as seen in Fig. 8.2. These structures correspond to the single multipolar excitations.

8.3 WAVEFORMS: DOPPLER, ABERRATION & LENSING

In addition to energy fluxes, we can also study qualitative strong-field effects in the waveforms from hierarchical triple systems. In Fig. 8.3 we show the Teukolsky function extracted at large distances for a small binary on circular motion at the ISCO of a non-rotating BH. We removed

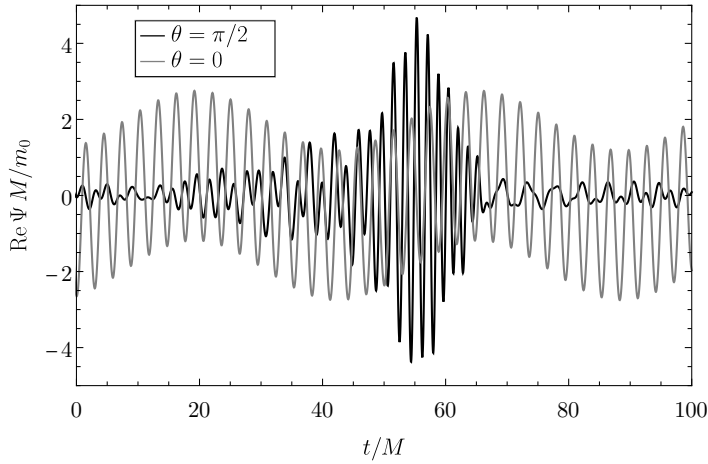


Figure 8.3: Teukolsky function Ψ measured by a stationary observer at large distances (either edge- or face-on, $\theta = \pi/2, 0$ respectively), for a stellar binary around the ISCO of a non-rotating BH (we removed the CM contribution, which just causes a low-frequency modulation). The orbital CM period is $T_{\text{CM}} \approx 93M$ and at $t = 0M$ the observer is aligned with the small binary. Doppler effect induces frequency shifts, relativistic beaming and gravitational lensing modulations in the amplitude. The maximum blue-shift is well described by $\omega_{\text{max}} = \omega'_0 Y ((Y + v_{\text{CM}})/(Y - v_{\text{CM}}))^{1/2}$, with $Y = \sqrt{1 - 2M/r_{\text{CM}}}$, $M\omega'_0 = 1$ the proper frequency and v_{CM} the CM velocity [156, 290]. In this case, $\omega_{\text{max}}/\omega'_0 \approx 1.4$.

the (linear) CM contribution, which only induces a low-frequency modulation. Observers on the equatorial plane see gravitational and Doppler-induced frequency shifts, consistent with analytical predictions when the CM is moving towards the observer [156, 290]. The amplitude of the wave can vary by orders of magnitude because of relativistic beaming [161, 162, 170] and gravitational lensing [424, 435]. Relativistic beaming focuses radiation along the direction of motion, and is significant for fast CM motion (in this case $v_{\text{CM}} \approx 0.4$). Hence, when the binary is moving away from the observer, the radiation reaching it is small, and vice-versa. The maximum amplitude does not occur precisely when the stellar binary is moving towards the observer ($t \sim 70M$ in Fig. 8.3) but slightly before, when it is still behind the SMBH with respect to the observer. This is due to lensing by the central SMBH, which distorts the path taken by GWs and concentrates radiation on certain directions, amplifying the signal [338, 339]. This effect is more relevant for larger frequencies, closer to the geometric optics limit when the radiation wavelength is much smaller than the SMBH radius. These different effects are illustrated in Fig. 8.4, which corresponds to two snapshots of an animation representing the time evolution of wave emission of the hierarchical triple system.

Observers facing the plane of motion “face-on” ($\theta = 0$) do not measure such modulations since the motion of the CM is now transverse.

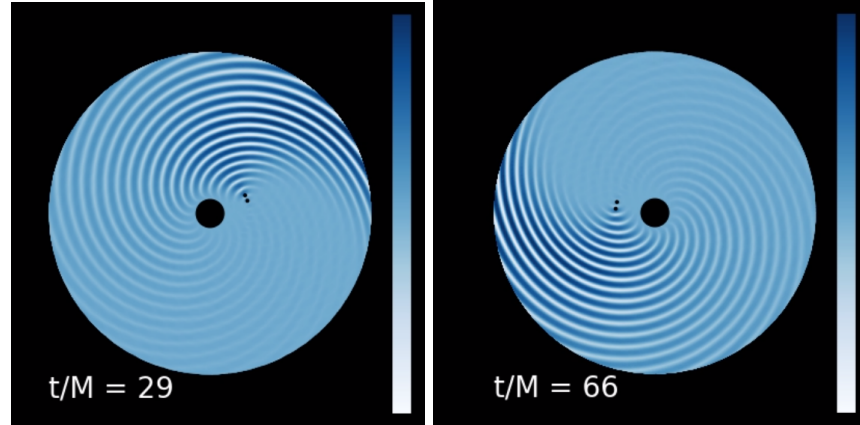


Figure 8.4: Snapshots of the time-evolution of the hierarchical triple system with the **CM** of the small binary orbiting the **SMBH** at the **ISCO** anti-clockwise. The shaded blues illustrate the wave emission by the system projected on the equatorial plane. There is a focus of radiation along the direction of motion, corresponding to relativistic beaming. We also observe the distortion of the path taken by waves due to gravitational pull exerted by the central **BH**.

The only feature is a modulation in amplitude coming from the **CM** motion, which has also been reported in post-Newtonian studies of triple systems [170].

8.4 DISCUSSION

This chapter highlights both the versatility of **BH** perturbation theory and the robustness of our numerical framework to study **GW** emission in more complicated systems than a standard binary. Effects like **GW** lensing, aberration and amplitude modulations are naturally built-in, without the need to prescribe slow-motion approximations and force the orbital motion into the quadrupolar approximation. As a drawback, we need to sum over various multipoles in order to resolve the length scales of the small binary.

One could question if it is physically possible for a stellar-mass binary to get so close to a **SMBH** before being disrupted. While quantifying a detectability rate for the resonances we studied goes beyond the scope of our work, we can make an estimate based on the Hills mechanism already mentioned in Chapter 4 [436–438]. Disruption occurs if the tidal forces induced by the central **BH** overcome the binary's self-gravity, which happens at a radius $r_{\text{CM}} \sim 2\delta r (M/2m_p)^{1/3}$. The binary's frequency will be related to its separation by the Kepler's law $\omega_0 \sim \sqrt{2m_p/\delta r_{\text{CM}}^3}$. We thus find $r_{\text{CM}} \lesssim 1/(M\omega_0)^{2/3}M$. Already for $M\omega_0 = 0.2$, tidal disruption happens at $r_{\text{CM}} \sim 5.84M$, smaller than the **ISCO** of a Schwarzschild **BH**. Thus, small binaries very close to a central **BH** and oscillating at relevant frequencies of the system

have astrophysical interest. This is supported by more sophisticated numerical works [439].

We neglected spin-spin effects in the motion of the binary. The corrections are proportional to $\sigma = qJ/m_0^2$, with J the angular momentum of the binary [440]. Again using Kepler's law, one finds that corrections to the motion scale like $\sigma \propto q^{2/3}$, which are extremely small for the systems we consider.

We also did not consider a situation where the small binary is coalescing, or when its CM describes a highly eccentric orbit around a spinning SMBH [77]. As the binary gets closer to the LR in these orbits, the resonant excitation of the SMBH's modes is enhanced and can lead to the excitation of superradiant modes [103]. Another interesting hierarchical triple system is a pair of same-sized BHs and a third lighter compact object orbiting around them. These spacetimes have been shown to have global properties not present in isolated BHs (e.g. global QNMs) [441, 442] and our results suggest that the lighter object can excite these global modes.

Part III

BINARIES IN ASTROPHYSICAL
ENVIRONMENTS

GALACTIC BLACK HOLE

In the Introduction, we went to great lengths to illustrate that the lack of relativistic models has arguably been the major flaw of studies on environmental effects for GW astronomy. In the last part of this thesis we will use standard techniques of BH perturbation theory to develop a generic, fully-relativistic formalism to handle environmental effects in EMRIs in spherically-symmetric, but otherwise generic backgrounds [184, 189, 443–448]. The main novelty in our approach is to treat perturbations to matter on the same ground as those induced by the binary in the gravitational field, which allows to capture for free environmental effects such as dynamical friction, accretion, and halo feedback. This is inspired in studies of perturbations to relativistic stars [447], but here we want to apply it to extended distributions of matter surrounding BHs.

Our starting point is therefore a static, spherically symmetric space-time (2.16) describing a BH immersed in some environment, like an accretion disk or DM halo. The environment is characterized in general by an anisotropic fluid with energy-momentum tensor

$$T_{\mu\nu}^{\text{env}} = \rho u_\mu u_\nu + p_r k_\mu k_\nu + p_t \Pi_{\mu\nu}, \quad (9.1)$$

where ρ is the total energy density of the fluid, p_r and p_t are its radial and tangential pressure, respectively, u^μ the 4-velocity of the fluid, k^μ a unit spacelike vector orthogonal to u^μ , such that $k^\mu k_\mu = 1$ and $u^\mu k_\mu = 0$, and $\Pi_{\mu\nu} = g_{\mu\nu} + u_\mu u_\nu - k_\mu k_\nu$ is a projection operator orthogonal to u^μ and k^μ (environmental quantities are hereafter denoted with a superscript “env”). We now envision a secondary object of mass m_p (a star, asteroid or stellar-mass BH for example) orbiting the primary BH and causing perturbations to the geometry and matter energy-momentum tensor

$$g_{\mu\nu} = g_{\mu\nu}^{(0)} + g_{\mu\nu}^{(1)}, \quad T_{\mu\nu}^{\text{env}} = T_{\mu\nu}^{\text{env}(0)} + T_{\mu\nu}^{\text{env}(1)}, \quad (9.2)$$

where a superscript “(1)” denotes perturbations to the background “(0)”. The 0-th order Einstein’s equations give

$$\frac{A'}{A} = \frac{2m + 4\pi r^3 p_r^{(0)}}{r(r-2m)}, \quad (9.3)$$

$$\rho^{(0)} = \frac{m'}{4\pi r^2}, \quad (9.4)$$

$$\frac{dp_r^{(0)}}{dr} = -p_r^{(0)} \frac{2r - 2m + 4\pi r^3 p_r^{(0)} - rm'}{r(r-2m)}, \quad (9.5)$$

$$p_t^{(0)} = \frac{mm'}{8\pi r^2(r-2m)} + \frac{2rm' - m}{2(r-2m)} p_r^{(0)} \quad (9.6)$$

where the prime denotes a derivative with respect to r , and $m = m(r)$ is the mass function

$$m(r) = \frac{r}{2} (1 - B(r)). \quad (9.7)$$

In Appendix D, we derive a set of “wave-like” partial differential equations governing the time evolution of gravitational and matter perturbations for this setup. We extend the framework introduced in Sec. 2.1.3 to include matter perturbations. Also, recall that spherical symmetry allows us to separate this problem in the axial and polar sectors. For the axial sector, gravitational perturbations decouple from matter ones, and we obtain a single master equation with an effective potential

$$\mathcal{L}_1 \Psi^{\text{ax}} - V^{\text{ax}} \Psi^{\text{ax}} = S^{\text{ax}}, \quad (9.8)$$

where $\mathcal{L}_v = v^2 \partial^2 / \partial r_*^2 - \partial^2 / \partial t^2$ denotes the wave operator with characteristic speed of propagation v . Axial perturbations propagate with the speed of light $v = 1$, and in vacuum the equation above corresponds to the Regge-Wheeler equation (2.39). The source depends on the motion of the secondary object (which we explicitly compute for circular motion in the Appendix D).

The polar sector is more involved because matter perturbations source gravitational ones and vice-versa. We re-expressed the problem as a set of 3 equations for $\vec{\Psi} = (S, K, \delta\rho)$

$$\hat{\mathcal{L}} \vec{\Psi} = \hat{\mathbf{B}} \partial_{r_*} \vec{\Psi} + \hat{\mathbf{A}} \vec{\Psi} + \vec{S}, \quad (9.9)$$

with $S = A/r(H_0 - K)$, and $\hat{\mathcal{L}} \vec{\Psi} = (\mathcal{L}_1 S, \mathcal{L}_1 K, \mathcal{L}_{c_{s_r}} \delta\rho)$, i.e., S, K have characteristic velocity $v = 1$, and $\delta\rho$ has $v = c_{s_r}$. We recall K and H_0 are the gravitational perturbations given by Eq. (2.19) and $\delta\rho$ is the perturbation of the energy density of the fluid. c_{s_r} is the speed of sound along the radial direction and depends on the internal properties of the environment, i.e. its equation of state. This relates the pressure with density perturbations via

$$\delta p_{t,r}^{\ell m}(t, r) = c_{s_t}^2(r) \delta\rho^{\ell m}(t, r). \quad (9.10)$$

where $c_{s_r}(r)$ and $c_{s_t}(r)$ are, respectively, the radial and transverse sound speeds.

9.1 BLACK HOLES IN DARK MATTER HALOS

9.1.1 *The Hernquist Profile*

We now want to apply our framework to a particular background describing a BH surrounded by a galactic DM halo. Observations and large-scale simulations guide the profile of the halo matter distribution. Here, we pick Hernquist-type distributions appropriate to describe central bulges of galaxies and elliptical galaxies at the Newtonian level [90]. Their matter density is

$$\rho = \frac{Ma_0}{2\pi r(r+a_0)^3}, \quad (9.11)$$

where M is the total mass of the “halo” and a_0 a typical lengthscale, where for astrophysical solutions $a_0 \gg M$. Recall that the Milky Way halo has $\sim 10^{12}M_\odot$ extended along $\sim 10^2$ kpc, which in geometric units gives $M/a_0 \sim 10^{-6}$. Our choice is mainly practical since the Hernquist profile has “well-behaved” mathematical properties in comparison with other popular profiles such as the Navarro-Frenk-White [52], Jaffe [449] or King [450] which are known to have pathological behavior at large distances.

The Hernquist model – as well as others in the same “family” [52, 90, 449, 450] – have an increased density in the cores of the galaxies. However, in the presence of a BH at the core, the density profile is zero close to the horizon [109, 111, 124]. The DM profile develops a cusp close to the horizon, with a length scale dictated by the BH. The density profile vanishes at the horizon. The precise details of the profile depend on the equation of state, but eventually give way to Hernquist-like profiles.

9.1.2 *The Einstein Cluster*

Now let us place a BH at the center of the Hernquist profile (9.11) and find a spherically symmetric GR geometry which on small scales describes a BH and on large scales describes matter distributed according to (9.11). We can follow Einstein in his construction of a stationary system of many gravitating masses, an “Einstein Cluster” [451, 452], and generalize it to include a central BH. This recipe takes particles in all possible circular geodesics, and deals with an “average” stress-energy tensor [451, 452], characterized by the matter density ρ .

The Einstein construction assumes then an effective energy momentum tensor $\langle T^{\mu\nu} \rangle = \frac{n}{m_p} \langle p^\mu p^\nu \rangle$, with n the number density of particles with mass m_p , and p^μ the four-momentum satisfying the geodesic equations. This construction is equivalent to having an anisotropic material with energy-momentum tensor as in Eq. (9.1) with only tangential pressure $p_t^{(0)}$, and vanishing radial pressure ($p_r^{(0)} = 0$).

The second step in the Einstein Cluster construction is to assign a mass function $m(r)$ to the system. We explore the following choice inspired by the Hernquist profile

$$m(r) = M_{\text{BH}} + \frac{Mr^2}{(a_0 + r)^2} \left(1 - \frac{2M_{\text{BH}}}{r}\right)^2. \quad (9.12)$$

At small distances, this profile describes a source of mass M_{BH} and at large distances recovers the mass function of the Hernquist distribution. Note that for astrophysical systems, the mass of the halo is much bigger than the mass of the BH, so we have the hierarchy $a_0 \gg M \gg M_{\text{BH}}$. We experimented with other mass functions and the qualitative conclusions below do not change.

Plugging this mass function in the Einstein's equations, we obtain a simple analytic solution for the background spacetime

$$A(r) = \left(1 - \frac{2M_{\text{BH}}}{r}\right) e^{Y(r)}, \quad (9.13)$$

$$Y(r) = -\pi \sqrt{\frac{M}{\xi}} + 2 \sqrt{\frac{M}{\xi}} \arctan \frac{r + a_0 - M}{\sqrt{M\xi}}, \quad (9.14)$$

$$\xi = 2a_0 - M + 4M_{\text{BH}}. \quad (9.15)$$

$$4\pi\rho(r) = \frac{2M(a_0 + 2M_{\text{BH}})(1 - 2M_{\text{BH}}/r)}{r(r + a_0)^3}. \quad (9.16)$$

Let us dissect some of its properties. It has a horizon at $r_{\text{H}} = 2M_{\text{BH}}$, as Schwarzschild, and a curvature singularity at $r = 0$, thus describing a BH spacetime. At large distances away from the BH, the Newtonian potential recovers that of the Hernquist profile, and the spacetime is asymptotically flat. The ADM mass is $M + M_{\text{BH}}$. For astrophysical relevant solutions, the gravitational potential at far away distances is dominated by the halo and the Ricci scalar behaves as $R \sim 4Ma_0/r^4$, while as it approaches the horizon it goes as $R \sim M/(a_0^2 M_{\text{BH}})$, which can be made small in a controlled way. For non-astrophysical parameters it is possible to have pathological solutions. For example if $M > 2(a_0 + 2M_{\text{BH}})$, there are curvature singularities at $r = M - a_0 \pm \sqrt{M^2 - 2Ma_0 - 4M M_{\text{BH}}}$.

The weak and strong energy conditions are satisfied everywhere. However, since the matter density vanishes at the horizon but the tangential pressure remains finite, the dominant energy condition will be violated close to it. As we discussed above, the near-horizon region is very depleted so this violation should have little impact on the dynamics, as the pressure and density can be made arbitrarily small in this region.

Close to the central BH we find that the redshift factor $e^Y \sim 1 - 2M/a_0$, a property that is generic for other configurations [105, 107, 453].

9.1.3 Redshift and Light Rings

The spacetime above can be used as a proxy to explore the phenomenology of BHs and GWs from objects deep in the galactic potential. Let us start by doing the simplest thing one can do when faced with a new spacetime geometry, which is to study geodesic motion. The location of the LR can be computed as in Section 5.1 and is given by the roots of $r(r_{\text{LR}}) = 3m(r_{\text{LR}})$. With this radius determined, we can then compute the LR frequency Ω_{LR} , the Lyapunov exponent λ_{L} and the critical impact parameter b_{c} for the capture of high-frequency waves which were introduced previously in Chapter 5. Expanding these quantities in power of M/a_0 (which we recall needs to be small for astrophysical setups), we find up to order $\mathcal{O}(1/a_0^3)$

$$r_{\text{LR}} \approx 3M_{\text{BH}} \left(1 + \frac{MM_{\text{BH}}}{a_0^2} \right), \quad (9.17)$$

$$M_{\text{BH}}\Omega_{\text{LR}} \approx \frac{1}{3\sqrt{3}} \left(1 - \frac{M}{a_0} + \frac{M(M + 18M_{\text{BH}})}{6a_0^2} \right), \quad (9.18)$$

$$M_{\text{BH}}\lambda_{\text{L}} \approx \frac{1}{3\sqrt{3}} \left(1 - \frac{M}{a_0} + \frac{M^2}{a_0^2} \right), \quad (9.19)$$

$$b_{\text{c}} = 3\sqrt{3}M_{\text{BH}} \left(1 + \frac{M}{a_0} + \frac{M(5M - 18M_{\text{BH}})}{6a_0^2} \right), \quad (9.20)$$

The first order correction linear in M/a_0 is simply signaling a redshift of the mass scale of the system $M \rightarrow M(1 + M/a_0)$. The first “non-linear” corrections in M/a_0 , that would indicate the presence of new physics, appear at orders of magnitude which are too small to be detectable by BH imaging experiments. We therefore conclude that tests on the nature of BHs based on LR physics like the ones performed by the Event Horizon Telescope and the GRAVITY collaboration [281, 454] are not going to be spoiled by the presence of a non-vacuum environment. *A priori*, this is expected because the matter around the LR region is very depleted but it is reassuring to see it be derived from the formalism without the need to rely on Newtonian-like approximations. Results are similar for other orbits of interest, like the ISCO.

9.2 AXIAL SECTOR

Having understood geodesic motion in our playground model for a BH surrounded by a DM halo, we move on to the study of its dynamics at a perturbative level, as introduced in Sec. 2.1.3. We start with the more straightforward axial sector, where gravitational perturbations completely decouple from matter ones. Consequently, it is governed by the single master wave equation in Eq. (D.25).

9.2.1 QNMs and Love Numbers

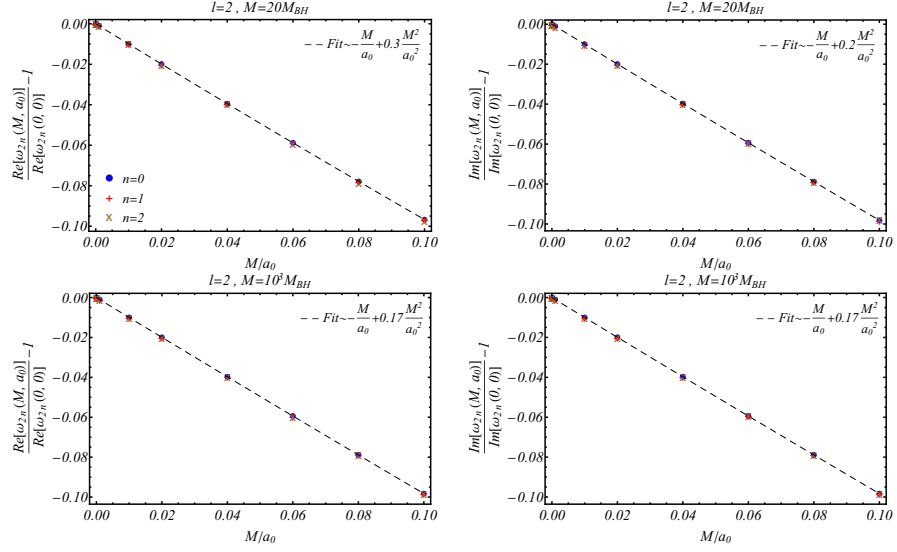


Figure 9.1: *Top panel*: Real and imaginary part deviations of galactic axial QNMs $\omega_{\ell n}(M, a_0)$, with $M = 20M_{\text{BH}}$, from the vacuum Schwarzschild QNMs $\omega_{\ell n}(0, 0)$ for $\ell = 2$ as a function of the compactness M/a_0 . Different plot markers denote different overtones. The dashed black line represents a fit to the relative difference for powers of M/a_0 . *Bottom panel*: Same as the top panel with $M = 10^3 M_{\text{BH}}$. The fit agrees with the LR corrections obtained in Eq. (9.18).

Following the same steps as in Chapter 3, we can solve the axial problem in the static limit and compute the Love numbers of this configuration. We obtain a closed-form analytical expression in the small M limit

$$k_{\ell=2}^B = \frac{Ma_0^4(5 + 12 \log(a_0 + 2M_{\text{BH}}))}{3(M + M_{\text{BH}})^5}. \quad (9.21)$$

The scaling with M and a_0 agrees with our results in Chapter 3 (cf. Eq (3.108)).

We also computed the QNMs of the axial sector using standard direct integration and spectral routines [188, 455, 456]¹. Our results are summarized in Fig. 9.1 for the quadrupole. We have accurately computed the fundamental mode and the first two overtones for various halo masses. We find that QNMs depend solely on the compactness M/a_0 and only change slightly when the halo mass M is increased by two orders of magnitude. We fitted the relative differences to the QNMs

¹ The computation of the axial QNM spectrum was conducted by Kyriakos Destounis and Rodrigo Panosso Macedo

with respect to vacuum to powers of M/a_0 . In the astrophysical limit $M \gg M_{\text{BH}}$

$$\frac{\omega_{\ell n}(M, a_0)}{\omega_{\ell n}(0, 0)} \sim 1 - \frac{M}{a_0} + 0.17 \frac{M^2}{a_0^2} + \mathcal{O}\left(\frac{M^3}{a_0^3}\right). \quad (9.22)$$

The first-order correction in M/a_0 is again giving the redshift of the dynamics. Remarkably, the second-order agrees with the correction on the LR frequency as in Eq. (9.18). This behavior of the QNMs is consistent with the interpretation discussed on Chapter 5 that they correspond to high-frequency waves trapped at the LR that are slowly escaping out.

9.2.2 Extreme-mass-ratio systems

ℓ	m	\dot{E}_∞^t	\dot{E}_∞^f	$\dot{E}_\infty^{\text{BHPT}}$
2	1	8.1629e-7	8.1631e-7	8.1631e-7
		6.9156e-7	6.9158e-7	
2	2	1.7068e-4	1.7062e-4	1.7062e-4
		1.6077e-4	1.6208e-4	
3	2	2.5198e-7	2.5199e-7	2.5198e-7
		2.1611e-7	2.1612e-7	
3	3	2.5490e-5	2.5473e-5	2.5471e-5
		2.3163e-5	2.3140e-5	
4	3	5.7750e-8	5.7749e-8	5.7749e-8
		5.0252e-8	5.0252e-8	
4	4	4.7352e-6	4.7260e-6	4.7253e-6
		4.0458e-6	4.0823e-6	

Table 9.1: Energy flux (in units of m_p^2/M_{BH}^2) emitted in GWs to infinity in different modes by a particle in a circular orbit at radius $r_p = 7.9456M_{\text{BH}}$ around a BH surrounded by a Hernquist-type DM halo. We show results for vacuum (first line of each mode) and for a halo with $(c_{s_r}, c_{s_t}) = (0.9, 0)$, $M = 10M_{\text{BH}}$ and $a_0 = 10M$ (second line of each mode). \dot{E}_∞^t is computed with the time-domain framework, whereas \dot{E}_∞^f are computed in the frequency domain and $\dot{E}_\infty^{\text{BHPT}}$ corresponds to results available online from the BH perturbation toolkit, available only in vacuum. $\ell = m$ modes correspond to polar excitations whereas $\ell = m + 1$ correspond to axial ones.

Finally, we can study the EMRI problem, where we put a point particle orbiting the central BH (details for the source term are presented in Appendix D). We solved the problem numerically using the time-domain framework introduced in Sec. 2.2, but also in the

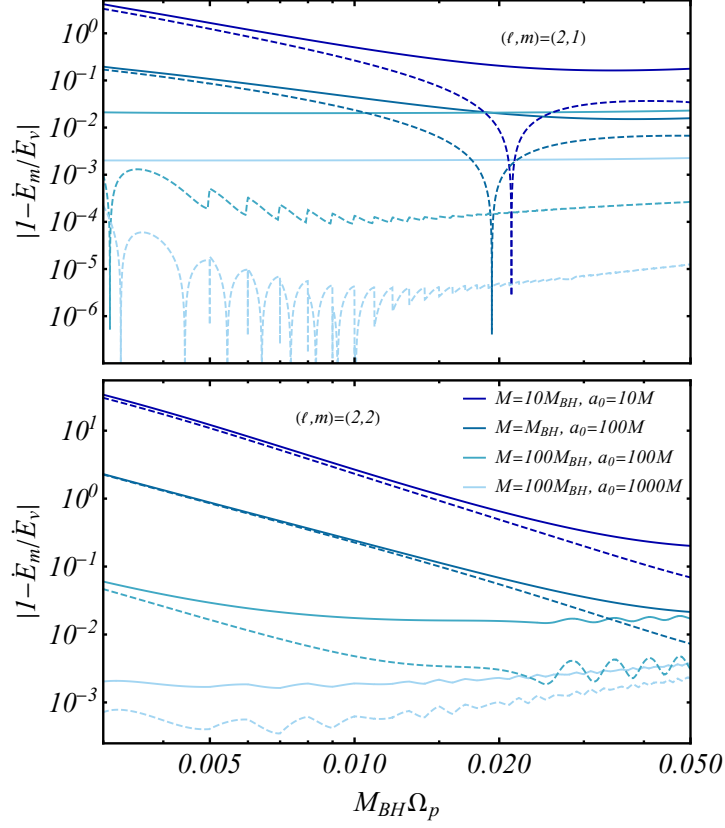


Figure 9.2: *Top panel:* Relative difference between the energy flux emitted by a circular EMRI in the dominant axial mode $\ell = 2$, $m = 1$ as a function of the orbital frequency Ω_p , for different halo configurations (\dot{E}_m) and in vacuum (\dot{E}_v) (solid lines). Dashed lines represent the same comparison but with the vacuum fluxes redshifted according to Eq. (9.25). The frequencies correspond to a secondary at radius ranging from $r_p = 50M_{\text{BH}}$ down to $r_p = 6M_{\text{BH}}$; *Bottom panel:* Same as the top panel but for the dominant polar mode $\ell = 2$, $m = 2$. In this case, the redshift correction correctly captures the variation of the flux with the orbital frequency.

frequency-domain following Ref. [457]². We have tested our procedure and routines in the vacuum limit, i.e. using a geometry [176] with a low value of the halo mass $M = 10^{-6}M_{\text{BH}}$, comparing the GW fluxes with those available online from the Black Hole Perturbation Toolkit [434]. Results are summarized in Table 9.1 (for now let us focus the discussion on the axial modes with $\ell = m + 1$), and compare favorably both between different implementations and with the Black Hole Perturbation Toolkit in vacuum.

It is clear from Table 9.1 that, for a fixed BH mass, the fluxes are smaller in the presence of a halo. One could then wonder that when

² The frequency-domain computations were led by Prof. Andrea Maselli. As in the time-domain, this code uses a smoothed distribution to approximate the point particle, $\sqrt{2\pi}\sigma\delta(r - r_p) = \exp(-(r - r_p)^2/(2\sigma^2))$ where the width σ is varied to ensure numerical convergence.

accumulated over many orbits, this would significantly change the inspiral. Typically, relative differences of $\sim 1\%$ in the energy fluxes may result in observable differences in the waveform of an EMRI. However, we know that the EMRI is evolving in a nontrivial gravitational potential of the DM halo, so a decreasing flux might just signal some kind of redshift effect. Let us focus on realistic astrophysical systems, for which there is the scale hierarchy $a_0 \gg M \gg M_{\text{BH}}$. To linear order in M/a_0 ,

$$\frac{dr}{dr_*} \approx \left(1 - \frac{M}{a_0}\right) \frac{dr}{dr_*^{\text{vac}}}, \quad (9.23)$$

where r_*^{vac} is the tortoise coordinate in a Schwarzschild geometry (2.16). For compact EMRIs ($r_p \sim 10M_{\text{BH}}$), $S^{\text{ax}} \approx (1 - 3M/a_0) S_{\text{vac}}^{\text{ax}}$. Combining these, expanding Eq. (D.25) to linear order in M/a_0 we find (in the frequency domain)

$$\frac{d^2 \Psi^{\text{ax}}}{d(r_*^{\text{vac}})^2} + \left(\frac{\omega^2}{\gamma^2} - V_{\text{Schw}}^{\text{ax}}\right) \Psi^{\text{ax}} = \gamma S_{\text{Schw}}^{\text{ax}}, \quad (9.24)$$

where $\gamma = 1 - M/a_0$ is a redshift factor. Thus, to linear order in γ the axial signal from the EMRI immersed in the Hernquist halo is identical to that from a Schwarzschild BH, with redshifted frequency and mass; in other words, the two setups are equivalent with the identification

$$\left(\Omega_p^{\text{vac}}, \omega^{\text{vac}}, m_p^{\text{vac}}\right) \rightarrow \left(\frac{\Omega_p}{\gamma}, \frac{\omega}{\gamma}, \gamma m_p\right). \quad (9.25)$$

In the top panel of Fig. 9.2, we present numerical results that confirm this. We show fluxes as a function of the frequency of the GWs being measured by a distant stationary observer. *A priori*, this direct comparison gives differences between a vacuum and a non-vacuum environment that are seemingly large. However, when we apply the redshift correction above, the fluxes in the presence of the halo are indeed well described by redshifted fluxes in vacuum. The agreement is better for larger halo mass M , and smaller compactness M/a_0 . For realistic galactic configurations, it leads to relative differences that are extremely small and not expected to be observable. Note that for small scales, $a_0 \omega \lesssim 1$, the radiation wavelength is larger than the halo itself, and redshift is suppressed.

9.3 POLAR SECTOR

We now to move the polar sector, which dominates GW emission.

9.3.1 Boundary conditions and sound speed

One of the major technical problems associated with the evolution of polar perturbations in non-vacuum backgrounds is that gravitational

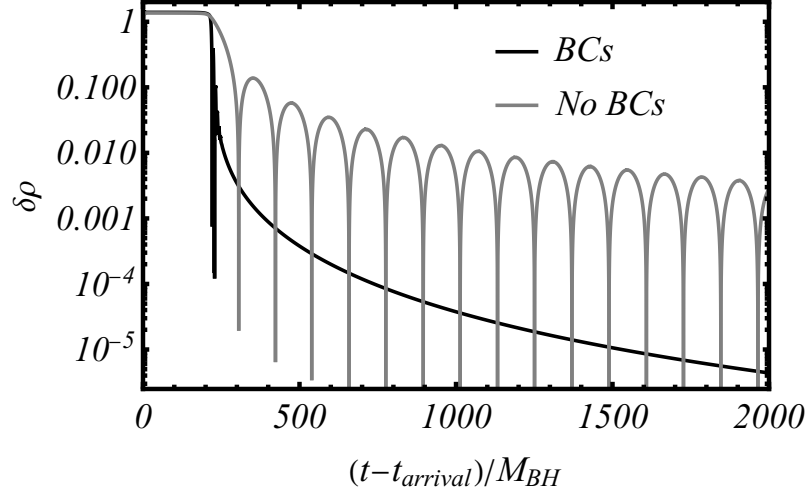


Figure 9.3: Evolution of $\delta\rho$ in a Schwarzschild background with $c_{s_r} = 0.9$, $c_{s_t} = 0.0$ when different boundary conditions are imposed. $t_{arrival}$ is the time of arrival of the first direct signal coming from the initial data prescribed. When no boundary conditions are imposed (*No BCs*), and $\delta\rho$ is left free at the **BH** horizon, an oscillatory tail of the form $\delta\rho \propto t^{-5/6} \sin(\mu_{\text{eff}} c_{s_r})$ sets in at late times, with $\mu_{\text{eff}} = (1 - c_{s_r}^2) / 8c_{s_r}^2 M_{\text{BH}}$. This is analogous to having a scalar field of mass $\mu_{\text{eff}} c_{s_r}$. On the other hand, when Dirichlet boundary conditions (*BCs*), $\delta\rho = 0$, are imposed at a cutoff radius r_{cut} (here $r_{\text{cut}} = 3M_{\text{BH}}$), we find a universal power-law decay independent of r_{cut} and c_{s_r} , consistent with $\delta\rho \propto t^{-3}$.

perturbations are coupled to the matter sector. However, in our setup, at far away distances and very close to the **BH** horizon, the matter density ρ vanishes, and the field equations reduce to the case of a vacuum **BH**. When this happens, the gravitational sector decouples from matter (and vice-versa).

Considering first the case where the sound speeds introduced in Eq. (9.10) are *constant* and taking the following ansatz for the density perturbation

$$\delta\rho = r^\alpha (r - 2M_{\text{BH}})^\beta \Psi_\rho, \quad (9.26)$$

we obtain that Ψ_ρ obeys to

$$\mathcal{L}_{c_{s_r}} \Psi_\rho = V_\rho \Psi_\rho, \quad (9.27)$$

$$\alpha = \frac{1}{4} \left(-5 + \frac{1 + 4c_{s_t}^2}{c_{s_r}^2} \right), \quad (9.28)$$

$$\beta = -\frac{3}{4} - \frac{1}{4c_{s_r}^2}, \quad (9.29)$$

$$V_\rho \approx \mathcal{O}(r^{-2}), \quad r \rightarrow \infty \quad (9.30)$$

$$V_\rho \approx \left(\frac{1 - c_{s_r}^2}{8c_{s_r}^2 M_{\text{BH}}} \right), \quad r \rightarrow 2M_{\text{BH}}. \quad (9.31)$$

These properties are similar to the ones of a massive scalar field with effective mass $\mu_{\text{eff}} = \frac{1-c_{s_r}^2}{8c_{s_r}^2 M_{\text{BH}}}$. Based on previous results for this system [458–460], the scattering of a Gaussian pulse should lead to an oscillatory power-law with $\Psi_\rho \propto t^{-5/6} \sin(\mu_{\text{eff}} c_{s_r} t)$, due to wave backscattering near the horizon.

To confirm this, we evolved the homogeneous version of the evolution equation for ρ (D.37) in a Schwarzschild background with initial data

$$\begin{aligned} \delta\rho \Big|_{t=0} &= 0, \\ \partial_t \delta\rho \Big|_{t=0} &= \exp\left[-(r_* - 100M_{\text{BH}})^2/2\right]. \end{aligned} \quad (9.32)$$

The results presented in Fig. 9.3 for the $\ell = 2$ mode (in gray) agree with the expected behavior, and this was verified for different initial data and c_{s_r} .

However, since the matter profile vanishes at the horizon and spatial infinity, physical configurations should have asymptotically vanishing sound speed at these boundaries. If we impose a power-law decay at the boundary for c_{s_r} , then $\delta\rho$ has to satisfy Dirichlet boundary conditions $\delta\rho = 0$ in order to be regular at the boundaries. We repeated the same numerical experiment as above, but now keeping c_{s_r} constant and imposing Dirichlet boundary conditions at a cutoff radius r_{cut} close to the BH horizon. In this case ($c_{s_t} = 0$), the late-time behavior should be $\delta\rho = t^{-3}$ for all multipoles, but now due to backscattering at far-away distances [458]. This decay is independent of ℓ because the homogeneous part of the evolution equation for $\delta\rho$ in Eq. (D.37) is independent of ℓ for $c_{s_t} = 0$. Once again, we verified this numerically (in black in Fig. 9.3), independently of the cutoff radius r_{cut} and the sound speed c_{s_r} .

9.3.2 QNM spectral stability

Taking into account the results of the previous section, from now on we impose vanishing sound speed c_{s_r} at an interior cutoff radius close to the BH horizon. Since in the polar sector, matter perturbations are coupled to gravitational ones we expect two families of modes, one traveling at the speed of light and determined by gravity, and the other traveling at the speed of sound c_{s_r} and controlled by the matter distribution.

We repeated the scattering experiment of the previous section, with the same initial data given by Eq. (9.32) but for the metric function K , and for a very compact halo configuration with $M = 10M_{\text{BH}}$ and $a_0/M = 10$, to enhance the physical effects. We chose for the profile of the radial speed of sound

$$c_{s_r} = \left(\frac{2M_{\text{BH}} + a_0}{r + a_0}\right)^4, \quad (9.33)$$

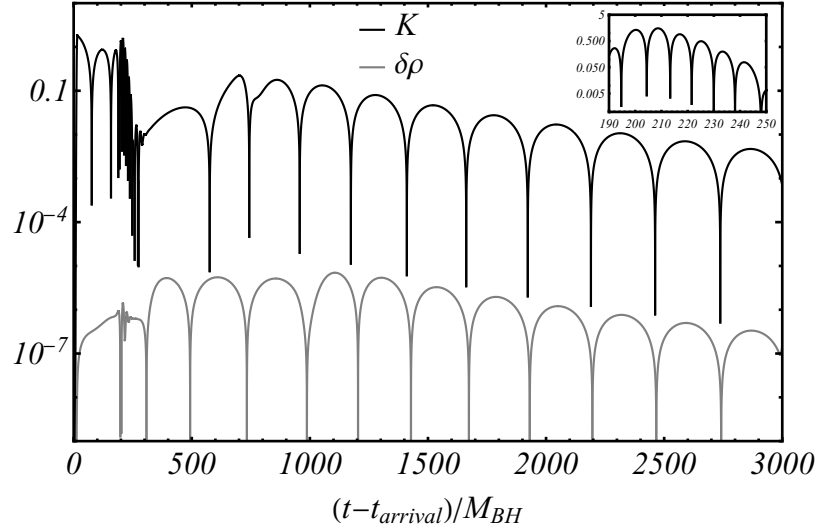


Figure 9.4: Evolution of the metric and density perturbation K , $\delta\rho$, with $M = 10M_{\text{BH}}$, $a_0 = 10M$. We impose Dirichlet conditions at $r_{\text{cut}} = 3M_{\text{BH}}$ and $c_{s,r} = [(2M_{\text{BH}} + a_0) / (r + a_0)]^4$, so that the radial speed of sound asymptotes to zero at large distances. At early times, a standard BH ringdown is excited, as can be seen in the inset for K ; at late times, the signal is dominated by a slowly-decaying, fluid-driven mode with period $\sim a_0$. There is a mutual conversion between gravitational and matter density waves, which is a manifestation of the spectral instability of BH QNMs. The qualitative conclusions are independent of the initial data given and the profile chosen for $c_{s,r}$.

but our qualitative conclusions are similar for other choices. In the polar sector, we do not use the hyperboloidal layers introduced in Section 2.2.3, because matter waves do not travel at the speed of light and therefore do not reach null infinity.

Our results are shown in Fig. 9.4 for the quadrupole $\ell = 2$ mode. Initially, we observe a standard BH ringdown, as highlighted in the inset, with a frequency close to the fundamental Schwarzschild QNM with $\omega_{\ell=2}^{\text{Schw}} = 0.374 - 0.089i$. At late times, the signal is dominated by a long-lived fluid mode, whose period is of the order of the typical length scale of the halo a_0 . We also observe the conversion between GWs and matter waves, and vice-versa. In practice, this is a fluid mode and corresponds to a concrete manifestation of the QNM spectral instability discussed in Chapter 6 for an astrophysically motivated system.

9.3.3 Extreme-mass-ratio systems

We now revisit the EMRI problem. Again, there is good agreement between the results from different codes and the ones from the Black Perturbation Toolkit in vacuum, as shown in Table 9.1 (polar modes

are the ones with $\ell = m$). Since polar fluctuations couple to the fluid, it is harder to do the redshift analysis presented above for the axial sector. Nonetheless, we can directly apply the redshift corrections in Eq. (9.25) to the energy fluxes carried by GWs and compare. This is illustrated in the bottom panel of Fig. 9.2, where it is clear that polar perturbations are less prone to redshift effects, even in regions of the parameter space corresponding to large, near-galactic scales.

Our results indicate the tantalizing possibility of using GW astronomy to strongly constrain smaller scale distributions around BHs. At $\omega M_{\text{BH}} = 0.02$, the relative flux difference between a vacuum and a BH immersed in a halo with $M = 0.1M_{\text{BH}}$ and $a_0 = 10^2M, 10^3M$ is $\sim 10\%, 1\%$ respectively. These numbers are well within reach of next-generation detectors [414].

9.4 DISCUSSION

This chapter served mainly as a proof-of-concept for the ability of our framework to study environmental effects in GW physics at a full relativistic level. A natural next step is to apply it to other environments, for example by taking input from recent General Relativistic Magnetohydrodynamical simulations of accretion [86, 87], or to add rotation to the central BH.

Our example shows that environments can easily destabilize the BH spectra, as had recently been suggested with toy models [80, 173, 350, 351, 353] and discussed in Chapter 5. It is unknown at this point if environmental resonances can be excited by supermassive BHs, long-before merger. Also, we did not explore the effect of the environment in the late-time polynomial tails that follow the ringdown, nor in GW memory [461, 462]. Formally, these are zero frequency signals that should be sensitive to the full gravitational potential, possibly being more prone to changes due to the presence of a non-vacuum environment.

The relative differences in the energy flux carried by GWs appears to be more significant for lower frequencies. This behavior is particularly relevant in light of the recent announcement by the International Pulsar Timing Array of a stochastic GW background produced by BH binaries with billions of solar masses [34–37, 463–466]. In fact, preliminary studies suggest that the inclusion of environmental effects describes better the observed spectrum in the lower-frequency end [464, 465].

Our works [176, 177] spurred a series of further explorations applying the Einstein Cluster construction to other DM profiles [467–474]. One worth highlighting is the exhaustive survey of the phase space of geodesics in Ref. [468], including orbits with precession. Interestingly, there is a competition between the halo and GR effects in the direction of precession, which can transition from prograde to retrograde

for sufficiently compact configurations. The departure from vacuum typically results in non-integrable geodesics, which exhibit chaotic phenomena and resonant islands in the orbital phase space [475–477].

The complicated intrinsic properties of the anisotropic halo constituting the DM halo and the lack of a physical model for the sound speeds prevented us from studying matter fluxes, which should contain the information about accretion and dynamical friction on the EMRI. On our final discussion in the next chapter we present a strategy on how to overcome these drawbacks and our future steps in the study of environmental effects in GW astronomy.

CONCLUDING REMARKS

The formalism developed in the previous chapter has the potential to become a benchmarking tool for the systematic analysis of environmental effects in GW astronomy. This can ultimately be fed into the analysis pipelines used by various GW collaborations. For this reason, the codes we used are already publicly available [478]. Nonetheless, as we discussed at the end of the previous chapter, there are still challenges to overcome. In the system we studied, we did not consider matter fluxes, so we could not retrieve information about accretion and dynamical friction. Moreover, at this stage we do not know how to correctly evaluate the backreaction on the orbit and evolve the inspiral. In a vacuum binary we can consider an adiabatic approximation where the smaller body “flows through a sequence of geodesics” [31] of the background spacetime, determined by their respective conserved quantities: energy, angular momentum, and Carter constant (which is 0 in Schwarzschild). However, in non-vacuum, the fluxes will contain contributions from the gravitational binding energy of the binary but also from the environment, which need to be disentangled.

1. IMPROVE MODELING

The first step of our plan is therefore to understand better the modeling aspects just described. To do that, we will apply our formalism to simpler environments, starting with EMRIs surrounded by scalar fields [107, 108, 282, 479–481], for which we already have preliminary results.

In the long run, we would like to study EMRIs in thin accretion disks describing AGNs. In this case, our techniques can be combined with state-of-the-art General Relativistic Magnetohydrodynamic simulations, which are currently only using Newtonian physics [86, 87, 124]. This could also be relevant for computing the electromagnetic counterpart of binary coalescences in AGNs.

Moreover, accretion disks exhibit turbulence due to various phenomena, such as magnetorotational instability [482]. The GW signature associated with these turbulent flows has yet to be studied. Even though the typical matter densities are too low to expect individual events, they could contribute to a putative non-negligible stochastic GW background.

Finally, it will also be important to understand the most effective way to include rotation, which could be done either in terms of a small spin expansion or working in the tetrad formalism.

2. WAVEFORM IMPLEMENTATION

After the modeling stage is completed, we can start implementing them in state-of-art waveform models, like the FastEMRIWaveform package [83]. This is a modular code designed to facilitate custom changes. For example, one can simply add to the fluxes of energy and angular momentum the correction coming from a particular environment and have a ready-to-use code which generates waveforms for the new system in seconds. This strategy has been used for gas torques in thin accretion disks [84] and dynamical friction. Moreover, even though we have been focusing the discussion on EMRIs, BH perturbation theory agrees remarkably well with Numerical Relativity simulations up to mass-ratios of $\mathcal{O}(10)$ [33]. Consequently, it can also be useful to try to implement our results in Effective-One-Body [483, 484] and Inspiral-Merger-Ringdown [485, 486] models.

3. DETECTABILITY/MEASURABILITY FORECASTS

Once implemented, we can use the updated models to perform an exhaustive survey of their impact on the detectability and measurability of GW events. Following previous works [30, 84, 124], we want to answer the following questions:

- Considering mismodeling, statistical and instrumental systematic errors (which are currently unstudied), what is the expected level of accuracy of future waveforms and how strong environmental effects have to be to become distinguishable?
- If the strength of the environmental effects surpasses this threshold, with what precision can we infer the properties of the environment?
- What bias will we incur in parameter estimation if environmental effects are ignored and how will that hinder tests of GR?
- What is the degeneracy between corrections introduced by the environment and those of modified gravity [487]?
- What is the impact of relativistic modeling of environmental in EMRI population rates detectable by LISA?

This is certainly an ambitious plan which will require years of collaborative effort. Nonetheless, it is one that can bring precious dividends for a research topic that has been gaining widespread interest in recent years. This is exhibited by the increasing number of papers appearing every week on this topic, and by the organization

of conferences/workshops entirely dedicated to it. [LISA](#) and third-generation ground-based detectors will be operating by the end of next decade and therefore there is no better time to do the necessary theoretical work for them than *now*. I would like to end with a word of appreciation for all the generations of physicists who have dedicated their careers to [GW](#) astronomy. Their work has offered a once-in-a-lifetime opportunity for young scientists like me to be in the *right* place, at the *right* time, doing the *right* science, and be part of what most likely will be a period marked by incredible discoveries in gravity and astrophysics.

Part IV

APPENDIX

A

PERTURBATION THEORY IN QUANTUM MECHANICS

In this appendix we explain how the problem studied in Chapter 4 can be treated analytically using standard perturbation theory in Quantum Mechanics.

In the non-relativistic limit, the scalar cloud obeys an equation which is formally equivalent to Schrödinger's equation with a Coulomb potential governed by a single parameter

$$\alpha = M\mu. \quad (\text{A.1})$$

This can be seen by making the standard *ansatz* for the dynamical evolution of Φ [135, 236, 488]

$$\Phi(t, r^j) = \frac{1}{\sqrt{2\mu}} \left(\psi(t, r^j) e^{-i\mu t} + \psi^*(t, r^j) e^{i\mu t} \right), \quad (\text{A.2})$$

where ψ is a complex field which varies on timescales much larger than $1/\mu$. Then, one can expand the Klein-Gordon equation to first order in α and arrive at

$$i\partial_t \psi = \left(-\frac{1}{2\mu} \nabla^2 - \frac{\alpha}{r} \right) \psi, \quad (\text{A.3})$$

where we also kept only terms of order $\mathcal{O}(r^{-1})$.

The normalized eigenstates of the system are hydrogenic-like, with an adapted "fine structure constant" α and "reduced Bohr radius" a_0 [103, 270],

$$\psi_{n\ell m} = e^{-i(\omega_{n\ell m} - \mu)t} R_{n\ell}(r) Y_{\ell m}(\theta, \varphi), \quad (\text{A.4})$$

$$R_{n\ell}(r) = C \left(\frac{2r}{na_0} \right)^\ell L_{n-\ell-1}^{2\ell+1} \left(\frac{2r}{na_0} \right) e^{-\frac{r}{na_0}},$$

$$a_0 = \frac{1}{\mu\alpha}, \quad C = \sqrt{\left(\frac{2}{na_0} \right)^3 \frac{(n-\ell-1)!}{2n(n+\ell)!}}, \quad (\text{A.5})$$

where $L_{n-\ell-1}^{2\ell+1}$ is the generalized Laguerre polynomial [182]. We are adopting the convention for the quantum numbers used in Refs. [135, 268], where states are labeled by $n = \ell + 1, \ell + 2, \dots$. The eigenvalue is, up to terms of order α^5 [489]

$$\omega_{n\ell m} = \mu \left(1 - \frac{\alpha^2}{2n^2} - \frac{\alpha^4}{8n^4} + \frac{(2\ell - 3n + 1)\alpha^4}{n^4(\ell + 1/2)} \right) + \mathcal{O}(\alpha^5). \quad (\text{A.6})$$

We can estimate the size of the scalar cloud by computing the expectation value of the radius on a given state

$$\langle r \rangle = \int_0^\infty dr r^3 R_{n\ell}^2(r) = \frac{a_0}{2} (3n^2 - \ell(\ell + 1)) . \quad (\text{A.7})$$

When the binary companion is included, the tidal perturbation can be treated in the framework of perturbation theory in Quantum Mechanics. The tidal potential δV entering in Schrödinger's equation due to $\delta ds_{\text{tidal}}^2$ (4.2) is represented by a step function

$$\delta V = -\Theta(t - t_0) \frac{M_c \mu}{R} \sum_{m=-2}^2 \frac{4\pi}{5} \left(\frac{r}{R}\right)^2 Y_{\ell m}^*(\theta_c, \varphi_c) Y_{\ell m}(\theta, \varphi) , \quad (\text{A.8})$$

where t_0 is the instant when we turn it on and $\Theta(t)$ is the Heaviside function. Though there is an implicit time dependence, if one lets the system evolve for sufficient time, it will end in a final stationary state (ignoring the loss of energy at the BH horizon). To describe the final picture, time-independent perturbation theory is enough.

Let us recall its standard procedure. We are solving Schrödinger's equation

$$\mathcal{H} |\psi_i\rangle = \omega_i |\psi_i\rangle , \quad (\text{A.9})$$

$$\mathcal{H} = \mathcal{H}_0 + \lambda \delta V , \quad (\text{A.10})$$

where \mathcal{H}_0 is the Hamiltonian of the unperturbed problem, δV is the potential corresponding to the perturbation, and λ is a dimensionless expansion parameter varying between 0 (no perturbation) and 1 (full perturbation). Since we are now referring to a generic problem, we have dropped the triple indices of the "hydrogenic" spectrum and instead label different eigenstates $|\psi_i\rangle$ of the Hamiltonian (and the respective eigenvalue frequencies ω_i) by a single index ¹.

When the system is non-degenerate, the eigenstates $|\psi_k^{(0)}\rangle$ of the unperturbed problem - which are assumed to be known and in our case are given by Eq. (A.5) - are in one-to-one correspondence with the eigenvalues, $\omega_k^{(0)}$,

$$\mathcal{H}_0 |\psi_i^{(0)}\rangle = \omega_i^{(0)} |\psi_i^{(0)}\rangle , \quad (\text{A.11})$$

and $\{\psi_n^{(0)}\}$ form a complete orthonormal basis

$$\langle \psi_m^{(0)} | \psi_n^{(0)} \rangle = \delta_{mn} . \quad (\text{A.12})$$

Now, we expand the eigenstates of the perturbed system, ψ_i , in terms of the basis $\{\psi_k^{(0)}\}$

$$|\psi_i\rangle = \sum_k c_{ki} |\psi_k^{(0)}\rangle , \quad (\text{A.13})$$

¹ In Quantum Mechanics literature, it is common to use E for the (energy) eigenvalues, but since we are working in natural units, $\hbar = 1$, there is no distinction between them

and plugging this *ansatz* in (A.9), the coefficients c_{ki} and the eigenvalues ω_i can be obtained as a power series in λ . If the perturbation is small enough, we expect the first-order expansions to be a good approximation [490]

$$\omega_i = \omega_i^{(0)} + \lambda \omega_i^{(1)}, \quad (\text{A.14})$$

$$c_{ki} = c_{ki}^{(0)} + \lambda c_{ki}^{(1)}, \quad (\text{A.15})$$

$$\omega_i^{(1)} = \langle \psi_i^{(0)} | \delta V | \psi_i^{(0)} \rangle, \quad (\text{A.16})$$

$$c_{ki}^{(1)} = \frac{\langle \psi_k^{(0)} | \delta V | \psi_i^{(0)} \rangle}{\omega_i^{(0)} - \omega_k^{(0)}}, \quad k \neq i, \quad (\text{A.17})$$

where we omitted terms of order $\mathcal{O}(\lambda^2)$. In the end, we set $\lambda = 1$, which is the same as reabsorbing it in δV .

The timescales for the transitions between two modes can be estimated using time-dependent perturbation theory. This involves introducing the interaction picture and performing a Dyson series on the time-evolution operator. Since the eigenstates remain the same as in the time-independent unperturbed case, we will skip details on this procedure and directly import the result for the first-order correction on the coefficients c_{ki} for a step-function perturbation [491]

$$c_{ki}^{(1)} = \frac{\langle \psi_k | \delta V | \psi_i \rangle}{\omega_i - \omega_k} \left(1 - e^{-i(\omega_i - \omega_k)t} \right). \quad (\text{A.18})$$

Both the states $|\psi_i\rangle$ and frequencies ω_i should be understood as the ones for the unperturbed system, but we omit subscripts to avoid cluttering. Then, the probability of the transition $|i\rangle \rightarrow |k\rangle$ is

$$\left| c_{ki}^{(1)} \right|^2 = 4 \left| \frac{\langle \psi_k | \delta V | \psi_i \rangle}{\omega_i - \omega_k} \right|^2 \sin^2 \left(\frac{(\omega_k - \omega_i)t}{2} \right). \quad (\text{A.19})$$

Although we do not have a continuum spectrum, for large timescales we can take this limit. Then, at fixed t , we can treat the probabilities $\left| c_{ki}^{(1)} \right|^2$ as functions of

$$\Delta\omega_{ki} = |\omega_k - \omega_i|. \quad (\text{A.20})$$

Plotting it for different instants of time, one can verify this function becomes increasingly peaked around $\Delta\omega_{ki} = 0$ as t increases (check Fig. 5.8 of Ref. [491]). This central peak scales with t^2 and has a typical width of $1/t$. If we wait enough time Δt since the perturbation is introduced, the only transitions with appreciable probability are those satisfying

$$\Delta t = 2\pi / \Delta\omega_{ki}. \quad (\text{A.21})$$

The final conclusion is that the typical timescale Δt for the transition $|i\rangle \rightarrow |k\rangle$ to happen is

$$\Delta\omega_{ki} \Delta t \sim 1, \quad (\text{A.22})$$

which, if we momentarily insert factors of \hbar , can be seen as a manifestation of the energy-time uncertainty principle [491]

$$\Delta E \Delta t \sim \hbar. \quad (\text{A.23})$$

Returning to our problem, the initial data presented in Eq. (4.6) corresponds to the stationary state (reintroducing the triple “hydrogenic” indices)

$$|i\rangle \propto \left(|\psi_{211}^{(0)}\rangle - |\psi_{21-1}^{(0)}\rangle \right), \quad (\text{A.24})$$

up to a proportionality constant reflecting the renormalization done for numerical purposes. The final state should correspond to a stationary state $|f\rangle$ which we can compute using the machinery developed before. There is still a *caveat*, which is the degeneracy between states with the same quantum number m (A.5). Though a rotating BH will lift this degeneracy, the energy shifts due to the perturbations considered are orders of magnitude higher than the energy scale associated with the rotation. Thus, for non-degenerate perturbation theory to be controlled, we would have to perform it at higher orders than what we presented.

In the degenerate scenario, the equations presented are invalid (for example (A.17) diverges when $\omega_k^{(0)} = \omega_i^{(0)}$). Instead, we use the freedom in making a linear combination of unperturbed degenerate eigenstates, so that in every degenerate subspace, we pick a basis of the Hilbert space that diagonalizes the full Hamiltonian \mathcal{H} (A.10). After this step, we can apply non-degenerate perturbation theory, namely Eqs. (A.16) and (A.17), using the new “good” basis.

Finally, the numerical data we present in the main text corresponds to multipole expansions of the field Φ and not to the coefficients c_{ki} (A.13) describing the mix of the unperturbed states. To obtain these multipoles we have to select them from the space representation of the final state. The amplitude coefficients of the mode $|\psi_{n\ell m}\rangle$ are obtained via

$$c_{n\ell m} \propto \frac{\langle \psi_{n\ell m} | \delta V | i \rangle}{\omega_{21}^{(0)} - \omega_{n\ell}^{(0)}}, \quad (\text{A.25})$$

$$\phi_{n\ell m}(r) \propto c_{n\ell m} R_{n\ell}(r). \quad (\text{A.26})$$

In the end, we are interested in the ratio between amplitudes so the constant of proportionality is irrelevant. The matrix elements appearing here are explicitly presented in Eqs.(3.7) – (3.9) of Ref. [135]. Notice that the relative amplitude between modes with the same quantum numbers n and ℓ is completely determined by the angular integrals, and since these are (quasi)degenerate, they will also follow similar time evolutions. As a consequence, their relative amplitude is independent of time and the value of α , even at higher orders in perturbation theory. This is illustrated in Fig. 4.4 for ϕ_{n33}/ϕ_{n31} .

A summary of the time-independent perturbation theory for transitions between overtones is shown in Table 4.1 for $M\mu = 0.1$, $\epsilon = 10^{-8}$.

The relative amplitudes $c_{n\ell m}/c_{211}$ indicate that the perturbation is not that small. This is even more obvious if we compute the first order corrections to the frequency eigenvalues, which for this configuration are of $\mathcal{O}(10^{-3})$ for overtones $n > 3$, as illustrated in Table A.1. For this reason, when computing the timescales of the transitions (A.22), we used the first order corrected $\omega_{n\ell m}$.

Table A.1: First order corrected frequencies $\omega_{n\ell m}$ predicted by time-independent theory, for a non-rotating BH and a companion with the configuration $M\mu = 0.1$, $\epsilon = 10^{-8}$. A spinning BH would break the degeneracy between states with the same ℓ but different m quantum number. However, these corrections enter the frequency spectrum (A.6) only at order α^5 . For the above configuration, these would yield $\omega_{n33} - \omega_{n31} \sim 10^{-6}a/Mn^3$.

$(n \ell)$	$\omega_{n\ell m} \times 10^2$
2 1	9.9754
3 1	9.9224
4 1	9.7570
5 1	9.3980
4 3	9.9001

B

AN ISOTROPICALLY-EMITTING STAR

In this appendix, we provide some details on the calculation of the emission of isotropic stars in a Schwarzschild background spacetime. For that we need to describe the physics as seen by a freely-falling observer. The following builds on Refs. [1, 492, 493].

Consider two different observers: a static observer, i.e. characterized by a worldline with $r = \theta = \varphi = \text{const}$; and a free-falling observer, who starts from rest at spatial infinity and has a purely radial motion.

Let us start with the observer at rest at some radius r_e , which we take to be on the equatorial axis. Its proper reference frame has basis components

$$\omega^{\hat{t}} = \sqrt{1 - \frac{2M}{r}} dt, \quad \omega^{\hat{r}} = \frac{1}{\sqrt{1 - \frac{2M}{r}}} dr, \quad \omega^{\hat{\phi}} = r d\varphi. \quad (\text{B.1})$$

If we consider a photon emitted by a source at rest at infinity and received by the observer, its geodesic motion is fully determined by its energy E and its impact parameter b . The components of the photon's four momentum $p_\mu = dx_\mu/d\lambda$ read

$$\begin{aligned} p_t &= - \left(1 - \frac{2M}{r}\right) \frac{dt}{d\lambda} = -E, \\ p_r &= \frac{1}{\sqrt{1 - \frac{2M}{r}}} \frac{dr}{d\lambda} = \frac{E}{1 - \frac{2M}{r}} \sqrt{1 - \left(1 - \frac{2M}{r}\right) \frac{b^2}{r^2}}, \\ p_\varphi &= r^2 \frac{d\varphi}{d\lambda} = L = b E, \end{aligned} \quad (\text{B.2})$$

where we used the EOM in Eqs. (5.5).

We must now compute the $p^{\hat{t}}$ component of the momentum in the observer's reference frame

$$p^{\hat{t}} = (\omega^{\hat{t}})_\mu p^\mu = \frac{-1}{\sqrt{1 - \frac{2M}{r}}} p_t, \quad p^{\hat{r}} = (\omega^{\hat{r}})_\mu p^\mu = \sqrt{1 - \frac{2M}{r}} p_r. \quad (\text{B.3})$$

The ratio of observed to emitted energy is then

$$\frac{p^{\hat{t}}}{E} = \frac{1}{\sqrt{1 - \frac{2M}{r}}}, \quad (\text{B.4})$$

signaling a typical blueshift.

Moreover, the observer sees the photons come in at an angle α relative to its radial direction given by

$$\cos \alpha = -\frac{p^{\hat{r}}}{p^{\hat{t}}} = -\sqrt{1 - \left(1 - \frac{2M}{r}\right) \frac{b^2}{r^2}}. \quad (\text{B.5})$$

Consider now free-falling observers. The basis one-forms of their proper reference frame are

$$\omega^{\hat{t}} = dt + \frac{\sqrt{2M/r_e}}{1 - 2M/r_e} dr, \quad \omega^{\hat{r}} = \sqrt{\frac{2M}{r_e}} dt + \frac{1}{1 - 2M/r_e} dr, \quad (\text{B.6})$$

When a photon with energy at infinity E and impact parameter b reaches the observer at $r = r_e$ and $\theta = \pi/2$, its four momentum is given by (B.2). On the other hand, infalling observers will see the photon with an energy $p^{\hat{t}} = \omega^{\hat{t}} \cdot \mathbf{p}$ and an angle $\alpha = \cos^{-1}(-p^{\hat{r}}/p^{\hat{t}})$ to the radial direction. Repeating the same steps as before we recover the results of Ref. [492]

$$\mathcal{P} = \frac{p_r}{p_t} (1 - x_e^2) \quad , \quad x_e = \sqrt{\frac{2M}{r_e}} \quad (\text{B.7})$$

$$\cos \alpha = -\left(\frac{p^{\hat{r}}}{p^{\hat{t}}}\right) = -\frac{x_e + \mathcal{P}}{1 + \mathcal{P}x_e}, \quad (\text{B.8})$$

$$\frac{p^{\hat{t}}}{E} = -\frac{1 + \mathcal{P}x_e}{x_e^2 - 1} = \frac{1}{1 + x_e \cos \alpha}, \quad (\text{B.9})$$

$$\frac{b}{r_e} = \frac{\sin \alpha}{1 + x_e \cos \alpha}. \quad (\text{B.10})$$

C

UNSTABLE CIRCULAR GEODESICS

In this Appendix, we present results similar to the ones discussed in Section 7.3.2 but considering the point particle is on circular geodesics, i.e. with $a = 0M$ in Eqs. (7.13)-(7.16). Our results are summarized in Fig. C.1 (next page). We put the particle at a radius that yields the same frequency as those presented in Fig. 7.2. Apart from a change in the absolute values for the flux, the relaxation timescales are in complete agreement with the ones obtained before, indicating the artificial motion we considered is irrelevant to the excitation of the constant-density star's QNMs.

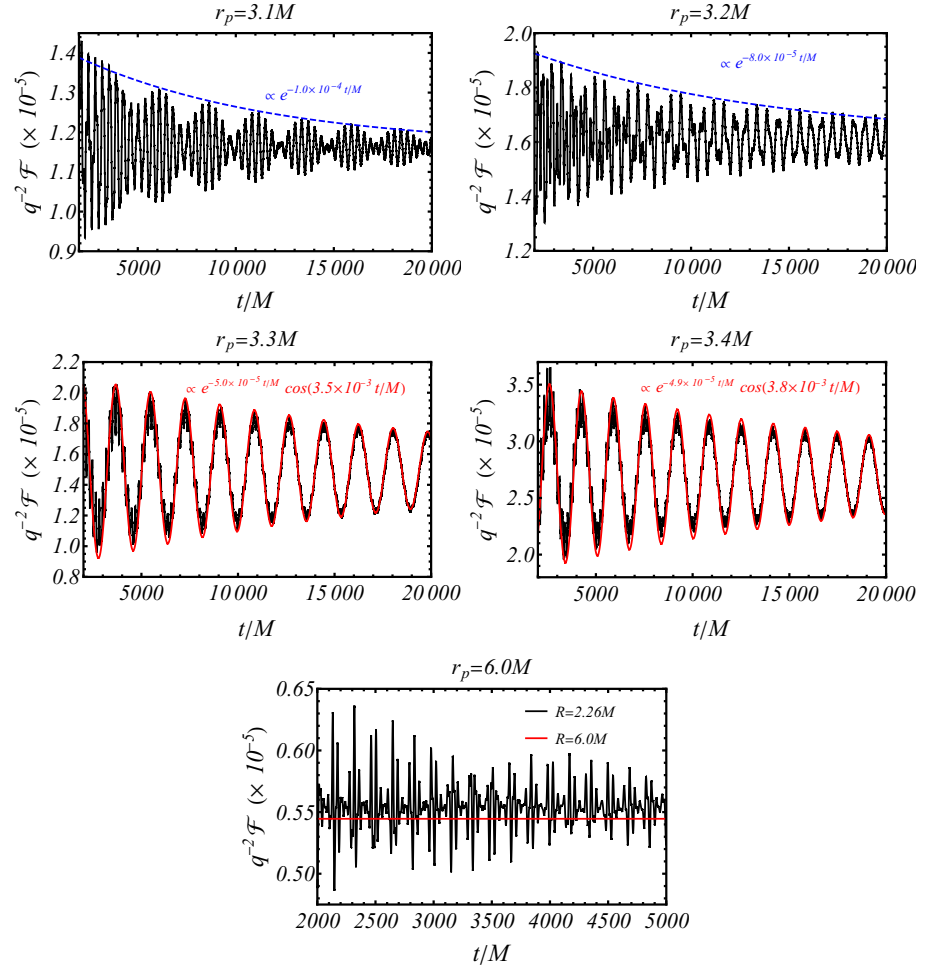


Figure C.1: Same analysis as in Fig. 7.2 but considering circular geodesics around Schwarzschild, i.e. $a = 0M$ in Eq. (7.13)-(7.16). We do not show an analogous plot for the $M\omega = 0.192$ since the particle would have to be put at the light-ring ($r_p = 3.0M$) and we are only considering timelike motion.

D

PERTURBATION EQUATIONS IN NON-VACUUM ENVIRONMENTS

In this appendix, we derive the full set of master wave-like partial differential equations that govern dynamical perturbations to spherically-symmetric but otherwise generic spacetimes given by the line element in Eq. (2.16). In Sec. 2.1.3 we already introduced the stepping stones of the formalism and now complement it with the perturbations to the matter sector. Recall that we are working in the Regge-Wheeler gauge (cf. Eq. (2.38)). Since we will not be discussing matter fluxes, we focus our discussion on $\ell \geq 2$ modes, which represent the radiative degrees of freedom of the gravitational field.

Matter perturbations are encoded through the fluid perturbations in the density and pressure perturbations

$$p_r^{(1)} = \sum_{\ell=2}^{\infty} \sum_{m=-\ell}^{\ell} \delta p_{r,\ell m}(t,r) Y_{\ell m}(\theta, \varphi), \quad (\text{D.1})$$

$$p_t^{(1)} = \sum_{\ell=2}^{\infty} \sum_{m=-\ell}^{\ell} \delta p_{t,\ell m}(t,r) Y_{\ell m}(\theta, \varphi), \quad (\text{D.2})$$

$$\rho^{(1)} = \sum_{\ell=2}^{\infty} \sum_{m=-\ell}^{\ell} \delta \rho_{\ell m}(t,r) Y_{\ell m}(\theta, \varphi), \quad (\text{D.3})$$

In addition, we also need to perturb the fluid's 4-velocity. These are described by three functions $\{U_{\ell m}(t,r), V_{\ell m}(t,r), W_{\ell m}(t,r)\}$ and the timelike condition $u^\mu u_\mu = -1$ (up to first order), which yields

$$u_{(1)}^t = \frac{1}{2A^{1/2}} \sum_{\ell=2}^{\infty} \sum_{m=-\ell}^{\ell} H_0^{\ell m} Y_{\ell m}, \quad (\text{D.4})$$

$$u_{(1)}^r = \frac{A^{1/2}}{B} \frac{1}{4\pi(p_r + \rho)} \sum_{\ell=2}^{\infty} \sum_{m=-\ell}^{\ell} W_{\ell m} Y_{\ell m}, \quad (\text{D.5})$$

$$u_{(1)}^\theta = \frac{A^{1/2}}{4\pi(p_t + \rho)r^2} \sum_{\ell=2}^{\infty} \sum_{m=-\ell}^{\ell} \left[V_{\ell m} \partial_\theta - \frac{U_{\ell m}}{\sin \theta} \partial_\varphi \right] Y_{\ell m}, \quad (\text{D.6})$$

$$u_{(1)}^\varphi = \frac{A^{1/2}}{4\pi(p_t + \rho)r^2 \sin^2 \theta} \sum_{\ell=2}^{\infty} \sum_{m=-\ell}^{\ell} \left[V_{\ell m} \partial_\varphi + \frac{U_{\ell m}}{\sin \theta} \partial_\theta \right] Y_{\ell m}. \quad (\text{D.7})$$

where we are now suppressing all coordinate dependences and the superscript (0) to improve readability. The perturbed unit spacelike vector k^μ orthogonal to u^μ ($k^\mu k_\mu = 1$ and $k^\mu u_\mu = 0$) is then

$$k_t^{(1)} = -\frac{A}{B^{3/2}} \frac{1}{4\pi(p_r + \rho)} \sum_{\ell=2}^{\infty} \sum_{m=-\ell}^{\ell} W_{\ell m} Y_{\ell m}, \quad (\text{D.8})$$

$$k_r^{(1)} = \frac{1}{2\sqrt{B}} \sum_{\ell=2}^{\infty} \sum_{m=-\ell}^{\ell} H_2^{\ell m} Y_{\ell m}, \quad (\text{D.9})$$

$$k_\theta^{(1)} = k_\varphi^{(1)} = 0, \quad (\text{D.10})$$

from which we can then build the perturbed projection operator $\Pi^{(1)} = g_{\mu\nu}^{(1)} + u_\mu^{(0)} u_\nu^{(1)} + u_\mu^{(1)} u_\nu^{(0)} - k_\mu^{(0)} k_\nu^{(1)} - k_\mu^{(1)} k_\nu^{(0)}$

$$\Pi_{t\theta}^{(1)} = \frac{A}{4\pi(p_t + \rho)} \sum_{\ell=2}^{\infty} \sum_{m=-\ell}^{\ell} [\csc\theta U_{\ell m} \partial_\varphi + V_{\ell m} \partial_\theta] Y_{\ell m}, \quad (\text{D.11})$$

$$\Pi_{t\varphi}^{(1)} = -\frac{A}{4\pi(p_t + \rho)} \sum_{\ell=2}^{\infty} \sum_{m=-\ell}^{\ell} [\sin\theta U_{\ell m} \partial_\theta + V_{\ell m} \partial_\varphi] Y_{\ell m} \quad (\text{D.12})$$

$$\Pi_{\theta\theta}^{(1)} = r^2 \sum_{\ell=2}^{\infty} \sum_{m=-\ell}^{\ell} K_{\ell m} Y_{\ell m}, \quad (\text{D.13})$$

$$\Pi_{\varphi\varphi}^{(1)} = \sin^2\theta \Pi_{\theta\theta}^{(1)}. \quad (\text{D.14})$$

Finally, we also need to assume a (barotropic) equation of state that relates the density and pressure perturbations

$$\delta p_{r,\ell m} = c_{s_r}^2 \delta \rho_{\ell m}, \quad (\text{D.15})$$

$$\delta p_{t,\ell m} = c_{s_t}^2 \delta \rho_{\ell m}, \quad (\text{D.16})$$

where $c_{s_r} = c_{s_r}(r)$ and $c_{s_t} = c_{s_t}(r)$ are the sound speed along the radial and tangential directions. We can finally plug these in the energy-momentum tensor (9.1) and arrive at the components

$$\begin{aligned} T_{tt}^{\text{env}(1)} &= A \sum_{\ell=2}^{\infty} \sum_{m=-\ell}^{\ell} (\delta \rho_{\ell m} - H_{\ell m}^0 \rho) Y_{\ell m}, \\ T_{tr}^{\text{env}(1)} &= -\sum_{\ell=2}^{\infty} \sum_{m=-\ell}^{\ell} \left[\frac{A}{4\pi B^2} W_{\ell m} + H_{\ell m}^1 \rho \right] Y_{\ell m}, \\ T_{t\theta}^{\text{env}(1)} &= \frac{A}{4\pi} \sum_{\ell=2}^{\infty} \sum_{m=-\ell}^{\ell} [\csc\theta U_{\ell m} \partial_\varphi - V_{\ell m} \partial_\theta] Y_{\ell m}, \\ T_{t\varphi}^{\text{env}(1)} &= \frac{-A}{4\pi} \sum_{\ell=2}^{\infty} \sum_{m=-\ell}^{\ell} [V_{\ell m} \partial_\varphi + U_{\ell m} \sin\theta \partial_\theta] Y_{\ell m}, \\ T_{rr}^{\text{env}(1)} &= \frac{1}{B} \sum_{\ell=2}^{\infty} \sum_{m=-\ell}^{\ell} (p_r H_{\ell m}^2 + \delta p_{r,\ell m}) Y_{\ell m}, \\ T_{\theta\theta}^{\text{env}(1)} &= r^2 \sum_{\ell=2}^{\infty} \sum_{m=-\ell}^{\ell} (p_t K_{\ell m} + \delta p_{t,\ell m}) Y_{\ell m}, \\ T_{\varphi\varphi}^{\text{env}(1)} &= T_{\theta\theta}^{\text{halo}(1)} \sin^2\theta. \end{aligned} \quad (\text{D.17})$$

D.1 ENERGY-MOMENTUM TENSOR OF THE SECONDARY FOR CIRCULAR ORBITS

We are interested in studying EMRIs, so the source of our perturbations is a point particle orbiting the background spacetime, with energy-momentum tensor given by Eq. (2.10). We will focus on circular orbits at some fixed radius r_p and spherical symmetry allows us to consider motion only on the equatorial plane, i.e. $\theta_p = \pi/2$. The 4-velocity of the source is [328]

$$u_p = \left(\frac{E_p}{A_p}, 0, 0, \frac{L_p}{r_p^2} \right), \quad (\text{D.18})$$

where $A_p = A(r_p)$ and E_p and L_p are the energy and angular momentum per unit rest mass of the orbiting body [328]

$$E_p = \frac{A_p}{\sqrt{A_p - r_p^2 \Omega_p^2}}, \quad L_p = \frac{\Omega_p r_p^2}{\sqrt{A_p - r_p^2 \Omega_p^2}}. \quad (\text{D.19})$$

with the angular orbital frequency $\varphi_p(t) = \Omega_p t$ given by

$$\Omega_p = \sqrt{\frac{A'_p}{2r_p}}, \quad (\text{D.20})$$

where recall that a prime denotes a derivative with respect to r .

For this orbital configuration, the tensor harmonics expansion (2.34) for the energy-momentum tensor of the secondary greatly simplifies. We have $\mathcal{A}_{\ell m} = \mathcal{A}_{\ell m}^1 = \mathcal{B}_{\ell m} = \mathcal{Q}_{\ell m} = 0$, while the non-vanishing coefficients can be expressed in terms of the orbital parameters as follows

$$\begin{aligned} \mathcal{A}_{\ell m}^0 &= \frac{m_p \sqrt{AB} E_p}{r^2} Y_{\ell m}^* \delta_{r_p}, \\ \mathcal{B}_{\ell m}^0 &= \frac{m_p i \sqrt{AB} L_p}{r^3 \sqrt{(n+1)}} \delta_{r_p} \partial_\phi Y_{\ell m}^*, \\ \mathcal{Q}_{\ell m}^0 &= -\frac{m_p \sqrt{AB} L_p}{r^3 \sqrt{(n+1)}} \delta_{r_p} \partial_\theta Y_{\ell m}^*, \\ \mathcal{G}_{\ell m} &= \frac{m_p L_p^2 \sqrt{AB}}{r^4 \sqrt{2} E_p} \delta_{r_p} Y_{\ell m}^*, \\ \mathcal{D}_{\ell m} &= \frac{m_p i L_p^2 \sqrt{AB}}{E_p r^4 \sqrt{2n(n+1)}} \delta_{r_p} \partial_{\theta\phi} Y_{\ell m}^*, \\ \mathcal{F}_{\ell m} &= \frac{m_p L_p^2 \sqrt{AB}}{r^4 2 E_p \sqrt{2n(n+1)}} \delta_{r_p} (\partial_{\phi\phi} - \partial_{\theta\theta}) Y_{\ell m}^*, \end{aligned} \quad (\text{D.21})$$

where $n = \ell(\ell+1)/2 - 1$, $Y_{\ell m}^* = Y_{\ell m}^*(\pi/2, \Omega_p t)$ and $\delta_{r_p} = \delta(r - r_p)$.

D.2 MASTER EQUATIONS

We now have all the ingredients necessary to derive a set of partial differential equations for the axial and polar sectors. For the sake of clarity, hereafter, we will drop the sum over the multipolar indices.

D.2.1 Axial Sector

We start off with the simpler axial sector where gravitational perturbations decouple from the matter sector. We need to find a solution for $h_0^{\ell m}$, $h_1^{\ell m}$ and $U^{\ell m}$. Start by rewriting $\partial h_0^{\ell m} / \partial t$ using the combination of $\mathcal{E}_{\theta\theta} - \mathcal{E}_{\phi\phi} / \sin^2 \theta$, where

$$\mathcal{E}_{\mu\nu} = G_{\mu\nu}^{(1)} - 8\pi(T_{\mu\nu}^{\text{env}(1)} + T_{\mu\nu}^p), \quad (\text{D.22})$$

and $G_{\mu\nu}^{(1)}$ is the perturbed Einstein tensor. We arrive at

$$\frac{\partial h_0}{\partial t} = AB \frac{dh_1}{dr} + \frac{A(1 - B + rB')}{2r} h_1 - i \frac{4\sqrt{2}\pi r^2 A}{\sqrt{n(1+n)}} \mathcal{D}, \quad (\text{D.23})$$

where from now on we omit the angular indexes to avoid cluttering

If we define the variable

$$\Psi^{\text{ax}} = \frac{\sqrt{AB}}{r} h_1, \quad (\text{D.24})$$

the $\mathcal{E}_{r\theta}$ component provides a second-order non-homogeneous differential equation for Ψ^{ax} . In terms of the generalized tortoise coordinate $dr_*/dr = (AB)^{-1/2}$, the master equation for the axial metric perturbations can be written as

$$\left[-\frac{\partial^2}{\partial t^2} + \frac{\partial^2}{\partial r_*^2} - V^{\text{ax}} \right] \Psi^{\text{ax}} = S^{\text{ax}}, \quad (\text{D.25})$$

where the potential reads

$$V^{\text{ax}} = \frac{A}{r^2} \left[\ell(\ell + 1) - \frac{6m(r)}{r} + m'(r) \right], \quad (\text{D.26})$$

with $m(r) = r(1 - B(r))/2$ and the source term is

$$S^{\text{ax}} = i \frac{2\sqrt{2}\pi r^2}{\sqrt{n(n+1)}} \left(\frac{A'}{A} \mathcal{D} + \frac{\partial \mathcal{D}}{\partial r} \right). \quad (\text{D.27})$$

In the vacuum limit, i.e. $M \rightarrow 0$, or alternatively $r \rightarrow \infty$, the equation above reduces to the Regge-Wheeler master equation (2.39) which governs axial perturbations in Schwarzschild. Notice that both at the BH horizon and at infinity the effective potential goes to zero. Therefore, the master function behaves as wave, with physical solutions corresponding to ingoing waves at the horizon and outgoing at large distances.

D.2.2 Polar Sector

We now move to the polar sector, which is more involved because matter perturbations couple to gravitational ones. First, we redefine the perturbations

$$H_0 = K + \frac{r}{A}S, \quad (\text{D.28})$$

$$H_1 = \frac{r}{A}\tilde{H}_1. \quad (\text{D.29})$$

This choice is inspired in studies of perturbations around relativistic stars [447] and the factoring of r and A captures the asymptotic behavior at, respectively, large distances and near the BH horizon.

- $\mathcal{E}_{\theta\theta} - \mathcal{E}_{\varphi\varphi}/\sin^2\theta$ gives an algebraic relation for H_2

$$H_2 = K + \frac{r}{A}S - \frac{16\pi r^2}{\sqrt{2n(n+1)}}\mathcal{F}. \quad (\text{D.30})$$

- $\mathcal{E}_{r\theta}$ gives a relation between \tilde{H}_1 and the other perturbations which we use to substitute $\partial\tilde{H}_1/\partial t$ and $\partial^2\tilde{H}_1/(\partial t\partial r_*)$ when necessary

$$\begin{aligned} \frac{\partial\tilde{H}_1}{\partial t} &= \sqrt{\frac{A}{B}}\frac{\partial S}{\partial r_*} + \frac{A}{r}S + \frac{A^2}{r^2B}(1-B+8\pi r^2 p_r)K \\ &\quad - \frac{8\pi}{\sqrt{2n(n+1)}}\frac{A^2}{B}(1+B+8\pi r^2 p_r)\mathcal{F}. \end{aligned} \quad (\text{D.31})$$

- $\mathcal{E}_{tt} = 8\pi T_{tt}$ yields a constraint between K , S and $\delta\rho$

$$\begin{aligned} \frac{\partial^2 K}{\partial r_*^2} &= \sqrt{\frac{B}{A}}\frac{\partial S}{\partial r_*} - \frac{1}{2r}\sqrt{\frac{A}{B}}(1+3B-8\pi r^2\rho)\frac{\partial K}{\partial r_*} \\ &\quad + A\left(\frac{\ell(\ell+1)}{r^2} - 8\pi\rho\right)K \\ &\quad + \left(\frac{\ell(\ell+1)+4B}{2r} - 8\pi r(\rho+p_r)\right)S \\ &\quad - 8\pi A\delta\rho - 8\pi A^0 - \frac{16\pi ABr}{\sqrt{2n(n+1)}}\frac{\partial\mathcal{F}}{\partial r} \\ &\quad + \frac{8\pi A}{\sqrt{2n(n+1)}}(16\pi r^2\rho - 4B - 2 - \ell(\ell+1))\mathcal{F}. \end{aligned} \quad (\text{D.32})$$

- $\mathcal{E}_{tt} - AB\mathcal{E}_{rr}$ gives the first second-order “wavelike” equation for K

$$\begin{aligned}
& - \frac{\partial^2 K}{\partial^2 t} + \frac{\partial^2 K}{\partial^2 r_*} + \frac{2\sqrt{AB}}{r} \frac{\partial K}{\partial r_*} \\
& + \frac{A}{r^2} [8\pi r^2 (\rho + p_r) + 2 - 2B - \ell(\ell + 1)] K \\
& = -8\pi A (1 - c_{s_r}^2) \delta\rho + \frac{2}{r} (B - 4\pi r^2 (\rho + p_r)) S \\
& - \frac{8\pi A}{\sqrt{2n(n+1)}} (2 + 2B + \ell(\ell + 1) - 16\pi r^2 \rho) \mathcal{F} \\
& - \frac{16\pi A B r}{\sqrt{2n(n+1)}} \frac{\partial \mathcal{F}}{\partial r} - 8\pi A^0.
\end{aligned} \tag{D.33}$$

- $\mathcal{E}_{\theta\theta} + \mathcal{E}_{\varphi\varphi}/\sin^2\theta$ gives another second-order “wavelike” equation for S , where we used the previous equations to substitute the necessary derivatives

$$\begin{aligned}
& - \frac{\partial^2 S}{\partial^2 t} + \frac{\partial^2 S}{\partial^2 r_*} \\
& + \frac{A}{r^2} (4\pi r^2 (\rho + 3p_r) + B - 1 - \ell(\ell + 1)) S \\
& = -\frac{A^2}{r^3 B} \left[7B^2 + (1 + 8\pi r^2 p_r)^2 \right. \\
& \left. - 8B (1 + 4\pi r^2 p_r - 2\pi (p_t + \rho)) \right] K \\
& - 16\pi \frac{a^2}{r} (c_{s_r}^2 - c_{s_t}^2) \delta\rho + 8\pi\sqrt{2} \frac{A^2}{r} \mathcal{G}_{\ell m} \\
& - \frac{8\pi}{\sqrt{2n(n+1)}} \frac{A^2}{rB} \left[5B^2 + B(\ell(\ell + 1) - 4 - 32\pi r^2 p_r) \right. \\
& \left. - (1 + 8\pi r^2 p_r)^2 \right] \mathcal{F} \\
& - \frac{16\pi A}{\sqrt{2n(n+1)}} \left(\frac{A}{2} (1 + B + 8\pi r^2 p_r) \frac{\partial \mathcal{F}_{\ell m}}{\partial r} + r \frac{\partial^2 \mathcal{F}}{\partial t^2} \right).
\end{aligned} \tag{D.34}$$

- The final “wavelike” equation for $\delta\rho$ is obtained from the conservation of the perturbed energy-momentum tensor of the surrounding fluid. $\nabla_\mu T_{\text{env}(1)}^{\mu\theta} = 0$ gives

$$\begin{aligned}
\frac{\partial V}{\partial t} & = (\rho + p_r) \left(K + \frac{r}{A} S \right) - 4\pi c_{s_t}^2 \delta\rho \\
& + \frac{32\pi^2 r^2}{\sqrt{2n(n+1)}} (p_t - p_r) \mathcal{F}.
\end{aligned} \tag{D.35}$$

- whereas $\nabla_\mu T_{\text{env}(1)}^{\mu r} = 0$

$$\begin{aligned}
& \frac{\partial W}{\partial t} = -4\pi r \frac{B^2}{A^2} (p_r + \rho) \frac{\partial \tilde{H}_1}{\partial t} - 4\pi B c_{s_r}^2 \sqrt{\frac{B}{A}} \frac{\partial \delta \rho}{\partial r_*} \\
& - 2\pi r \frac{B}{A} \sqrt{\frac{B}{A}} (p_r + \rho) \frac{\partial S}{\partial r_*} + 2\pi B \sqrt{\frac{B}{A}} (2p_t - p_r + \rho) \frac{\partial K}{\partial r_*} \\
& + 2\pi \frac{B}{A} (1 - 2B + 8\pi r^2 p_r) (p_r + \rho) S \\
& + 4\pi \frac{B}{r} (B - 1 + 8\pi r^2 p_r) (p_r + \rho) K \\
& + \frac{2\pi B}{r} \left[(1 + c_{s_r}^2) (1 + 8\pi r^2 p_r) - B (1 + 5c_{s_r}^2 - 4c_{s_t}^2 + 4rc_{s_r} c'_{s_r}) \right] \delta \rho \\
& - \frac{64\pi^2 r B}{\sqrt{2n(n+1)}} (1 - B + 8\pi r^2 p_r) (p_r + \rho) \mathcal{F}. \tag{D.36}
\end{aligned}$$

- Doing $\nabla_\mu T_{\text{env}(1)}^{\mu r} = 0$ and using the previous relations we finally arrive at

$$\begin{aligned}
& - \frac{\partial^2 \delta \rho}{\partial t^2} + c_{s_r}^2 \frac{\partial^2 \delta \rho}{\partial r_*^2} \\
& + \frac{1}{2r} \sqrt{\frac{A}{B}} \left[(c_{s_r}^2 - 1) (1 + 8\pi r^2 p_r) \right. \\
& + B (1 + 7c_{s_r}^2 - 4c_{s_t}^2 + 8rc_{s_r} c'_{s_r}) \left. \right] \frac{\partial \delta \rho}{\partial r_*} \\
& - \frac{A}{2r^2 B} \left[(1 + c_{s_r}^2) (1 + 8\pi r^2 p_r)^2 \right. \\
& + 2B \left[c_{s_t}^2 (4 + \ell + \ell^2 + 16\pi r^2 (p_r - \rho)) \right. \\
& - 1 + c_{s_r}^2 (8\pi r^2 (\rho - 3p_r)) - 5 + rc_{s_r} c'_{s_r} (8\pi r^2 (\rho - 2p_r) - 3) \left. \right] \\
& + B^2 \left(1 + 5c_{s_r}^2 - 4c_{s_t}^2 - 4r^2 (c'_{s_r})^2 + 8rc_{s_t} c'_{s_t} - 2rc_{s_r} (5c'_{s_r} + 2rc''_{s_r}) \right) \left. \right] \delta \rho \\
& = \mathcal{S}_\rho, \tag{D.37}
\end{aligned}$$

with the source term

$$\begin{aligned}
\mathcal{S}_\rho = & -\frac{r}{A} (p_r + \rho) \frac{\partial^2 \mathcal{S}}{\partial r_*^2} - \frac{1}{4r} \sqrt{\frac{A}{B}} \left[72\pi r^2 p_r^2 + 4(3B - 2)p_t + \rho \right. \\
& + p_r (9 - 13B + 8\pi r^2 (\rho - 8p_t)) - B (\rho + 2r(2p_t' + \rho')) \left. \right] \frac{\partial \mathcal{K}}{\partial r_*} \\
& - \frac{1}{4A\sqrt{AB}} \left[-2rB (p_r + \rho) A' - A \left[24\pi r^2 p_r^2 + \rho + 2r\rho (8\pi r\rho + B') \right. \right. \\
& + p_r (1 - 13B + 2r (20\pi r\rho + B')) - B (4p_t + 17\rho + 6r\rho') \left. \left. \right] \right] \frac{\partial \mathcal{S}}{\partial r_*} \\
& - \frac{A}{2r^2 B} \left[64\pi^2 r^4 p_r^3 + \rho + 8\pi r^2 p_r^2 (2 - 5B + 8\pi r^2 \rho) \right. \\
& + B \left[\rho (B - 2 + 24\pi r^2 \rho) - 2p_t (\ell^2 + \ell - 2 + 2B - 32\pi r^2 \rho) \right. \\
& + 4r (B - 1) \rho' \left. \right] + p_r \left[1 + 5B^2 + 16\pi r^2 \rho^2 \right. \\
& + 2B(\ell^2 + \ell - 3 + 8\pi r^2 (6p_t + \rho + 2r\rho')) \left. \left. \right] \right] \mathcal{K} \\
& - \frac{1}{4rB} \left[64\pi^2 r^4 p_r^3 + \rho + 8\pi r^2 p_r^2 (2 - 7B + 8\pi r^2 \rho) \right. \\
& + B \left[4p_t (1 - \ell - \ell^2 - 2B) + \rho (10B - 3 - 32\pi r^2 \rho) \right. \\
& + 2r (4B - 1) \rho' \left. \right] + p_r \left[1 + 2B^2 + 16\pi r^2 \rho + B((1 + 2\ell)^2 \right. \\
& - 8\pi r^2 (4p_t + 15\rho + 2r\rho')) \left. \left. \right] \right] \mathcal{S} \\
& - 4\pi (\rho - p_r + 2p_t) \mathcal{A}^0 - 4\pi\sqrt{2}A (p_r + \rho) \mathcal{G} \\
& - \frac{4\pi Ar}{\sqrt{2(2n+1)}} \left[40\pi r^2 p_r^2 - 4p_t - 5(B - 1)\rho \right. \\
& + p_r (5 - B + 40\pi r^2 \rho) \left. \right] \frac{\partial \mathcal{F}}{\partial r} \\
& + \frac{8\pi}{\sqrt{2n(n+1)}} \frac{A}{B} \left[64\pi r^4 p_r^3 + \rho + 16\pi r^2 p_r^2 (1 + 4\pi r^2 \rho) \right. \\
& + B \left[\rho (3 - 4B + 24\pi r^2 \rho) - 3(B - 3)\rho' \right. \\
& - 2p_t (4B + \ell^2 + \ell - 2 - 32\pi r^2 \rho) \left. \right] \\
& + p_r \left[1 + 4B^2 + 16\pi r^2 \rho + B(2\ell(1 + \ell) \right. \\
& - 1 + 8\pi r^2 (12p_t + 7\rho + 3r\rho')) \left. \left. \right] \right] \mathcal{F}. \tag{D.38}
\end{aligned}$$

There are many points worth highlighting. First, if we set the mass of the halo to zero, $M = 0$, the evolution equation for $\delta\rho$ decouples from the gravitational perturbations and becomes sourceless. This means if no initial data is given to $\delta\rho$, it remains 0 for the whole evolution, as it should for an EMRI in vacuum. Moreover, one can check explicitly by direct substitution that the vacuum Eqs. (D.33) and (D.34), together with the constraint in Eq. (D.32), are completely equivalent to the Zerilli equation in Eq. (2.39). Asymptotic flatness then guarantees this equivalence as $r \rightarrow \infty$.

We already discussed the asymptotic behavior of $\delta\rho$ in the main text, in Section 9.3.1. It is clear that S also behaves as wave propagating at the speed of light both at infinity and at the BH horizon, similarly to the master Zerilli function. From the homogeneous part of the evolution equation for K , one could naively assume that it would decay as $1/r$ at large distances. However, note that K is also being sourced by S . If as $r \rightarrow \infty$, S is represented by an outgoing wave, $S \sim S_0^\infty e^{-i\omega(t-r_*)}$, then writing $K \sim (K_0^\infty + K_1^\infty/r) e^{-i\omega(t-r_*)}$ and expanding Eq. (D.33) in powers of r for large distances we find

$$K_0^\infty = -\frac{i}{\omega} S_0^\infty, \quad (\text{D.39})$$

so K also behaves as a wave asymptotically. In fact, at far-away distances the relation between K and the Zerilli master function is [188]

$$K \underset{r \rightarrow \infty}{=} \frac{d\Psi_Z}{dr_*}. \quad (\text{D.40})$$

Moreover, for monochromatic waves and at large distances $d\Psi_Z/dr_* = i\omega\Psi_Z = -d\Psi_Z/dt$. Thus, for circular orbits we can use the absolute value of K to evaluate the flux of energy carried by GWs to infinity as determined by Eq. (2.45).

We have also mentioned that the $\ell = 0$ and $\ell = 1$ modes are “non-physical” in GR and can be removed in a region of spacetime by a gauge transformation. In fact, for $\ell \leq 1$ the Regge-Wheeler gauge is not completely fixed because there are less independent spherical harmonics (recall the discussion below Eq. (2.45)). In fact, Eq. (D.30) is actually identically 0 for $\ell \leq 1$ (i.e. it becomes $0 = 0$).

However, what is the actual meaning of gravitational perturbations for the lower multipoles, since they do not contribute to radiative degrees of freedom? The answer to this question is explained in detail in Appendix G of Ref. [187] (see also Refs. [184, 494]). The $\ell = 0$ axial mode is identically 0, while the respective $\ell = 1$ case gives a perturbation to the angular momentum of the configuration. In the case of an orbiting particle, it would correspond to its conserved angular momentum. In a similar fashion, the $\ell = 0$ polar mode leads to a correction in the mass of the system, e.g. by adding the mass of the particle to the mass of the central object. Finally, for the Regge-Wheeler gauge in which we adopt coordinates centered at the unperturbed

spacetime, the $\ell = 1$ polar mode yields the transformation to the center-of-momentum of the total system. In a Newtonian analysis, this would correspond to the appearance of a fictitious force because the reference frame of the central BH is not inertial.

BIBLIOGRAPHY

- [1] Charles W. Misner, K. S. Thorne, and J. A. Wheeler. *Gravitation*. San Francisco: W. H. Freeman, 1973. ISBN: 978-0-7167-0344-0, 978-0-691-17779-3.
- [2] Robert M. Wald. *General Relativity*. Chicago, USA: Chicago Univ. Pr., 1984. DOI: [10.7208/chicago/9780226870373.001.0001](https://doi.org/10.7208/chicago/9780226870373.001.0001).
- [3] B. Carter. "Axisymmetric Black Hole Has Only Two Degrees of Freedom." In: *Phys. Rev. Lett.* 26 (6 1971), pp. 331–333. DOI: [10.1103/PhysRevLett.26.331](https://doi.org/10.1103/PhysRevLett.26.331). URL: <https://link.aps.org/doi/10.1103/PhysRevLett.26.331>.
- [4] B. P. Abbott et al. "Properties of the Binary Black Hole Merger GW150914." In: *Phys. Rev. Lett.* 116 (24 2016), p. 241102. DOI: [10.1103/PhysRevLett.116.241102](https://doi.org/10.1103/PhysRevLett.116.241102). URL: <https://link.aps.org/doi/10.1103/PhysRevLett.116.241102>.
- [5] B. P. Abbott et al. "GWTC-1: A Gravitational-Wave Transient Catalog of Compact Binary Mergers Observed by LIGO and Virgo during the First and Second Observing Runs." In: *Phys. Rev. X* 9.3 (2019), p. 031040. DOI: [10.1103/PhysRevX.9.031040](https://doi.org/10.1103/PhysRevX.9.031040). arXiv: [1811.12907](https://arxiv.org/abs/1811.12907) [[astro-ph.HE](#)].
- [6] R. Abbott et al. "GWTC-2.1: Deep Extended Catalog of Compact Binary Coalescences Observed by LIGO and Virgo During the First Half of the Third Observing Run." In: (Aug. 2021). arXiv: [2108.01045](https://arxiv.org/abs/2108.01045) [[gr-qc](#)].
- [7] R. Abbott et al. "GWTC-3: Compact Binary Coalescences Observed by LIGO and Virgo During the Second Part of the Third Observing Run." In: (Nov. 2021). arXiv: [2111.03606](https://arxiv.org/abs/2111.03606) [[gr-qc](#)].
- [8] B. P. Abbott et al. "GW170817: Observation of Gravitational Waves from a Binary Neutron Star Inspiral." In: *Phys. Rev. Lett.* 119.16 (2017), p. 161101. DOI: [10.1103/PhysRevLett.119.161101](https://doi.org/10.1103/PhysRevLett.119.161101). arXiv: [1710.05832](https://arxiv.org/abs/1710.05832) [[gr-qc](#)].
- [9] B. P. Abbott et al. "Multi-messenger Observations of a Binary Neutron Star Merger." In: *Astrophys. J. Lett.* 848.2 (2017), p. L12. DOI: [10.3847/2041-8213/aa91c9](https://doi.org/10.3847/2041-8213/aa91c9). arXiv: [1710.05833](https://arxiv.org/abs/1710.05833) [[astro-ph.HE](#)].
- [10] B. P. Abbott et al. "Gravitational Waves and Gamma-rays from a Binary Neutron Star Merger: GW170817 and GRB 170817A." In: *Astrophys. J. Lett.* 848.2 (2017), p. L13. DOI: [10.3847/2041-8213/aa920c](https://doi.org/10.3847/2041-8213/aa920c). arXiv: [1710.05834](https://arxiv.org/abs/1710.05834) [[astro-ph.HE](#)].

- [11] R. Abbott et al. "Observation of Gravitational Waves from Two Neutron Star–Black Hole Coalescences." In: *Astrophys. J. Lett.* 915.1 (2021), p. L5. DOI: [10.3847/2041-8213/ac082e](https://doi.org/10.3847/2041-8213/ac082e). arXiv: [2106.15163](https://arxiv.org/abs/2106.15163) [astro-ph.HE].
- [12] R. Abbott et al. "GW190412: Observation of a Binary-Black-Hole Coalescence with Asymmetric Masses." In: *Phys. Rev. D* 102.4 (2020), p. 043015. DOI: [10.1103/PhysRevD.102.043015](https://doi.org/10.1103/PhysRevD.102.043015). arXiv: [2004.08342](https://arxiv.org/abs/2004.08342) [astro-ph.HE].
- [13] R. Abbott et al. "GW190814: Gravitational Waves from the Coalescence of a 23 Solar Mass Black Hole with a 2.6 Solar Mass Compact Object." In: *Astrophys. J. Lett.* 896.2 (2020), p. L44. DOI: [10.3847/2041-8213/ab960f](https://doi.org/10.3847/2041-8213/ab960f). arXiv: [2006.12611](https://arxiv.org/abs/2006.12611) [astro-ph.HE].
- [14] R. Abbott et al. "GW190521: A Binary Black Hole Merger with a Total Mass of $150M_{\odot}$." In: *Phys. Rev. Lett.* 125.10 (2020), p. 101102. DOI: [10.1103/PhysRevLett.125.101102](https://doi.org/10.1103/PhysRevLett.125.101102). arXiv: [2009.01075](https://arxiv.org/abs/2009.01075) [gr-qc].
- [15] Katerina Chatziioannou. "Neutron star tidal deformability and equation of state constraints." In: *Gen. Rel. Grav.* 52.11 (2020), p. 109. DOI: [10.1007/s10714-020-02754-3](https://doi.org/10.1007/s10714-020-02754-3). arXiv: [2006.03168](https://arxiv.org/abs/2006.03168) [gr-qc].
- [16] R. Abbott et al. "Population of Merging Compact Binaries Inferred Using Gravitational Waves through GWTC-3." In: *Phys. Rev. X* 13 (1 2023), p. 011048. DOI: [10.1103/PhysRevX.13.011048](https://doi.org/10.1103/PhysRevX.13.011048). URL: <https://link.aps.org/doi/10.1103/PhysRevX.13.011048>.
- [17] R. Abbott et al. "Tests of General Relativity with GWTC-3." In: (Dec. 2021). arXiv: [2112.06861](https://arxiv.org/abs/2112.06861) [gr-qc].
- [18] B. P. Abbott et al. "Prospects for observing and localizing gravitational-wave transients with Advanced LIGO, Advanced Virgo and KAGRA." In: *Living Rev. Rel.* 21.1 (2018), p. 3. DOI: [10.1007/s41114-020-00026-9](https://doi.org/10.1007/s41114-020-00026-9). arXiv: [1304.0670](https://arxiv.org/abs/1304.0670) [gr-qc].
- [19] Michele Maggiore et al. "Science Case for the Einstein Telescope." In: *JCAP* 03 (2020), p. 050. DOI: [10.1088/1475-7516/2020/03/050](https://doi.org/10.1088/1475-7516/2020/03/050). arXiv: [1912.02622](https://arxiv.org/abs/1912.02622) [astro-ph.CO].
- [20] Matthew Evans et al. "A Horizon Study for Cosmic Explorer: Science, Observatories, and Community." In: (Sept. 2021). arXiv: [2109.09882](https://arxiv.org/abs/2109.09882) [astro-ph.IM].
- [21] Vicky Kalogera et al. "The Next Generation Global Gravitational Wave Observatory: The Science Book." In: (Nov. 2021). arXiv: [2111.06990](https://arxiv.org/abs/2111.06990) [gr-qc].
- [22] Pau Amaro-Seoane et al. "Laser Interferometer Space Antenna." In: *arXiv e-prints* (Feb. 2017). DOI: [10.48550/arXiv.1702.00786](https://doi.org/10.48550/arXiv.1702.00786). arXiv: [1702.00786](https://arxiv.org/abs/1702.00786) [astro-ph.IM].

- [23] Pau Amaro-Seoane et al. “Astrophysics with the Laser Interferometer Space Antenna.” In: *Living Rev. Rel.* 26.1 (2023), p. 2. DOI: [10.1007/s41114-022-00041-y](https://doi.org/10.1007/s41114-022-00041-y). arXiv: [2203.06016](https://arxiv.org/abs/2203.06016) [gr-qc].
- [24] Antoine Klein et al. “Science with the space-based interferometer eLISA: Supermassive black hole binaries.” In: *Phys. Rev. D* 93.2 (2016), p. 024003. DOI: [10.1103/PhysRevD.93.024003](https://doi.org/10.1103/PhysRevD.93.024003). arXiv: [1511.05581](https://arxiv.org/abs/1511.05581) [gr-qc].
- [25] M. C. Begelman, R. D. Blandford, and M. J. Rees. “Massive black hole binaries in active galactic nuclei.” In: *Nature* 287.5780 (Sept. 1980), pp. 307–309. DOI: [10.1038/287307a0](https://doi.org/10.1038/287307a0).
- [26] Stanislav Babak, Jonathan Gair, Alberto Sesana, Enrico Barausse, Carlos F. Sopuerta, Christopher P. L. Berry, Emanuele Berti, Pau Amaro-Seoane, Antoine Petiteau, and Antoine Klein. “Science with the space-based interferometer LISA. V: Extreme mass-ratio inspirals.” In: *Phys. Rev. D* 95.10 (2017), p. 103012. DOI: [10.1103/PhysRevD.95.103012](https://doi.org/10.1103/PhysRevD.95.103012). arXiv: [1703.09722](https://arxiv.org/abs/1703.09722) [gr-qc].
- [27] Leor Barack et al. “Black holes, gravitational waves and fundamental physics: a roadmap.” In: *Class. Quant. Grav.* 36.14 (2019), p. 143001. DOI: [10.1088/1361-6382/ab0587](https://doi.org/10.1088/1361-6382/ab0587). arXiv: [1806.05195](https://arxiv.org/abs/1806.05195) [gr-qc].
- [28] Tanja Hinderer and Eanna E. Flanagan. “Two timescale analysis of extreme mass ratio inspirals in Kerr. I. Orbital Motion.” In: *Phys. Rev. D* 78 (2008), p. 064028. DOI: [10.1103/PhysRevD.78.064028](https://doi.org/10.1103/PhysRevD.78.064028). arXiv: [0805.3337](https://arxiv.org/abs/0805.3337) [gr-qc].
- [29] Pierre Auclair et al. “Cosmology with the Laser Interferometer Space Antenna.” In: (Apr. 2022). arXiv: [2204.05434](https://arxiv.org/abs/2204.05434) [astro-ph.CO].
- [30] K. G. Arun et al. “New horizons for fundamental physics with LISA.” In: *Living Rev. Rel.* 25.1 (2022), p. 4. DOI: [10.1007/s41114-022-00036-9](https://doi.org/10.1007/s41114-022-00036-9). arXiv: [2205.01597](https://arxiv.org/abs/2205.01597) [gr-qc].
- [31] Scott A. Hughes, Niels Warburton, Gaurav Khanna, Alvin J. K. Chua, and Michael L. Katz. “Adiabatic waveforms for extreme mass-ratio inspirals via multivoice decomposition in time and frequency.” In: *Phys. Rev. D* 103.10 (2021), p. 104014. DOI: [10.1103/PhysRevD.103.104014](https://doi.org/10.1103/PhysRevD.103.104014). arXiv: [2102.02713](https://arxiv.org/abs/2102.02713) [gr-qc].
- [32] Barry Wardell, Adam Pound, Niels Warburton, Jeremy Miller, Leanne Durkan, and Alexandre Le Tiec. “Gravitational waveforms for compact binaries from second-order self-force theory.” In: (Dec. 2021). arXiv: [2112.12265](https://arxiv.org/abs/2112.12265) [gr-qc].
- [33] Angelica Albertini, Alessandro Nagar, Adam Pound, Niels Warburton, Barry Wardell, Leanne Durkan, and Jeremy Miller. “Comparing second-order gravitational self-force, numerical relativity, and effective one body waveforms from inspiralling, quasicircular, and nonspinning black hole binaries.” In: *Phys.*

- Rev. D* 106.8 (2022), p. 084061. DOI: [10.1103/PhysRevD.106.084061](https://doi.org/10.1103/PhysRevD.106.084061). arXiv: [2208.01049](https://arxiv.org/abs/2208.01049) [gr-qc].
- [34] Gabriella Agazie et al. “The NANOGrav 15 yr Data Set: Evidence for a Gravitational-wave Background.” In: *Astrophys. J. Lett.* 951.1 (2023), p. L8. DOI: [10.3847/2041-8213/acdac6](https://doi.org/10.3847/2041-8213/acdac6). arXiv: [2306.16213](https://arxiv.org/abs/2306.16213) [astro-ph.HE].
- [35] J. Antoniadis et al. “The second data release from the European Pulsar Timing Array III. Search for gravitational wave signals.” In: (June 2023). arXiv: [2306.16214](https://arxiv.org/abs/2306.16214) [astro-ph.HE].
- [36] Gabriella Agazie et al. “The NANOGrav 15-year Data Set: Constraints on Supermassive Black Hole Binaries from the Gravitational Wave Background.” In: (June 2023). arXiv: [2306.16220](https://arxiv.org/abs/2306.16220) [astro-ph.HE].
- [37] J. Antoniadis et al. “The second data release from the European Pulsar Timing Array: V. Implications for massive black holes, dark matter and the early Universe.” In: (June 2023). arXiv: [2306.16227](https://arxiv.org/abs/2306.16227) [astro-ph.CO].
- [38] D. Lynden-Bell and M. J. Rees. “On Quasars, Dust and the Galactic Centre.” In: *Monthly Notices of the Royal Astronomical Society* 152.4 (July 1971), pp. 461–475. ISSN: 0035-8711. DOI: [10.1093/mnras/152.4.461](https://doi.org/10.1093/mnras/152.4.461). eprint: <https://academic.oup.com/mnras/article-pdf/152/4/461/9402718/mnras152-0461.pdf>. URL: <https://doi.org/10.1093/mnras/152.4.461>.
- [39] Andrzej Soltan. “Masses of quasars.” In: *Monthly Notices of the Royal Astronomical Society* 200.1 (Sept. 1982), pp. 115–122. ISSN: 0035-8711. DOI: [10.1093/mnras/200.1.115](https://doi.org/10.1093/mnras/200.1.115). eprint: <https://academic.oup.com/mnras/article-pdf/200/1/115/9402782/mnras200-0115.pdf>. URL: <https://doi.org/10.1093/mnras/200.1.115>.
- [40] Reinhard Genzel, Frank Eisenhauer, and Stefan Gillessen. “The Galactic Center massive black hole and nuclear star cluster.” In: *Reviews of Modern Physics* 82.4 (Oct. 2010), pp. 3121–3195. DOI: [10.1103/RevModPhys.82.3121](https://doi.org/10.1103/RevModPhys.82.3121). arXiv: [1006.0064](https://arxiv.org/abs/1006.0064) [astro-ph.GA].
- [41] Tuan Do et al. “Relativistic redshift of the star S0-2 orbiting the Galactic center supermassive black hole.” In: *Science* 365.6454 (2019), pp. 664–668. DOI: [10.1126/science.aav8137](https://doi.org/10.1126/science.aav8137). arXiv: [1907.10731](https://arxiv.org/abs/1907.10731) [astro-ph.GA].
- [42] GRAVITY Collaboration et al. “Detection of the gravitational redshift in the orbit of the star S2 near the Galactic centre massive black hole.” In: *Astronomy and Astrophysics* 615, L15 (July 2018), p. L15. DOI: [10.1051/0004-6361/201833718](https://doi.org/10.1051/0004-6361/201833718). arXiv: [1807.09409](https://arxiv.org/abs/1807.09409) [astro-ph.GA].

- [43] Marta Volonteri, Francesco Haardt, and Piero Madau. “The Assembly and Merging History of Supermassive Black Holes in Hierarchical Models of Galaxy Formation.” In: *The Astrophysical Journal* 582.2 (2003), p. 559. DOI: [10.1086/344675](https://doi.org/10.1086/344675). URL: <https://dx.doi.org/10.1086/344675>.
- [44] Mitchell C. Begelman, Marta Volonteri, and Martin J. Rees. “Formation of supermassive black holes by direct collapse in pre-galactic haloes.” In: *Monthly Notices of the Royal Astronomical Society* 370.1 (July 2006), pp. 289–298. ISSN: 0035-8711. DOI: [10.1111/j.1365-2966.2006.10467.x](https://academic.oup.com/mnras/article-pdf/370/1/289/3406434/mnras0370-0289.pdf). eprint: <https://academic.oup.com/mnras/article-pdf/370/1/289/3406434/mnras0370-0289.pdf>. URL: <https://doi.org/10.1111/j.1365-2966.2006.10467.x>.
- [45] The Event Horizon Telescope Collaboration. “First Sagittarius A* Event Horizon Telescope Results. I. The Shadow of the Supermassive Black Hole in the Center of the Milky Way.” In: *The Astrophysical Journal Letters* 930.L12 (2022). URL: <https://doi.org/10.3847/2041-8213/ac6674>.
- [46] Event Horizon Telescope Collaboration. “First M87 Event Horizon Telescope Results. I. The Shadow of the Supermassive Black Hole.” In: *The Astrophysical Journal Letters* 875.1, L1 (Apr. 2019), p. L1. DOI: [10.3847/2041-8213/ab0ec7](https://doi.org/10.3847/2041-8213/ab0ec7). arXiv: [1906.11238](https://arxiv.org/abs/1906.11238) [astro-ph.GA].
- [47] N. I. Shakura and R. A. Sunyaev. “Black holes in binary systems. Observational appearance.” In: *Astron. Astrophys.* 24 (1973), pp. 337–355.
- [48] Marek A. Abramowicz and P. Chris Fragile. “Foundations of Black Hole Accretion Disk Theory.” In: *Living Rev. Rel.* 16 (2013), p. 1. DOI: [10.12942/lrr-2013-1](https://doi.org/10.12942/lrr-2013-1). arXiv: [1104.5499](https://arxiv.org/abs/1104.5499) [astro-ph.HE].
- [49] Andrea Derdzinski and Lucio Mayer. “In-situ extreme mass ratio inspirals via sub-parsec formation and migration of stars in thin, gravitationally unstable AGN discs.” In: (May 2022). DOI: [10.1093/mnras/stad749](https://doi.org/10.1093/mnras/stad749). arXiv: [2205.10382](https://arxiv.org/abs/2205.10382) [astro-ph.GA].
- [50] K. C. Freeman. “On the Disks of Spiral and So Galaxies.” In: *The Astrophysical Journal* 160 (June 1970), p. 811. DOI: [10.1086/150474](https://doi.org/10.1086/150474).
- [51] V. C. Rubin, Jr. Ford W. K., and N. Thonnard. “Rotational properties of 21 SC galaxies with a large range of luminosities and radii, from NGC 4605 (R=4kpc) to UGC 2885 (R=122kpc).” In: *The Astrophysical Journal* 238 (June 1980), pp. 471–487. DOI: [10.1086/158003](https://doi.org/10.1086/158003).

- [52] Julio F. Navarro, Carlos S. Frenk, and Simon D. M. White. “The Structure of cold dark matter halos.” In: *Astrophys. J.* 462 (1996), pp. 563–575. DOI: [10.1086/177173](https://doi.org/10.1086/177173). arXiv: [astro-ph/9508025](https://arxiv.org/abs/astro-ph/9508025).
- [53] Risa H. Wechsler and Jeremy L. Tinker. “The Connection between Galaxies and their Dark Matter Halos.” In: *Ann. Rev. Astron. Astrophys.* 56 (2018), pp. 435–487. DOI: [10.1146/annurev-astro-081817-051756](https://doi.org/10.1146/annurev-astro-081817-051756). arXiv: [1804.03097](https://arxiv.org/abs/1804.03097) [[astro-ph.GA](https://arxiv.org/abs/astro-ph.GA)].
- [54] R. Schödel, A. Feldmeier, N. Neumayer, L. Meyer, and S. Yelda. “The nuclear cluster of the Milky Way: our primary testbed for the interaction of a dense star cluster with a massive black hole.” In: *Classical and Quantum Gravity* 31.24, 244007 (Dec. 2014), p. 244007. DOI: [10.1088/0264-9381/31/24/244007](https://doi.org/10.1088/0264-9381/31/24/244007). arXiv: [1411.4504](https://arxiv.org/abs/1411.4504) [[astro-ph.GA](https://arxiv.org/abs/astro-ph.GA)].
- [55] Verónica Vázquez-Aceves, Lorenz Zwick, Elisa Bortolas, Pedro R. Capelo, Pau Amaro-Seoane, Lucio Mayer, and Xian Chen. “Revised event rates for extreme and extremely large mass-ratio inspirals.” In: *Mon. Not. Roy. Astron. Soc.* 510.2 (2022), pp. 2379–2390. DOI: [10.1093/mnras/stab3485](https://doi.org/10.1093/mnras/stab3485). arXiv: [2108.00135](https://arxiv.org/abs/2108.00135) [[astro-ph.GA](https://arxiv.org/abs/astro-ph.GA)].
- [56] M. J. Valtonen, S. Mikkola, D. Merritt, A. Gopakumar, H. J. Lehto, T. Hyvönen, H. Rampadarath, R. Saunders, M. Basta, and R. Hudec. “Measuring the Spin of the Primary Black Hole in OJ287.” In: *Astrophysics Journal* 709.2 (Feb. 2010), pp. 725–732. DOI: [10.1088/0004-637X/709/2/725](https://doi.org/10.1088/0004-637X/709/2/725). arXiv: [0912.1209](https://arxiv.org/abs/0912.1209) [[astro-ph.HE](https://arxiv.org/abs/astro-ph.HE)].
- [57] P. Pihajoki et al. “PRECURSOR FLARES IN OJ 287.” In: *The Astrophysical Journal* 764.1 (2013), p. 5. DOI: [10.1088/0004-637X/764/1/5](https://doi.org/10.1088/0004-637X/764/1/5). URL: <https://dx.doi.org/10.1088/0004-637X/764/1/5>.
- [58] Lixin Jane Dai, Steven V. Fuerst, and Roger Blandford. “Quasi-periodic flares from star-accretion-disc collisions.” In: *Monthly Notices of the Royal Astronomical Society* 402.3 (Mar. 2010), pp. 1614–1624. DOI: [10.1111/j.1365-2966.2009.16038.x](https://doi.org/10.1111/j.1365-2966.2009.16038.x). arXiv: [0906.0800](https://arxiv.org/abs/0906.0800) [[astro-ph.HE](https://arxiv.org/abs/astro-ph.HE)].
- [59] Imre Bartos, Bence Kocsis, Zoltán Haiman, and Szabolcs Márka. “Rapid and Bright Stellar-mass Binary Black Hole Mergers in Active Galactic Nuclei.” In: *The Astrophysical Journal* 835.2, 165 (Feb. 2017), p. 165. DOI: [10.3847/1538-4357/835/2/165](https://doi.org/10.3847/1538-4357/835/2/165). arXiv: [1602.03831](https://arxiv.org/abs/1602.03831) [[astro-ph.HE](https://arxiv.org/abs/astro-ph.HE)].
- [60] Hiromichi Tagawa, Zoltán Haiman, and Bence Kocsis. “Formation and Evolution of Compact-object Binaries in AGN Disks.” In: *The Astrophysical Journal* 898.1 (2020), p. 25. DOI: [10.3847/1538-4357/ab9b8c](https://doi.org/10.3847/1538-4357/ab9b8c). URL: <https://dx.doi.org/10.3847/1538-4357/ab9b8c>.

- [61] Hiromichi Tagawa, Bence Kocsis, Zoltán Haiman, Imre Bartos, Kazuyuki Omukai, and Johan Samsing. “Mass-gap Mergers in Active Galactic Nuclei.” In: *The Astrophysical Journal* 908.2, 194 (Feb. 2021), p. 194. DOI: [10.3847/1538-4357/abd555](https://doi.org/10.3847/1538-4357/abd555). arXiv: [2012.00011](https://arxiv.org/abs/2012.00011) [astro-ph.HE].
- [62] V. Gayathri, Y. Yang, H. Tagawa, Z. Haiman, and I. Bartos. “Black Hole Mergers of AGN Origin in LIGO-Virgo’s O1-O3a Observing Periods.” In: *The Astrophysical Journal Letters* 920.2, L42 (Oct. 2021), p. L42. DOI: [10.3847/2041-8213/ac2cc1](https://doi.org/10.3847/2041-8213/ac2cc1). arXiv: [2104.10253](https://arxiv.org/abs/2104.10253) [gr-qc].
- [63] M.J. Graham et al. “Candidate Electromagnetic Counterpart to the Binary Black Hole Merger Gravitational Wave Event S190521g.” In: *Phys. Rev. Lett.* 124.25 (2020), p. 251102. DOI: [10.1103/PhysRevLett.124.251102](https://doi.org/10.1103/PhysRevLett.124.251102). arXiv: [2006.14122](https://arxiv.org/abs/2006.14122) [astro-ph.HE].
- [64] Juan Calderón Bustillo, Samson H. W. Leong, Koustav Chandra, Barry McKernan, and K. E. S. Ford. “GW190521 as a black-hole merger coincident with the ZTF19abnrhr flare.” In: (Dec. 2021). arXiv: [2112.12481](https://arxiv.org/abs/2112.12481) [gr-qc].
- [65] L. Filipe O. Costa, Rita Franco, and Vitor Cardoso. “Gravitational Magnus effect.” In: *Physical Review D* 98.2, 024026 (July 2018), p. 024026. DOI: [10.1103/PhysRevD.98.024026](https://doi.org/10.1103/PhysRevD.98.024026). arXiv: [1805.01097](https://arxiv.org/abs/1805.01097) [gr-qc].
- [66] Zhen Pan and Huan Yang. “Formation Rate of Extreme Mass Ratio Inspirals in Active Galactic Nuclei.” In: *Phys. Rev. D* 103.10 (2021), p. 103018. DOI: [10.1103/PhysRevD.103.103018](https://doi.org/10.1103/PhysRevD.103.103018). arXiv: [2101.09146](https://arxiv.org/abs/2101.09146) [astro-ph.HE].
- [67] Zhen Pan, Zhenwei Lyu, and Huan Yang. “Wet extreme mass ratio inspirals may be more common for spaceborne gravitational wave detection.” In: *Phys. Rev. D* 104.6 (2021), p. 063007. DOI: [10.1103/PhysRevD.104.063007](https://doi.org/10.1103/PhysRevD.104.063007). arXiv: [2104.01208](https://arxiv.org/abs/2104.01208) [astro-ph.HE].
- [68] H. Bondi and F. Hoyle. “On the mechanism of accretion by stars.” In: *Monthly Notices of the Royal Astronomical Society* 104 (Jan. 1944), p. 273. DOI: [10.1093/mnras/104.5.273](https://doi.org/10.1093/mnras/104.5.273).
- [69] Richard G. Edgar. “A Review of Bondi-Hoyle-Lyttleton accretion.” In: *New Astron. Rev.* 48 (2004), pp. 843–859. DOI: [10.1016/j.newar.2004.06.001](https://doi.org/10.1016/j.newar.2004.06.001). arXiv: [astro-ph/0406166](https://arxiv.org/abs/astro-ph/0406166).
- [70] S. Chandrasekhar. “Dynamical Friction. I. General Considerations: the Coefficient of Dynamical Friction.” In: *Astrophysics Journal* 97 (Mar. 1943), p. 255. DOI: [10.1086/144517](https://doi.org/10.1086/144517).
- [71] Eve C. Ostriker. “Dynamical friction in a gaseous medium.” In: *Astrophys. J.* 513 (1999), p. 252. DOI: [10.1086/306858](https://doi.org/10.1086/306858). arXiv: [astro-ph/9810324](https://arxiv.org/abs/astro-ph/9810324).

- [72] P. Goldreich and S. Tremaine. “Disk-satellite interactions.” In: *Astrophysics Journal* 241 (Oct. 1980), pp. 425–441. DOI: [10.1086/158356](https://doi.org/10.1086/158356).
- [73] Hidekazu Tanaka, Taku Takeuchi, and William R. Ward. “Three-Dimensional Interaction between a Planet and an Isothermal Gaseous Disk. I. Corotation and Lindblad Torques and Planet Migration.” In: *The Astrophysical Journal* 565.2 (2002), p. 1257. DOI: [10.1086/324713](https://doi.org/10.1086/324713). URL: <https://dx.doi.org/10.1086/324713>.
- [74] P. B. Ivanov, J. C. B. Papaloizou, and A. G. Polnarev. “The evolution of a supermassive binary caused by an accretion disc.” In: *Monthly Notices of the Royal Astronomical Society* 307.1 (July 1999), pp. 79–90. ISSN: 0035-8711. DOI: [10.1046/j.1365-8711.1999.02623.x](https://doi.org/10.1046/j.1365-8711.1999.02623.x). URL: <https://doi.org/10.1046/j.1365-8711.1999.02623.x>.
- [75] D. Syer and C. J. Clarke. “Satellites in discs: regulating the accretion luminosity.” In: *Monthly Notices of the Royal Astronomical Society* 277.3 (Dec. 1995), pp. 758–766. ISSN: 0035-8711. DOI: [10.1093/mnras/277.3.758](https://doi.org/10.1093/mnras/277.3.758). eprint: <https://academic.oup.com/mnras/article-pdf/277/3/758/3774449/mnras277-0758.pdf>. URL: <https://doi.org/10.1093/mnras/277.3.758>.
- [76] Sandip K. Chakrabarti. “Gravitational wave emission from a binary black hole system in the presence of an accretion disk.” In: *Phys. Rev. D* 53 (1996), pp. 2901–2907. DOI: [10.1103/PhysRevD.53.2901](https://doi.org/10.1103/PhysRevD.53.2901). arXiv: [astro-ph/9603117](https://arxiv.org/abs/astro-ph/9603117).
- [77] Vitor Cardoso, Caio F. B. Macedo, and Rodrigo Vicente. “Eccentricity evolution of compact binaries and applications to gravitational-wave physics.” In: *Phys. Rev. D* 103.2 (2021), p. 023015. DOI: [10.1103/PhysRevD.103.023015](https://doi.org/10.1103/PhysRevD.103.023015). arXiv: [2010.15151 \[gr-qc\]](https://arxiv.org/abs/2010.15151).
- [78] Bence Kocsis, Nicolas Yunes, and Abraham Loeb. “Observable Signatures of EMRI Black Hole Binaries Embedded in Thin Accretion Disks.” In: *Phys. Rev. D* 84 (2011), p. 024032. DOI: [10.1103/PhysRevD.86.049907](https://doi.org/10.1103/PhysRevD.86.049907). arXiv: [1104.2322 \[astro-ph.GA\]](https://arxiv.org/abs/1104.2322).
- [79] Nicolas Yunes, Bence Kocsis, Abraham Loeb, and Zoltan Haiman. “Imprint of Accretion Disk-Induced Migration on Gravitational Waves from Extreme Mass Ratio Inspirals.” In: *Phys. Rev. Lett.* 107 (2011), p. 171103. DOI: [10.1103/PhysRevLett.107.171103](https://doi.org/10.1103/PhysRevLett.107.171103). arXiv: [1103.4609 \[astro-ph.CO\]](https://arxiv.org/abs/1103.4609).
- [80] Enrico Barausse, Vitor Cardoso, and Paolo Pani. “Can environmental effects spoil precision gravitational-wave astrophysics?” In: *Phys. Rev. D* 89.10 (2014), p. 104059. DOI: [10.1103/PhysRevD.89.104059](https://doi.org/10.1103/PhysRevD.89.104059). arXiv: [1404.7149 \[gr-qc\]](https://arxiv.org/abs/1404.7149).

- [81] Vitor Cardoso and Andrea Maselli. “Constraints on the astrophysical environment of binaries with gravitational-wave observations.” In: *Astron. Astrophys.* 644 (2020), A147. DOI: [10.1051/0004-6361/202037654](https://doi.org/10.1051/0004-6361/202037654). arXiv: [1909.05870](https://arxiv.org/abs/1909.05870) [astro-ph.HE].
- [82] Alvin J. K. Chua, Michael L. Katz, Niels Warburton, and Scott A. Hughes. “Rapid generation of fully relativistic extreme-mass-ratio-inspiral waveform templates for LISA data analysis.” In: *Phys. Rev. Lett.* 126.5 (2021), p. 051102. DOI: [10.1103/PhysRevLett.126.051102](https://doi.org/10.1103/PhysRevLett.126.051102). arXiv: [2008.06071](https://arxiv.org/abs/2008.06071) [gr-qc].
- [83] Michael L. Katz, Alvin J. K. Chua, Lorenzo Speri, Niels Warburton, and Scott A. Hughes. “Fast extreme-mass-ratio-inspiral waveforms: New tools for millihertz gravitational-wave data analysis.” In: *Phys. Rev. D* 104.6 (2021), p. 064047. DOI: [10.1103/PhysRevD.104.064047](https://doi.org/10.1103/PhysRevD.104.064047). arXiv: [2104.04582](https://arxiv.org/abs/2104.04582) [gr-qc].
- [84] Lorenzo Speri, Andrea Antonelli, Laura Sberna, Stanislav Babak, Enrico Barausse, Jonathan R. Gair, and Michael L. Katz. “Measuring accretion-disk effects with gravitational waves from extreme mass ratio inspirals.” In: (July 2022). arXiv: [2207.10086](https://arxiv.org/abs/2207.10086) [gr-qc].
- [85] Lorenz Zwick, Pedro R. Capelo, and Lucio Mayer. “Priorities in gravitational waveforms for future space-borne detectors: vacuum accuracy or environment?” In: (Sept. 2022). DOI: [10.1093/mnras/stad707](https://doi.org/10.1093/mnras/stad707). arXiv: [2209.04060](https://arxiv.org/abs/2209.04060) [gr-qc].
- [86] A. Derdzinski, D. D’Orazio, P. Duffell, Z. Haiman, and A. MacFadyen. “Evolution of gas disc–embedded intermediate mass ratio inspirals in the *LISA* band.” In: *Mon. Not. Roy. Astron. Soc.* 501.3 (2021), pp. 3540–3557. DOI: [10.1093/mnras/staa3976](https://doi.org/10.1093/mnras/staa3976). arXiv: [2005.11333](https://arxiv.org/abs/2005.11333) [astro-ph.HE].
- [87] Lorenz Zwick, Andrea Derdzinski, Mudit Garg, Pedro R. Capelo, and Lucio Mayer. “Dirty waveforms: multiband harmonic content of gas-embedded gravitational wave sources.” In: (Oct. 2021). arXiv: [2110.09097](https://arxiv.org/abs/2110.09097) [astro-ph.HE].
- [88] Bernard F. Schutz. “Determining the Hubble Constant from Gravitational Wave Observations.” In: *Nature* 323 (1986), pp. 310–311. DOI: [10.1038/323310a0](https://doi.org/10.1038/323310a0).
- [89] Daniel E. Holz and Scott A. Hughes. “Using gravitational-wave standard sirens.” In: *Astrophys. J.* 629 (2005), pp. 15–22. DOI: [10.1086/431341](https://doi.org/10.1086/431341). arXiv: [astro-ph/0504616](https://arxiv.org/abs/astro-ph/0504616).
- [90] Lars Hernquist. “An Analytical Model for Spherical Galaxies and Bulges.” In: *The Astrophysical Journal* 356 (June 1990), p. 359. DOI: [10.1086/168845](https://doi.org/10.1086/168845).

- [91] Richard Massey, Thomas Kitching, and Johan Richard. “The dark matter of gravitational lensing.” In: *Rept. Prog. Phys.* 73 (2010), p. 086901. DOI: [10.1088/0034-4885/73/8/086901](https://doi.org/10.1088/0034-4885/73/8/086901). arXiv: [1001.1739](https://arxiv.org/abs/1001.1739) [astro-ph.CO].
- [92] Qi Guo, Simon White, Cheng Li, and Michael Boylan-Kolchin. “How do galaxies populate Dark Matter halos?” In: *Mon. Not. Roy. Astron. Soc.* 404 (2010), p. 1111. DOI: [10.1111/j.1365-2966.2010.16341.x](https://doi.org/10.1111/j.1365-2966.2010.16341.x). arXiv: [0909.4305](https://arxiv.org/abs/0909.4305) [astro-ph.CO].
- [93] Fabrizio Nesti and Paolo Salucci. “The Dark Matter halo of the Milky Way, AD 2013.” In: *JCAP* 07 (2013), p. 016. DOI: [10.1088/1475-7516/2013/07/016](https://doi.org/10.1088/1475-7516/2013/07/016). arXiv: [1304.5127](https://arxiv.org/abs/1304.5127) [astro-ph.GA].
- [94] David H. Weinberg, James S. Bullock, Fabio Governato, Rachel Kuzio de Naray, and Annika H. G. Peter. “Cold dark matter: controversies on small scales.” In: *Proc. Nat. Acad. Sci.* 112 (2015), pp. 12249–12255. DOI: [10.1073/pnas.1308716112](https://doi.org/10.1073/pnas.1308716112). arXiv: [1306.0913](https://arxiv.org/abs/1306.0913) [astro-ph.CO].
- [95] Antonino Del Popolo and Morgan Le Delliou. “Small scale problems of the Λ CDM model: a short review.” In: *Galaxies* 5.1 (2017), p. 17. DOI: [10.3390/galaxies5010017](https://doi.org/10.3390/galaxies5010017). arXiv: [1606.07790](https://arxiv.org/abs/1606.07790) [astro-ph.CO].
- [96] Ben Moore. “Evidence against dissipation-less dark matter from observations of galaxy haloes.” In: *Nature* 6491 (1994), pp. 629–631. DOI: [10.1038/370629a0](https://doi.org/10.1038/370629a0).
- [97] Julio F. Navarro, Carlos S. Frenk, and Simon D. M. White. “A Universal density profile from hierarchical clustering.” In: *Astrophys. J.* 490 (1997), pp. 493–508. DOI: [10.1086/304888](https://doi.org/10.1086/304888). arXiv: [astro-ph/9611107](https://arxiv.org/abs/astro-ph/9611107).
- [98] Gianfranco Bertone and Dan Hooper. “History of dark matter.” In: *Rev. Mod. Phys.* 90 (4 2018), p. 045002. DOI: [10.1103/RevModPhys.90.045002](https://doi.org/10.1103/RevModPhys.90.045002). URL: <https://link.aps.org/doi/10.1103/RevModPhys.90.045002>.
- [99] B. J. Carr and S. W. Hawking. “Black Holes in the Early Universe.” In: *Monthly Notices of the Royal Astronomical Society* 168.2 (Aug. 1974), pp. 399–415. ISSN: 0035-8711. DOI: [10.1093/mnras/168.2.399](https://doi.org/10.1093/mnras/168.2.399). eprint: <https://academic.oup.com/mnras/article-pdf/168/2/399/8079885/mnras168-0399.pdf>. URL: <https://doi.org/10.1093/mnras/168.2.399>.
- [100] B. J. Carr, Kazunori Kohri, Yuuiti Sendouda, and Jun’ichi Yokoyama. “New cosmological constraints on primordial black holes.” In: *Phys. Rev. D* 81 (2010), p. 104019. DOI: [10.1103/PhysRevD.81.104019](https://doi.org/10.1103/PhysRevD.81.104019). arXiv: [0912.5297](https://arxiv.org/abs/0912.5297) [astro-ph.CO].

- [101] R. D. Peccei and Helen R. Quinn. “CP Conservation in the Presence of Pseudoparticles.” In: *Phys. Rev. Lett.* 38 (25 1977), pp. 1440–1443. DOI: [10.1103/PhysRevLett.38.1440](https://doi.org/10.1103/PhysRevLett.38.1440). URL: <https://link.aps.org/doi/10.1103/PhysRevLett.38.1440>.
- [102] Asimina Arvanitaki, Savas Dimopoulos, Sergei Dubovsky, Ne-manja Kaloper, and John March-Russell. “String axiverse.” In: *Phys. Rev. D* 81 (12 2010), p. 123530. DOI: [10.1103/PhysRevD.81.123530](https://doi.org/10.1103/PhysRevD.81.123530). URL: <https://link.aps.org/doi/10.1103/PhysRevD.81.123530>.
- [103] Richard Brito, Vitor Cardoso, and Paolo Pani. “Superradiance.” In: *Lect. Notes Phys.* 906 (2015), pp.1–237. DOI: [10.1007/978-3-319-19000-6](https://doi.org/10.1007/978-3-319-19000-6). arXiv: [1501.06570](https://arxiv.org/abs/1501.06570) [gr-qc].
- [104] Lam Hui. “Wave Dark Matter.” In: *Ann. Rev. Astron. Astrophys.* 59 (2021), pp. 247–289. DOI: [10.1146/annurev-astro-120920-010024](https://doi.org/10.1146/annurev-astro-120920-010024). arXiv: [2101.11735](https://arxiv.org/abs/2101.11735) [astro-ph.CO].
- [105] Steven L. Liebling and Carlos Palenzuela. “Dynamical Boson Stars.” In: *Living Rev. Rel.* 15 (2012), p. 6. DOI: [10.12942/lrr-2012-6](https://doi.org/10.12942/lrr-2012-6). arXiv: [1202.5809](https://arxiv.org/abs/1202.5809) [gr-qc].
- [106] Lam Hui, Jeremiah P. Ostriker, Scott Tremaine, and Edward Witten. “Ultralight scalars as cosmological dark matter.” In: *Phys. Rev. D* 95.4 (2017), p. 043541. DOI: [10.1103/PhysRevD.95.043541](https://doi.org/10.1103/PhysRevD.95.043541). arXiv: [1610.08297](https://arxiv.org/abs/1610.08297) [astro-ph.CO].
- [107] Lorenzo Annulli, Vitor Cardoso, and Rodrigo Vicente. “Response of ultralight dark matter to supermassive black holes and binaries.” In: *Phys. Rev. D* 102.6 (2020), p. 063022. DOI: [10.1103/PhysRevD.102.063022](https://doi.org/10.1103/PhysRevD.102.063022). arXiv: [2009.00012](https://arxiv.org/abs/2009.00012) [gr-qc].
- [108] Vitor Cardoso, Taishi Ikeda, Rodrigo Vicente, and Miguel Zilhão. “Parasitic black holes: The swallowing of a fuzzy dark matter soliton.” In: *Phys. Rev. D* 106.12 (2022), p. L121302. DOI: [10.1103/PhysRevD.106.L121302](https://doi.org/10.1103/PhysRevD.106.L121302). arXiv: [2207.09469](https://arxiv.org/abs/2207.09469) [gr-qc].
- [109] Paolo Gondolo and Joseph Silk. “Dark matter annihilation at the galactic center.” In: *Phys. Rev. Lett.* 83 (1999), pp. 1719–1722. DOI: [10.1103/PhysRevLett.83.1719](https://doi.org/10.1103/PhysRevLett.83.1719). arXiv: [astro-ph/9906391](https://arxiv.org/abs/astro-ph/9906391).
- [110] Piero Ullio, HongSheng Zhao, and Marc Kamionkowski. “A Dark matter spike at the galactic center?” In: *Phys. Rev. D* 64 (2001), p. 043504. DOI: [10.1103/PhysRevD.64.043504](https://doi.org/10.1103/PhysRevD.64.043504). arXiv: [astro-ph/0101481](https://arxiv.org/abs/astro-ph/0101481).
- [111] Laleh Sadeghian, Francesc Ferrer, and Clifford M. Will. “Dark matter distributions around massive black holes: A general relativistic analysis.” In: *Phys. Rev. D* 88.6 (2013), p. 063522. DOI: [10.1103/PhysRevD.88.063522](https://doi.org/10.1103/PhysRevD.88.063522). arXiv: [1305.2619](https://arxiv.org/abs/1305.2619) [astro-ph.GA].

- [112] David Merritt, Milos Milosavljevic, Licia Verde, and Raul Jimenez. “Dark matter spikes and annihilation radiation from the galactic center.” In: *Phys. Rev. Lett.* 88 (2002), p. 191301. DOI: [10.1103/PhysRevLett.88.191301](https://doi.org/10.1103/PhysRevLett.88.191301). arXiv: [astro-ph/0201376](https://arxiv.org/abs/astro-ph/0201376).
- [113] Gianfranco Bertone and David Merritt. “Time-dependent models for dark matter at the Galactic Center.” In: *Phys. Rev. D* 72 (2005), p. 103502. DOI: [10.1103/PhysRevD.72.103502](https://doi.org/10.1103/PhysRevD.72.103502). arXiv: [astro-ph/0501555](https://arxiv.org/abs/astro-ph/0501555).
- [114] Thomas Lacroix. “Dynamical constraints on a dark matter spike at the Galactic Centre from stellar orbits.” In: *Astron. Astrophys.* 619 (2018), A46. DOI: [10.1051/0004-6361/201832652](https://doi.org/10.1051/0004-6361/201832652). arXiv: [1801.01308](https://arxiv.org/abs/1801.01308) [[astro-ph.GA](https://arxiv.org/abs/astro-ph.GA)].
- [115] A. Amorim et al. “Scalar field effects on the orbit of S2 star.” In: *Mon. Not. Roy. Astron. Soc.* 489.4 (2019), pp. 4606–4621. DOI: [10.1093/mnras/stz2300](https://doi.org/10.1093/mnras/stz2300). arXiv: [1908.06681](https://arxiv.org/abs/1908.06681) [[astro-ph.GA](https://arxiv.org/abs/astro-ph.GA)].
- [116] R. Abuter et al. “Mass distribution in the Galactic Center based on interferometric astrometry of multiple stellar orbits.” In: *Astron. Astrophys.* 657 (2022), p. L12. DOI: [10.1051/0004-6361/202142465](https://doi.org/10.1051/0004-6361/202142465). arXiv: [2112.07478](https://arxiv.org/abs/2112.07478) [[astro-ph.GA](https://arxiv.org/abs/astro-ph.GA)].
- [117] Zhao-Qiang Shen, Guan-Wen Yuan, Cheng-Zi Jiang, Yue-Lin Sming Tsai, Qiang Yuan, and Yi-Zhong Fan. “Exploring dark matter spike distribution around the Galactic centre with stellar orbits.” In: (Mar. 2023). arXiv: [2303.09284](https://arxiv.org/abs/2303.09284) [[astro-ph.GA](https://arxiv.org/abs/astro-ph.GA)].
- [118] Man Ho Chan and Chak Man Lee. “Indirect Evidence for Dark Matter Density Spikes around Stellar-mass Black Holes.” In: *Astrophys. J. Lett.* 943.2 (2023), p. L11. DOI: [10.3847/2041-8213/acaafa](https://doi.org/10.3847/2041-8213/acaafa). arXiv: [2212.05664](https://arxiv.org/abs/2212.05664) [[astro-ph.HE](https://arxiv.org/abs/astro-ph.HE)].
- [119] Enrico Barausse, Vitor Cardoso, and Paolo Pani. “Can environmental effects spoil precision gravitational-wave astrophysics?” In: *Phys. Rev. D* 89 (10 2014), p. 104059. DOI: [10.1103/PhysRevD.89.104059](https://doi.org/10.1103/PhysRevD.89.104059). URL: <https://link.aps.org/doi/10.1103/PhysRevD.89.104059>.
- [120] Rodrigo Vicente and Vitor Cardoso. “Dynamical friction of black holes in ultralight dark matter.” In: *Phys. Rev. D* 105.8 (2022), p. 083008. DOI: [10.1103/PhysRevD.105.083008](https://doi.org/10.1103/PhysRevD.105.083008). arXiv: [2201.08854](https://arxiv.org/abs/2201.08854) [[gr-qc](https://arxiv.org/abs/gr-qc)].
- [121] Dina Traykova, Katy Clough, Thomas Helfer, Emanuele Berti, Pedro G. Ferreira, and Lam Hui. “Dynamical friction from scalar dark matter in the relativistic regime.” In: *Phys. Rev. D* 104.10 (2021), p. 103014. DOI: [10.1103/PhysRevD.104.103014](https://doi.org/10.1103/PhysRevD.104.103014). arXiv: [2106.08280](https://arxiv.org/abs/2106.08280) [[gr-qc](https://arxiv.org/abs/gr-qc)].

- [122] Robin Buehler and Vincent Desjacques. “Dynamical friction in fuzzy dark matter: Circular orbits.” In: *Phys. Rev. D* 107.2 (2023), p. 023516. DOI: [10.1103/PhysRevD.107.023516](https://doi.org/10.1103/PhysRevD.107.023516). arXiv: [2207.13740](https://arxiv.org/abs/2207.13740) [astro-ph.CO].
- [123] Dina Traykova, Rodrigo Vicente, Katy Clough, Thomas Helfer, Emanuele Berti, Pedro G. Ferreira, and Lam Hui. “Relativistic drag forces on black holes from scalar dark matter clouds of all sizes.” In: (May 2023). arXiv: [2305.10492](https://arxiv.org/abs/2305.10492) [gr-qc].
- [124] Nicholas Speeney, Andrea Antonelli, Vishal Baibhav, and Emanuele Berti. “Impact of relativistic corrections on the detectability of dark-matter spikes with gravitational waves.” In: *Phys. Rev. D* 106.4 (2022), p. 044027. DOI: [10.1103/PhysRevD.106.044027](https://doi.org/10.1103/PhysRevD.106.044027). arXiv: [2204.12508](https://arxiv.org/abs/2204.12508) [gr-qc].
- [125] Bradley J. Kavanagh, David A. Nichols, Gianfranco Bertone, and Daniele Gaggero. “Detecting dark matter around black holes with gravitational waves: Effects of dark-matter dynamics on the gravitational waveform.” In: *Phys. Rev. D* 102.8 (2020), p. 083006. DOI: [10.1103/PhysRevD.102.083006](https://doi.org/10.1103/PhysRevD.102.083006). arXiv: [2002.12811](https://arxiv.org/abs/2002.12811) [gr-qc].
- [126] Adam Coogan, Gianfranco Bertone, Daniele Gaggero, Bradley J. Kavanagh, and David A. Nichols. “Measuring the dark matter environments of black hole binaries with gravitational waves.” In: (Aug. 2021). arXiv: [2108.04154](https://arxiv.org/abs/2108.04154) [gr-qc].
- [127] Richard Brito, Vitor Cardoso, and Paolo Pani. “Black holes as particle detectors: evolution of superradiant instabilities.” In: *Class. Quant. Grav.* 32.13 (2015), p. 134001. DOI: [10.1088/0264-9381/32/13/134001](https://doi.org/10.1088/0264-9381/32/13/134001). arXiv: [1411.0686](https://arxiv.org/abs/1411.0686) [gr-qc].
- [128] Richard Brito, Shrobona Ghosh, Enrico Barausse, Emanuele Berti, Vitor Cardoso, Irina Dvorkin, Antoine Klein, and Paolo Pani. “Stochastic and resolvable gravitational waves from ultralight bosons.” In: *Phys. Rev. Lett.* 119.13 (2017), p. 131101. DOI: [10.1103/PhysRevLett.119.131101](https://doi.org/10.1103/PhysRevLett.119.131101). arXiv: [1706.05097](https://arxiv.org/abs/1706.05097) [gr-qc].
- [129] Richard Brito, Shrobona Ghosh, Enrico Barausse, Emanuele Berti, Vitor Cardoso, Irina Dvorkin, Antoine Klein, and Paolo Pani. “Gravitational wave searches for ultralight bosons with LIGO and LISA.” In: *Phys. Rev. D* 96.6 (2017), p. 064050. DOI: [10.1103/PhysRevD.96.064050](https://doi.org/10.1103/PhysRevD.96.064050). arXiv: [1706.06311](https://arxiv.org/abs/1706.06311) [gr-qc].
- [130] Maximiliano Isi, Ling Sun, Richard Brito, and Andrew Melatos. “Directed searches for gravitational waves from ultralight bosons.” In: (2018). arXiv: [1810.03812](https://arxiv.org/abs/1810.03812) [gr-qc].

- [131] Chen Yuan, Richard Brito, and Vitor Cardoso. “Probing ultralight dark matter with future ground-based gravitational-wave detectors.” In: *Phys. Rev. D* 104.4 (2021), p. 044011. DOI: [10.1103/PhysRevD.104.044011](https://doi.org/10.1103/PhysRevD.104.044011). arXiv: [2106.00021](https://arxiv.org/abs/2106.00021) [gr-qc].
- [132] Leo Tsukada, Thomas Callister, Andrew Matas, and Patrick Meyers. “First search for a stochastic gravitational-wave background from ultralight bosons.” In: *Phys. Rev. D* 99.10 (2019), p. 103015. DOI: [10.1103/PhysRevD.99.103015](https://doi.org/10.1103/PhysRevD.99.103015). arXiv: [1812.09622](https://arxiv.org/abs/1812.09622) [astro-ph.HE].
- [133] Leo Tsukada, Richard Brito, William E. East, and Nils Siemonsen. “Modeling and searching for a stochastic gravitational-wave background from ultralight vector bosons.” In: *Phys. Rev. D* 103.8 (2021), p. 083005. DOI: [10.1103/PhysRevD.103.083005](https://doi.org/10.1103/PhysRevD.103.083005). arXiv: [2011.06995](https://arxiv.org/abs/2011.06995) [astro-ph.HE].
- [134] Vitor Cardoso, Francisco Duque, and Taishi Ikeda. “Tidal effects and disruption in superradiant clouds: a numerical investigation.” In: *Phys. Rev. D* 101.6 (2020), p. 064054. DOI: [10.1103/PhysRevD.101.064054](https://doi.org/10.1103/PhysRevD.101.064054). arXiv: [2001.01729](https://arxiv.org/abs/2001.01729) [gr-qc].
- [135] Daniel Baumann, Horng Sheng Chia, and Rafael A. Porto. “Probing Ultralight Bosons with Binary Black Holes.” In: *Phys. Rev. D* 99.4 (2019), p. 044001. DOI: [10.1103/PhysRevD.99.044001](https://doi.org/10.1103/PhysRevD.99.044001). arXiv: [1804.03208](https://arxiv.org/abs/1804.03208) [gr-qc].
- [136] Daniel Baumann, Horng Sheng Chia, Rafael A. Porto, and John Stout. “Gravitational Collider Physics.” In: *Phys. Rev. D* 101.8 (2020), p. 083019. DOI: [10.1103/PhysRevD.101.083019](https://doi.org/10.1103/PhysRevD.101.083019). arXiv: [1912.04932](https://arxiv.org/abs/1912.04932) [gr-qc].
- [137] Daniel Baumann, Gianfranco Bertone, John Stout, and Giovanni Maria Tomaselli. “Sharp Signals of Boson Clouds in Black Hole Binary Inspirals.” In: *Phys. Rev. Lett.* 128.22 (2022), p. 221102. DOI: [10.1103/PhysRevLett.128.221102](https://doi.org/10.1103/PhysRevLett.128.221102). arXiv: [2206.01212](https://arxiv.org/abs/2206.01212) [gr-qc].
- [138] R. Abbott et al. “GW190814: Gravitational Waves from the Coalescence of a 23 Solar Mass Black Hole with a 2.6 Solar Mass Compact Object.” In: *Astrophys. J. Lett.* 896.2 (2020), p. L44. DOI: [10.3847/2041-8213/ab960f](https://doi.org/10.3847/2041-8213/ab960f). arXiv: [2006.12611](https://arxiv.org/abs/2006.12611) [astro-ph.HE].
- [139] R. Abbott et al. “GW190521: A Binary Black Hole Merger with a Total Mass of $150 M_{\odot}$.” In: *Phys. Rev. Lett.* 125.10 (2020), p. 101102. DOI: [10.1103/PhysRevLett.125.101102](https://doi.org/10.1103/PhysRevLett.125.101102). arXiv: [2009.01075](https://arxiv.org/abs/2009.01075) [gr-qc].
- [140] B.P. Abbott et al. “GW190425: Observation of a Compact Binary Coalescence with Total Mass $\sim 3.4M_{\odot}$.” In: *Astrophys. J. Lett.* 892 (2020), p. L3. DOI: [10.3847/2041-8213/ab75f5](https://doi.org/10.3847/2041-8213/ab75f5). arXiv: [2001.01761](https://arxiv.org/abs/2001.01761) [astro-ph.HE].

- [141] Bin Liu and Dong Lai. “Hierarchical Black-Hole Mergers in Multiple Systems: Constrain the Formation of GW190412, GW190814 and GW190521-like events.” In: (Sept. 2020). arXiv: [2009.10068](https://arxiv.org/abs/2009.10068) [astro-ph.HE].
- [142] Giacomo Fragione, Abraham Loeb, and Frederic A. Rasio. “On the Origin of GW190521-like events from repeated black hole mergers in star clusters.” In: *Astrophys. J.* 902.1 (2020), p. L26. DOI: [10.3847/2041-8213/abbc0a](https://doi.org/10.3847/2041-8213/abbc0a). arXiv: [2009.05065](https://arxiv.org/abs/2009.05065) [astro-ph.GA].
- [143] Miguel A.S. Martinez et al. “Black Hole Mergers from Hierarchical Triples in Dense Star Clusters.” In: *Astrophys. J.* 903.1 (2020), p. 67. DOI: [10.3847/1538-4357/abba25](https://doi.org/10.3847/1538-4357/abba25). arXiv: [2009.08468](https://arxiv.org/abs/2009.08468) [astro-ph.GA].
- [144] Wenbin Lu, Paz Beniamini, and Clément Bonnerot. “On the formation of GW190814.” In: (Sept. 2020). DOI: [10.1093/mnras/staa3372](https://doi.org/10.1093/mnras/staa3372). arXiv: [2009.10082](https://arxiv.org/abs/2009.10082) [astro-ph.HE].
- [145] Imre Bartos, Bence Kocsis, Zolt Haiman, and Szabolcs Márka. “Rapid and Bright Stellar-mass Binary Black Hole Mergers in Active Galactic Nuclei.” In: *Astrophys. J.* 835.2 (2017), p. 165. DOI: [10.3847/1538-4357/835/2/165](https://doi.org/10.3847/1538-4357/835/2/165). arXiv: [1602.03831](https://arxiv.org/abs/1602.03831) [astro-ph.HE].
- [146] Nicholas C. Stone, Brian D. Metzger, and Zoltán Haiman. “Assisted inspirals of stellar mass black holes embedded in AGN discs: solving the ‘final au problem’.” In: *Monthly Notices of the Royal Astronomical Society* 464.1 (Sept. 2016), pp. 946–954. ISSN: 0035-8711. DOI: [10.1093/mnras/stw2260](https://doi.org/10.1093/mnras/stw2260). eprint: <https://academic.oup.com/mnras/article-pdf/464/1/946/18512767/stw2260.pdf>. URL: <https://doi.org/10.1093/mnras/stw2260>.
- [147] Xian Chen and Wen-Biao Han. “A New Type of Extreme-mass-ratio Inspirals Produced by Tidal Capture of Binary Black Holes.” In: *Communications Physics* 1 (2018), p. 53. DOI: [10.1038/s42005-018-0053-0](https://doi.org/10.1038/s42005-018-0053-0). arXiv: [1801.05780](https://arxiv.org/abs/1801.05780) [astro-ph.HE].
- [148] Alexandre Toubiana et al. “Detectable environmental effects in GW190521-like black-hole binaries with LISA.” In: (Oct. 2020). arXiv: [2010.06056](https://arxiv.org/abs/2010.06056) [astro-ph.HE].
- [149] Ryan M. O’Leary, Yohai Meiron, and Bence Kocsis. “Dynamical formation signatures of black hole binaries in the first detected mergers by LIGO.” In: *Astrophys. J. Lett.* 824.1 (2016), p. L12. DOI: [10.3847/2041-8205/824/1/L12](https://doi.org/10.3847/2041-8205/824/1/L12). arXiv: [1602.02809](https://arxiv.org/abs/1602.02809) [astro-ph.HE].

- [150] Carl L. Rodriguez, Meagan Morscher, Long Wang, Sourav Chatterjee, Frederic A. Rasio, and Rainer Spurzem. “Million-body star cluster simulations: comparisons between Monte Carlo and direct N-body.” In: *Monthly Notices of the Royal Astronomical Society* 463.2 (Dec. 2016), pp. 2109–2118. DOI: [10.1093/mnras/stw2121](https://doi.org/10.1093/mnras/stw2121). arXiv: [1601.04227](https://arxiv.org/abs/1601.04227) [astro-ph.IM].
- [151] Simon F. Portegies Zwart and Stephen L. W. McMillan. “Black Hole Mergers in the Universe.” In: 528.1 (2000), pp. L17–L20. DOI: [10.1086/312422](https://doi.org/10.1086/312422). URL: <https://doi.org/10.1086%2F312422>.
- [152] A. Tokovinin, S. Thomas, M. Sterzik, and S. Udry. “Tertiary companions to close spectroscopic binaries.” In: *A&A* 450.2 (May 2006), pp. 681–693. DOI: [10.1051/0004-6361:20054427](https://doi.org/10.1051/0004-6361:20054427). arXiv: [astro-ph/0601518](https://arxiv.org/abs/astro-ph/0601518) [astro-ph].
- [153] Theodor Pribulla and Slavek M. Rucinski. “Contact binaries with additional components. 1. the extant data.” In: *Astron. J.* 131 (2006), pp. 2986–3007. DOI: [10.1086/503871](https://doi.org/10.1086/503871). arXiv: [astro-ph/0601610](https://arxiv.org/abs/astro-ph/0601610).
- [154] Travis Robson, Neil J. Cornish, Nicola Tamanini, and Silvia Toonen. “Detecting hierarchical stellar systems with LISA.” In: *Phys. Rev. D* 98.6 (2018), p. 064012. DOI: [10.1103/PhysRevD.98.064012](https://doi.org/10.1103/PhysRevD.98.064012). arXiv: [1806.00500](https://arxiv.org/abs/1806.00500) [gr-qc].
- [155] Eric Poisson and Clifford M. Will. *Gravity: Newtonian, Post-Newtonian, Relativistic*. Cambridge University Press, 2014. DOI: [10.1017/CB09781139507486](https://doi.org/10.1017/CB09781139507486).
- [156] S. Cisneros, G. Goedecke, C. Beetle, and M. Engelhardt. “On the Doppler effect for light from orbiting sources in Kerr-type metrics.” In: *Monthly Notices of the Royal Astronomical Society* 448.3 (Mar. 2015), pp. 2733–2736. ISSN: 0035-8711. DOI: [10.1093/mnras/stv172](https://doi.org/10.1093/mnras/stv172). eprint: <https://academic.oup.com/mnras/article-pdf/448/3/2733/6007665/stv172.pdf>. URL: <https://doi.org/10.1093/mnras/stv172>.
- [157] Yohai Meiron, Bence Kocsis, and Abraham Loeb. “Detecting triple systems with gravitational wave observations.” In: *Astrophys. J.* 834.2 (2017), p. 200. DOI: [10.3847/1538-4357/834/2/200](https://doi.org/10.3847/1538-4357/834/2/200). arXiv: [1604.02148](https://arxiv.org/abs/1604.02148) [astro-ph.HE].
- [158] Lisa Randall and Zhong-Zhi Xianyu. “A Direct Probe of Mass Density Near Inspiring Binary Black Holes.” In: *Astrophys. J.* 878.2 (2019), p. 75. DOI: [10.3847/1538-4357/ab20c6](https://doi.org/10.3847/1538-4357/ab20c6). arXiv: [1805.05335](https://arxiv.org/abs/1805.05335) [gr-qc].
- [159] Kaze W.K. Wong, Vishal Baibhav, and Emanuele Berti. “Binary radial velocity measurements with space-based gravitational-wave detectors.” In: *Mon. Not. Roy. Astron. Soc.* 488.4 (2019),

- pp. 5665–5670. DOI: [10.1093/mnras/stz2077](https://doi.org/10.1093/mnras/stz2077). arXiv: [1902.01402](https://arxiv.org/abs/1902.01402) [astro-ph.HE].
- [160] Wen-Biao Han and Xian Chen. “Testing general relativity using binary extreme-mass-ratio inspirals.” In: *Mon. Not. Roy. Astron. Soc.* 485.1 (2019), pp. L29–L33. DOI: [10.1093/mnrasl/slz021](https://doi.org/10.1093/mnrasl/slz021). arXiv: [1801.07060](https://arxiv.org/abs/1801.07060) [gr-qc].
- [161] Alejandro Torres-Orjuela, Xian Chen, Zhoujian Cao, Pau Amaro-Seoane, and Peng Peng. “Detecting the Beaming Effect of Gravitational Waves.” In: *Phys. Rev. D* 100.6 (2019), p. 063012. DOI: [10.1103/PhysRevD.100.063012](https://doi.org/10.1103/PhysRevD.100.063012). arXiv: [1806.09857](https://arxiv.org/abs/1806.09857) [astro-ph.HE].
- [162] Alejandro Torres-Orjuela, Xian Chen, and Pau Amaro-Seoane. “Phase shift of gravitational waves induced by aberration.” In: *Phys. Rev. D* 101 (2020), p. 083028. DOI: [10.1103/PhysRevD.101.083028](https://doi.org/10.1103/PhysRevD.101.083028). arXiv: [2001.00721](https://arxiv.org/abs/2001.00721) [astro-ph.HE].
- [163] Yoshihide Kozai. “Secular perturbations of asteroids with high inclination and eccentricity.” In: *Astronomical Journal* 67 (Nov. 1962), pp. 591–598. DOI: [10.1086/108790](https://doi.org/10.1086/108790).
- [164] Smadar Naoz. “The Eccentric Kozai-Lidov Effect and Its Applications.” In: *Annual Review of Astronomy and Astrophysics* 54.1 (2016), pp. 441–489. DOI: [10.1146/annurev-astro-081915-023315](https://doi.org/10.1146/annurev-astro-081915-023315). eprint: <https://doi.org/10.1146/annurev-astro-081915-023315>. URL: <https://doi.org/10.1146/annurev-astro-081915-023315>.
- [165] Bao-Minh Hoang, Smadar Naoz, Bence Kocsis, Will Farr, and Jess McIver. “Detecting Supermassive Black Hole–induced Binary Eccentricity Oscillations with LISA.” In: *Astrophys. J. Lett.* 875.2 (2019), p. L31. DOI: [10.3847/2041-8213/ab14f7](https://doi.org/10.3847/2041-8213/ab14f7). arXiv: [1903.00134](https://arxiv.org/abs/1903.00134) [astro-ph.HE].
- [166] Lisa Randall and Zhong-Zhi Xianyu. “Observing Eccentricity Oscillations of Binary Black Holes in LISA.” In: (Feb. 2019). arXiv: [1902.08604](https://arxiv.org/abs/1902.08604) [astro-ph.HE].
- [167] Lisa Randall and Zhong-Zhi Xianyu. “Eccentricity Without Measuring Eccentricity: Discriminating Among Stellar Mass Black Hole Binary Formation Channels.” In: (July 2019). arXiv: [1907.02283](https://arxiv.org/abs/1907.02283) [astro-ph.HE].
- [168] Barnabás Deme, Bao-Minh Hoang, Smadar Naoz, and Bence Kocsis. “Detecting Kozai–Lidov Imprints on the Gravitational Waves of Intermediate-mass Black Holes in Galactic Nuclei.” In: *Astrophys. J.* 901.2 (2020), p. 125. DOI: [10.3847/1538-4357/abafa3](https://doi.org/10.3847/1538-4357/abafa3). arXiv: [2005.03677](https://arxiv.org/abs/2005.03677) [astro-ph.HE].

- [169] Bence Kocsis and Janna Levin. “Repeated bursts from relativistic scattering of compact objects in galactic nuclei.” In: *Phys. Rev. D* 85 (12 2012), p. 123005. DOI: [10.1103/PhysRevD.85.123005](https://doi.org/10.1103/PhysRevD.85.123005). URL: <https://link.aps.org/doi/10.1103/PhysRevD.85.123005>.
- [170] Priti Gupta, Haruka Suzuki, Hirotada Okawa, and Kei-ichi Maeda. “Gravitational Waves from Hierarchical Triple Systems with Kozai-Lidov Oscillation.” In: *Phys. Rev. D* 101.10 (2020), p. 104053. DOI: [10.1103/PhysRevD.101.104053](https://doi.org/10.1103/PhysRevD.101.104053). arXiv: [1911.11318](https://arxiv.org/abs/1911.11318) [gr-qc].
- [171] Vitor Cardoso and Francisco Duque. “Environmental effects in gravitational-wave physics: Tidal deformability of black holes immersed in matter.” In: *Phys. Rev. D* 101.6 (2020), p. 064028. DOI: [10.1103/PhysRevD.101.064028](https://doi.org/10.1103/PhysRevD.101.064028). arXiv: [1912.07616](https://arxiv.org/abs/1912.07616) [gr-qc].
- [172] Vitor Cardoso, Francisco Duque, and Arianna Foschi. “Light ring and the appearance of matter accreted by black holes.” In: *Phys. Rev. D* 103.10 (2021), p. 104044. DOI: [10.1103/PhysRevD.103.104044](https://doi.org/10.1103/PhysRevD.103.104044). arXiv: [2102.07784](https://arxiv.org/abs/2102.07784) [gr-qc].
- [173] Emanuele Berti, Vitor Cardoso, Mark Ho-Yeuk Cheung, Francesco Di Filippo, Francisco Duque, Paul Martens, and Shinji Mukohyama. “Stability of the fundamental quasinormal mode in time-domain observations against small perturbations.” In: *Phys. Rev. D* 106.8 (2022), p. 084011. DOI: [10.1103/PhysRevD.106.084011](https://doi.org/10.1103/PhysRevD.106.084011). arXiv: [2205.08547](https://arxiv.org/abs/2205.08547) [gr-qc].
- [174] Vitor Cardoso and Francisco Duque. “Resonances, black hole mimickers, and the greenhouse effect: Consequences for gravitational-wave physics.” In: *Phys. Rev. D* 105.10 (2022), p. 104023. DOI: [10.1103/PhysRevD.105.104023](https://doi.org/10.1103/PhysRevD.105.104023). arXiv: [2204.05315](https://arxiv.org/abs/2204.05315) [gr-qc].
- [175] Vitor Cardoso, Francisco Duque, and Gaurav Khanna. “Gravitational tuning forks and hierarchical triple systems.” In: *Phys. Rev. D* 103.8 (2021), p. L081501. DOI: [10.1103/PhysRevD.103.L081501](https://doi.org/10.1103/PhysRevD.103.L081501). arXiv: [2101.01186](https://arxiv.org/abs/2101.01186) [gr-qc].
- [176] Vitor Cardoso, Kyriakos Destounis, Francisco Duque, Rodrigo Panosso Macedo, and Andrea Maselli. “Black holes in galaxies: Environmental impact on gravitational-wave generation and propagation.” In: *Phys. Rev. D* 105.6 (2022), p. L061501. DOI: [10.1103/PhysRevD.105.L061501](https://doi.org/10.1103/PhysRevD.105.L061501). arXiv: [2109.00005](https://arxiv.org/abs/2109.00005) [gr-qc].
- [177] Vitor Cardoso, Kyriakos Destounis, Francisco Duque, Rodrigo Panosso Macedo, and Andrea Maselli. “Gravitational Waves from Extreme-Mass-Ratio Systems in Astrophysical Environments.” In: *Phys. Rev. Lett.* 129.24 (2022), p. 241103. DOI: [10.1103/PhysRevLett.129.241103](https://doi.org/10.1103/PhysRevLett.129.241103). arXiv: [2210.01133](https://arxiv.org/abs/2210.01133) [gr-qc].

- [178] S. Chandrasekhar. *The Mathematical Theory of Black Holes*. International series of monographs on physics. Oxford University Press, 1992. ISBN: 9780198520504. URL: <https://books.google.pt/books?id=l6BaRwAACAAJ>.
- [179] Adam Pound and Barry Wardell. “Black hole perturbation theory and gravitational self-force.” In: (Jan. 2021). DOI: [10.1007/978-981-15-4702-7_38-1](https://doi.org/10.1007/978-981-15-4702-7_38-1). arXiv: [2101.04592](https://arxiv.org/abs/2101.04592) [gr-qc].
- [180] Adam Pound, Barry Wardell, Niels Warburton, and Jeremy Miller. “Second-Order Self-Force Calculation of Gravitational Binding Energy in Compact Binaries.” In: *Phys. Rev. Lett.* 124.2 (2020), p. 021101. DOI: [10.1103/PhysRevLett.124.021101](https://doi.org/10.1103/PhysRevLett.124.021101). arXiv: [1908.07419](https://arxiv.org/abs/1908.07419) [gr-qc].
- [181] Andrew Spiers, Adam Pound, and Jordan Moxon. “Second-order Teukolsky formalism in Kerr spacetime: formulation and nonlinear source.” In: (May 2023). arXiv: [2305.19332](https://arxiv.org/abs/2305.19332) [gr-qc].
- [182] *NIST Digital Library of Mathematical Functions*. <http://dlmf.nist.gov/>, Release 1.0.26 of 2020-03-15. F. W. J. Olver, A. B. Olde Daalhuis, D. W. Lozier, B. I. Schneider, R. F. Boisvert, C. W. Clark, B. R. Miller, B. V. Saunders, H. S. Cohl, and M. A. McClain, eds. URL: <http://dlmf.nist.gov/>.
- [183] Norichika Sago, Hiroyuki Nakano, and Misao Sasaki. “Gauge problem in the gravitational selfforce. 1. Harmonic gauge approach in the Schwarzschild background.” In: *Phys. Rev. D* 67 (2003), p. 104017. DOI: [10.1103/PhysRevD.67.104017](https://doi.org/10.1103/PhysRevD.67.104017). arXiv: [gr-qc/0208060](https://arxiv.org/abs/gr-qc/0208060).
- [184] Karl Martel and Eric Poisson. “Gravitational perturbations of the Schwarzschild spacetime: A Practical covariant and gauge-invariant formalism.” In: *Phys. Rev. D* 71 (2005), p. 104003. DOI: [10.1103/PhysRevD.71.104003](https://doi.org/10.1103/PhysRevD.71.104003). arXiv: [gr-qc/0502028](https://arxiv.org/abs/gr-qc/0502028).
- [185] Tullio Regge and John A. Wheeler. “Stability of a Schwarzschild singularity.” In: *Phys. Rev.* 108 (1957), pp. 1063–1069. DOI: [10.1103/PhysRev.108.1063](https://doi.org/10.1103/PhysRev.108.1063).
- [186] Frank J. Zerilli. “Effective potential for even parity Regge-Wheeler gravitational perturbation equations.” In: *Phys. Rev. Lett.* 24 (1970), pp. 737–738. DOI: [10.1103/PhysRevLett.24.737](https://doi.org/10.1103/PhysRevLett.24.737).
- [187] F. J. Zerilli. “Gravitational field of a particle falling in a schwarzschild geometry analyzed in tensor harmonics.” In: *Phys. Rev. D* 2 (1970), pp. 2141–2160. DOI: [10.1103/PhysRevD.2.2141](https://doi.org/10.1103/PhysRevD.2.2141).
- [188] Emanuele Berti, Vitor Cardoso, and Andrei O. Starinets. “Quasi-normal modes of black holes and black branes.” In: *Class. Quant. Grav.* 26 (2009), p. 163001. DOI: [10.1088/0264-9381/26/16/163001](https://doi.org/10.1088/0264-9381/26/16/163001). arXiv: [0905.2975](https://arxiv.org/abs/0905.2975) [gr-qc].

- [189] Karl Martel. “Gravitational wave forms from a point particle orbiting a Schwarzschild black hole.” In: *Phys. Rev. D* 69 (2004), p. 044025. DOI: [10.1103/PhysRevD.69.044025](https://doi.org/10.1103/PhysRevD.69.044025). arXiv: [gr-qc/0311017](https://arxiv.org/abs/gr-qc/0311017).
- [190] Saul A. Teukolsky. “Perturbations of a rotating black hole. 1. Fundamental equations for gravitational electromagnetic and neutrino field perturbations.” In: *Astrophys. J.* 185 (1973), pp. 635–647. DOI: [10.1086/152444](https://doi.org/10.1086/152444).
- [191] Yasushi Mino, Misao Sasaki, Masaru Shibata, Hideyuki Tagoshi, and Takahiro Tanaka. “Black hole perturbation: Chapter 1.” In: *Prog. Theor. Phys. Suppl.* 128 (1997), pp. 1–121. DOI: [10.1143/PTPS.128.1](https://doi.org/10.1143/PTPS.128.1). arXiv: [gr-qc/9712057](https://arxiv.org/abs/gr-qc/9712057).
- [192] Nicholas Loutrel, Justin L. Ripley, Elena Giorgi, and Frans Pretorius. “Second Order Perturbations of Kerr Black Holes: Reconstruction of the Metric.” In: *Phys. Rev. D* 103.10 (2021), p. 104017. DOI: [10.1103/PhysRevD.103.104017](https://doi.org/10.1103/PhysRevD.103.104017). arXiv: [2008.11770 \[gr-qc\]](https://arxiv.org/abs/2008.11770).
- [193] Justin L. Ripley, Nicholas Loutrel, Elena Giorgi, and Frans Pretorius. “Numerical computation of second order vacuum perturbations of Kerr black holes.” In: *Phys. Rev. D* 103 (2021), p. 104018. DOI: [10.1103/PhysRevD.103.104018](https://doi.org/10.1103/PhysRevD.103.104018). arXiv: [2010.00162 \[gr-qc\]](https://arxiv.org/abs/2010.00162).
- [194] William Krivan, Pablo Laguna, Philippos Papadopoulos, and Nils Andersson. “Dynamics of perturbations of rotating black holes.” In: *Phys. Rev. D* 56 (1997), pp. 3395–3404. DOI: [10.1103/PhysRevD.56.3395](https://doi.org/10.1103/PhysRevD.56.3395). arXiv: [gr-qc/9702048](https://arxiv.org/abs/gr-qc/9702048).
- [195] Enrique Pazos-Ávalos and Carlos O. Lousto. “Numerical integration of the Teukolsky equation in the time domain.” In: *Physical Review D* 72.8 (2005). ISSN: 1550-2368. DOI: [10.1103/physrevd.72.084022](https://doi.org/10.1103/physrevd.72.084022). URL: <http://dx.doi.org/10.1103/PhysRevD.72.084022>.
- [196] Pranesh A. Sundararajan, Gaurav Khanna, and Scott A. Hughes. “Towards adiabatic waveforms for inspiral into Kerr black holes. I. A New model of the source for the time domain perturbation equation.” In: *Phys. Rev. D* 76 (2007), p. 104005. DOI: [10.1103/PhysRevD.76.104005](https://doi.org/10.1103/PhysRevD.76.104005). arXiv: [gr-qc/0703028 \[gr-qc\]](https://arxiv.org/abs/gr-qc/0703028).
- [197] Anil Zenginoglu and Gaurav Khanna. “Null infinity waveforms from extreme-mass-ratio inspirals in Kerr spacetime.” In: *Phys. Rev. X* 1 (2011), p. 021017. DOI: [10.1103/PhysRevX.1.021017](https://doi.org/10.1103/PhysRevX.1.021017). arXiv: [1108.1816 \[gr-qc\]](https://arxiv.org/abs/1108.1816).
- [198] Lior M. Burko and Gaurav Khanna. “Late-time Kerr tails: Generic and non-generic initial data sets, ‘up’ modes, and superposition.” In: *Class. Quant. Grav.* 28 (2011), p. 025012. DOI: [10.1088/0264-9381/28/2/025012](https://doi.org/10.1088/0264-9381/28/2/025012). arXiv: [1001.0541 \[gr-qc\]](https://arxiv.org/abs/1001.0541).

- [199] Anil Zenginoğlu, Gaurav Khanna, and Lior M. Burko. “Intermediate behavior of Kerr tails.” In: *Gen. Rel. Grav.* 46 (2014), p. 1672. DOI: [10.1007/s10714-014-1672-8](https://doi.org/10.1007/s10714-014-1672-8). arXiv: [1208.5839](https://arxiv.org/abs/1208.5839) [gr-qc].
- [200] Pranesh A. Sundararajan, Gaurav Khanna, Scott A. Hughes, and Steve Drasco. “Towards adiabatic waveforms for inspiral into Kerr black holes: II. Dynamical sources and generic orbits.” In: *Phys. Rev. D* 78 (2008), p. 024022. DOI: [10.1103/PhysRevD.78.024022](https://doi.org/10.1103/PhysRevD.78.024022). arXiv: [0803.0317](https://arxiv.org/abs/0803.0317) [gr-qc].
- [201] Pranesh A. Sundararajan, Gaurav Khanna, and Scott A. Hughes. “Binary black hole merger gravitational waves and recoil in the large mass ratio limit.” In: *Phys. Rev. D* 81 (2010), p. 104009. DOI: [10.1103/PhysRevD.81.104009](https://doi.org/10.1103/PhysRevD.81.104009). arXiv: [1003.0485](https://arxiv.org/abs/1003.0485) [gr-qc].
- [202] Enrico Barausse, Alessandra Buonanno, Scott A. Hughes, Gaurav Khanna, Stephen O’Sullivan, and Yi Pan. “Modeling multipolar gravitational-wave emission from small mass-ratio mergers.” In: *Phys. Rev. D* 85 (2012), p. 024046. DOI: [10.1103/PhysRevD.85.024046](https://doi.org/10.1103/PhysRevD.85.024046). arXiv: [1110.3081](https://arxiv.org/abs/1110.3081) [gr-qc].
- [203] Ramon Lopez-Aleman, Gaurav Khanna, and Jorge Pullin. “Perturbative evolution of particle orbits around Kerr black holes: Time domain calculation.” In: *Class. Quant. Grav.* 20 (2003), pp. 3259–3268. DOI: [10.1088/0264-9381/20/14/320](https://doi.org/10.1088/0264-9381/20/14/320). arXiv: [gr-qc/0303054](https://arxiv.org/abs/gr-qc/0303054).
- [204] Anil Zenginoglu. “Hyperboloidal foliations and scri-fixing.” In: *Class. Quant. Grav.* 25 (2008), p. 145002. DOI: [10.1088/0264-9381/25/14/145002](https://doi.org/10.1088/0264-9381/25/14/145002). arXiv: [0712.4333](https://arxiv.org/abs/0712.4333) [gr-qc].
- [205] Rodrigo Panosso Macedo. “Hyperboloidal framework for the Kerr spacetime.” In: *Class. Quant. Grav.* 37.6 (2020), p. 065019. DOI: [10.1088/1361-6382/ab6e3e](https://doi.org/10.1088/1361-6382/ab6e3e). arXiv: [1910.13452](https://arxiv.org/abs/1910.13452) [gr-qc].
- [206] Sjoert van Velzen, Alexander J. Mendez, Julian H. Krolik, and Varoujan Gorjian. “Discovery of transient infrared emission from dust heated by stellar tidal disruption flares.” In: *Astrophys. J.* 829.1 (2016), p. 19. DOI: [10.3847/0004-637X/829/1/19](https://doi.org/10.3847/0004-637X/829/1/19). arXiv: [1605.04304](https://arxiv.org/abs/1605.04304) [astro-ph.HE].
- [207] Thomas W. S. Holoien et al. “Discovery and Early Evolution of ASASSN-19bt, the First TDE Detected by TESS.” In: *Astrophys. J.* 883 (2019), p. 111. DOI: [10.3847/1538-4357/ab3c66](https://doi.org/10.3847/1538-4357/ab3c66). arXiv: [1904.09293](https://arxiv.org/abs/1904.09293) [astro-ph.HE].
- [208] Thierry Mora and Clifford M. Will. “A PostNewtonian diagnostic of quasiequilibrium binary configurations of compact objects.” In: *Phys. Rev. D* 69 (2004). [Erratum: *Phys. Rev. D* 71, 129901(E)(2005)], p. 104021. DOI: [10.1103/PhysRevD.71.129901](https://doi.org/10.1103/PhysRevD.71.129901), [10.1103/PhysRevD.69.104021](https://doi.org/10.1103/PhysRevD.69.104021). arXiv: [gr-qc/0312082](https://arxiv.org/abs/gr-qc/0312082) [gr-qc].

- [209] Justin E. Vines and Eanna E. Flanagan. “Post-1-Newtonian quadrupole tidal interactions in binary systems.” In: *Phys. Rev. D* 88 (2013), p. 024046. DOI: [10.1103/PhysRevD.88.024046](https://doi.org/10.1103/PhysRevD.88.024046). arXiv: [1009.4919](https://arxiv.org/abs/1009.4919) [gr-qc].
- [210] Eanna E. Flanagan and Tanja Hinderer. “Constraining neutron star tidal Love numbers with gravitational wave detectors.” In: *Phys. Rev. D* 77 (2008), p. 021502. DOI: [10.1103/PhysRevD.77.021502](https://doi.org/10.1103/PhysRevD.77.021502). arXiv: [0709.1915](https://arxiv.org/abs/0709.1915) [astro-ph].
- [211] Tanja Hinderer et al. “Effects of neutron-star dynamic tides on gravitational waveforms within the effective-one-body approach.” In: *Phys. Rev. Lett.* 116.18 (2016), p. 181101. DOI: [10.1103/PhysRevLett.116.181101](https://doi.org/10.1103/PhysRevLett.116.181101). arXiv: [1602.00599](https://arxiv.org/abs/1602.00599) [gr-qc].
- [212] Taylor Binnington and Eric Poisson. “Relativistic theory of tidal Love numbers.” In: *Phys. Rev. D* 80 (2009), p. 084018. DOI: [10.1103/PhysRevD.80.084018](https://doi.org/10.1103/PhysRevD.80.084018). arXiv: [0906.1366](https://arxiv.org/abs/0906.1366) [gr-qc].
- [213] Thibault Damour and Alessandro Nagar. “Relativistic tidal properties of neutron stars.” In: *Phys. Rev. D* 80 (2009), p. 084035. DOI: [10.1103/PhysRevD.80.084035](https://doi.org/10.1103/PhysRevD.80.084035). arXiv: [0906.0096](https://arxiv.org/abs/0906.0096) [gr-qc].
- [214] Tanja Hinderer. “Tidal Love numbers of neutron stars.” In: *Astrophys. J.* 677 (2008). Erratum: *ibid.* 697, 964 (2009), pp. 1216–1220. DOI: [10.1086/533487](https://doi.org/10.1086/533487). arXiv: [0711.2420](https://arxiv.org/abs/0711.2420) [astro-ph].
- [215] Luca Baiotti. “Gravitational waves from neutron star mergers and their relation to the nuclear equation of state.” In: *Prog. Part. Nucl. Phys.* 109 (2019), p. 103714. DOI: [10.1016/j.pnpnp.2019.103714](https://doi.org/10.1016/j.pnpnp.2019.103714). arXiv: [1907.08534](https://arxiv.org/abs/1907.08534) [astro-ph.HE].
- [216] B. P. Abbott et al. “GW170817: Measurements of neutron star radii and equation of state.” In: *Phys. Rev. Lett.* 121.16 (2018), p. 161101. DOI: [10.1103/PhysRevLett.121.161101](https://doi.org/10.1103/PhysRevLett.121.161101). arXiv: [1805.11581](https://arxiv.org/abs/1805.11581) [gr-qc].
- [217] Vitor Cardoso, Edgardo Franzin, Andrea Maselli, Paolo Pani, and Guilherme Raposo. “Testing strong-field gravity with tidal Love numbers.” In: *Phys. Rev. D* 95.8 (2017). [Addendum: *Phys.Rev.D* 95, 089901 (2017)], p. 084014. DOI: [10.1103/PhysRevD.95.084014](https://doi.org/10.1103/PhysRevD.95.084014). arXiv: [1701.01116](https://arxiv.org/abs/1701.01116) [gr-qc].
- [218] Andrea Maselli, Paolo Pani, Vitor Cardoso, Tiziano Abdelsalhin, Leonardo Gualtieri, and Valeria Ferrari. “Probing Planckian corrections at the horizon scale with LISA binaries.” In: *Phys. Rev. Lett.* 120.8 (2018), p. 081101. DOI: [10.1103/PhysRevLett.120.081101](https://doi.org/10.1103/PhysRevLett.120.081101). arXiv: [1703.10612](https://arxiv.org/abs/1703.10612) [gr-qc].
- [219] Andrea Maselli, Paolo Pani, Vitor Cardoso, Tiziano Abdelsalhin, Leonardo Gualtieri, and Valeria Ferrari. “From micro to macro and back: probing near-horizon quantum structures with gravitational waves.” In: (2018). arXiv: [1811.03689](https://arxiv.org/abs/1811.03689) [gr-qc].

- [220] Paolo Pani and Andrea Maselli. “Love in Extrema Ratio.” In: (2019). DOI: [10.1142/S0218271819440012](https://doi.org/10.1142/S0218271819440012). arXiv: [1905.03947](https://arxiv.org/abs/1905.03947) [gr-qc].
- [221] Sayak Datta. “Probing horizon scale quantum effects with Love.” In: *Class. Quant. Grav.* 39.22 (2022), p. 225016. DOI: [10.1088/1361-6382/ac9ae4](https://doi.org/10.1088/1361-6382/ac9ae4). arXiv: [2107.07258](https://arxiv.org/abs/2107.07258) [gr-qc].
- [222] Norman Gürlebeck. “No-hair theorem for Black Holes in Astrophysical Environments.” In: *Phys. Rev. Lett.* 114.15 (2015), p. 151102. DOI: [10.1103/PhysRevLett.114.151102](https://doi.org/10.1103/PhysRevLett.114.151102). arXiv: [1503.03240](https://arxiv.org/abs/1503.03240) [gr-qc].
- [223] Philippe Landry and Eric Poisson. “Tidal deformation of a slowly rotating material body. External metric.” In: *Phys. Rev. D* 91 (2015), p. 104018. DOI: [10.1103/PhysRevD.91.104018](https://doi.org/10.1103/PhysRevD.91.104018). arXiv: [1503.07366](https://arxiv.org/abs/1503.07366) [gr-qc].
- [224] Paolo Pani, Leonardo Gualtieri, Andrea Maselli, and Valeria Ferrari. “Tidal deformations of a spinning compact object.” In: *Phys. Rev. D* 92.2 (2015), p. 024010. DOI: [10.1103/PhysRevD.92.024010](https://doi.org/10.1103/PhysRevD.92.024010). arXiv: [1503.07365](https://arxiv.org/abs/1503.07365) [gr-qc].
- [225] Alexandre Le Tiec, Marc Casals, and Edgardo Franzin. “Tidal Love numbers of Kerr black holes.” In: *Phys. Rev. D* 103 (8 2021), p. 084021. DOI: [10.1103/PhysRevD.103.084021](https://doi.org/10.1103/PhysRevD.103.084021). URL: <https://link.aps.org/doi/10.1103/PhysRevD.103.084021>.
- [226] Alexandre Le Tiec and Marc Casals. “Spinning Black Holes Fall in Love.” In: *Phys. Rev. Lett.* 126 (13 2021), p. 131102. DOI: [10.1103/PhysRevLett.126.131102](https://doi.org/10.1103/PhysRevLett.126.131102). URL: <https://link.aps.org/doi/10.1103/PhysRevLett.126.131102>.
- [227] Horng Sheng Chia. “Tidal deformation and dissipation of rotating black holes.” In: *Phys. Rev. D* 104.2 (2021), p. 024013. DOI: [10.1103/PhysRevD.104.024013](https://doi.org/10.1103/PhysRevD.104.024013). arXiv: [2010.07300](https://arxiv.org/abs/2010.07300) [gr-qc].
- [228] Panagiotis Charalambous, Sergei Dubovsky, and Mikhail M. Ivanov. “Hidden Symmetry of Vanishing Love Numbers.” In: *Phys. Rev. Lett.* 127.10 (2021), p. 101101. DOI: [10.1103/PhysRevLett.127.101101](https://doi.org/10.1103/PhysRevLett.127.101101). arXiv: [2103.01234](https://arxiv.org/abs/2103.01234) [hep-th].
- [229] Jibril Ben Achour, Etera R. Livine, Shinji Mukohyama, and Jean-Philippe Uzan. “Hidden symmetry of the static response of black holes: applications to Love numbers.” In: *JHEP* 07 (2022), p. 112. DOI: [10.1007/JHEP07\(2022\)112](https://doi.org/10.1007/JHEP07(2022)112). arXiv: [2202.12828](https://arxiv.org/abs/2202.12828) [gr-qc].
- [230] Lam Hui, Austin Joyce, Riccardo Penco, Luca Santoni, and Adam R. Solomon. “Near-zone symmetries of Kerr black holes.” In: *JHEP* 09 (2022), p. 049. DOI: [10.1007/JHEP09\(2022\)049](https://doi.org/10.1007/JHEP09(2022)049). arXiv: [2203.08832](https://arxiv.org/abs/2203.08832) [hep-th].

- [231] Vitor Cardoso and Paolo Pani. “Testing the nature of dark compact objects: a status report.” In: *Living Rev. Rel.* 22.1 (2019), p. 4. DOI: [10.1007/s41114-019-0020-4](https://doi.org/10.1007/s41114-019-0020-4). arXiv: [1904.05363](https://arxiv.org/abs/1904.05363) [gr-qc].
- [232] Laura Bernard. “Dipolar tidal effects in scalar-tensor theories.” In: (2019). arXiv: [1906.10735](https://arxiv.org/abs/1906.10735) [gr-qc].
- [233] Vitor Cardoso, Masashi Kimura, Andrea Maselli, and Leonardo Senatore. “Black Holes in an Effective Field Theory Extension of General Relativity.” In: *Phys. Rev. Lett.* 121.25 (2018), p. 251105. DOI: [10.1103/PhysRevLett.121.251105](https://doi.org/10.1103/PhysRevLett.121.251105). arXiv: [1808.08962](https://arxiv.org/abs/1808.08962) [gr-qc].
- [234] Stephon Alexander and Nicolas Yunes. “Chern-Simons Modified General Relativity.” In: *Phys. Rept.* 480 (2009), pp. 1–55. DOI: [10.1016/j.physrep.2009.07.002](https://doi.org/10.1016/j.physrep.2009.07.002). arXiv: [0907.2562](https://arxiv.org/abs/0907.2562) [hep-th].
- [235] D. Vogt and P. S. Letelier. “Newtonian and General Relativistic Models of Spherical Shells - II.” In: *Mon. Not. Roy. Astron. Soc.* 406 (2010), pp. 2689–2700. DOI: [10.1111/j.1365-2966.2010.16863.x](https://doi.org/10.1111/j.1365-2966.2010.16863.x). arXiv: [1006.2280](https://arxiv.org/abs/1006.2280) [gr-qc].
- [236] Raissa F. P. Mendes and Huan Yang. “Tidal deformability of boson stars and dark matter clumps.” In: *Class. Quant. Grav.* 34.18 (2017), p. 185001. DOI: [10.1088/1361-6382/aa842d](https://doi.org/10.1088/1361-6382/aa842d). arXiv: [1606.03035](https://arxiv.org/abs/1606.03035) [astro-ph.CO].
- [237] K. S. Thorne. “Multipole Expansions of Gravitational Radiation.” In: *Rev. Mod. Phys.* 52 (1980), pp. 299–339. DOI: [10.1103/RevModPhys.52.299](https://doi.org/10.1103/RevModPhys.52.299).
- [238] J. David Brown and Viqar Husain. “Black holes with short hair.” In: *Int. J. Mod. Phys. D* 6 (1997), pp. 563–573. DOI: [10.1142/S0218271897000340](https://doi.org/10.1142/S0218271897000340). arXiv: [gr-qc/9707027](https://arxiv.org/abs/gr-qc/9707027) [gr-qc].
- [239] K. S. Thorne and A. Campolattaro. “Erratum: Non-Radial Pulsation of General-Relativistic Stellar Models. I. Analytic Analysis for $L \geq 2$.” In: *Astrophysics Journal* 152 (1968), p. 673. DOI: [10.1086/149586](https://doi.org/10.1086/149586).
- [240] W. Israel. “Singular hypersurfaces and thin shells in general relativity.” In: *Nuovo Cim.* B44S10 (1966). [Nuovo Cim.B44,1(1966)], p. 1. DOI: [10.1007/BF02710419](https://doi.org/10.1007/BF02710419), [10.1007/BF02712210](https://doi.org/10.1007/BF02712210).
- [241] P. R. Brady, J. Louko, and Eric Poisson. “Stability of a shell around a black hole.” In: *Phys. Rev. D* 44 (1991), pp. 1891–1894. DOI: [10.1103/PhysRevD.44.1891](https://doi.org/10.1103/PhysRevD.44.1891).
- [242] Eric Poisson and Matt Visser. “Thin shell wormholes: Linearization stability.” In: *Phys. Rev. D* 52 (1995), pp. 7318–7321. DOI: [10.1103/PhysRevD.52.7318](https://doi.org/10.1103/PhysRevD.52.7318). arXiv: [gr-qc/9506083](https://arxiv.org/abs/gr-qc/9506083) [gr-qc].

- [243] Francisco S. N. Lobo and Paulo Crawford. “Stability analysis of dynamic thin shells.” In: *Class. Quant. Grav.* 22 (2005), pp. 4869–4886. DOI: [10.1088/0264-9381/22/22/012](https://doi.org/10.1088/0264-9381/22/22/012). arXiv: [gr-qc/0507063](https://arxiv.org/abs/gr-qc/0507063) [gr-qc].
- [244] Goncalo A. S. Dias and Jose P. S. Lemos. “Thin-shell wormholes in d -dimensional general relativity: Solutions, properties, and stability.” In: *Phys. Rev. D* 82 (2010), p. 084023. DOI: [10.1103/PhysRevD.82.084023](https://doi.org/10.1103/PhysRevD.82.084023). arXiv: [1008.3376](https://arxiv.org/abs/1008.3376) [gr-qc].
- [245] Philip LeMaitre and Eric Poisson. “Equilibrium and stability of thin spherical shells in Newtonian and relativistic gravity.” In: (2019). arXiv: [1909.06253](https://arxiv.org/abs/1909.06253) [gr-qc].
- [246] Eric Poisson. *A Relativist’s Toolkit: The Mathematics of Black-Hole Mechanics*. Cambridge University Press, 2009. DOI: [10.1017/CB09780511606601](https://doi.org/10.1017/CB09780511606601).
- [247] Paolo Pani, Emanuele Berti, Vitor Cardoso, Yanbei Chen, and Richard Norte. “Gravitational wave signatures of the absence of an event horizon. I. Nonradial oscillations of a thin-shell gravastar.” In: *Phys. Rev. D* 80 (2009), p. 124047. DOI: [10.1103/PhysRevD.80.124047](https://doi.org/10.1103/PhysRevD.80.124047). arXiv: [0909.0287](https://arxiv.org/abs/0909.0287) [gr-qc].
- [248] P. T. Leung, Y. T. Liu, W. M. Suen, C. Y. Tam, and K. Young. “Perturbative approach to the quasinormal modes of dirty black holes.” In: *Phys. Rev. D* 59 (1999), p. 044034. DOI: [10.1103/PhysRevD.59.044034](https://doi.org/10.1103/PhysRevD.59.044034). arXiv: [gr-qc/9903032](https://arxiv.org/abs/gr-qc/9903032).
- [249] P. T. Leung, Y. T. Liu, W. M. Suen, C. Y. Tam, and K. Young. “Quasinormal modes of dirty black holes.” In: *Phys. Rev. Lett.* 78 (1997), pp. 2894–2897. DOI: [10.1103/PhysRevLett.78.2894](https://doi.org/10.1103/PhysRevLett.78.2894). arXiv: [gr-qc/9903031](https://arxiv.org/abs/gr-qc/9903031) [gr-qc].
- [250] Nami Uchikata, Shijun Yoshida, and Paolo Pani. “Tidal deformability and I-Love-Q relations for gravastars with polytropic thin shells.” In: *Phys. Rev. D* 94.6 (2016), p. 064015. DOI: [10.1103/PhysRevD.94.064015](https://doi.org/10.1103/PhysRevD.94.064015). arXiv: [1607.03593](https://arxiv.org/abs/1607.03593) [gr-qc].
- [251] Ryan McManus, Emanuele Berti, David E. Kaplan, and Surjeet Rajendran. “Quasinormal modes and stability of firewalls.” In: *Phys. Rev. D* 102.10 (2020), p. 104031. DOI: [10.1103/PhysRevD.102.104031](https://doi.org/10.1103/PhysRevD.102.104031). arXiv: [2007.15525](https://arxiv.org/abs/2007.15525) [gr-qc].
- [252] Matt Visser and David L. Wiltshire. “Stable gravastars: An Alternative to black holes?” In: *Class. Quant. Grav.* 21 (2004), pp. 1135–1152. DOI: [10.1088/0264-9381/21/4/027](https://doi.org/10.1088/0264-9381/21/4/027). arXiv: [gr-qc/0310107](https://arxiv.org/abs/gr-qc/0310107) [gr-qc].
- [253] Nami Uchikata and Shijun Yoshida. “Slowly rotating thin shell gravastars.” In: *Class. Quant. Grav.* 33.2 (2016), p. 025005. DOI: [10.1088/0264-9381/33/2/025005](https://doi.org/10.1088/0264-9381/33/2/025005). arXiv: [1506.06485](https://arxiv.org/abs/1506.06485) [gr-qc].

- [254] Valerio De Luca and Paolo Pani. “Tidal deformability of dressed black holes and tests of ultralight bosons in extended mass ranges.” In: *JCAP* 08 (2021), p. 032. DOI: [10.1088/1475-7516/2021/08/032](https://doi.org/10.1088/1475-7516/2021/08/032). arXiv: [2106.14428](https://arxiv.org/abs/2106.14428) [gr-qc].
- [255] Valerio De Luca, Andrea Maselli, and Paolo Pani. “Modeling frequency-dependent tidal deformability for environmental black hole mergers.” In: *Phys. Rev. D* 107.4 (2023), p. 044058. DOI: [10.1103/PhysRevD.107.044058](https://doi.org/10.1103/PhysRevD.107.044058). arXiv: [2212.03343](https://arxiv.org/abs/2212.03343) [gr-qc].
- [256] Theo Torres, Mohamed Ould El Hadj, Shi-Qian Hu, and Ruth Gregory. “Regge pole description of scattering by dirty black holes.” In: *Phys. Rev. D* 107.6 (2023), p. 064028. DOI: [10.1103/PhysRevD.107.064028](https://doi.org/10.1103/PhysRevD.107.064028). arXiv: [2211.17147](https://arxiv.org/abs/2211.17147) [gr-qc].
- [257] Takuya Katagiri, Hiroyuki Nakano, and Kazuyuki Omukai. “Stability of relativistic tidal response against small potential modification.” In: (Apr. 2023). arXiv: [2304.04551](https://arxiv.org/abs/2304.04551) [gr-qc].
- [258] Asimina Arvanitaki and Sergei Dubovsky. “Exploring the String Axiverse with Precision Black Hole Physics.” In: *Phys. Rev. D* 83 (2011), p. 044026. DOI: [10.1103/PhysRevD.83.044026](https://doi.org/10.1103/PhysRevD.83.044026). arXiv: [1004.3558](https://arxiv.org/abs/1004.3558) [hep-th].
- [259] Asimina Arvanitaki, Masha Baryakhtar, Savas Dimopoulos, Sergei Dubovsky, and Robert Lasenby. “Black Hole Mergers and the QCD Axion at Advanced LIGO.” In: *Phys. Rev. D* 95.4 (2017), p. 043001. DOI: [10.1103/PhysRevD.95.043001](https://doi.org/10.1103/PhysRevD.95.043001). arXiv: [1604.03958](https://arxiv.org/abs/1604.03958) [hep-ph].
- [260] Miguel C. Ferreira, Caio F. B. Macedo, and Vitor Cardoso. “Orbital fingerprints of ultralight scalar fields around black holes.” In: *Phys. Rev. D* 96.8 (2017), p. 083017. DOI: [10.1103/PhysRevD.96.083017](https://doi.org/10.1103/PhysRevD.96.083017). arXiv: [1710.00830](https://arxiv.org/abs/1710.00830) [gr-qc].
- [261] Mateja Boskovic, Francisco Duque, Miguel C. Ferreira, Filipe S. Miguel, and Vitor Cardoso. “Motion in time-periodic backgrounds with applications to ultralight dark matter haloes at galactic centers.” In: *Phys. Rev. D* 98 (2018), p. 024037. DOI: [10.1103/PhysRevD.98.024037](https://doi.org/10.1103/PhysRevD.98.024037). arXiv: [1806.07331](https://arxiv.org/abs/1806.07331) [gr-qc].
- [262] Vitor Cardoso, Sayan Chakrabarti, Paolo Pani, Emanuele Berti, and Leonardo Gualtieri. “Floating and sinking: The Imprint of massive scalars around rotating black holes.” In: *Phys. Rev. Lett.* 107 (2011), p. 241101. DOI: [10.1103/PhysRevLett.107.241101](https://doi.org/10.1103/PhysRevLett.107.241101). arXiv: [1109.6021](https://arxiv.org/abs/1109.6021) [gr-qc].
- [263] Jun Zhang and Huan Yang. “Gravitational floating orbits around hairy black holes.” In: *Phys. Rev. D* 99.6 (2019), p. 064018. DOI: [10.1103/PhysRevD.99.064018](https://doi.org/10.1103/PhysRevD.99.064018). arXiv: [1808.02905](https://arxiv.org/abs/1808.02905) [gr-qc].
- [264] Jun Zhang and Huan Yang. “Dynamic Signatures of Black Hole Binaries with Superradiant Clouds.” In: (2019). arXiv: [1907.13582](https://arxiv.org/abs/1907.13582) [gr-qc].

- [265] Taishi Ikeda, Richard Brito, and Vitor Cardoso. “Blasts of Light from Axions.” In: *Phys. Rev. Lett.* 122.8 (2019), p. 081101. DOI: [10.1103/PhysRevLett.122.081101](https://doi.org/10.1103/PhysRevLett.122.081101). arXiv: [1811.04950](https://arxiv.org/abs/1811.04950) [gr-qc].
- [266] Mateja Boskovic, Richard Brito, Vitor Cardoso, Taishi Ikeda, and Helvi Witek. “Axionic instabilities and new black hole solutions.” In: *Phys. Rev. D* 99.3 (2019), p. 035006. DOI: [10.1103/PhysRevD.99.035006](https://doi.org/10.1103/PhysRevD.99.035006). arXiv: [1811.04945](https://arxiv.org/abs/1811.04945) [gr-qc].
- [267] Asimina Arvanitaki, Masha Baryakhtar, and Xinlu Huang. “Discovering the QCD Axion with Black Holes and Gravitational Waves.” In: *Phys. Rev. D* 91.8 (2015), p. 084011. DOI: [10.1103/PhysRevD.91.084011](https://doi.org/10.1103/PhysRevD.91.084011). arXiv: [1411.2263](https://arxiv.org/abs/1411.2263) [hep-ph].
- [268] Emanuele Berti, Richard Brito, Caio F. B. Macedo, Guilherme Raposo, and Joao Luis Rosa. “Ultralight boson cloud depletion in binary systems.” In: *Phys. Rev. D* 99.10 (2019), p. 104039. DOI: [10.1103/PhysRevD.99.104039](https://doi.org/10.1103/PhysRevD.99.104039). arXiv: [1904.03131](https://arxiv.org/abs/1904.03131) [gr-qc].
- [269] Vitor Cardoso and Paolo Pani. “Tidal acceleration of black holes and superradiance.” In: *Class. Quant. Grav.* 30 (2013), p. 045011. DOI: [10.1088/0264-9381/30/4/045011](https://doi.org/10.1088/0264-9381/30/4/045011). arXiv: [1205.3184](https://arxiv.org/abs/1205.3184) [gr-qc].
- [270] Steven L. Detweiler. “KLEIN-GORDON EQUATION AND ROTATING BLACK HOLES.” In: *Phys. Rev. D* 22 (1980), pp. 2323–2326. DOI: [10.1103/PhysRevD.22.2323](https://doi.org/10.1103/PhysRevD.22.2323).
- [271] Stephanie Taylor and Eric Poisson. “Nonrotating black hole in a post-Newtonian tidal environment.” In: *Phys. Rev. D* 78 (2008), p. 084016. DOI: [10.1103/PhysRevD.78.084016](https://doi.org/10.1103/PhysRevD.78.084016). arXiv: [0806.3052](https://arxiv.org/abs/0806.3052) [gr-qc].
- [272] Helvi Witek, Vitor Cardoso, Akihiro Ishibashi, and Ulrich Sperhake. “Superradiant instabilities in astrophysical systems.” In: *Phys. Rev. D* 87.4 (2013), p. 043513. DOI: [10.1103/PhysRevD.87.043513](https://doi.org/10.1103/PhysRevD.87.043513). arXiv: [1212.0551](https://arxiv.org/abs/1212.0551) [gr-qc].
- [273] Hirotaka Yoshino and Hideo Kodama. “Gravitational radiation from an axion cloud around a black hole: Superradiant phase.” In: *PTEP* 2014 (2014), 043E02. DOI: [10.1093/ptep/ptu029](https://doi.org/10.1093/ptep/ptu029). arXiv: [1312.2326](https://arxiv.org/abs/1312.2326) [gr-qc].
- [274] Jerome A. Orosz, Jeffrey E. McClintock, Jason P. Aufdenberg, Ronald A. Remillard, Mark J. Reid, Ramesh Narayan, and Lijun Gou. “THE MASS OF THE BLACK HOLE IN CYGNUS X-1.” In: *The Astrophysical Journal* 742.2 (2011), p. 84. ISSN: 1538-4357. DOI: [10.1088/0004-637x/742/2/84](https://doi.org/10.1088/0004-637x/742/2/84). URL: <http://dx.doi.org/10.1088/0004-637x/742/2/84>.
- [275] Paolo Pani, Vitor Cardoso, Leonardo Gualtieri, Emanuele Berti, and Akihiro Ishibashi. “Black hole bombs and photon mass bounds.” In: *Phys. Rev. Lett.* 109 (2012), p. 131102. DOI: [10.1103/PhysRevLett.109.131102](https://doi.org/10.1103/PhysRevLett.109.131102). arXiv: [1209.0465](https://arxiv.org/abs/1209.0465) [gr-qc].

- [276] Vitor Cardoso, Óscar J. C. Dias, Gavin S. Hartnett, Matthew Middleton, Paolo Pani, and Jorge E. Santos. “Constraining the mass of dark photons and axion-like particles through black-hole superradiance.” In: *JCAP* 1803.03 (2018), p. 043. DOI: [10.1088/1475-7516/2018/03/043](https://doi.org/10.1088/1475-7516/2018/03/043). arXiv: [1801.01420](https://arxiv.org/abs/1801.01420) [gr-qc].
- [277] Hirotaka Yoshino and Hideo Kodama. “Probing the string axiverse by gravitational waves from Cygnus X-1.” In: *PTEP* 2015.6 (2015), 061E01. DOI: [10.1093/ptep/ptv067](https://doi.org/10.1093/ptep/ptv067). arXiv: [1407.2030](https://arxiv.org/abs/1407.2030) [gr-qc].
- [278] Ling Sun, Richard Brito, and Maximiliano Isi. “Search for ultra-light bosons in Cygnus X-1 with Advanced LIGO.” In: (2019). arXiv: [1909.11267](https://arxiv.org/abs/1909.11267) [gr-qc].
- [279] R. Abuter et al. “Detection of the gravitational redshift in the orbit of the star S2 near the Galactic centre massive black hole.” In: *Astron. Astrophys.* 615 (2018), p. L15. DOI: [10.1051/0004-6361/201833718](https://doi.org/10.1051/0004-6361/201833718). arXiv: [1807.09409](https://arxiv.org/abs/1807.09409) [astro-ph.GA].
- [280] Smadar Naoz, Clifford M. Will, Enrico Ramirez-Ruiz, Aurelien Hees, Andrea M. Ghez, and Tuan Do. “A hidden friend for the galactic center black hole, Sgr A*.” In: (2019). arXiv: [1912.04910](https://arxiv.org/abs/1912.04910) [astro-ph.GA].
- [281] R. Abuter et al. “Detection of the gravitational redshift in the orbit of the star S2 near the Galactic centre massive black hole.” In: *Astron. Astrophys.* 615 (2018), p. L15. DOI: [10.1051/0004-6361/201833718](https://doi.org/10.1051/0004-6361/201833718). arXiv: [1807.09409](https://arxiv.org/abs/1807.09409) [astro-ph.GA].
- [282] Daniel Baumann, Gianfranco Bertone, John Stout, and Giovanni Maria Tomaselli. “Ionization of gravitational atoms.” In: *Phys. Rev. D* 105.11 (2022), p. 115036. DOI: [10.1103/PhysRevD.105.115036](https://doi.org/10.1103/PhysRevD.105.115036). arXiv: [2112.14777](https://arxiv.org/abs/2112.14777) [gr-qc].
- [283] Giovanni Maria Tomaselli, Thomas F. M. Spijksma, and Gianfranco Bertone. “Dynamical Friction in Gravitational Atoms.” In: (May 2023). arXiv: [2305.15460](https://arxiv.org/abs/2305.15460) [gr-qc].
- [284] Byron D Tapley, S Bettadpur, M Watkins, and Ch Reigber. “The gravity recovery and climate experiment: Mission overview and early results.” In: *Geophysical Research Letters* 31.9 (2004).
- [285] MR Drinkwater, R Floberghagen, R Haagmans, D Muzi, and A Popescu. “GOCE: ESA’s first Earth Explorer Core mission.” In: *Earth gravity field from space—From sensors to earth sciences*. Springer, 2003, pp. 419–432.
- [286] Ignazio Ciufolini, Antonio Paolozzi, and Claudio Paris. “Overview of the LARES Mission: orbit, error analysis and technological aspects.” In: *Journal of Physics: Conference Series*. Vol. 354. 1. IOP Publishing, 2012, p. 012002.

- [287] Vitor Cardoso and Leonardo Gualtieri. "Testing the black hole 'no-hair' hypothesis." In: *Class. Quant. Grav.* 33.17 (2016), p. 174001. DOI: [10.1088/0264-9381/33/17/174001](https://doi.org/10.1088/0264-9381/33/17/174001). arXiv: [1607.03133](https://arxiv.org/abs/1607.03133) [gr-qc].
- [288] Kazunori Akiyama et al. "First M87 Event Horizon Telescope Results. I. The Shadow of the Supermassive Black Hole." In: *Astrophys. J.* 875.1 (2019), p. L1. DOI: [10.3847/2041-8213/ab0ec7](https://doi.org/10.3847/2041-8213/ab0ec7). arXiv: [1906.11238](https://arxiv.org/abs/1906.11238) [astro-ph.GA].
- [289] R. Abuter et al. "Detection of the Schwarzschild precession in the orbit of the star S2 near the Galactic centre massive black hole." In: *Astron. Astrophys.* 636 (2020), p. L5. DOI: [10.1051/0004-6361/202037813](https://doi.org/10.1051/0004-6361/202037813). arXiv: [2004.07187](https://arxiv.org/abs/2004.07187) [astro-ph.GA].
- [290] C. T. Cunningham and J. M. Bardeen. "The Optical Appearance of a Star Orbiting an Extreme Kerr Black Hole." In: *Astrophysical Journal Letters* 173 (May 1972), p. L137. DOI: [10.1086/180933](https://doi.org/10.1086/180933).
- [291] J.-P. Luminet. "Image of a spherical black hole with thin accretion disk." In: *Astron. Astrophys.* 75 (1979), pp. 228–235.
- [292] Heino Falcke, Fulvio Melia, and Eric Agol. "Viewing the shadow of the black hole at the galactic center." In: *Astrophys. J. Lett.* 528 (2000), p. L13. DOI: [10.1086/312423](https://doi.org/10.1086/312423). arXiv: [astro-ph/9912263](https://arxiv.org/abs/astro-ph/9912263).
- [293] Vitor Cardoso and Rodrigo Vicente. "Moving black holes: energy extraction, absorption cross-section and the ring of fire." In: *Phys. Rev. D* 100.8 (2019), p. 084001. DOI: [10.1103/PhysRevD.100.084001](https://doi.org/10.1103/PhysRevD.100.084001). arXiv: [1906.10140](https://arxiv.org/abs/1906.10140) [gr-qc].
- [294] Samuel E. Gralla, Alexandru Lupsasca, and Daniel P. Marrone. "The shape of the black hole photon ring: A precise test of strong-field general relativity." In: *Phys. Rev. D* 102.12 (2020), p. 124004. DOI: [10.1103/PhysRevD.102.124004](https://doi.org/10.1103/PhysRevD.102.124004). arXiv: [2008.03879](https://arxiv.org/abs/2008.03879) [gr-qc].
- [295] Pedro V. P. Cunha and Carlos A. R. Herdeiro. "Shadows and strong gravitational lensing: a brief review." In: *Gen. Rel. Grav.* 50.4 (2018), p. 42. DOI: [10.1007/s10714-018-2361-9](https://doi.org/10.1007/s10714-018-2361-9). arXiv: [1801.00860](https://arxiv.org/abs/1801.00860) [gr-qc].
- [296] S. Chandrasekhar and Steven L. Detweiler. "The quasi-normal modes of the Schwarzschild black hole." In: *Proc. Roy. Soc. Lond. A* 344 (1975), pp. 441–452. DOI: [10.1098/rspa.1975.0112](https://doi.org/10.1098/rspa.1975.0112).
- [297] C. V. Vishveshwara. "Scattering of Gravitational Radiation by a Schwarzschild Black-hole." In: *Nature* 227 (1970), pp. 936–938. DOI: [10.1038/227936a0](https://doi.org/10.1038/227936a0).
- [298] William H. Press. "Long Wave Trains of Gravitational Waves from a Vibrating Black Hole." In: *The Astrophysical Journal Letters* 170 (Dec. 1971), p. L105. DOI: [10.1086/180849](https://doi.org/10.1086/180849).

- [299] E. W. Leaver. “An Analytic representation for the quasi normal modes of Kerr black holes.” In: *Proc. Roy. Soc. Lond. A* 402 (1985), pp. 285–298. DOI: [10.1098/rspa.1985.0119](https://doi.org/10.1098/rspa.1985.0119).
- [300] Edward W. Leaver. “Spectral decomposition of the perturbation response of the Schwarzschild geometry.” In: *Phys. Rev. D* 34 (1986), pp. 384–408. DOI: [10.1103/PhysRevD.34.384](https://doi.org/10.1103/PhysRevD.34.384).
- [301] Kostas D. Kokkotas and Bernd G. Schmidt. “Quasinormal modes of stars and black holes.” In: *Living Rev. Rel.* 2 (1999), p. 2. DOI: [10.12942/lrr-1999-2](https://doi.org/10.12942/lrr-1999-2). arXiv: [gr-qc/9909058](https://arxiv.org/abs/gr-qc/9909058).
- [302] Steven L. Detweiler. “BLACK HOLES AND GRAVITATIONAL WAVES. III. THE RESONANT FREQUENCIES OF ROTATING HOLES.” In: *Astrophys. J.* 239 (1980), pp. 292–295. DOI: [10.1086/158109](https://doi.org/10.1086/158109).
- [303] Olaf Dreyer, Bernard J. Kelly, Badri Krishnan, Lee Samuel Finn, David Garrison, and Ramon Lopez-Aleman. “Black hole spectroscopy: Testing general relativity through gravitational wave observations.” In: *Class. Quant. Grav.* 21 (2004), pp. 787–804. DOI: [10.1088/0264-9381/21/4/003](https://doi.org/10.1088/0264-9381/21/4/003). arXiv: [gr-qc/0309007](https://arxiv.org/abs/gr-qc/0309007).
- [304] Emanuele Berti, Vitor Cardoso, and Clifford M. Will. “On gravitational-wave spectroscopy of massive black holes with the space interferometer LISA.” In: *Phys. Rev. D* 73 (2006), p. 064030. DOI: [10.1103/PhysRevD.73.064030](https://doi.org/10.1103/PhysRevD.73.064030). arXiv: [gr-qc/0512160](https://arxiv.org/abs/gr-qc/0512160).
- [305] B. P. Abbott et al. “Tests of general relativity with GW150914.” In: *Phys. Rev. Lett.* 116.22 (2016). [Erratum: *Phys.Rev.Lett.* 121, 129902 (2018)], p. 221101. DOI: [10.1103/PhysRevLett.116.221101](https://doi.org/10.1103/PhysRevLett.116.221101). arXiv: [1602.03841](https://arxiv.org/abs/1602.03841) [gr-qc].
- [306] S. Detweiler. “Black holes and gravitational waves. III - The resonant frequencies of rotating holes.” In: *Astrophysics Journal* 239 (July 1980), pp. 292–295. DOI: [10.1086/158109](https://doi.org/10.1086/158109).
- [307] Vishal Baibhav, Mark Ho-Yeuk Cheung, Emanuele Berti, Vitor Cardoso, Gregorio Carullo, Roberto Cotesta, Walter Del Pozzo, and Francisco Duque. “Agnostic black hole spectroscopy: quasi-normal mode content of numerical relativity waveforms and limits of validity of linear perturbation theory.” In: (Feb. 2023). arXiv: [2302.03050](https://arxiv.org/abs/2302.03050) [gr-qc].
- [308] R. Abbott et al. “Tests of general relativity with binary black holes from the second LIGO-Virgo gravitational-wave transient catalog.” In: *Phys. Rev. D* 103.12 (2021), p. 122002. DOI: [10.1103/PhysRevD.103.122002](https://doi.org/10.1103/PhysRevD.103.122002). arXiv: [2010.14529](https://arxiv.org/abs/2010.14529) [gr-qc].
- [309] Gregorio Carullo, Danny Laghi, Nathan K. Johnson-McDaniel, Walter Del Pozzo, Oscar J. C. Dias, Mahdi Godazgar, and Jorge E. Santos. “Constraints on Kerr-Newman black holes from merger-ringdown gravitational-wave observations.” In: *Phys.*

- Rev. D* 105.6 (2022), p. 062009. DOI: [10.1103/PhysRevD.105.062009](https://doi.org/10.1103/PhysRevD.105.062009). arXiv: [2109.13961](https://arxiv.org/abs/2109.13961) [gr-qc].
- [310] Gregorio Carullo, Danny Laghi, John Veitch, and Walter Del Pozzo. “Bekenstein-Hod Universal Bound on Information Emission Rate Is Obeyed by LIGO-Virgo Binary Black Hole Remnants.” In: *Phys. Rev. Lett.* 126.16 (2021), p. 161102. DOI: [10.1103/PhysRevLett.126.161102](https://doi.org/10.1103/PhysRevLett.126.161102). arXiv: [2103.06167](https://arxiv.org/abs/2103.06167) [gr-qc].
- [311] Andrea Maselli, Paolo Pani, Leonardo Gualtieri, and Emanuele Berti. “Parametrized ringdown spin expansion coefficients: a data-analysis framework for black-hole spectroscopy with multiple events.” In: *Phys. Rev. D* 101.2 (2020), p. 024043. DOI: [10.1103/PhysRevD.101.024043](https://doi.org/10.1103/PhysRevD.101.024043). arXiv: [1910.12893](https://arxiv.org/abs/1910.12893) [gr-qc].
- [312] Gregorio Carullo. “Enhancing modified gravity detection from gravitational-wave observations using the parametrized ringdown spin expansion coefficients formalism.” In: *Phys. Rev. D* 103.12 (2021), p. 124043. DOI: [10.1103/PhysRevD.103.124043](https://doi.org/10.1103/PhysRevD.103.124043). arXiv: [2102.05939](https://arxiv.org/abs/2102.05939) [gr-qc].
- [313] Matthew Giesler, Maximiliano Isi, Mark A. Scheel, and Saul Teukolsky. “Black Hole Ringdown: The Importance of Overtones.” In: *Phys. Rev. X* 9.4 (2019), p. 041060. DOI: [10.1103/PhysRevX.9.041060](https://doi.org/10.1103/PhysRevX.9.041060). arXiv: [1903.08284](https://arxiv.org/abs/1903.08284) [gr-qc].
- [314] Iara Ota and Cecilia Chirenti. “Overtones or higher harmonics? Prospects for testing the no-hair theorem with gravitational wave detections.” In: *Phys. Rev. D* 101.10 (2020), p. 104005. DOI: [10.1103/PhysRevD.101.104005](https://doi.org/10.1103/PhysRevD.101.104005). arXiv: [1911.00440](https://arxiv.org/abs/1911.00440) [gr-qc].
- [315] Swetha Bhagwat, Xisco Jimenez Forteza, Paolo Pani, and Valeria Ferrari. “Ringdown overtones, black hole spectroscopy, and no-hair theorem tests.” In: *Phys. Rev. D* 101.4 (2020), p. 044033. DOI: [10.1103/PhysRevD.101.044033](https://doi.org/10.1103/PhysRevD.101.044033). arXiv: [1910.08708](https://arxiv.org/abs/1910.08708) [gr-qc].
- [316] Arnab Dhani. “Importance of mirror modes in binary black hole ringdown waveform.” In: *Phys. Rev. D* 103.10 (2021), p. 104048. DOI: [10.1103/PhysRevD.103.104048](https://doi.org/10.1103/PhysRevD.103.104048). arXiv: [2010.08602](https://arxiv.org/abs/2010.08602) [gr-qc].
- [317] Maximiliano Isi, Matthew Giesler, Will M. Farr, Mark A. Scheel, and Saul A. Teukolsky. “Testing the no-hair theorem with GW150914.” In: *Phys. Rev. Lett.* 123.11 (2019), p. 111102. DOI: [10.1103/PhysRevLett.123.111102](https://doi.org/10.1103/PhysRevLett.123.111102). arXiv: [1905.00869](https://arxiv.org/abs/1905.00869) [gr-qc].
- [318] Maximiliano Isi, Will M. Farr, Matthew Giesler, Mark A. Scheel, and Saul A. Teukolsky. “Testing the Black-Hole Area Law with GW150914.” In: *Phys. Rev. Lett.* 127.1 (2021), p. 011103. DOI: [10.1103/PhysRevLett.127.011103](https://doi.org/10.1103/PhysRevLett.127.011103). arXiv: [2012.04486](https://arxiv.org/abs/2012.04486) [gr-qc].
- [319] Maximiliano Isi and Will M. Farr. “Revisiting the ringdown of GW150914.” In: (Feb. 2022). arXiv: [2202.02941](https://arxiv.org/abs/2202.02941) [gr-qc].

- [320] Sizheng Ma, Ling Sun, and Yanbei Chen. “Using rational filters to uncover the first ringdown overtone in GW150914.” In: *Phys. Rev. D* 107.8 (2023), p. 084010. DOI: [10.1103/PhysRevD.107.084010](https://doi.org/10.1103/PhysRevD.107.084010). arXiv: [2301.06639](https://arxiv.org/abs/2301.06639) [gr-qc].
- [321] Eliot Finch and Christopher J. Moore. “Searching for a ringdown overtone in GW150914.” In: *Phys. Rev. D* 106.4 (2022), p. 043005. DOI: [10.1103/PhysRevD.106.043005](https://doi.org/10.1103/PhysRevD.106.043005). arXiv: [2205.07809](https://arxiv.org/abs/2205.07809) [gr-qc].
- [322] Alessandra Buonanno, Gregory B. Cook, and Frans Pretorius. “Inspirals, merger and ring-down of equal-mass black-hole binaries.” In: *Phys. Rev. D* 75 (2007), p. 124018. DOI: [10.1103/PhysRevD.75.124018](https://doi.org/10.1103/PhysRevD.75.124018). arXiv: [gr-qc/0610122](https://arxiv.org/abs/gr-qc/0610122) [gr-qc].
- [323] Lionel London, Deirdre Shoemaker, and James Healy. “Modeling ringdown: Beyond the fundamental quasinormal modes.” In: *Phys. Rev. D* 90.12 (2014). [Erratum: *Phys.Rev.D* 94, 069902 (2016)], p. 124032. DOI: [10.1103/PhysRevD.90.124032](https://doi.org/10.1103/PhysRevD.90.124032). arXiv: [1404.3197](https://arxiv.org/abs/1404.3197) [gr-qc].
- [324] Roberto Cotesta, Gregorio Carullo, Emanuele Berti, and Vitor Cardoso. “On the detection of ringdown overtones in GW150914.” In: (Jan. 2022). arXiv: [2201.00822](https://arxiv.org/abs/2201.00822) [gr-qc].
- [325] Mark Ho-Yeuk Cheung et al. “Nonlinear Effects in Black Hole Ringdown.” In: *Phys. Rev. Lett.* 130.8 (2023), p. 081401. DOI: [10.1103/PhysRevLett.130.081401](https://doi.org/10.1103/PhysRevLett.130.081401). arXiv: [2208.07374](https://arxiv.org/abs/2208.07374) [gr-qc].
- [326] Keefe Mitman et al. “Nonlinearities in Black Hole Ringdowns.” In: *Phys. Rev. Lett.* 130.8 (2023), p. 081402. DOI: [10.1103/PhysRevLett.130.081402](https://doi.org/10.1103/PhysRevLett.130.081402). arXiv: [2208.07380](https://arxiv.org/abs/2208.07380) [gr-qc].
- [327] Valeria Ferrari and Bahram Mashhoon. “New approach to the quasinormal modes of a black hole.” In: *Phys. Rev. D* 30 (1984), pp. 295–304. DOI: [10.1103/PhysRevD.30.295](https://doi.org/10.1103/PhysRevD.30.295).
- [328] Vitor Cardoso, Alex S. Miranda, Emanuele Berti, Helvi Witek, and Wilson T. Zanchin. “Geodesic stability, Lyapunov exponents and quasinormal modes.” In: *Phys. Rev. D* 79 (2009), p. 064016. DOI: [10.1103/PhysRevD.79.064016](https://doi.org/10.1103/PhysRevD.79.064016). arXiv: [0812.1806](https://arxiv.org/abs/0812.1806) [hep-th].
- [329] Sai Iyer. “Black-hole normal modes: A WKB approach. II. Schwarzschild black holes.” In: *Phys. Rev. D* 35 (12 1987), pp. 3632–3636. DOI: [10.1103/PhysRevD.35.3632](https://doi.org/10.1103/PhysRevD.35.3632). URL: <https://link.aps.org/doi/10.1103/PhysRevD.35.3632>.
- [330] M. Bauböck et al. “Modeling the orbital motion of Sgr A*’s near-infrared flares.” In: *Astron. Astrophys.* 635 (2020), A143. DOI: [10.1051/0004-6361/201937233](https://doi.org/10.1051/0004-6361/201937233). arXiv: [2002.08374](https://arxiv.org/abs/2002.08374) [astro-ph.HE].
- [331] R. Abuter et al. “The flux distribution of Sgr A*.” In: *Astron. Astrophys.* 638 (2020), A2. DOI: [10.1051/0004-6361/202037717](https://doi.org/10.1051/0004-6361/202037717). arXiv: [2004.07185](https://arxiv.org/abs/2004.07185) [astro-ph.GA].

- [332] Joseph F. Dolan. “Dying Pulse Trains in Cygnus XR-1: Evidence for an Event Horizon?” In: *Publications of the Astronomical Society of the Pacific* 113.786 (Aug. 2001), pp. 974–982. DOI: [10.1086/322917](https://doi.org/10.1086/322917).
- [333] Joseph F. Dolan and Daria C Auerswald. “A Search for Dying Pulse Trains in Cyg X-1 using RXTE.” In: *arXiv e-prints*, arXiv:1104.3164 (Apr. 2011), arXiv:1104.3164. arXiv: [1104.3164](https://arxiv.org/abs/1104.3164) [astro-ph.HE].
- [334] I. D. Novikov and Ja. B. Zeldovich. “Physics of relativistic collapse.” In: *International Conference on Relativistic Theories of Gravitation*. Vol. 1. 1965.
- [335] M. A. Podurets. “Asymptotic Behavior of the Optical Luminosity of a Star in Gravitational Collapse.” In: *Soviet Astronomy* 8 (June 1965), p. 868.
- [336] William L. Ames and Kip S. Thorne. “The Optical Appearance of a Star that is Collapsing Through its Gravitational Radius.” In: *Astrophysics Journal* 151 (Feb. 1968), p. 659. DOI: [10.1086/149465](https://doi.org/10.1086/149465).
- [337] J. M. Cohen, M. F. Struble, K. R. Pechenick, and B. Kuharetz. “Observable Blueshifts Near Compact Objects.” In: *Astrophysics and Space Science* 88.2 (Dec. 1982), pp. 307–312. DOI: [10.1007/BF01092704](https://doi.org/10.1007/BF01092704).
- [338] Yasusada Nambu and Sousuke Noda. “Wave Optics in Black Hole Spacetimes: Schwarzschild Case.” In: *Class. Quant. Grav.* 33 (2016), p. 075011. DOI: [10.1088/0264-9381/33/7/075011](https://doi.org/10.1088/0264-9381/33/7/075011). arXiv: [1502.05468](https://arxiv.org/abs/1502.05468) [gr-qc].
- [339] Yasusada Nambu, Sousuke Noda, and Yuichiro Sakai. “Wave Optics in Spacetimes with Compact Gravitating Object.” In: *Phys. Rev. D* 100.6 (2019), p. 064037. DOI: [10.1103/PhysRevD.100.064037](https://doi.org/10.1103/PhysRevD.100.064037). arXiv: [1905.01793](https://arxiv.org/abs/1905.01793) [gr-qc].
- [340] Huan Yang, David A. Nichols, Fan Zhang, Aaron Zimmerman, Zhongyang Zhang, and Yanbei Chen. “Quasinormal-mode spectrum of Kerr black holes and its geometric interpretation.” In: *Phys. Rev. D* 86 (2012), p. 104006. DOI: [10.1103/PhysRevD.86.104006](https://doi.org/10.1103/PhysRevD.86.104006). arXiv: [1207.4253](https://arxiv.org/abs/1207.4253) [gr-qc].
- [341] Vitor Cardoso, Edgardo Franzin, and Paolo Pani. “Is the gravitational-wave ringdown a probe of the event horizon?” In: *Phys. Rev. Lett.* 116.17 (2016). [Erratum: *Phys.Rev.Lett.* 117, 089902 (2016)], p. 171101. DOI: [10.1103/PhysRevLett.116.171101](https://doi.org/10.1103/PhysRevLett.116.171101). arXiv: [1602.07309](https://arxiv.org/abs/1602.07309) [gr-qc].

- [342] Vitor Cardoso, Seth Hopper, Caio F. B. Macedo, Carlos Palenzuela, and Paolo Pani. “Gravitational-wave signatures of exotic compact objects and of quantum corrections at the horizon scale.” In: *Phys. Rev. D* 94.8 (2016), p. 084031. DOI: [10.1103/PhysRevD.94.084031](https://doi.org/10.1103/PhysRevD.94.084031). arXiv: [1608.08637](https://arxiv.org/abs/1608.08637) [gr-qc].
- [343] Huan Yang. “Relating Black Hole Shadow to Quasinormal Modes for Rotating Black Holes.” In: (Jan. 2021). arXiv: [2101.11129](https://arxiv.org/abs/2101.11129) [gr-qc].
- [344] Enno Harms, Sebastiano Bernuzzi, Alessandro Nagar, and An Zenginoglu. “A new gravitational wave generation algorithm for particle perturbations of the Kerr spacetime.” In: *Class. Quant. Grav.* 31.24 (2014), p. 245004. DOI: [10.1088/0264-9381/31/24/245004](https://doi.org/10.1088/0264-9381/31/24/245004). arXiv: [1406.5983](https://arxiv.org/abs/1406.5983) [gr-qc].
- [345] Michael D. Johnson et al. “Universal interferometric signatures of a black hole’s photon ring.” In: *Sci. Adv.* 6.12 (2020), eaaz1310. DOI: [10.1126/sciadv.aaz1310](https://doi.org/10.1126/sciadv.aaz1310). arXiv: [1907.04329](https://arxiv.org/abs/1907.04329) [astro-ph.IM].
- [346] Peter Galison et al. “The Next Generation Event Horizon Telescope Collaboration: History, Philosophy, and Culture.” In: *Galaxies* 11.1 (2023), p. 32. DOI: [10.3390/galaxies11010032](https://doi.org/10.3390/galaxies11010032). arXiv: [2304.02463](https://arxiv.org/abs/2304.02463) [physics.hist-ph].
- [347] Michael D. Johnson et al. “Key Science Goals for the Next-Generation Event Horizon Telescope.” In: *Galaxies* 11 (2023), p. 61. DOI: [10.3390/galaxies11030061](https://doi.org/10.3390/galaxies11030061). arXiv: [2304.11188](https://arxiv.org/abs/2304.11188) [astro-ph.HE].
- [348] E. Brian Davies. *Linear Operators and their Spectra*. Cambridge Studies in Advanced Mathematics. Cambridge University Press, 2007. DOI: [10.1017/CB09780511618864](https://doi.org/10.1017/CB09780511618864).
- [349] José Luis Jaramillo, Rodrigo Panosso Macedo, and Lamis Al Sheikh. “Pseudospectrum and Black Hole Quasinormal Mode Instability.” In: *Phys. Rev. X* 11.3 (2021), p. 031003. DOI: [10.1103/PhysRevX.11.031003](https://doi.org/10.1103/PhysRevX.11.031003). arXiv: [2004.06434](https://arxiv.org/abs/2004.06434) [gr-qc].
- [350] José Luis Jaramillo, Rodrigo Panosso Macedo, and Lamis Al Sheikh. “Gravitational wave signatures of black hole quasinormal mode instability.” In: (May 2021). arXiv: [2105.03451](https://arxiv.org/abs/2105.03451) [gr-qc].
- [351] Kyriakos Destounis, Rodrigo Panosso Macedo, Emanuele Berti, Vitor Cardoso, and José Luis Jaramillo. “Pseudospectrum of Reissner-Nordström black holes: Quasinormal mode instability and universality.” In: *Phys. Rev. D* 104.8 (2021), p. 084091. DOI: [10.1103/PhysRevD.104.084091](https://doi.org/10.1103/PhysRevD.104.084091). arXiv: [2107.09673](https://arxiv.org/abs/2107.09673) [gr-qc].

- [352] Hans-Peter Nollert. “About the significance of quasinormal modes of black holes.” In: *Phys. Rev. D* 53 (8 1996), pp. 4397–4402. DOI: [10.1103/PhysRevD.53.4397](https://doi.org/10.1103/PhysRevD.53.4397). URL: <https://link.aps.org/doi/10.1103/PhysRevD.53.4397>.
- [353] Mark Ho-Yeuk Cheung, Kyriakos Destounis, Rodrigo Panosso Macedo, Emanuele Berti, and Vitor Cardoso. “Destabilizing the Fundamental Mode of Black Holes: The Elephant and the Flea.” In: *Phys. Rev. Lett.* 128.11 (2022), p. 111103. DOI: [10.1103/PhysRevLett.128.111103](https://doi.org/10.1103/PhysRevLett.128.111103). arXiv: [2111.05415](https://arxiv.org/abs/2111.05415) [gr-qc].
- [354] Zachary Mark, Aaron Zimmerman, Song Ming Du, and Yanbei Chen. “A recipe for echoes from exotic compact objects.” In: *Phys. Rev. D* 96.8 (2017), p. 084002. DOI: [10.1103/PhysRevD.96.084002](https://doi.org/10.1103/PhysRevD.96.084002). arXiv: [1706.06155](https://arxiv.org/abs/1706.06155) [gr-qc].
- [355] Lam Hui, Daniel Kabat, and Sam S. C. Wong. “Quasinormal modes, echoes and the causal structure of the Green’s function.” In: *JCAP* 12 (2019), p. 020. DOI: [10.1088/1475-7516/2019/12/020](https://doi.org/10.1088/1475-7516/2019/12/020). arXiv: [1909.10382](https://arxiv.org/abs/1909.10382) [gr-qc].
- [356] Vitor Cardoso, Masashi Kimura, Andrea Maselli, Emanuele Berti, Caio F. B. Macedo, and Ryan McManus. “Parametrized black hole quasinormal ringdown: Decoupled equations for nonrotating black holes.” In: *Phys. Rev. D* 99.10 (2019), p. 104077. DOI: [10.1103/PhysRevD.99.104077](https://doi.org/10.1103/PhysRevD.99.104077). arXiv: [1901.01265](https://arxiv.org/abs/1901.01265) [gr-qc].
- [357] Ryan McManus, Emanuele Berti, Caio F. B. Macedo, Masashi Kimura, Andrea Maselli, and Vitor Cardoso. “Parametrized black hole quasinormal ringdown. II. Coupled equations and quadratic corrections for nonrotating black holes.” In: *Phys. Rev. D* 100.4 (2019), p. 044061. DOI: [10.1103/PhysRevD.100.044061](https://doi.org/10.1103/PhysRevD.100.044061). arXiv: [1906.05155](https://arxiv.org/abs/1906.05155) [gr-qc].
- [358] P. T. Leung, Y. T. Liu, W. M. Suen, C. Y. Tam, and K. Young. “Quasinormal modes of dirty black holes.” In: *Phys. Rev. Lett.* 78 (1997), pp. 2894–2897. DOI: [10.1103/PhysRevLett.78.2894](https://doi.org/10.1103/PhysRevLett.78.2894). arXiv: [gr-qc/9903031](https://arxiv.org/abs/gr-qc/9903031).
- [359] Adrian Ka-Wai Chung, Joseph Gais, Mark Ho-Yeuk Cheung, and Tjonnie G. F. Li. “Searching for ultralight bosons with supermassive black hole ringdown.” In: *Phys. Rev. D* 104.8 (2021), p. 084028. DOI: [10.1103/PhysRevD.104.084028](https://doi.org/10.1103/PhysRevD.104.084028). arXiv: [2107.05492](https://arxiv.org/abs/2107.05492) [gr-qc].
- [360] Reinaldo J. Gleiser, Carlos O. Nicasio, Richard H. Price, and Jorge Pullin. “Gravitational radiation from Schwarzschild black holes: The Second order perturbation formalism.” In: *Phys. Rept.* 325 (2000), pp. 41–81. DOI: [10.1016/S0370-1573\(99\)00048-4](https://doi.org/10.1016/S0370-1573(99)00048-4). arXiv: [gr-qc/9807077](https://arxiv.org/abs/gr-qc/9807077).

- [361] Manuela Campanelli and Carlos O. Lousto. “Second order gauge invariant gravitational perturbations of a Kerr black hole.” In: *Phys. Rev. D* 59 (1999), p. 124022. DOI: [10.1103/PhysRevD.59.124022](https://doi.org/10.1103/PhysRevD.59.124022). arXiv: [gr-qc/9811019](https://arxiv.org/abs/gr-qc/9811019).
- [362] Yosef Zlochower, Roberto Gomez, Sascha Husa, Luis Lehner, and Jeffrey Winicour. “Mode coupling in the nonlinear response of black holes.” In: *Phys. Rev. D* 68 (2003), p. 084014. DOI: [10.1103/PhysRevD.68.084014](https://doi.org/10.1103/PhysRevD.68.084014). arXiv: [gr-qc/0306098](https://arxiv.org/abs/gr-qc/0306098).
- [363] Hiroyuki Nakano and Kunihito Ioka. “Second Order Quasi-Normal Mode of the Schwarzschild Black Hole.” In: *Phys. Rev. D* 76 (2007), p. 084007. DOI: [10.1103/PhysRevD.76.084007](https://doi.org/10.1103/PhysRevD.76.084007). arXiv: [0708.0450 \[gr-qc\]](https://arxiv.org/abs/0708.0450).
- [364] Kunihito Ioka and Hiroyuki Nakano. “Second and higher-order quasi-normal modes in binary black hole mergers.” In: *Phys. Rev. D* 76 (2007), p. 061503. DOI: [10.1103/PhysRevD.76.061503](https://doi.org/10.1103/PhysRevD.76.061503). arXiv: [0704.3467 \[astro-ph\]](https://arxiv.org/abs/0704.3467).
- [365] Satoshi Okuzumi, Kunihito Ioka, and Masa-aki Sakagami. “Possible Discovery of Nonlinear Tail and Quasinormal Modes in Black Hole Ringdown.” In: *Phys. Rev. D* 77 (2008), p. 124018. DOI: [10.1103/PhysRevD.77.124018](https://doi.org/10.1103/PhysRevD.77.124018). arXiv: [0803.0501 \[gr-qc\]](https://arxiv.org/abs/0803.0501).
- [366] Enrique Pazos, David Brizuela, Jose M. Martin-Garcia, and Manuel Tiglio. “Mode coupling of Schwarzschild perturbations: Ringdown frequencies.” In: *Phys. Rev. D* 82 (2010), p. 104028. DOI: [10.1103/PhysRevD.82.104028](https://doi.org/10.1103/PhysRevD.82.104028). arXiv: [1009.4665 \[gr-qc\]](https://arxiv.org/abs/1009.4665).
- [367] Laura Sberna, Pablo Bosch, William E. East, Stephen R. Green, and Luis Lehner. “Nonlinear effects in the black hole ringdown: Absorption-induced mode excitation.” In: *Phys. Rev. D* 105.6 (2022), p. 064046. DOI: [10.1103/PhysRevD.105.064046](https://doi.org/10.1103/PhysRevD.105.064046). arXiv: [2112.11168 \[gr-qc\]](https://arxiv.org/abs/2112.11168).
- [368] C. Molina, Paolo Pani, Vitor Cardoso, and Leonardo Gualtieri. “Gravitational signature of Schwarzschild black holes in dynamical Chern-Simons gravity.” In: *Phys. Rev. D* 81 (2010), p. 124021. DOI: [10.1103/PhysRevD.81.124021](https://doi.org/10.1103/PhysRevD.81.124021). arXiv: [1004.4007 \[gr-qc\]](https://arxiv.org/abs/1004.4007).
- [369] Webpages with Mathematica notebooks and numerical quasi-normal mode tables:
<https://paolopani.weebly.com/notebooks.html>
<https://centra.tecnico.ulisboa.pt/network/grit/files/>
<https://pages.jh.edu/eberti2/ringdown/>.
- [370] Richard H. Price. “Nonspherical Perturbations of Relativistic Gravitational Collapse. I. Scalar and Gravitational Perturbations.” In: *Phys. Rev. D* 5 (10 1972), pp. 2419–2438. DOI: [10.1103/PhysRevD.5.2419](https://doi.org/10.1103/PhysRevD.5.2419). URL: <https://link.aps.org/doi/10.1103/PhysRevD.5.2419>.

- [371] Vitor Cardoso and Paolo Pani. “Tests for the existence of black holes through gravitational wave echoes.” In: *Nature Astron.* 1.9 (2017), pp. 586–591. DOI: [10.1038/s41550-017-0225-y](https://doi.org/10.1038/s41550-017-0225-y). arXiv: [1709.01525](https://arxiv.org/abs/1709.01525) [gr-qc].
- [372] Maximiliano Isi and Will M. Farr. “Analyzing black-hole ring-downs.” In: (July 2021). arXiv: [2107.05609](https://arxiv.org/abs/2107.05609) [gr-qc].
- [373] Naritaka Oshita and Niayesh Afshordi. “Probing microstructure of black hole spacetimes with gravitational wave echoes.” In: *Phys. Rev. D* 99.4 (2019), p. 044002. DOI: [10.1103/PhysRevD.99.044002](https://doi.org/10.1103/PhysRevD.99.044002). arXiv: [1807.10287](https://arxiv.org/abs/1807.10287) [gr-qc].
- [374] Naritaka Oshita, Daichi Tsuna, and Niayesh Afshordi. “Quantum Black Hole Seismology I: Echoes, Ergospheres, and Spectra.” In: *Phys. Rev. D* 102.2 (2020), p. 024045. DOI: [10.1103/PhysRevD.102.024045](https://doi.org/10.1103/PhysRevD.102.024045). arXiv: [2001.11642](https://arxiv.org/abs/2001.11642) [gr-qc].
- [375] Naritaka Oshita, Daichi Tsuna, and Niayesh Afshordi. “Quantum Black Hole Seismology II: Applications to Astrophysical Black Holes.” In: *Phys. Rev. D* 102.2 (2020), p. 024046. DOI: [10.1103/PhysRevD.102.024046](https://doi.org/10.1103/PhysRevD.102.024046). arXiv: [2004.06276](https://arxiv.org/abs/2004.06276) [gr-qc].
- [376] Jahed Abedi and Niayesh Afshordi. “Echoes from the Abyss: A Status Update.” In: (Jan. 2020). arXiv: [2001.00821](https://arxiv.org/abs/2001.00821) [gr-qc].
- [377] Alex B. Nielsen, Collin D. Capano, Ofek Birnholtz, and Julian Westerweck. “Parameter estimation and statistical significance of echoes following black hole signals in the first Advanced LIGO observing run.” In: *Phys. Rev. D* 99.10 (2019), p. 104012. DOI: [10.1103/PhysRevD.99.104012](https://doi.org/10.1103/PhysRevD.99.104012). arXiv: [1811.04904](https://arxiv.org/abs/1811.04904) [gr-qc].
- [378] Nami Uchikata, Hiroyuki Nakano, Tatsuya Narikawa, Norichika Sago, Hideyuki Tagoshi, and Takahiro Tanaka. “Searching for black hole echoes from the LIGO-Virgo Catalog GWTC-1.” In: *Phys. Rev. D* 100.6 (2019), p. 062006. DOI: [10.1103/PhysRevD.100.062006](https://doi.org/10.1103/PhysRevD.100.062006). arXiv: [1906.00838](https://arxiv.org/abs/1906.00838) [gr-qc].
- [379] Jahed Abedi, Hannah Dykaar, and Niayesh Afshordi. “Echoes from the Abyss: Tentative evidence for Planck-scale structure at black hole horizons.” In: *Phys. Rev. D* 96.8 (2017), p. 082004. DOI: [10.1103/PhysRevD.96.082004](https://doi.org/10.1103/PhysRevD.96.082004). arXiv: [1612.00266](https://arxiv.org/abs/1612.00266) [gr-qc].
- [380] Jahed Abedi and Niayesh Afshordi. “Echoes from the Abyss: A highly spinning black hole remnant for the binary neutron star merger GW170817.” In: *JCAP* 11 (2019), p. 010. DOI: [10.1088/1475-7516/2019/11/010](https://doi.org/10.1088/1475-7516/2019/11/010). arXiv: [1803.10454](https://arxiv.org/abs/1803.10454) [gr-qc].
- [381] Sayak Datta, Richard Brito, Sukanta Bose, Paolo Pani, and Scott A. Hughes. “Tidal heating as a discriminator for horizons in extreme mass ratio inspirals.” In: *Phys. Rev. D* 101.4 (2020), p. 044004. DOI: [10.1103/PhysRevD.101.044004](https://doi.org/10.1103/PhysRevD.101.044004). arXiv: [1910.07841](https://arxiv.org/abs/1910.07841) [gr-qc].

- [382] Vitor Cardoso, Adrian del Rio, and Masashi Kimura. “Distinguishing black holes from horizonless objects through the excitation of resonances during inspiral.” In: *Phys. Rev. D* 100 (2019). [Erratum: *Phys.Rev.D* 101, 069902 (2020)], p. 084046. DOI: [10.1103/PhysRevD.100.084046](https://doi.org/10.1103/PhysRevD.100.084046). arXiv: [1907.01561](https://arxiv.org/abs/1907.01561) [gr-qc].
- [383] Elisa Maggio, Maarten van de Meent, and Paolo Pani. “Extreme mass-ratio inspirals around a spinning horizonless compact object.” In: *Phys. Rev. D* 104.10 (2021), p. 104026. DOI: [10.1103/PhysRevD.104.104026](https://doi.org/10.1103/PhysRevD.104.104026). arXiv: [2106.07195](https://arxiv.org/abs/2106.07195) [gr-qc].
- [384] Kwinten Fransen, Gideon Koekoek, Rob Tielemans, and Bert Vercknocke. “Modeling and detecting resonant tides of exotic compact objects.” In: *Phys. Rev. D* 104.4 (2021), p. 044044. DOI: [10.1103/PhysRevD.104.044044](https://doi.org/10.1103/PhysRevD.104.044044). arXiv: [2005.12286](https://arxiv.org/abs/2005.12286) [gr-qc].
- [385] Yun Fang, Rong-Zhen Guo, and Qing-Guo Huang. “Tests for the existence of horizon through gravitational waves from a small binary in the vicinity of a massive object.” In: *Phys. Lett. B* 822 (2021), p. 136654. DOI: [10.1016/j.physletb.2021.136654](https://doi.org/10.1016/j.physletb.2021.136654). arXiv: [2108.04511](https://arxiv.org/abs/2108.04511) [astro-ph.CO].
- [386] Norichika Sago and Takahiro Tanaka. “Oscillations in the extreme mass-ratio inspiral gravitational wave phase correction as a probe of a reflective boundary of the central black hole.” In: *Phys. Rev. D* 104.6 (2021), p. 064009. DOI: [10.1103/PhysRevD.104.064009](https://doi.org/10.1103/PhysRevD.104.064009). arXiv: [2106.07123](https://arxiv.org/abs/2106.07123) [gr-qc].
- [387] Pierre Heidmann, Nicholas Speeney, Emanuele Berti, and Ibrahima Bah. “Cavity effect in the quasinormal mode spectrum of topological stars.” In: (May 2023). arXiv: [2305.14412](https://arxiv.org/abs/2305.14412) [gr-qc].
- [388] S. L. Shapiro and S. A. Teukolsky. *Black holes, white dwarfs, and neutron stars: The physics of compact objects*. 1983. ISBN: 978-0-471-87316-7.
- [389] Paolo Pani and Valeria Ferrari. “On gravitational-wave echoes from neutron-star binary coalescences.” In: *Class. Quant. Grav.* 35.15 (2018), 15LT01. DOI: [10.1088/1361-6382/aacb8f](https://doi.org/10.1088/1361-6382/aacb8f). arXiv: [1804.01444](https://arxiv.org/abs/1804.01444) [gr-qc].
- [390] Joe Keir. “Slowly decaying waves on spherically symmetric spacetimes and ultracompact neutron stars.” In: *Class. Quant. Grav.* 33.13 (2016), p. 135009. DOI: [10.1088/0264-9381/33/13/135009](https://doi.org/10.1088/0264-9381/33/13/135009). arXiv: [1404.7036](https://arxiv.org/abs/1404.7036) [gr-qc].
- [391] Vitor Cardoso, Luís C. B. Crispino, Caio F. B. Macedo, Hirotada Okawa, and Paolo Pani. “Light rings as observational evidence for event horizons: long-lived modes, ergoregions and nonlinear instabilities of ultracompact objects.” In: *Phys. Rev. D* 90.4 (2014), p. 044069. DOI: [10.1103/PhysRevD.90.044069](https://doi.org/10.1103/PhysRevD.90.044069). arXiv: [1406.5510](https://arxiv.org/abs/1406.5510) [gr-qc].

- [392] A.A. Starobinski. "Amplification of waves during reflection from a rotating black hole." In: *Zh. Eksp. Teor. Fiz.* 64 (1973). (Sov. Phys. - JETP, 37, 28, 1973), p. 48.
- [393] A. A. Starobinski and S. M. Churilov. "Amplification of electromagnetic and gravitational waves scattered by a rotating black hole." In: *Zh. Eksp. Teor. Fiz.* 65 (1973). (Sov. Phys. - JETP, 38, 1, 1973), p. 3.
- [394] H. Georgi. *The Physics of Waves*. Prentice Hall, 1993. ISBN: 9780136656210. URL: <https://books.google.pt/books?id=gajvAAAAMAAJ>.
- [395] M. Davis, R. Ruffini, W.H. Press, and R.H. Price. "Gravitational radiation from a particle falling radially into a schwarzschild black hole." In: *Phys. Rev. Lett.* 27 (1971), pp. 1466–1469. DOI: [10.1103/PhysRevLett.27.1466](https://doi.org/10.1103/PhysRevLett.27.1466).
- [396] Vitor Cardoso and Jose' P.S. Lemos. "Gravitational radiation from collisions at the speed of light: A Massless particle falling into a Schwarzschild black hole." In: *Phys. Lett. B* 538 (2002), pp. 1–5. DOI: [10.1016/S0370-2693\(02\)01961-5](https://doi.org/10.1016/S0370-2693(02)01961-5). arXiv: [gr-qc/0202019](https://arxiv.org/abs/gr-qc/0202019).
- [397] Emanuele Berti, Vitor Cardoso, Tanja Hinderer, Madalena Lemos, Frans Pretorius, Ulrich Sperhake, and Nicolas Yunes. "Semi-analytical estimates of scattering thresholds and gravitational radiation in ultrarelativistic black hole encounters." In: *Phys. Rev. D* 81 (2010), p. 104048. DOI: [10.1103/PhysRevD.81.104048](https://doi.org/10.1103/PhysRevD.81.104048). arXiv: [1003.0812 \[gr-qc\]](https://arxiv.org/abs/1003.0812).
- [398] K. D. Kokkotas. "Pulsating relativistic stars." In: *Les Houches School of Physics: Astrophysical Sources of Gravitational Radiation*. Sept. 1995, pp. 89–102. arXiv: [gr-qc/9603024](https://arxiv.org/abs/gr-qc/9603024).
- [399] Zeferino Andrade and Richard H. Price. "Excitation of the odd parity quasinormal modes of compact objects." In: *Phys. Rev. D* 60 (1999), p. 104037. DOI: [10.1103/PhysRevD.60.104037](https://doi.org/10.1103/PhysRevD.60.104037). arXiv: [gr-qc/9902062](https://arxiv.org/abs/gr-qc/9902062).
- [400] V. Ferrari and K. D. Kokkotas. "Scattering of particles by neutron stars: Time evolutions for axial perturbations." In: *Phys. Rev. D* 62 (2000), p. 107504. DOI: [10.1103/PhysRevD.62.107504](https://doi.org/10.1103/PhysRevD.62.107504). arXiv: [gr-qc/0008057](https://arxiv.org/abs/gr-qc/0008057).
- [401] Kazuhiro Tominaga, Motoyuki Saijo, and Kei-ichi Maeda. "Gravitational waves from a spinning particle scattered by a relativistic star: Axial mode case." In: *Phys. Rev. D* 63 (2001), p. 124012. DOI: [10.1103/PhysRevD.63.124012](https://doi.org/10.1103/PhysRevD.63.124012). arXiv: [gr-qc/0009055](https://arxiv.org/abs/gr-qc/0009055).
- [402] P. C. Peters. "Gravitational Radiation and the Motion of Two Point Masses." In: *Phys. Rev.* 136 (1964), B1224–B1232. DOI: [10.1103/PhysRev.136.B1224](https://doi.org/10.1103/PhysRev.136.B1224).

- [403] R. H. Fowler and C. N. H. Lock. "Approximate solutions of linear differential equations." In: *Proceedings London Mathematical Society* s2-20.1 (1922), p. 127. DOI: [10.1103/PhysRevD.103.084021](https://doi.org/10.1103/PhysRevD.103.084021).
- [404] A. H. Nayfeh. *Perturbation Methods*. Wiley, 2000.
- [405] Asimina Arvanitaki, Savas Dimopoulos, Sergei Dubovsky, Neemanja Kaloper, and John March-Russell. "String Axiverse." In: *Phys. Rev. D* 81 (2010), p. 123530. DOI: [10.1103/PhysRevD.81.123530](https://doi.org/10.1103/PhysRevD.81.123530). arXiv: [0905.4720](https://arxiv.org/abs/0905.4720) [hep-th].
- [406] Kurt Hinterbichler. "Theoretical aspects of massive gravity." In: *Rev. Mod. Phys.* 84 (2 2012), pp. 671–710. DOI: [10.1103/RevModPhys.84.671](https://doi.org/10.1103/RevModPhys.84.671). URL: <https://link.aps.org/doi/10.1103/RevModPhys.84.671>.
- [407] Claudia de Rham. "Massive Gravity." In: *Living Rev. Rel.* 17 (2014), p. 7. DOI: [10.12942/lrr-2014-7](https://doi.org/10.12942/lrr-2014-7). arXiv: [1401.4173](https://arxiv.org/abs/1401.4173) [hep-th].
- [408] William H. Press and Saul A. Teukolsky. "Floating Orbits, Superradiant Scattering and the Black-hole Bomb." In: *Nature* 238 (1972), pp. 211–212. DOI: [10.1038/238211a0](https://doi.org/10.1038/238211a0).
- [409] Nicolas Yunes, Paolo Pani, and Vitor Cardoso. "Gravitational Waves from Quasicircular Extreme Mass-Ratio Inspirals as Probes of Scalar-Tensor Theories." In: *Phys. Rev. D* 85 (2012), p. 102003. DOI: [10.1103/PhysRevD.85.102003](https://doi.org/10.1103/PhysRevD.85.102003). arXiv: [1112.3351](https://arxiv.org/abs/1112.3351) [gr-qc].
- [410] F. Paul Esposito. "Absorption of Gravitational Energy by a Viscous Compressible Fluid." In: *Astrophysics Journal* 165 (Apr. 1971), p. 165. DOI: [10.1086/150884](https://doi.org/10.1086/150884).
- [411] D. Papadopoulos and F. P. Esposito. "Absorption of gravitational energy by a viscous compressible fluid in a curved spacetime." In: *Astrophysics Journal* 292 (May 1985), pp. 330–338. DOI: [10.1086/163163](https://doi.org/10.1086/163163).
- [412] Bence Kocsis and Abraham Loeb. "Brightening of an Accretion Disk Due to Viscous Dissipation of Gravitational Waves During the Coalescence of Supermassive Black Holes." In: *Phys. Rev. Lett.* 101 (2008), p. 041101. DOI: [10.1103/PhysRevLett.101.041101](https://doi.org/10.1103/PhysRevLett.101.041101). arXiv: [0803.0003](https://arxiv.org/abs/0803.0003) [astro-ph].
- [413] Abraham Loeb. "Upper Limit on the Dissipation of Gravitational Waves in Gravitationally Bound Systems." In: *Astrophys. J. Lett.* 890.2 (2020), p. L16. DOI: [10.3847/2041-8213/ab72ab](https://doi.org/10.3847/2041-8213/ab72ab). arXiv: [2001.01730](https://arxiv.org/abs/2001.01730) [astro-ph.HE].
- [414] Béatrice Bonga, Huan Yang, and Scott A. Hughes. "Tidal resonance in extreme mass-ratio inspirals." In: *Phys. Rev. Lett.* 123.10 (2019), p. 101103. DOI: [10.1103/PhysRevLett.123.101103](https://doi.org/10.1103/PhysRevLett.123.101103). arXiv: [1905.00030](https://arxiv.org/abs/1905.00030) [gr-qc].

- [415] Huan Yang, Béatrice Bonga, Zhipeng Peng, and Gongjie Li. “Relativistic Mean Motion Resonance.” In: *Phys. Rev. D* 100.12 (2019), p. 124056. DOI: [10.1103/PhysRevD.100.124056](https://doi.org/10.1103/PhysRevD.100.124056). arXiv: [1910.07337](https://arxiv.org/abs/1910.07337) [gr-qc].
- [416] Priti Gupta, Lorenzo Speri, Béatrice Bonga, Alvin J. K. Chua, and Takahiro Tanaka. “Modeling transient resonances in extreme-mass-ratio inspirals.” In: *Phys. Rev. D* 106.10 (2022), p. 104001. DOI: [10.1103/PhysRevD.106.104001](https://doi.org/10.1103/PhysRevD.106.104001). arXiv: [2205.04808](https://arxiv.org/abs/2205.04808) [gr-qc].
- [417] Lorenzo Speri and Jonathan R. Gair. “Assessing the impact of transient orbital resonances.” In: *Phys. Rev. D* 103.12 (2021), p. 124032. DOI: [10.1103/PhysRevD.103.124032](https://doi.org/10.1103/PhysRevD.103.124032). arXiv: [2103.06306](https://arxiv.org/abs/2103.06306) [gr-qc].
- [418] Michael Zevin, Johan Samsing, Carl Rodriguez, Carl-Johan Haster, and Enrico Ramirez-Ruiz. “Eccentric Black Hole Mergers in Dense Star Clusters: The Role of Binary–Binary Encounters.” In: *Astrophys. J.* 871.1 (2019), p. 91. DOI: [10.3847/1538-4357/aaf6ec](https://doi.org/10.3847/1538-4357/aaf6ec). arXiv: [1810.00901](https://arxiv.org/abs/1810.00901) [astro-ph.HE].
- [419] Fabio Antonini and Hagai B. Perets. “Secular evolution of compact binaries near massive black holes: Gravitational wave sources and other exotica.” In: *Astrophys. J.* 757 (2012), p. 27. DOI: [10.1088/0004-637X/757/1/27](https://doi.org/10.1088/0004-637X/757/1/27). arXiv: [1203.2938](https://arxiv.org/abs/1203.2938) [astro-ph.GA].
- [420] Fabio Antonini, Sourav Chatterjee, Carl L. Rodriguez, Meagan Morscher, Bharath Pattabiraman, Vicky Kalogera, and Frederic A. Rasio. “BLACK HOLE MERGERS AND BLUE STRAGGLERS FROM HIERARCHICAL TRIPLES FORMED IN GLOBULAR CLUSTERS.” In: *The Astrophysical Journal* 816.2 (2016), p. 65. DOI: [10.3847/0004-637x/816/2/65](https://doi.org/10.3847/0004-637x/816/2/65). URL: <https://doi.org/10.3847%2F0004-637x%2F816%2F2%2F65>.
- [421] Bao-Minh Hoang, Smadar Naoz, Bence Kocsis, Frederic A. Rasio, and Fani Dosopoulou. “Black Hole Mergers in Galactic Nuclei Induced by the Eccentric Kozai–Lidov Effect.” In: *The Astrophysical Journal* 856.2 (2018), p. 140. DOI: [10.3847/1538-4357/aaafce](https://doi.org/10.3847/1538-4357/aaafce). URL: <https://doi.org/10.3847%2F1538-4357%2Faaafce>.
- [422] Haruka Suzuki, Priti Gupta, Hirotada Okawa, and Kei-ichi Maeda. “Post-Newtonian Kozai-Lidov Mechanism and its Effect on Cumulative Shift of Periastron Time of Binary Pulsar.” In: (June 2020). DOI: [10.1093/mnras/staa3081](https://doi.org/10.1093/mnras/staa3081). arXiv: [2006.11545](https://arxiv.org/abs/2006.11545) [gr-qc].
- [423] Jose María Ezquiaga and Miguel Zumalacárregui. “Gravitational wave lensing beyond general relativity: birefringence, echoes and shadows.” In: (Sept. 2020). arXiv: [2009.12187](https://arxiv.org/abs/2009.12187) [gr-qc].

- [424] Jose María Ezquiaga, Daniel E. Holz, Wayne Hu, Macarena Lagos, and Robert M. Wald. “Phase effects from strong gravitational lensing of gravitational waves.” In: (Aug. 2020). arXiv: [2008.12814](https://arxiv.org/abs/2008.12814) [gr-qc].
- [425] Hang Yu and Yanbei Chen. “A Direct Determination of Supermassive Black Hole Properties with Gravitational-wave Radiation from Surrounding Stellar-mass Black Hole Binaries.” In: (Sept. 2020). arXiv: [2009.02579](https://arxiv.org/abs/2009.02579) [gr-qc].
- [426] E. M. Purcell, H. C. Torrey, and R. V. Pound. “Resonance Absorption by Nuclear Magnetic Moments in a Solid.” In: *Phys. Rev.* 69 (1-2 1946), pp. 37–38. DOI: [10.1103/PhysRev.69.37](https://doi.org/10.1103/PhysRev.69.37). URL: <https://link.aps.org/doi/10.1103/PhysRev.69.37>.
- [427] C. Sauvan, J. P. Hugonin, I. S. Maksymov, and P. Lalanne. “Theory of the Spontaneous Optical Emission of Nanosize Photonic and Plasmon Resonators.” In: *Phys. Rev. Lett.* 110 (23 2013), p. 237401. DOI: [10.1103/PhysRevLett.110.237401](https://doi.org/10.1103/PhysRevLett.110.237401). URL: <https://link.aps.org/doi/10.1103/PhysRevLett.110.237401>.
- [428] Jonathan Thornburg, Barry Wardell, and Maarten van de Meent. “Excitation of Kerr quasinormal modes in extreme-mass-ratio inspirals.” In: *Phys. Rev. Res.* 2.1 (2020), p. 013365. DOI: [10.1103/PhysRevResearch.2.013365](https://doi.org/10.1103/PhysRevResearch.2.013365). arXiv: [1906.06791](https://arxiv.org/abs/1906.06791) [gr-qc].
- [429] Richard H. Price, Sourabh Nampalliwar, and Gaurav Khanna. “Black hole binary inspiral: Analysis of the plunge.” In: *Phys. Rev. D* 93.4 (2016), p. 044060. DOI: [10.1103/PhysRevD.93.044060](https://doi.org/10.1103/PhysRevD.93.044060). arXiv: [1508.04797](https://arxiv.org/abs/1508.04797) [gr-qc].
- [430] Emanuele Berti, Vitor Cardoso, and Marc Casals. “Eigenvalues and eigenfunctions of spin-weighted spheroidal harmonics in four and higher dimensions.” In: *Phys. Rev. D* 73 (2006). [Erratum: *Phys.Rev.D* 73, 109902 (2006)], p. 024013. DOI: [10.1103/PhysRevD.73.109902](https://doi.org/10.1103/PhysRevD.73.109902). arXiv: [gr-qc/0511111](https://arxiv.org/abs/gr-qc/0511111).
- [431] Leonardo Gualtieri, Emanuele Berti, Vitor Cardoso, and Ulrich Sperhake. “Transformation of the multipolar components of gravitational radiation under rotations and boosts.” In: *Phys. Rev. D* 78 (2008), p. 044024. DOI: [10.1103/PhysRevD.78.044024](https://doi.org/10.1103/PhysRevD.78.044024). arXiv: [0805.1017](https://arxiv.org/abs/0805.1017) [gr-qc].
- [432] Alexei Starobinsky and Semyon Churilov. “Amplification of electromagnetic and gravitational waves scattered by a rotating.” In: *Journal of Experimental and Theoretical Physics - J EXP THEOR PHYS* 38 (Jan. 1974).
- [433] S. A. Teukolsky and W. H. Press. “Perturbations of a rotating black hole. III. Interaction of the hole with gravitational and electromagnetic radiation.” In: *The Astrophysics Journal* 193 (Oct. 1974), pp. 443–461. DOI: [10.1086/153180](https://doi.org/10.1086/153180).

- [434] *Black Hole Perturbation Toolkit*. (bhptoolkit.org).
- [435] Jose María Ezquiaga, Wayne Hu, and Macarena Lagos. “Apparent Superluminality of Lensed Gravitational Waves.” In: (May 2020). arXiv: [2005.10702](https://arxiv.org/abs/2005.10702) [[astro-ph.CO](#)].
- [436] J. G. Hills. “Hyper-velocity and tidal stars from binaries disrupted by a massive Galactic black hole.” In: *Nature* 331.6158 (Feb. 1988), pp. 687–689. doi: [10.1038/331687a0](https://doi.org/10.1038/331687a0).
- [437] Eric Addison, Pablo Laguna, and Shane Larson. “Busting Up Binaries: Encounters Between Compact Binaries and a Supermassive Black Hole.” In: (Jan. 2015). arXiv: [1501.07856](https://arxiv.org/abs/1501.07856) [[astro-ph.HE](#)].
- [438] Haruka Suzuki, Yusuke Nakamura, and Shoichi Yamada. “General Relativistic Effects on Hill Stability of Multi-Body Systems I: Stability of Three-Body Systems Containing a Massive Black Hole.” In: (Sept. 2020). arXiv: [2009.06999](https://arxiv.org/abs/2009.06999) [[gr-qc](#)].
- [439] Harriet Brown, Shiho Kobayashi, Elena M. Rossi, and Re’em Sari. “Tidal Disruption of Inclined or Eccentric Binaries by Massive Black Holes.” In: *Mon. Not. Roy. Astron. Soc.* 477.4 (2018), pp. 5682–5691. doi: [10.1093/mnras/sty1069](https://doi.org/10.1093/mnras/sty1069). arXiv: [1804.02911](https://arxiv.org/abs/1804.02911) [[astro-ph.HE](#)].
- [440] Paul I. Jefremov, Oleg Yu. Tsupko, and Gennady S. Bisnovatyi-Kogan. “Innermost stable circular orbits of spinning test particles in Schwarzschild and Kerr space-times.” In: *Phys. Rev. D* 91.12 (2015), p. 124030. doi: [10.1103/PhysRevD.91.124030](https://doi.org/10.1103/PhysRevD.91.124030). arXiv: [1503.07060](https://arxiv.org/abs/1503.07060) [[gr-qc](#)].
- [441] Laura Bernard, Vitor Cardoso, Taishi Ikeda, and Miguel Zilhão. “Physics of black hole binaries: Geodesics, relaxation modes, and energy extraction.” In: *Phys. Rev. D* 100.4 (2019), p. 044002. doi: [10.1103/PhysRevD.100.044002](https://doi.org/10.1103/PhysRevD.100.044002). arXiv: [1905.05204](https://arxiv.org/abs/1905.05204) [[gr-qc](#)].
- [442] Taishi Ikeda, Laura Bernard, Vitor Cardoso, and Miguel Zilhão. “Black hole binaries and light fields: gravitational molecules.” In: (Sept. 2020). arXiv: [2010.00008](https://arxiv.org/abs/2010.00008) [[gr-qc](#)].
- [443] Kip S. Thorne and Alfonso Campolattaro. “Non-Radial Pulsation of General-Relativistic Stellar Models. I. Analytic Analysis for $L \geq 2$.” In: *The Astrophysical Journal* 149 (Sept. 1967), p. 591. doi: [10.1086/149288](https://doi.org/10.1086/149288).
- [444] Steven L. Detweiler and L. Lindblom. “On the nonradial pulsations of general relativistic stellar models.” In: *Astrophys. J.* 292 (1985), pp. 12–15. doi: [10.1086/163127](https://doi.org/10.1086/163127).
- [445] Subrahmanyan Chandrasekhar and V. Ferrari. “On the non-radial oscillations of a star.” In: *Proc. Roy. Soc. Lond. A* 432 (1991). Ed. by K. C. Wali, pp. 247–279. doi: [10.1098/rspa.1991.0016](https://doi.org/10.1098/rspa.1991.0016).

- [446] Y. Kojima. “Equations governing the nonradial oscillations of a slowly rotating relativistic star.” In: *Phys. Rev. D* 46 (1992), pp. 4289–4303. DOI: [10.1103/PhysRevD.46.4289](https://doi.org/10.1103/PhysRevD.46.4289).
- [447] Gabrielle Allen, Nils Andersson, Kostas D. Kokkotas, and Bernard F. Schutz. “Gravitational waves from pulsating stars: Evolving the perturbation equations for a relativistic star.” In: *Phys. Rev. D* 58 (1998), p. 124012. DOI: [10.1103/PhysRevD.58.124012](https://doi.org/10.1103/PhysRevD.58.124012). arXiv: [gr-qc/9704023](https://arxiv.org/abs/gr-qc/9704023).
- [448] Olivier Sarbach and Manuel Tiglio. “Gauge invariant perturbations of Schwarzschild black holes in horizon penetrating coordinates.” In: *Phys. Rev. D* 64 (2001), p. 084016. DOI: [10.1103/PhysRevD.64.084016](https://doi.org/10.1103/PhysRevD.64.084016). arXiv: [gr-qc/0104061](https://arxiv.org/abs/gr-qc/0104061).
- [449] W. Jaffe. “A simple model for the distribution of light in spherical galaxies.” In: *Monthly Notices of The Royal Astronomical Society* 202 (Mar. 1983), pp. 995–999. DOI: [10.1093/mnras/202.4.995](https://doi.org/10.1093/mnras/202.4.995).
- [450] Ivan King. “The structure of star clusters. I. an empirical density law.” In: *The Astrophysical Journal* 67 (Oct. 1962), p. 471. DOI: [10.1086/108756](https://doi.org/10.1086/108756).
- [451] Albert Einstein. “On a stationary system with spherical symmetry consisting of many gravitating masses.” In: *Annals Math.* 40 (1939), pp. 922–936. DOI: [10.2307/1968902](https://doi.org/10.2307/1968902).
- [452] Andrea Geralico, Francesca Pompei, and Remo Ruffini. “On Einstein clusters.” In: *Int. J. Mod. Phys. Conf. Ser.* 12 (2012). Ed. by Remo Ruffini, pp. 146–173. DOI: [10.1142/S2010194512006356](https://doi.org/10.1142/S2010194512006356).
- [453] H. C. Plummer. “On the problem of distribution in globular star clusters.” In: *Monthly Notices of the Royal Astronomical Society* 71 (Mar. 1911), pp. 460–470. DOI: [10.1093/mnras/71.5.460](https://doi.org/10.1093/mnras/71.5.460).
- [454] Kazunori Akiyama et al. “First M87 Event Horizon Telescope Results. I. The Shadow of the Supermassive Black Hole.” In: *Astrophys. J. Lett.* 875 (2019), p. L1. DOI: [10.3847/2041-8213/ab0ec7](https://doi.org/10.3847/2041-8213/ab0ec7). arXiv: [1906.11238](https://arxiv.org/abs/1906.11238) [[astro-ph.GA](https://arxiv.org/abs/1906.11238)].
- [455] Aron Jansen. “Overdamped modes in Schwarzschild-de Sitter and a Mathematica package for the numerical computation of quasinormal modes.” In: *Eur. Phys. J. Plus* 132.12 (2017), p. 546. DOI: [10.1140/epjp/i2017-11825-9](https://doi.org/10.1140/epjp/i2017-11825-9). arXiv: [1709.09178](https://arxiv.org/abs/1709.09178) [[gr-qc](https://arxiv.org/abs/1709.09178)].
- [456] Vitor Cardoso, Joao L. Costa, Kyriakos Destounis, Peter Hintz, and Aron Jansen. “Quasinormal modes and Strong Cosmic Censorship.” In: *Phys. Rev. Lett.* 120.3 (2018), p. 031103. DOI: [10.1103/PhysRevLett.120.031103](https://doi.org/10.1103/PhysRevLett.120.031103). arXiv: [1711.10502](https://arxiv.org/abs/1711.10502) [[gr-qc](https://arxiv.org/abs/1711.10502)].

- [457] Vitor Cardoso, Caio F. B. Macedo, Paolo Pani, and Valeria Ferrari. “Black holes and gravitational waves in models of minicharged dark matter.” In: *JCAP* 05 (2016). [Erratum: *JCAP* 04, E01 (2020)], p. 054. DOI: [10.1088/1475-7516/2016/05/054](https://doi.org/10.1088/1475-7516/2016/05/054). arXiv: [1604.07845](https://arxiv.org/abs/1604.07845) [hep-ph].
- [458] E. S. C. Ching, P. T. Leung, W. M. Suen, and K. Young. “Wave propagation in gravitational systems: Late time behavior.” In: *Phys. Rev. D* 52 (1995), pp. 2118–2132. DOI: [10.1103/PhysRevD.52.2118](https://doi.org/10.1103/PhysRevD.52.2118). arXiv: [gr-qc/9507035](https://arxiv.org/abs/gr-qc/9507035).
- [459] Shahar Hod and Tsvi Piran. “Late time tails in gravitational collapse of a selfinteracting (massive) scalar field and decay of a selfinteracting scalar hair.” In: *Phys. Rev. D* 58 (1998), p. 044018. DOI: [10.1103/PhysRevD.58.044018](https://doi.org/10.1103/PhysRevD.58.044018). arXiv: [gr-qc/9801059](https://arxiv.org/abs/gr-qc/9801059).
- [460] Hiroko Koyama and Akira Tomimatsu. “Asymptotic tails of massive scalar fields in Schwarzschild background.” In: *Phys. Rev. D* 64 (2001), p. 044014. DOI: [10.1103/PhysRevD.64.044014](https://doi.org/10.1103/PhysRevD.64.044014). arXiv: [gr-qc/0103086](https://arxiv.org/abs/gr-qc/0103086).
- [461] Marc Favata. “The gravitational-wave memory effect.” In: *Class. Quant. Grav.* 27 (2010). Ed. by Zsuzsa Marka and Szabolcs Marka, p. 084036. DOI: [10.1088/0264-9381/27/8/084036](https://doi.org/10.1088/0264-9381/27/8/084036). arXiv: [1003.3486](https://arxiv.org/abs/1003.3486) [gr-qc].
- [462] Demetrios Christodoulou. “Nonlinear nature of gravitation and gravitational-wave experiments.” In: *Phys. Rev. Lett.* 67 (12 1991), pp. 1486–1489. DOI: [10.1103/PhysRevLett.67.1486](https://doi.org/10.1103/PhysRevLett.67.1486). URL: <https://link.aps.org/doi/10.1103/PhysRevLett.67.1486>.
- [463] Clemente Smarra et al. “The second data release from the European Pulsar Timing Array: VI. Challenging the ultralight dark matter paradigm.” In: (June 2023). arXiv: [2306.16228](https://arxiv.org/abs/2306.16228) [astro-ph.HE].
- [464] Anish Ghoshal and Alessandro Strumia. “Probing the Dark Matter density with gravitational waves from super-massive binary black holes.” In: (June 2023). arXiv: [2306.17158](https://arxiv.org/abs/2306.17158) [astro-ph.CO].
- [465] John Ellis, Malcolm Fairbairn, Gert Hütsi, Juhan Raidal, Juan Urrutia, Ville Vaskonen, and Hardi Veermäe. “Gravitational Waves from SMBH Binaries in Light of the NANOGrav 15-Year Data.” In: (June 2023). arXiv: [2306.17021](https://arxiv.org/abs/2306.17021) [astro-ph.CO].
- [466] Adeela Afzal et al. “The NANOGrav 15 yr Data Set: Search for Signals from New Physics.” In: *Astrophys. J. Lett.* 951.1 (2023), p. L11. DOI: [10.3847/2041-8213/acdc91](https://doi.org/10.3847/2041-8213/acdc91). arXiv: [2306.16219](https://arxiv.org/abs/2306.16219) [astro-ph.HE].
- [467] R. A. Konoplya and A. Zhidenko. “Solutions of the Einstein Equations for a Black Hole Surrounded by a Galactic Halo.” In: *Astrophys. J.* 933.2 (2022), p. 166. DOI: [10.3847/1538-4357/ac76bc](https://doi.org/10.3847/1538-4357/ac76bc). arXiv: [2202.02205](https://arxiv.org/abs/2202.02205) [gr-qc].

- [468] Kyriakos Destounis, Arun Kulathingal, Kostas D. Kokkotas, and Georgios O. Papadopoulos. “Gravitational-wave imprints of compact and galactic-scale environments in extreme-mass-ratio binaries.” In: *Phys. Rev. D* 107.8 (2023), p. 084027. DOI: [10.1103/PhysRevD.107.084027](https://doi.org/10.1103/PhysRevD.107.084027). arXiv: [2210.09357](https://arxiv.org/abs/2210.09357) [gr-qc].
- [469] Enzo Figueiredo, Andrea Maselli, and Vitor Cardoso. “Black holes surrounded by generic dark matter profiles: appearance and gravitational-wave emission.” In: (Mar. 2023). arXiv: [2303.08183](https://arxiv.org/abs/2303.08183) [gr-qc].
- [470] Yuqian Zhao, Bing Sun, Kai Lin, and Zhoujian Cao. “The Gravitational Ringing of a Spherically Symmetric Black Hole Surrounded by Dark Matter Spike.” In: (Mar. 2023). arXiv: [2303.09215](https://arxiv.org/abs/2303.09215) [gr-qc].
- [471] Ning Dai, Yungui Gong, Yang Zhao, and Tong Jiang. “Extreme mass ratio inspirals in galaxies with dark matter halos.” In: (Jan. 2023). arXiv: [2301.05088](https://arxiv.org/abs/2301.05088) [gr-qc].
- [472] Ramin G. Daghighi and Gabor Kunstatter. “Spacetime Metrics and Ringdown Waveforms for Galactic Black Holes Surrounded by a Dark Matter Spike.” In: *Astrophys. J.* 940.1 (2022), p. 33. DOI: [10.3847/1538-4357/ac940b](https://doi.org/10.3847/1538-4357/ac940b). arXiv: [2206.04195](https://arxiv.org/abs/2206.04195) [astro-ph.GA].
- [473] Takahisa Igata, Tomohiro Harada, Hiromi Saida, and Yohsuke Takamori. “Periastron shifts in dark matter distribution around a black hole.” In: (Jan. 2022). arXiv: [2202.00202](https://arxiv.org/abs/2202.00202) [gr-qc].
- [474] Chao Zhang, Tao Zhu, and Anzhong Wang. “Gravitational axial perturbations of Schwarzschild-like black holes in dark matter halos.” In: *Phys. Rev. D* 104.12 (2021), p. 124082. DOI: [10.1103/PhysRevD.104.124082](https://doi.org/10.1103/PhysRevD.104.124082). arXiv: [2111.04966](https://arxiv.org/abs/2111.04966) [gr-qc].
- [475] Christopher Moore, Alvin Chua, and Jonathan Gair. “Gravitational waves from extreme mass ratio inspirals around bumpy black holes.” In: *Classical and Quantum Gravity* 34 (Oct. 2017). DOI: [10.1088/1361-6382/aa85fa](https://doi.org/10.1088/1361-6382/aa85fa).
- [476] Kyriakos Destounis and Kostas D. Kokkotas. “Gravitational-wave glitches: Resonant islands and frequency jumps in nonintegrable extreme-mass-ratio inspirals.” In: *Phys. Rev. D* 104.6 (2021), p. 064023. DOI: [10.1103/PhysRevD.104.064023](https://doi.org/10.1103/PhysRevD.104.064023). arXiv: [2108.02782](https://arxiv.org/abs/2108.02782) [gr-qc].
- [477] Kyriakos Destounis, Federico Angeloni, Massimo Vaglio, and Paolo Pani. “Extreme-mass-ratio inspirals into rotating boson stars: nonintegrability, chaos, and transient resonances.” In: (May 2023). arXiv: [2305.05691](https://arxiv.org/abs/2305.05691) [gr-qc].
- [478] *grit repo.* (centra.tecnico.ulisboa.pt/network/grit/files/).

- [479] Lorenzo Annulli, Vitor Cardoso, and Rodrigo Vicente. “Stirred and shaken: Dynamical behavior of boson stars and dark matter cores.” In: *Phys. Lett. B* 811 (2020), p. 135944. DOI: [10.1016/j.physletb.2020.135944](https://doi.org/10.1016/j.physletb.2020.135944). arXiv: [2007.03700](https://arxiv.org/abs/2007.03700) [astro-ph.HE].
- [480] Jorge F. M. Delgado, Carlos A. R. Herdeiro, and Eugen Radu. “EMRIs around $j = 1$ black holes with synchronised hair.” In: (May 2023). arXiv: [2305.02333](https://arxiv.org/abs/2305.02333) [gr-qc].
- [481] Shaun David Brocus Fell, Lavinia Heisenberg, and Doğa Veske. “Detecting Fundamental Vector Fields with LISA.” In: (Apr. 2023). arXiv: [2304.14129](https://arxiv.org/abs/2304.14129) [gr-qc].
- [482] Steven A. Balbus and John F. Hawley. “A Powerful Local Shear Instability in Weakly Magnetized Disks. I. Linear Analysis.” In: *Astrophys. J.* 376 (July 1991), p. 214. DOI: [10.1086/170270](https://doi.org/10.1086/170270).
- [483] Andrea Taracchini et al. “Effective-one-body model for black-hole binaries with generic mass ratios and spins.” In: *Phys. Rev. D* 89.6 (2014), p. 061502. DOI: [10.1103/PhysRevD.89.061502](https://doi.org/10.1103/PhysRevD.89.061502). arXiv: [1311.2544](https://arxiv.org/abs/1311.2544) [gr-qc].
- [484] Alejandro Bohé et al. “Improved effective-one-body model of spinning, nonprecessing binary black holes for the era of gravitational-wave astrophysics with advanced detectors.” In: *Phys. Rev. D* 95.4 (2017), p. 044028. DOI: [10.1103/PhysRevD.95.044028](https://doi.org/10.1103/PhysRevD.95.044028). arXiv: [1611.03703](https://arxiv.org/abs/1611.03703) [gr-qc].
- [485] Sascha Husa, Sebastian Khan, Mark Hannam, Michael Pürrer, Frank Ohme, Xisco Jiménez Forteza, and Alejandro Bohé. “Frequency-domain gravitational waves from nonprecessing black-hole binaries. I. New numerical waveforms and anatomy of the signal.” In: *Phys. Rev. D* 93.4 (2016), p. 044006. DOI: [10.1103/PhysRevD.93.044006](https://doi.org/10.1103/PhysRevD.93.044006). arXiv: [1508.07250](https://arxiv.org/abs/1508.07250) [gr-qc].
- [486] Sebastian Khan, Sascha Husa, Mark Hannam, Frank Ohme, Michael Pürrer, Xisco Jiménez Forteza, and Alejandro Bohé. “Frequency-domain gravitational waves from nonprecessing black-hole binaries. II. A phenomenological model for the advanced detector era.” In: *Phys. Rev. D* 93.4 (2016), p. 044007. DOI: [10.1103/PhysRevD.93.044007](https://doi.org/10.1103/PhysRevD.93.044007). arXiv: [1508.07253](https://arxiv.org/abs/1508.07253) [gr-qc].
- [487] Andrea Maselli, Nicola Franchini, Leonardo Gualtieri, Thomas P. Sotiriou, Susanna Barsanti, and Paolo Pani. “Detecting new fundamental fields with LISA.” In: (June 2021). arXiv: [2106.11325](https://arxiv.org/abs/2106.11325) [gr-qc].
- [488] Don N. Page. “Classical and quantum decay of oscillatons: Oscillating selfgravitating real scalar field solitons.” In: *Phys. Rev. D* 70 (2004), p. 023002. DOI: [10.1103/PhysRevD.70.023002](https://doi.org/10.1103/PhysRevD.70.023002). arXiv: [gr-qc/0310006](https://arxiv.org/abs/gr-qc/0310006) [gr-qc].

- [489] Daniel Baumann, Horng Sheng Chia, John Stout, and Lotte ter Haar. "The Spectra of Gravitational Atoms." In: *JCAP* 12 (2019), p. 006. DOI: [10.1088/1475-7516/2019/12/006](https://doi.org/10.1088/1475-7516/2019/12/006). arXiv: [1908.10370](https://arxiv.org/abs/1908.10370) [gr-qc].
- [490] D.J. Griffiths. *Introduction to Quantum Mechanics*. Cambridge University Press, 2017. ISBN: 9781107179868. URL: <https://books.google.pt/books?id=0h-nDAAAQBAJ>.
- [491] J.J. Sakurai and J. Napolitano. *Modern Quantum Mechanics*. Addison Wesley, 2011. ISBN: 9780805382914. URL: <https://books.google.pt/books?id=N4I-AQAACAAJ>.
- [492] C. T. Cunningham. "Optical appearance of distant objects to observers near and inside a Schwarzschild black hole." In: *Physical Review D* 12.2 (July 1975), pp. 323–328. DOI: [10.1103/PhysRevD.12.323](https://doi.org/10.1103/PhysRevD.12.323).
- [493] A. Siwek, B. Kusmierz, P. Gusin, J. Masajada, and A. Radosz. "Perceiving light rays above and below the horizon of a black hole in Schwarzschild spacetime." In: *J. Phys. Conf. Ser.* 574.1 (2015). Ed. by Elias C. Vagenas and Dimitros S. Vlachos, p. 012060. DOI: [10.1088/1742-6596/574/1/012060](https://doi.org/10.1088/1742-6596/574/1/012060).
- [494] Steven L. Detweiler and Eric Poisson. "Low multipole contributions to the gravitational selfforce." In: *Phys. Rev. D* 69 (2004), p. 084019. DOI: [10.1103/PhysRevD.69.084019](https://doi.org/10.1103/PhysRevD.69.084019). arXiv: [gr-qc/0312010](https://arxiv.org/abs/gr-qc/0312010).

DECLARATION

I declare that this document is an original work of my own and that it fulfills all the requirements of the Code of Conduct and Good Practices of the Universidade de Lisboa.

Name: Francisco Miguel Batista Duque
Student number: 84383

Lisbon, June 2023

Francisco Miguel Batista Duque

COLOPHON

This document was typeset using the typographical look-and-feel classicthesis developed by André Miede and Ivo Pletikosić. The style was inspired by Robert Bringhurst's seminal book on typography "*The Elements of Typographic Style*".

Final Version as of August 9, 2023 (draft v1).